AGH UNIVERSITY OF KRAKOW

FIELD OF SCIENCE: ENGINEERING AND TECHNOLOGY

SCIENTIFIC DISCIPLINE: AUTOMATION, ELECTRONIC, ELECTRICAL ENGINEERING AND SPACE TECHNOLOGIES

DOCTORAL DISSERTATION

Modeling and Analysis of Magnetic Components used in High-Frequency Power Electronics Systems

Author: **Piotr Szczerba, MSc**

Supervisor: Cezary Worek, PhD, DSc, Associate Professor

Completed at: AGH University of Krakow, Faculty of Computer Science, Electronics and Telecommunications, Institute of Electronics

Krakow, 2025

AKADEMIA GÓRNICZO-HUTNICZA IM. STANISŁAWA STASZICA W KRAKOWIE

DZIEDZINA: NAUKI INŻYNIERYJNO-TECHNICZNE

DYSCYPLINA: AUTOMATYKA, ELEKTRONIKA, ELEKTROTECHNIKA I TECHNOLOGIE KOSMICZNE

ROZPRAWA DOKTORSKA

Modelowanie i Analiza Elementów Magnetycznych Pracujących w Wysokoczęstotliwościowych Układach Energoelektronicznych

Autor: **mgr inż. Piotr Szczerba**

Promotor rozprawy: dr hab. inż. Cezary Worek, prof. AGH

Praca wykonana: Akademia Górniczo-Hutnicza w Krakowie, Wydział Informatyki, Elektroniki i Telekomunikacji, Instytut Elektroniki

Kraków, 2025

To Ania and Natalia, my two beloved ladies

Abstract

In high-frequency power electronic applications, power inductors often account for the majority of power losses, physical volume, and overall cost. Therefore, this research among other things addresses existing and proposes improved calculation and measurement techniques for the complex permeability and core power loss in ferrite-based magnetic components used in SMPSs. The new complex permeability measurement and calculation technique uses a series equivalent inductor model with a single fitting variable to closely reflect the physical behavior of the magnetic component and ensures accurate permeability estimation regardless of the inductor's size, geometry, winding configuration, or frequency range. The validation of the proposed model is performed both mathematically and through test-bench measurements. The results show that, if the inductor stray capacitor ESR loss tangent is correctly defined, then it is possible to obtain a relative fitting error of less than 2% across the entire frequency range. Based on complex permeability measurements, an enhanced inductor model is introduced, separating stray capacitance into winding- and core-related components, thereby improving AC loss modelling in SPICE based simulations. Regarding the core loss, a new core loss model dedicated to sinusoidal and rectangular AC voltages, called here an improved RESE (iRESE), is proposed. The iRESE extends the RESE by unifying the Steinmetz-based core loss model with the small-signal complex permeability model to comprehensively complete the entire core loss characteristics, regardless of the magnitude of the excitation signals, which was not previously possible. Moreover, it also considers the rectangular excitation of signals and the DC bias phenomenon commonly present in SMPSs, along with the magnetic permeability roll-off near the core saturation level and the influence of temperature changes. The model is structured to be modular, meaning that each part of it can be used separately according to the intended application. This is a unique approach that provides engineers and scientists with all the required information regarding core loss at once, as well as the flexibility to choose the approach depending on the application they are working on. The method was validated through test-bench measurements and includes error analysis to identify limitations in both

simulation and measurement setups. The results show a very good agreement between measurements and fitting results. However, the up-to-date SPICE simulation results are less precise due to the incomplete non-linear magnetizing current model, which is scheduled for future work. Although, developed for SMPSs, the approach is also applicable to other systems that use non-sinusoidal waveforms, such as electric vehicle inverters and wireless power systems.

Abstrakt

W wysokoczęstotliwościowych impulsowych przekształtnikach energoelektronicznych, elementy magnetyczne odpowiadają za większość strat mocy, objętość i koszt końcowego produktu. W związku z tym, niniejsza praca w głównej mierze skupia się na nowej metodzie pomiaru i obliczania przenikalności magnetycznej oraz strat w rdzeniach ferrytowych. Zaproponowana metoda pomiaru i obliczania zespolonej przenikalności magnetycznej oparta jest na szeregowym zastępczym modelu dławika z jedną zmienną dopasowującą. Takie podejście pozwala na wierne i fizyczne odwzorowanie zachowania elementu magnetycznego, a użycie jednej zmiennej dopasowującej zapewnia wysoką dokładność dopasowania, a także umożliwia precyzyjne obliczenie zespolonej przenikalności magnetycznej, niezależnie od rozmiaru, kształtu, konfiguracji uzwojenia czy częstotliwości pracy dławika. Weryfikacja zaproponowanego modelu została przeprowadzona matematycznie oraz za pomocą pomiarów na testowym stanowisku laboratoryjnym, osiągając błąd dopasowania poniżej 2% w całym przedziale badanej częstotliwości. Bazując na pomiarach laboratoryjnych skonstruowano ulepszony model obwodowy dławika. Model ten dzieli pojemność pasożytniczą na dwie części: jedną związaną z uzwojeniami oraz drugą związaną z rdzeniem, a także wprowadza częstotliwościowo zależną wartością ESR kondensatora pasożytniczego. Te wyniki mogą pomóc w opracowaniu ulepszonych modeli strat dławików oraz uniwersalnych modeli symulacyjnych (np. modeli SPICE). Praca wprowadza także nowy model strat mocy w rdzeniu – iRESE, będący rozwinięciem modelu RESE. Model iRESE rozszerza RESE poprzez unifikację modelu strat w rdzeniu opartym na równaniu Steinmetza z modelem małosygnałowym zespolonej przenikalności magnetycznej, aby kompleksowo opisać charakterystyki strat w rdzeniu bez względu na amplitudę sygnałów wzbudzenia, co wcześniej nie było możliwe. Dodatkowo zaproponowana metoda uwzględnia prostokątne sygnały wzbudzenia wraz ze składową stałą, co jest zjawiskiem powszechnie występującym w SMPS, a także spadek przenikalności magnetycznej w pobliżu nasycenia rdzenia oraz wpływ zmian temperatury na straty. Oprócz tego, model zbudowany jest modułowo, co

oznacza, że każda jego część może być użyta niezależnie. Jest to unikalne podejście, które dostarcza inżynierom i naukowcom wszelkich niezbędnych informacji dotyczących strat w rdzeniu, a jednocześnie daje swobodę wyboru metody w zależności od konkretnej aplikacji, nad którą pracują. Zaproponowana metoda została zweryfikowana podczas pomiarów laboratoryjnych, a także zawiera analizę błędów w celu identyfikacji potencjalnych ograniczeń symulacyjnych jak i pomiarowych. Wyniki wykazują bardzo dobrą zgodność pomiarów z wynikami dopasowania, jednak bieżące wyniki symulacji obwodowej SPICE są jeszcze mało precyzyjne z powodu niekompletnego nieliniowego modelu prądu magnesującego, którego rozbudowa planowana jest w następnej fazie prac badawczych. Choć zaproponowana metoda została opracowana dla zasilaczy impulsowych, można ją także stosować w innych systemach wykorzystujących przebiegi niesinusoidalne, takich jak np. falowniki pojazdów elektrycznych i bezprzewodowe systemy zasilania.

Acknowledgements

The possibility of being a doctor, not a medicine doctor in fact, but rather a doctor in the field of engineering was always a dream of mine. The dream I've been having since I graduated from my first alma mater over twenty years ago.

However, being a doctor is not an easy task, after all. If you want to start a PhD, except for being a highly motivated hard worker you must be a very, very lucky guy. The luck is to meet the right people at the right time, and I have met them, finally!

Therefore, I would like to thank, first and foremost, my supervisor, Cezary Worek, PhD, DSc, Associate Professor at AGH, for giving me the opportunity to start this PhD journey and for his valuable advice during the entire research process.

Additionally, the research would not have been possible without my industrial co-supervisor, Mr. Slawomir Ligenza, the Engineering Manager at Fideltronik Poland Sp. z o. o. R&D Center. Slawek, thanks a million for supporting me directly from day one and for your most precious technical knowledge.

My gratitude also goes to the management board of Fideltronik Poland Sp. z o. o. and Institute of Electronics at AGH for the extra out-of-duty time so much needed to do this research, for the financial support and also for the limitless access to the lab equipment. I really appreciate it.

The process of carrying out the PhD research and writing the dissertation is a difficult one, no doubt about that. The countless hours spent on doing experiments, calculations, reading and writing vast numbers of scientific papers take a toll on any researcher. During these harsh times, you need people around you to support you, give courage and strength to proceed ahead. These people are your family, the most important people in your life.

Ania, thank you very much for your patience and understanding. Natalka, I will not forget to the end of my days the times when you were telling me: “Daddy, I am your whole world, not your little PhD and your little papers. Put it away…” Yes, you are my whole world, darling. I do put it away. Girls, I love you so much.

Sincerely,

Piotr Szczerba

Table of Contents

List of Figures

List of Tables

List of Symbols

$\boldsymbol{cos}$	Cosine
$\boldsymbol{cosh}$	Hyperbolic Cosine
$\boldsymbol{coth}$	Hyperbolic Cotangent
$\boldsymbol{D}$	Converter Duty-Cycle Ratio
$\boldsymbol{D_{OUT}}$	Duty-Cycle Ratio Related to Secondary Side of Flyback Converter
$\boldsymbol{E}$	Electric Field [V/m]
$\boldsymbol{H_1, H_2}$	Complex Constants in Helmholtz Equation
$\boldsymbol{\widehat{I_m}}$	Magnitude of Magnetizing Current [A]
$\boldsymbol{I_p}$	Primary Inductor Current of Flyback Converter [A]
$\boldsymbol{J}$	Current Density [A/m^2]
$\boldsymbol{L_P}$	Primary Inductance of Flyback Converter [H]
$\boldsymbol{M_{nrev}}$	Non-Reversible Magnetization [A/m]
$\boldsymbol{M_s}$	Saturation Magnetization [A/m]
$\boldsymbol{\nabla}$	Three-Dimensional Gradient Operator (Nabla)
$\boldsymbol{N_l}$	Winding Number of Layers
$\boldsymbol{P_{IN}}$	Input Power of Flyback Converter [W]
$\boldsymbol{P_{OUT}}$	Output Power of Flyback Converter [W]
$\boldsymbol{\rho_w}$	Winding Conductor Resistivity [$\Omega \cdot m$]
$\boldsymbol{R_{wDC}}$	DC Resistance of the Winding Wire [Ω]
$\boldsymbol{\sigma_w}$	Winding Conductor Conductivity [S/m]
$\boldsymbol{sin}$	Sine
$\boldsymbol{sinh}$	Hyperbolic Sine
$\boldsymbol{t_{off}}$	Converter OFF Time [s]
$\boldsymbol{t_{on}}$	Converter ON Time [s]
$\boldsymbol{T_s}$	Converter Switching Period [s]
$\boldsymbol{V_{in}}$	Converter Input Voltage [V]
$\boldsymbol{V_{IN}}$	Input Voltage of Flyback Converter [V]
$\boldsymbol{V_{out}}$	Converter Output Voltage [V]
$\boldsymbol{V_P}$	Primary Inductor Voltage of Flyback Converter [V]
$\boldsymbol{V_{RO}}$	Reflected Output Voltage to Primary Side of Flyback Converter [V]
$\boldsymbol{V_S}$	Secondary Inductor Voltage of Flyback Converter [V]
$\boldsymbol{tanh}$	Hyperbolic Tangent

List of Abbreviations

AC	Alternating Current
B-H	Magnetic Flux Density - Magnetic Field Intensity
CCM	Continuous Conduction Mode
CM	Common Mode
CoFe	Cobalt-Iron Alloy
CWH	Composite Waveform Hypothesis
DC	Direct Current
DCM	Discontinuous Conduction Mode
DM	Differential Mode
DNSE	Double Natural Steinmetz Extension
EEL	Equivalent Elliptical Loop
EFC	Equivalent Foil Conductor
EGSE	Expanded Generalized Steinmetz Equation
EMI	Electromagnetic Interference
ESR	Equivalent Series Resistance
FEM	Finite Element Method
FeSi	Iron-Silicon Alloy
FGSE	Filtered Improved Generalized Steinmetz Equation
FWC	Waveform Coefficient
GaN	Gallium Nitride
GSE	Generalized Steinmetz Equation
iGSE	Improved Generalized Steinmetz Equation
i²GSE	Improved Improved Generalized Steinmetz Equation
IC	Integrated Circuit
IGBT	Insulated Gate Bipolar Transistor
IGCC	Improved Generalized Composite Calculation
iRESE	Improved Rectangular Extension of Steinmetz Equation
ISE	Improved Steinmetz Equation
LED	Light Emitting Diode
MAG AMP	Magnetic Amplifier
MnZn	Manganese-Zinc Alloy
MOSFET	Metal Oxide Semiconductor Field Effect Transistor
MPP	Molybdenum Permalloy Powder
MSE	Modified Steinmetz Equation
NiFe	Iron-Nickel Alloy
NiZn	Nickel-Zinc Alloy
NSE	Natural Steinmetz Extension
OSE	Original Steinmetz Equation
PA11	Polyamide 11
PCB	Printed Circuit Board
PF	Power Factor
PFC	Power Factor Correction
PWL	Piece Wise Linear
PWM	Pulse Width Modulation

RESE	Rectangular Extension of Steinmetz Equation
RF	Radio Frequency
RLC	Resistor-Inductor-Capacitor
SiC	Silicon Carbide
SMPS	Switch Mode Power Supply
SPICE	Simulation Program with Integrated Circuits Emphasis
SRF	Self-Resonant Frequency
SSLE	Stenglein Steinmetz Loss Equation
TDA	Time Domain Approximation
THD	Total Harmonic Distortion
VBA	Visual Basic for Applications
VNA	Vector Network Analyzer
WcSE	Waveform Coefficient Steinmetz Equation
WPT	Wireless Power Transfer

Chapter 1

1. Introduction.

1.1 Background.

Modern lifestyles demand the use of a wide range of electronic devices, such as computers, mobile phones, and household appliances, all of which are predominantly powered by the electricity derived from the fossil fuels. Simultaneously, there is a rising concern over an air pollution and global warming, primarily driven by the greenhouse gas emissions resulting from the combustion of the coal and the oil. In response, global authorities are promoting the transition to green energy sources, including electric vehicles and renewable energy solutions such as solar and wind power. However, the effective integration and operation of these technologies would not be possible without the implementation of highly efficient power electronics systems [1].

Power electronics systems, while essential to modern energy infrastructure, face several critical challenges. Foremost among these are the growing market and consumer expectations for devices that combine high efficiency with compactness, affordability, and reliability. Meeting these demands requires a fragile trade-off between minimizing power losses and reducing physical size. As devices shrink, power density, defined as the power handled per unit volume increases, leading to greater losses and intensified thermal stress. As a result, the maximum permissible operating temperature becomes a key factor limiting the continued miniaturization of power electronic components [1].

Recent advancements in semiconductor switching technologies, particularly the adoption of wide-bandgap materials like silicon carbide (SiC) and gallium nitride (GaN), have partially addressed the challenge of low conversion efficiency in high-frequency switch-mode power supplies (SMPS). These materials offer significant advantages over traditional silicon-based devices, including superior switching speed, higher breakdown voltage, and enhanced thermal conductivity. However, while these improvements significantly boost semiconductor performance, they are not sufficient to eliminate overall efficiency limitations in power converters. This is largely due to the losses associated with the magnetic components, such as inductors and transformers, which

often dominate total power loss in high-frequency operation and remain a major constraint [2].

These components are a key element in power electronic systems, responsible for a significant portion of the power losses and the overall volume of the final power supply system solutions. For this reason, it is advisable to expand knowledge about them and be able to optimize their design. Contemporary knowledge in the field of magnetic components, although very broad, is very dispersed, and selected phenomena are described using analytical equations, empirical formulas, or complex numerical models. For example, copper losses are described by Dowell's, Ferreira's, and modified Kazimierczuk's equations or, for a specific case, simulated using the FEM method [3-9]. This makes the design process much more difficult as the designer has to go through different solution concepts and calculations to find a sufficiently accurate match. This is a highly inefficient process, both in terms of the resources used and the time needed to reach a solution.

The better visualisation of the above is shown in Figure 1. If an inductor is not well optimized, at least two outcomes might happen. One of the outcomes is the oversizing. In this case, an inductor is made larger than its optimum size. The larger inductor requires more material and takes up more space on the printed circuit board (PCB) than is actually needed. It is contrary to the market requirements for a small and inexpensive device. This outcome represents the material waste and the waste of space.

On the other hand, the second outcome is downsizing. The inductor is made smaller than its optimum. In this case, the inductor must carry an excess amount of power through a limited volume of space. This means the higher power density requires additional thermal management to address the associated hot spots. The hot spots might easily cause the entire electronic system the inductor is part of to fail, or simply the device will not meet the customer's or the standard-based requirements regarding thermal management. Both outcomes provide for one point: the waste of time and money for an already poorly designed magnetic component, and another waste of time and money, which will be incurred in the future to undertake another iteration of the entire design process to achieve the desired optimal solution.

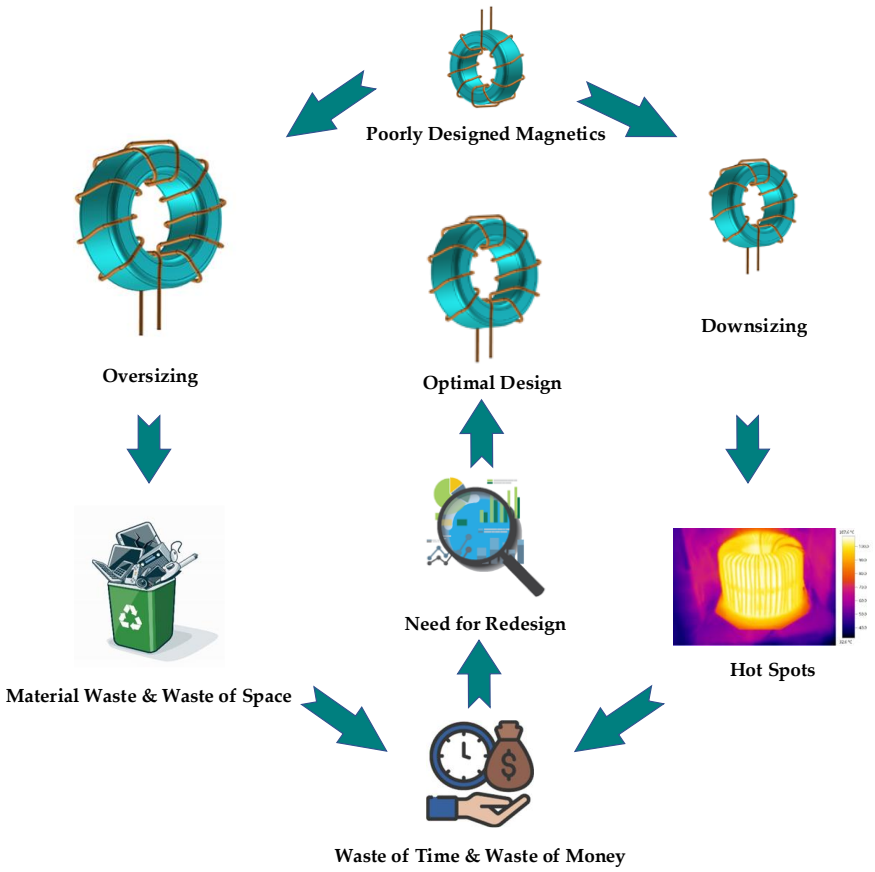

Figure 1: Magnetic Component Design Optimization Issues.

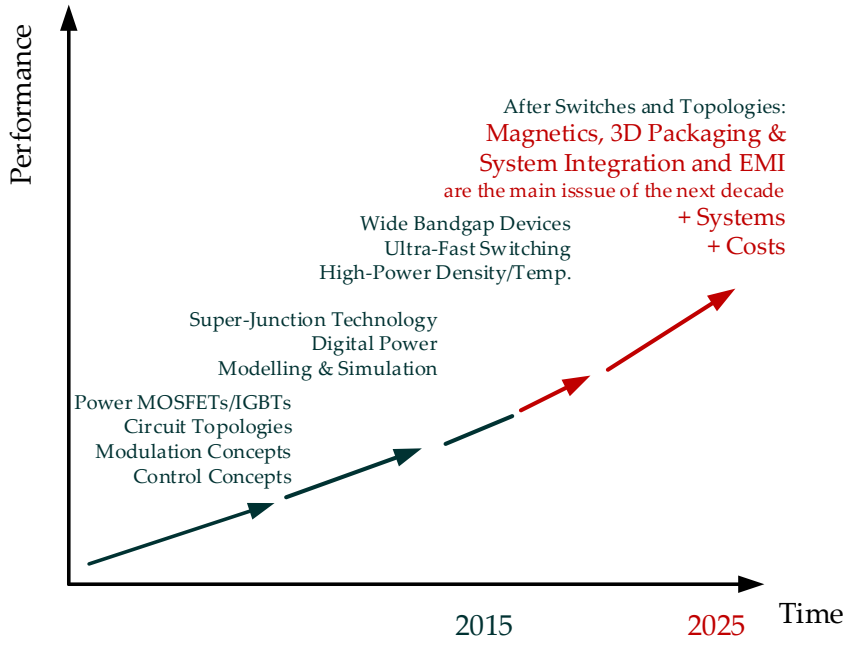

Figure 2: Power Electronics Industry Road Map and Challenges.

The power electronics industry has already foreseen these issues, pointing out that the design optimization of magnetic components is the key challenge at present, as shown in Figure 2 [10-11].

1.2 Objectives.

The research goal is to introduce innovative design and calculation procedures for calculating losses in magnetic components that are part of power electronic systems. Proven design procedures, which are based on analytical equations, empirical formulas and numerical models are a necessary condition, closely related to technical progress and the need to meet technical requirements in advanced commercial projects.
Research goals include, but are not limited to:

- Theoretical, analytical, and experimental verification of complex permeability.
- Theoretical, analytical, and experimental verification of the core loss and the core resistance.
- The design and development of the FEM models for simulation-based verification of the magnetic components' equivalent circuit models.
- The design and development of SPICE-based models for simulation-based verification of magnetic components' power loss and core resistance.
- The design of the test bench for experiments.
- Verification of presented methods and determination of their practical usefulness.
- Tools development for calculation and design of magnetic components (VBA, SMath) – verification of created tools and assessment of their practical usefulness.

1.3 Scope of the Thesis.

The thesis consists of seven chapters with the content shown in Figure 3 and described as follows:

Chapter 1 briefly discusses the background of the research and the challenges that face power electronic systems regarding market requirements for reliability, size, cost, efficiency, and associated power loss and thermal management issues. The key objectives and scope of the thesis are then defined.

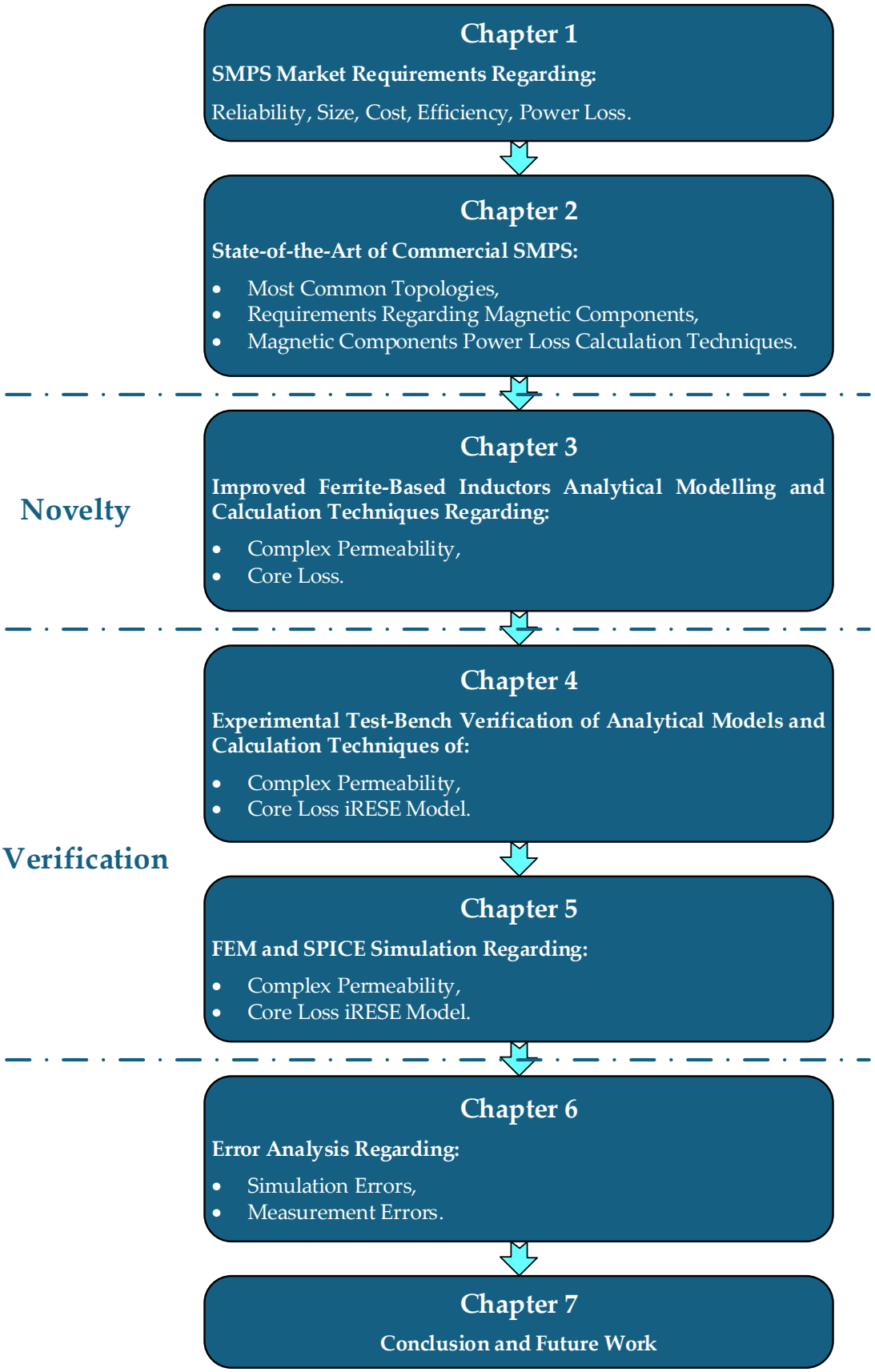

Figure 3: Structure of the PhD Dissertation.

Chapter 2 describes the most common topologies of SMPS converters, along with the requirements of the magnetic components used in commercial designs. The state-of-the-art power loss calculation techniques of the ferrite-based magnetic components are also discussed.

Chapter 3 introduces new, author-based analytical modelling and calculation techniques regarding complex permeability and core loss in ferrite-based inductors. A complex permeability iterative curve fitting technique is proposed, followed by an in-depth explanation of inductor resonance and the origin of parasitic components in the inductor equivalent model. This leads to the proposal of an improved equivalent model for the inductor, which can be further utilized in simulation software. Next, the improved RESE (iRESE) core loss model is proposed. It considers the influence of the DC bias, sinusoidal and non-sinusoidal excitation signals, permeability roll-off near saturation, and also combines two core loss models, which originate from the small- and large-signal domains. Moreover, the iRESE is structured in a modular manner, which is a unique approach. This means that each part can be used separately, according to the application it is intended for, giving engineers and scientists freedom of choice depending on the application they work on.

Chapter 4 introduces the experimental test-bench verification of the analytical models shown in Chapter 3. The chapter is split into two parts: (i) the first part deals with the small-signal measurement and calculation techniques of complex permeability using an impedance analyzer as a main tool, and (ii) the second part verifies the claims regarding the iRESE model. Firstly, verification is performed in the small-signal domain again, with the help of an impedance analyzer. At this stage, the unification of the complex permeability and Steinmetz-based core loss models occurs. Then, the model is verified in the large-signal domain by measuring the core loss of the tested inductors in a temperature-controlled environment, such as an oil bath. This is done using a two-winding method. Based on the results, curve fittings are performed to mathematically express the core loss characteristics and unify the proposed core loss model, regardless of the type of excitation signal and DC bias.

Chapter 5, through FEM and SPICE simulations, verifies the assumptions and claims made in Chapters 3 and 4, respectively. The FEM simulation has been used to verify the origin of the inductor stray capacitance; the information is required to build a precise equivalent inductor model. The SPICE simulation is used to verify the assumptions regarding the non-linear behavior of the core resistance and the core loss. This information is required to build a precise inductor SPICE model for circuit simulations.

Chapter 6, in its general form, highlights possible measurement and simulation errors and explains their origin. The identification of these errors is crucial for a better understanding of potential measurement discrepancies and their magnitude in relation to the obtained results.

Chapter 7 summarizes the dissertation, provides the final conclusion to the presented research work and describes potential areas for future development.

Chapter 2

2. Magnetic Components used in SMPS Converters.

2.1 Selected Topologies of SMPS Converters.

Over a hundred years ago, there was a war, not the First World War, one might expect, but the war between two genius individuals, Thomas Alva Edison and Nikola Tesla. The war was about the form of electricity, which should be generated, distributed and delivered to the companies and the people, and called by those at the time: *The War of Currents* [12]. Edison was championing the direct current (DC) system, while Tesla championed the alternating current (AC) system. The war was won by Nikola Tesla, and since then, the AC has been flowing in our sockets. However, is the AC really a winner these days?

In fact, nowadays, the electric grid mostly distributes AC power over long distances. This is not due to higher efficiency compared to the DC grid, but rather due to the ease of generating AC-type electricity and transforming it from one level to another through a chain of step-up and step-down transformers.

However, the DC grid slowly but surely wins its place on the market and substitutes the AC one. This is thanks to the reduced associated power losses and advances in the design of highly efficient power electronics converters, which transform the generated AC power into distributed DC power. Moreover, there are growing concerns about greenhouse gas emissions, and the green energy is now at the center of attention. DC battery systems mostly fuel green energy. Mobile phones, laptops, LEDs, solar cells, and electric vehicles all run on DC power.

The importance of power electronics in everybody's lives and the vast number of converters in existence today can be seen in Figure 4 [13-14]. It is not only this number that makes an impression, but also the variety of control schemes and the possibility of using power converters according to application-specific purposes throughout all types of industries, as depicted in Figure 5 and Figure 6, respectively [15-17].

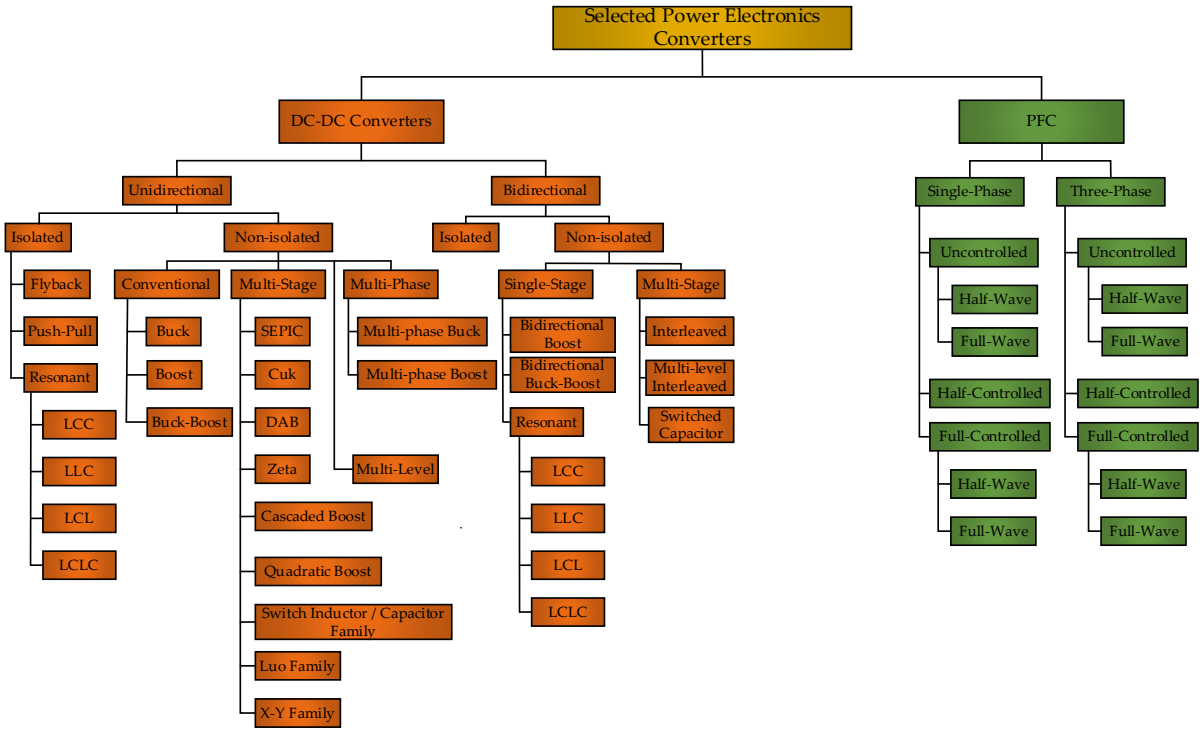

Figure 4: Classification of Selected Power Electronics Converters.

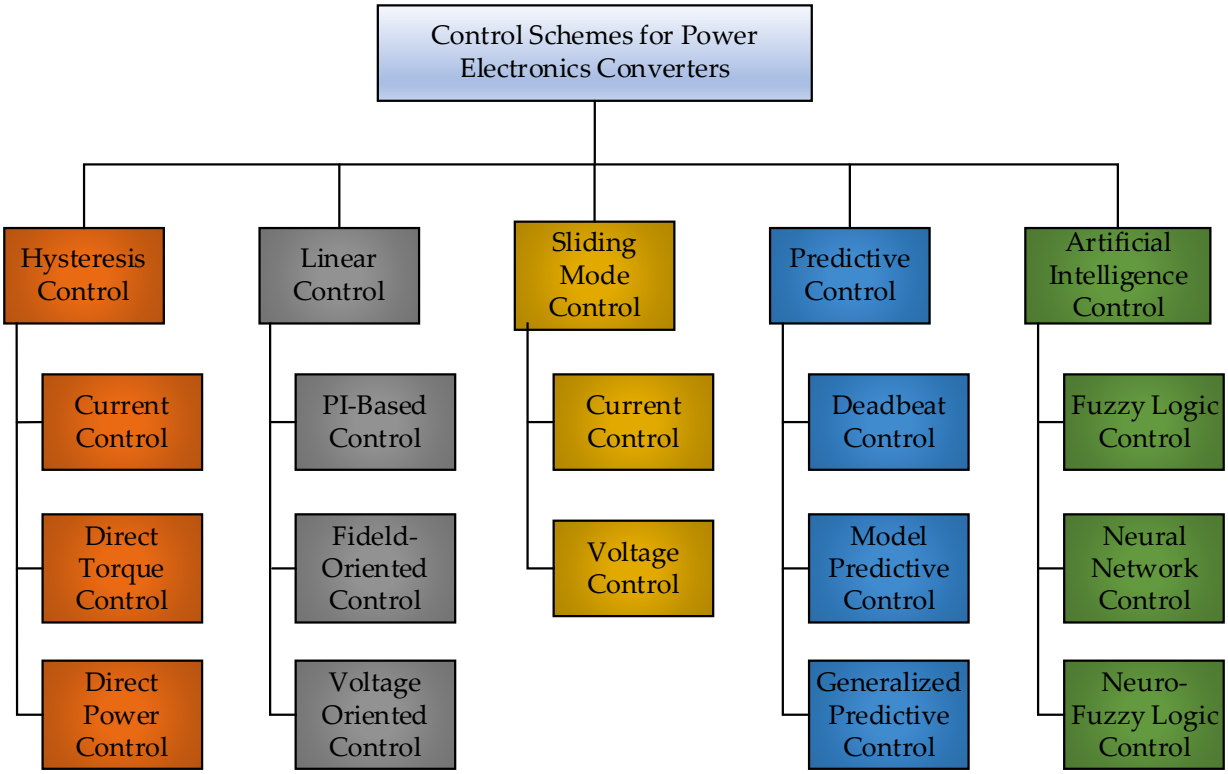

Figure 5: Control Schemes for Power Electronics Converters.

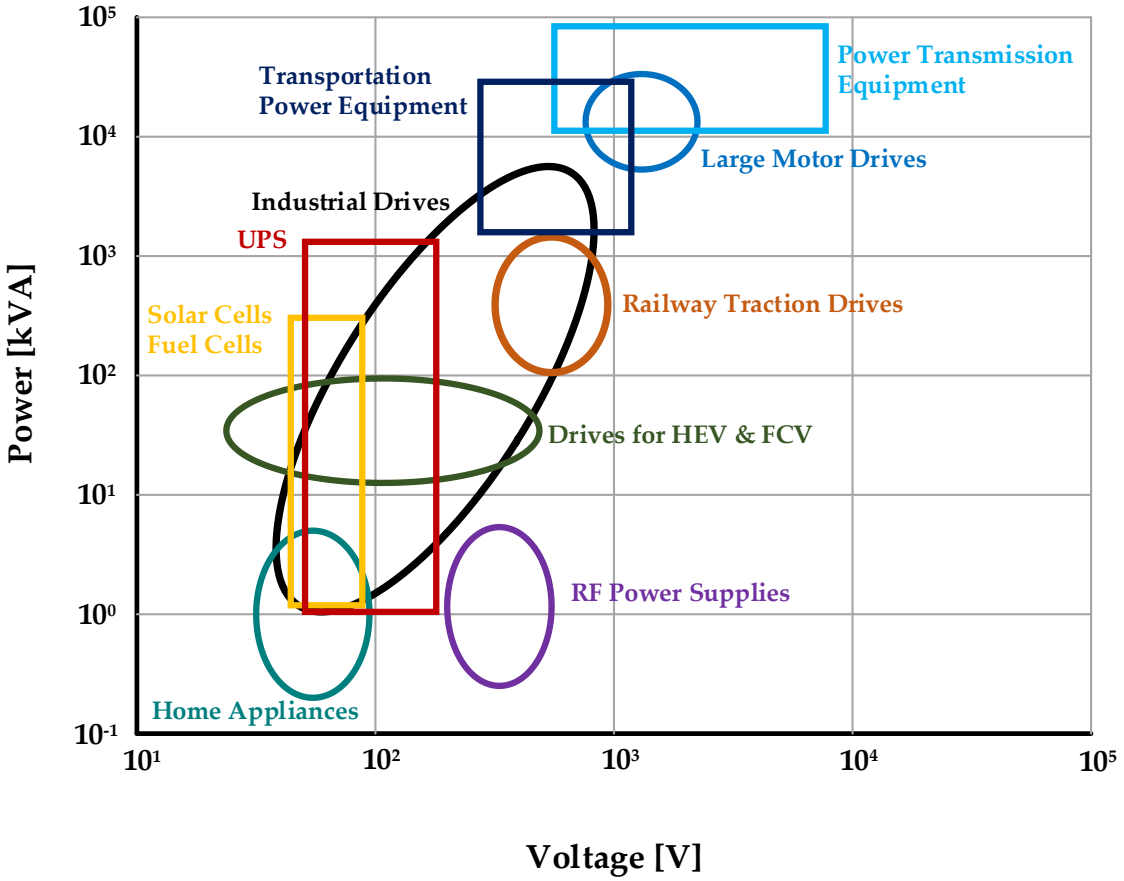

Figure 6: Application Roadmap of Different Power Electronics Equipment.

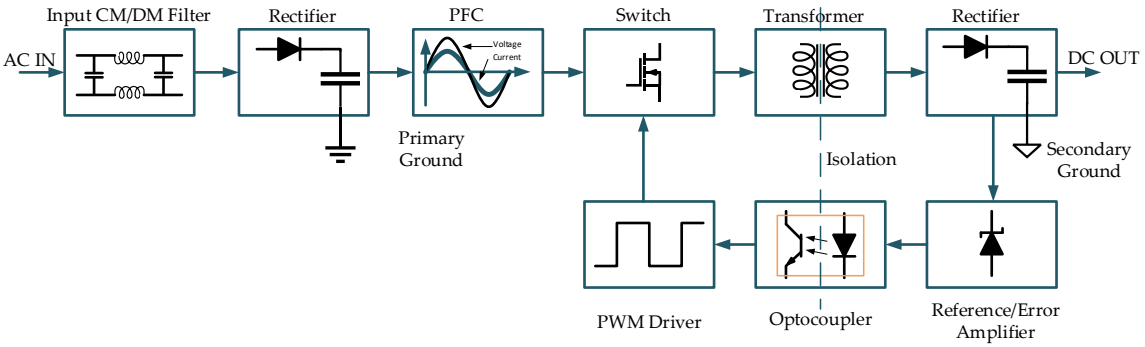

Figure 7: Block Diagram of AC-DC Switch Mode Power Supply.

The architecture of a typical switch-mode power supply is shown in Figure 7 [18]. In the beginning, the input common-mode and/or differential-mode filters remove any mains voltage transients that might otherwise enter and damage the power supply. The filters also work in the opposite way, preventing any electromagnetic interference (EMI) created within the high switching converter from being conducted to the AC mains.

If the input signal passes through the input filter stage, it is then directed to a bridge rectifier, which creates a pulsating DC voltage. This voltage is smoothed by a bulk

capacitor, which also provides the signal hold-up function.

Due to the numerous passive components used in the power supply and the high switching frequency, the initial mains signals are distorted. This distortion appears in the form of unwanted apparent power and a large number of harmonics. Therefore, the next stage required by the regulatory standards is the power factor correction (PFC) circuitry, usually made in the form of a boost converter. The PFC filters the noise made by the converter's switching circuitry, keeping the power factor (PF) close to unity and the total harmonic distortion (THD) close to zero.

The filtered and enhanced DC signal from the PFC goes to the transformer. There, the driver IC and the switching power semiconductors convert it to a highly alternating one to be carried by the transformer to the output stage. In this step, the transformer serves as an isolation barrier between the output and the input and its turns ratio permits a step-up or step-down function for the conducting signal.

The transformer secondary output is passed through an output rectifier to the load. Part of the signal is also fed to the feedback loop, which comprises a comparator, the optocoupler, and the PWM driver IC. The comparator compares the output signal against a reference one to provide tight regulation. The optocoupler provides galvanic isolation for the feedback to the primary PWM IC circuitry, which, based on the chosen control method, adjusts any deviations in the output signal. The type of control method chosen is application-specific, with a focus on minimizing both conducted and radiated EMI to meet regulatory standards, as shown in Figure 4 and Figure 5, respectively.

In this dissertation, however, only three power electronics converters will be discussed in more detail: the buck converter (a non-isolated step-down converter), the boost converter (a non-isolated step-up converter), and the flyback converter (an isolated step-down/step-up converter). These three converters are the backbones of modern converter architectures. They are most commonly used in the electronic systems of domestic appliances and LED lighting systems, which is the focus of this research.

The buck converter is a step-down converter that transforms a higher DC input voltage into a lower DC output voltage, based on the functionality of the control loop. The general principle of operation in the steady-state of continuous conduction mode (CCM) is depicted in Figure 8 [15, 19-20].

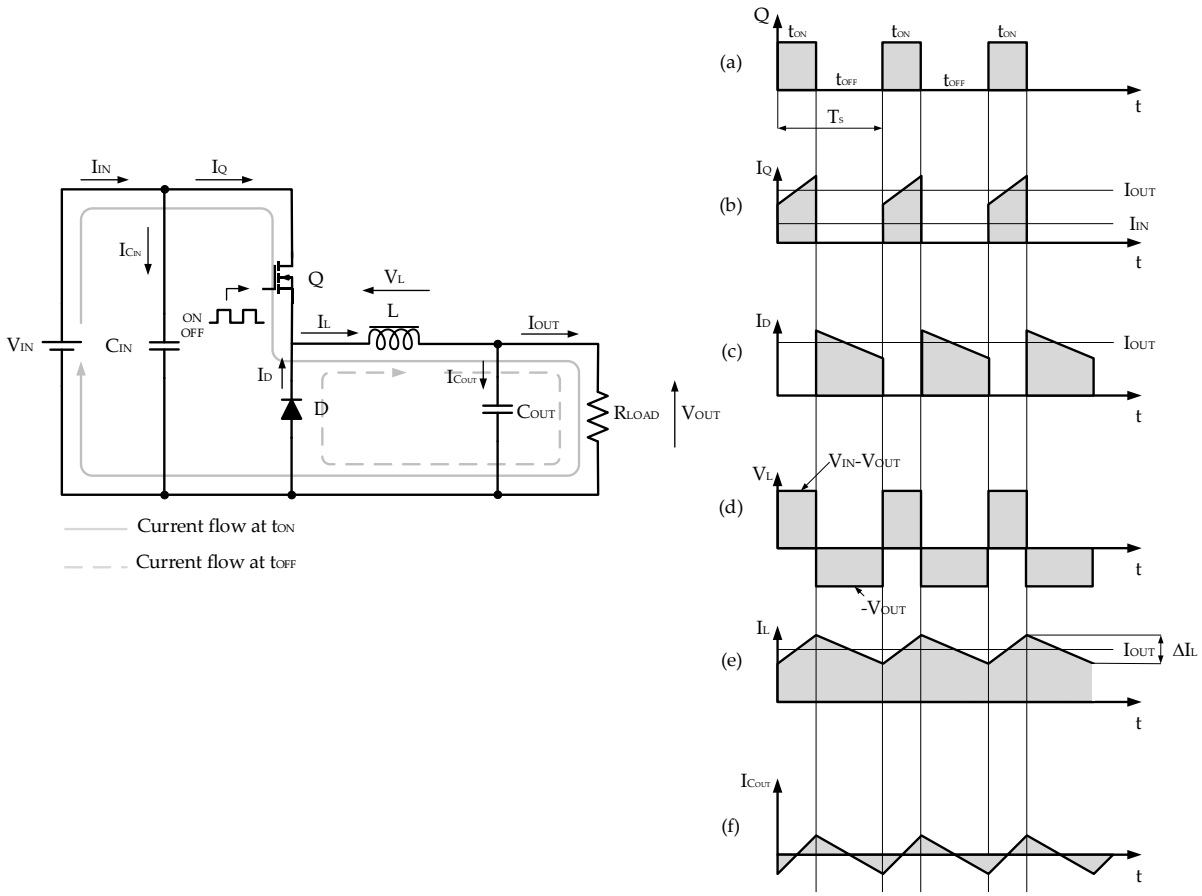

Figure 8: Buck Converter Operation in Continuous Conduction Mode; (**a**) t_{ON} and t_{OFF} State of the Switch Q; (**b**) Switch Q Current; (**c**) Freewheeling Diode D Current; (**d**) Inductor L Voltage; (**e**) Inductor L Current; (**f**) Output Capacitor C_{OUT} Current.

In the first part of the switching cycle, the switch Q is in the on-state and the free-wheeling diode D is reverse-biased. The whole current flows through the inductor L to the output capacitor C_{OUT} and to the load R_{LOAD}. In this state, the inductor magnetizes itself, storing energy within its magnetic field. When switch Q is in the off-state, the free-wheeling diode is forward-biased clamping one of the inductor nodes (so-called switching node) near the ground, changing its voltage bias. In this state, the inductor is demagnetizing itself, allowing the current to flow to the output.

As depicted in Figure 8d, the integral of the inductor voltage over one period of time in the steady-state of the continuous conduction mode must be equal to zero. This implies:

$$(V_{in} - V_{out}) \cdot t_{on} = V_{out}(T_s - t_{on}) \tag{1}$$

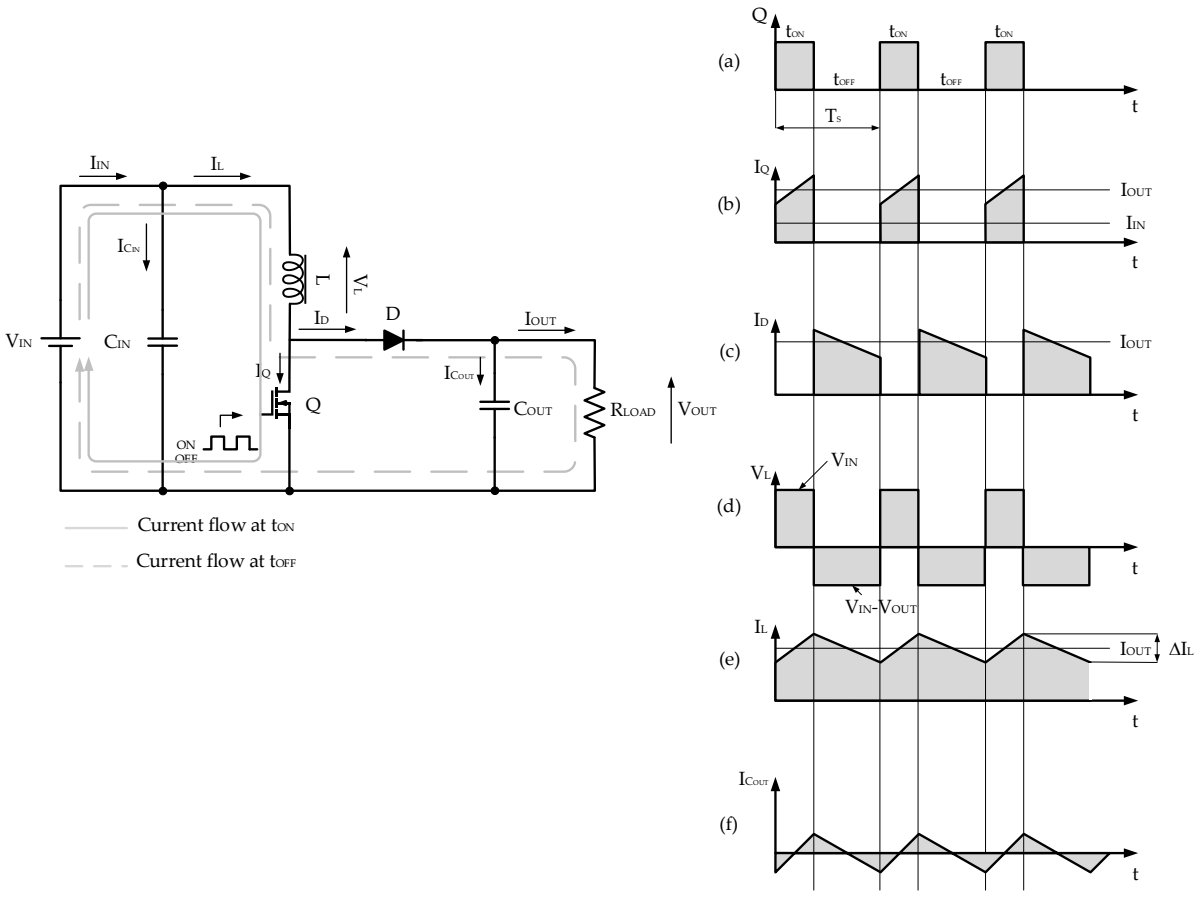

Figure 9: Boost Converter Operation in Continuous Conduction Mode; (**a**) t_{ON} and t_{OFF} State of the Switch Q; (**b**) Switch Q Current; (**c**) Diode D Current; (**d**) Inductor L Voltage; (**e**) Inductor L Current; (**f**) Output Capacitor C_{OUT} Current.

$$D = \frac{V_{out}}{V_{in}} = \frac{t_{on}}{T_s} \tag{2}$$

Equation (2) illustrates the main buck converter control principle, where the duty ratio D determines the relationship between the converter input and output voltage, as well as the duration of the switch Q being in the on-state. In contrast to the buck converter, the *boost converter* is a step-up converter, which boosts the DC input voltage to higher values. The converter itself and its principle of operation in steady-state CCM are depicted in Figure 9 [15, 19-20].

In the first part of the switching cycle, the switch Q is in the on-state, clamping one of the inductor nodes (the switching node) close to the ground. During this period, the inductor magnetizes itself and stores energy within its magnetic field. At the same time, diode D is reverse-biased, isolating the output stage from the input. When switch

Q switches to the off-state, diode D becomes forward-biased, and the load receives energy from the input, along with the energy stored by the inductor, which boosts the output voltage level above the input one.

Similar to the buck converter, the boost converter, the integral of the inductor voltage over one period of time in the steady-state of the continuous conduction mode equals zero, and thus:

$$V_{in} \cdot t_{on} = -(V_{in} - V_{out}) \cdot (T_s - t_{on}) \tag{3}$$

$$\frac{1}{1-D} = \frac{V_{out}}{V_{in}} = \frac{T_s}{t_{off}} \tag{4}$$

The equation (4) illustrates the main principle of the boost converter control, where the duty ratio D determines the relationship between the converter's input and output voltages, as well as the duration of the switch Q's on-state.

The last converter, whose working principle will be illustrated, is *the flyback converter*.

The converter itself and its principle of operation in steady-state CCM are depicted in Figure 10 [15, 19-20]. The main function of this type of converter is to introduce a galvanic isolation between the primary and secondary circuitry.

During the switch Q on-state, the current flows from the input through the primary winding of the transformer-like inductor to the ground. The inductor magnetizes itself during this period, storing the energy within its magnetic field. At the same time, the output diode D is reverse-biased, so the load is sourced from the output bulk capacitor.

During the switch Q off-state, the primary current is cut off. The voltage across the flyback inductor changes its bias and the diode D becomes forward-biased, conducting the energy stored in the inductor to the load and the bulk output capacitor. The design of the flyback converter is more complicated than the buck and the boost ones and the relationships that rule its control and design are as follows:

$$V_{RO} = \frac{D}{1-D} \cdot V_{IN} \tag{5}$$

$$L_P = \frac{(V_{IN} \cdot D)^2 \cdot T_S}{2 \cdot P_{IN}} \tag{6}$$

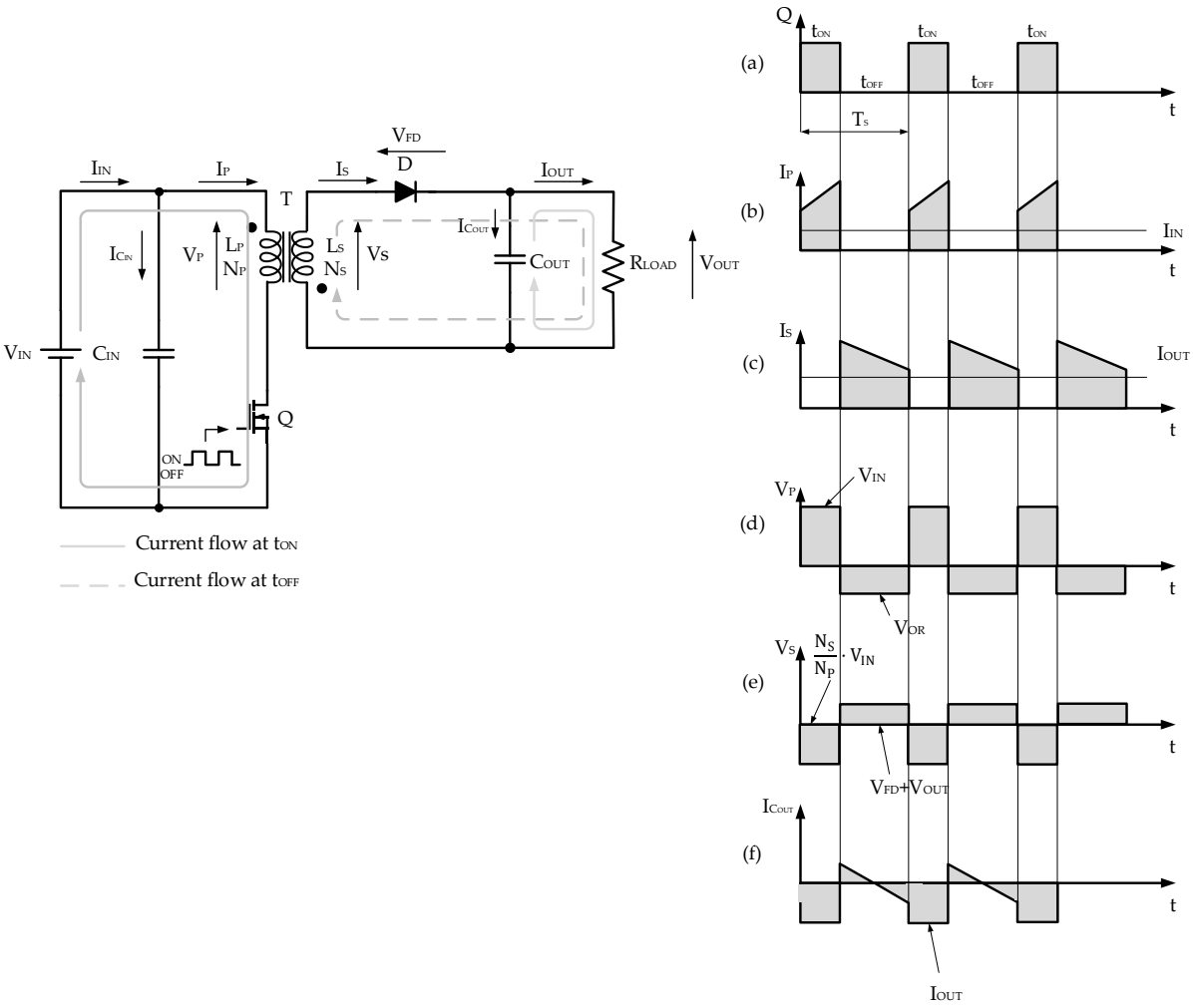

Figure 10: Flyback Converter Operation in Continuous Conduction Mode; (**a**) t_{ON} and t_{OFF} State of the Switch Q; (**b**) Inductor Primary Current I_p; (**c**) Inductor Secondary Current I_S; (**d**) Inductor Primary Voltage V_P; (**e**) Inductor Secondary Voltage V_S; (**f**) Output Capacitor C_{OUT} Current.

$$D = \sqrt{\frac{2 \cdot P_{IN} \cdot L_P}{T_S}} \cdot \frac{1}{V_{IN}} \tag{7}$$

$$D_{OUT} = \sqrt{\frac{2 \cdot P_{OUT} \cdot L_P}{T_s}} \cdot \frac{1}{V_{RO}} \tag{8}$$

The discontinuous conduction mode (DCM), the control principles, including the type of control, compensation, stability, converter transfer functions, the power loss of the entire converter and selection of the converter's remaining components except the magnetic one, are out of the scope of this thesis and left for the reader's self-study.

2.2 Properties of Magnetic Components used in SMPS Converters.

The SMPS converters can be used in numerous applications, and thus their magnetic components must be chosen accordingly to meet the application-specific requirements.

Several books, papers, manufacturers' application notes, and other online-based resources attempt to describe, categorize, classify, and evaluate magnetic components used in the power electronics industry [1], [4], [21-37]. This is not an easy task, as there are numerous applications, varying points of view, and multiple categories.

However, it can be assumed that the starting point for describing the magnetic component is first to realize what function it should perform within the electronic system it is going to be part of. Therefore, from the perspective of functionality, the magnetics can be divided into four major groups: storage, filtering, galvanic isolation (voltage/current adaptation), and coupling, as shown in Figure 11 [30-31].

The s*torage* group consists of inductors and inductor-like transformers. The inductor stores the energy within its magnetic field and releases it when the exciting current is removed. A similar situation occurs with inductor-like transformers, such as flyback transformers, where the transformer stores the energy supplied by the primary circuit and transfers it to the secondary one, depending on the primary voltage bias. This provides galvanic insulation between the circuits at the same time.

The *filtering* group consists of electromagnetic interference (EMI) filters and inductors. The EMI interference is generated within the power electronic converters due to the high-frequency switching of multiple semiconductor devices. It can be radiated through the air or transmitted through the wire conductors, interfering with communications or mains supply signals. Depending on the type of interference, the common-mode (CM) and/or the differential-mode (DM) filters can be used. These filters eliminate unwanted noise by converting it to heat, and in conjunction with capacitors, can also provide selective band-pass or band-stop filtering, eliminating EMI noise. The storage inductor, in conjunction with a capacitor, can also provide EMI and energy storage filtering by smoothing the current ripple superimposed on the DC output of the converter.

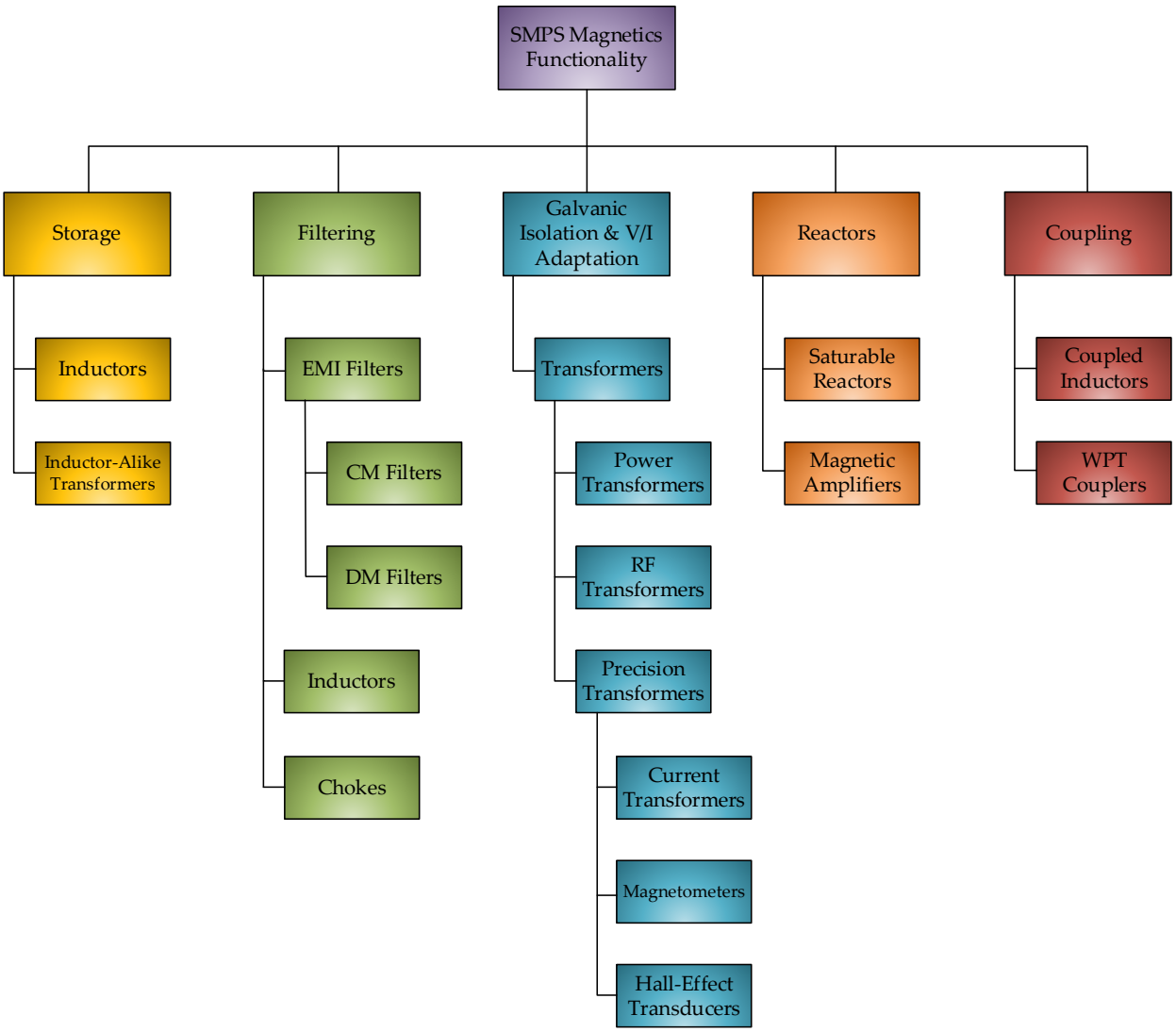

Figure 11: Functional Classification of Magnetic Components used in SMPS.

The *galvanic isolation & voltage/current adaptation* group consists of power transformers, RF transformers and precision transformers. The power transformers convert the AC energy from the primary level of voltage and current to the secondary level simultaneously, providing galvanic isolation between the primary and secondary circuits. The RF transformers operate at frequencies above 500 kHz, with their primary application being to couple the AC and decouple the DC signals from the output stage of the RF amplifier to the input of the next stage. They are also used in impedance-matching circuitry. The precision transformers consist of current transformers, fluxgate magnetometers, and Hall-effect transducers. Current transformers have one turn of wire on the primary side and several turns on the secondary. The secondary current is proportional to the primary current divided by the number of secondary turns. Current

transformers are extensively used in power electronics to measure the primary current without interfering with the primary circuit. The flux gate magnetometers, similar to Hall sensors, are extensively used in electric motor controllers, solar panel power inverters, and electric vehicle battery chargers for precise contactless current sensing [38-39].

The *reactors* group consists of saturable reactors and magnetic amplifiers (MAG AMPs). In saturable reactors, the DC that passes through the winding drives the device in and out of magnetic saturation. This changes the device flux transfer ratio and the output of the controlled device. These reactors are used for voltage and current control at high power in industrial furnaces and high-power voltage regulators. The magnetic amplifiers have similar functionality, except they are used in square wave and pulse wave applications as variable series impedance [40-41].

The *coupling* group consists of coupled inductors and wireless power transfer (WPT) couplers. The function of the coupled inductor is to transfer energy from the primary to the secondary winding that is wound on the same core. The coupled inductors are often used in interleaved multiphase power converters, where they allow for achieving higher efficiency and faster transients by reducing the number of components and the inductor size [42-43]. The WPT couplers are used to transmit energy in space via a high-frequency magnetic field, which is more convenient as it eliminates the need for cables or bolts [44-45].

2.3 Properties of Magnetic Materials used in SMPS Converters.

The topic of magnetic materials used in power electronics is also very broad. The right choice again depends on the application-specific requirements; however, it can be assumed that the desired characteristics of a magnetic core material should include [21], [30], [46]:

- high saturation flux density,
- high Curie temperature,
- low magnetostriction,
- high permeability,
- low coercivity,
- high resistivity,

- low power loss,
- broad usable frequency range,
- low size, volume and mass,
- long lifetime estimation,
- low cost.

The *high saturation flux density* characteristics mean that the core material can be exposed to higher peak current levels before it saturates, and thus it has higher power and energy handling capabilities. The higher saturation level, smaller magnetic core, and higher levels of integration and miniaturization are possible. However, a higher power density might cause a significant temperature rise in the magnetic component, which can reduce the saturation flux density level to a significant extent. This must be taken into account during the design process to avoid any possibility of thermal runaway and catastrophic failure, which could otherwise occur [21], [47].

At *the Curie* temperature, ferromagnetic, ferrimagnetic, and antiferromagnetic materials lose their magnetic characteristics and become paramagnetic. Therefore, the higher the Curie temperature, the wider the operating temperature range and the higher possible saturation and permeability levels of the magnetic material [21], [48-49].

The *magnetostriction* is a property of magnetic materials that causes a change in shape during the magnetization process. The dimensional change is associated with a distribution of distorted magnetic domains present in the magnetically ordered material under the influence of an externally applied magnetic field. Magnetostriction causes an energy loss due to frictional heating and is responsible for the low-pitch humming noise, which is both undesired [4], [21], [48], [49].

High permeability means fewer turns are required to achieve the desired inductance, resulting in less associated winding power loss and less material needed to build the coil. Moreover, for DC applications, especially in shielding, where the flux must be channelled through the material, the permeability must remain as high as possible [27].

Low coercivity means reduced B-H loop and thus less associated hysteresis loss [27].

High resistivity reduces the magnitude of the eddy currents induced in the magnetic core, and thus the magnitude of the eddy current-related power loss.

The core manufacturers deliver characteristics of the magnetic material, specifically *power loss* versus magnetic flux density, temperature, and frequency. These characteristics are specific to the given core material. The lowest power loss at a given operating point gives the highest conversion efficiency and the lowest temperature rise. The origin of the magnetic material power loss will be discussed in detail in the following paragraphs.

The *usable frequency range* of the magnetic material mostly depends on its natural and/or dimensional resonance, whichever occurs earlier, and the specific power loss at a given frequency. Above the limit described by the first or the second phenomenon, the complex permeability sharply drops and thus, the value of the inductance. The specific power loss, as given by the performance factor, should not exceed 200 mW/cm^3 [21].

The *low size, volume, and mass* requirements are associated with the mechanical strength of the magnetic component itself and other electronic components, e.g., printed circuit boards (PCBs), within which the magnetic component is embedded. Moreover, the market requirement for miniaturization and the specific power loss, as specified in datasheets, per unit of volume or unit of mass, must also be taken into account. The bigger or the heavier the magnetic component is, the greater the power loss.

The *long lifetime estimation* requirement assumes that the magnetic component should undergo several magnetization/demagnetization cycles, during which it experiences power loss, temperature gradients, and mechanical stresses, without deterioration of its performance for several years.

The *cost* requirement imposes the requirement mentioned in Chapter 1 for a device as cheap as possible, a key factor in the highly competitive and cost-sensitive power electronics market.

The magnetic materials themselves can be divided into three major groups: soft magnetic materials, hard magnetic materials and semi-hard magnetic materials [36-37]. The soft magnetic materials are the group that is mostly used in SMPS, and it is this group that the research is focusing on.

The soft magnetic materials can be divided into eight major groups: iron and low carbon steels, iron-silicon alloys, iron-nickel alloys, iron-cobalt alloys, ferrites, amorphous alloys, soft magnetic composites (powder alloys), and nanocrystalline alloys.

The commercially available *iron and low-carbon* magnets have high magnetic flux saturation levels reaching $B_s = 1.5 \div 2.15\,[T]$, permeability in the range of $10^3 \div 50 \cdot 10^4$ and the coercivity of $20 - 120\,[A/m]$. However, their low resistivity of $10^{-7}\,[\Omega \cdot \mathrm{m}]$ significantly limits their usable range to static and low-frequency applications, such as electromagnets, relays, small motors, and electromechanical mechanisms, where cost is a major concern [4], [28-29], [33-37], [50-56].

The *iron-silicon (FeSi) alloys* have higher resistivity than pure iron and low-carbon alloys, reaching up to $8 \cdot 10^{-7}\,[\Omega \cdot m]$, which effectively reduces the eddy current losses. Moreover, the silicon atoms embedded in the iron increase the alloy's relative permeability up to $8 \cdot 10^5$ decreasing hysteresis losses and lowering magnetostriction-related noise. However, adding the silicon to the iron structure decreases saturation magnetic flux density ($0.5 \div 2.12\,[T]$) and Curie temperature. The FeSi cores are typically used for line transformers, aircraft power transformers operating at $400Hz$, electric motors, generators, relays, and filter inductors operating below $5kHz$ [4], [28-29], [33-37], [50-56].

The *iron-nickel (NiFe) alloys* are available on the market in two versions, with high and low nickel content. The resistivity of these alloys is in the range of $4.8 \cdot 10^{-7} \div 5.8 \cdot 10^{-7}\,[\Omega \cdot m]$ and their saturation flux density vary from $0.6 \div 1.6\,[T]$ depending on the amount of nickel used. Most commercially available cores have a relative permeability of $40 \cdot 10^3 \div 100 \cdot 10^3$ with some reaching $300 \cdot 10^3$ (Ultraperm) and even 10^6 (Supermalloy) but at the cost of lowering the saturation magnetic flux density level. The Curie temperature is around $450^o\,[C]$. These cores are sensitive to mechanical stress, so they are placed in protective cases filled with damping medium. The NiFe alloys can be found in current transformers, wide-band transformers, saturable reactors, power inverters, DC-DC converters and magnetic sensors [4], [28-29], [33-37], [50-56].

The *cobalt-iron (CoFe) alloys* have the highest saturation flux density, reaching $2.4\,[T]$. Adding cobalt to iron increases the Curie temperature up to $950^o\,[C]$ (Vacoflux). The commercially available cores have relative permeability reaching 10^4 and even $8 \cdot$

10^4 (Supermendur) and resistivity of $3.5 \cdot 10^{-7}$ [$\Omega \cdot m$]. The application of CoFe alloys includes transformers where high flux densities and low power loss are required, as well as magnetic amplifiers and motors used in spaceborne devices [4], [28], [33-37], [50-56].

The *soft ferrite ceramics* are dense, hard, brittle, chemically inert and homogenous polycrystalline made of iron oxides (Fe_2O_4) mixed with oxides or carbonates. Usually, they are commercially available in the compounds of manganese and zinc ($MnZn$) or nickel and zinc ($NiZn$). In general, ferrites have high relative permeability in the range of $40 \div 10^5$ and high resistivity of $10^5 \div 10^7$ [$\Omega \cdot m$]. Ferrite cores are insulators and thus experience only hysteresis loss. The ferrites limiting factors are the low magnetic flux density saturation levels of around 0.3 [T] on average and the low Curie temperature in the range of $150 \div 300$ [^oC].

The manganese-zinc alloys ($MnZn$) usually have the permeability in the range of $500 \div 20000$, the magnetic flux density saturation levels within $0.35 \div 0.8$ [T], relatively low resistivity of $0.5 \div 2$ [$\Omega \cdot m$], and Curie temperature of $130 \div 280$ [^oC]. The $MnZn$ ferrites usable frequency range is up to 4 [MHz].

The nickel-zinc alloys ($NiZn$) have lower but stable relative permeability in the wide frequency range $20 \div 350$, high resistivity $10^3 \div 10^7$ [$\Omega \cdot m$], saturation magnetic flux density of up to 0.8 [T], Curie temperature around 300 [^oC] and operating frequency range of $0.1 \div 1$ [GHz]. The ferrites for microwave applications, such as spinels, garnets and hexaferrites, can even be used in the gigahertz switching range of up to 100 [GHz]. The soft ferrites are brittle and sensitive to mechanical stress; as the stress increases, the permeability also increases. They are commonly used in power electronics applications, e.g., in high-frequency power inductors and transformers, common-mode chokes, EMI high-impedance filters, antennas, and sensors [4], [28-29], [33-37], [50-56].

The *amorphous alloys* are compounds of iron and other magnetic materials, such as nickel and cobalt, that lack a regular, repetitive, and compact structure and are therefore known as metallic glasses. The relative permeability of these alloys is very high, ranging from 10^4 to 10^6. Their magnetic saturation point is in the range of 0.57 to 1.8 [T], while the resistivity is in the range of $10^{-6} \div 2 \cdot 10^{-6}$ [$\Omega \cdot m$]. The Curie temperature stays within the limit of $225 \div 420$ [^oC] and the usable frequency range is up to 250 [kHz] [4], [28-29], [33-37], [50-56].

The *powder alloys* are usually made of iron powders, molybdenum permalloy powders (MPP), or Kool Mμ© powders. The powder cores are made from thin particles of magnetic material coated with an inert insulator, which separates the particles from each other. The insulating material creates an embedded and evenly distributed air gap. This reduces the value of saturation flux, increases resistivity, reduces eddy currents and introduces a soft saturation characteristic. The usual permeability of powdered iron is in the range of $3 \div 550$, the saturation magnetic flux density is $0.5 \div 1.6$ $[T]$, the typical resistivity is around 1 $[\Omega \cdot m]$, and the Currie temperature ranges from $400 \div 770$ $[^{o}C]$. The usual usable frequency range is up to 100 $[kHz]$, while some MPP materials can be used up to 1 $[MHz]$. The iron powder cores for radio frequency applications can even be used in systems switching above 100 $[MHz]$. The MPPs cores are used in pulse and flyback transformers, EMI filters while Kool Mμ© cores are suited for DC bias applications, SMPS inductors, inductor for power factor correction (PFC) circuits and uninterruptable power supplies (UPS) [4], [28-29], [33-37], [50-56].

The *nanocrystalline alloys* combine the high permeability of amorphous materials with the low energy losses of ferrites. It makes them a good candidate for power electronics applications because their resistivity is around $0.8 \cdot 10^{-6} - 1.2 \cdot 10^{-6}$ $[\Omega \cdot m]$, the Curie temperature is up to 600 $[^{o}C]$ and usable frequency range of up to 150 $[kHz]$. The nanocrystalline alloys' permeability is in the range of $500 \div 3 \cdot 10^{5}$ while the saturation magnetic flux density is in the range of $1.2 \div 1.5$ $[T]$. However, these materials are susceptible to air gaps and eddy current losses within the core sheets, which cause overheating and limit the operating frequency range and possible core size reduction. These alloys are used in current transformers and common mode EMI filters [4], [28-29], [33-37], [50-56].

The soft magnetic alloys commonly used in SMPS converters are depicted in Figure 12, while their properties are compiled and presented in Table 1 [4], [28-29], [33-37], [50-56]. It is worth noting that the data presented in Table 1 is based on information collected from the literature and refers to a specific group of soft magnetic alloys, rather than a particular magnetic material. The information included in this table can be used as a starting point to indicate where to seek a magnetic material with the desired characteristics for a particular application.

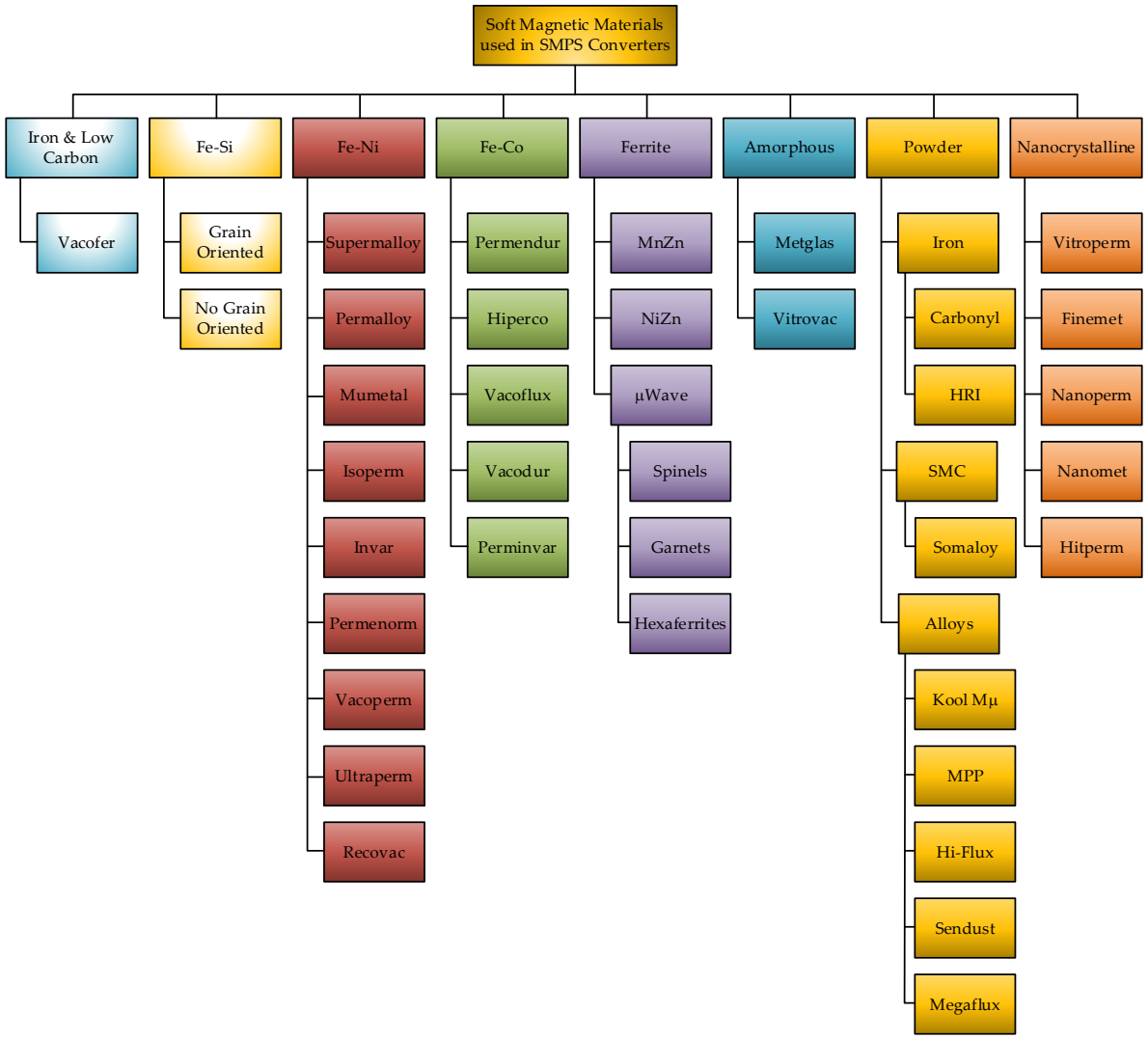

Figure 12: Soft Magnetic Alloys Commonly used in SMPS Converters.

Magnetic Alloy	Max. Relative Permeability Range μ_{max}	Coercive Field $H_c\ [A/m]$	Saturation $B_s\ [T]$	Curie Temperature $T_c\ [^oC]$	Saturation Magnetostriction $\lambda_s\ [ppm]$	Resistivity $\rho\ [\Omega m]$	Frequency Range
Iron and low-carbon steel	1000-50000	10-120	1.5-2.15	760-810	5	10^{-7}	50Hz-3000Hz
Fe-Si	3000-80000	4-80	0.5-2.12	690-765	0.5-10	$2.5 \cdot 10^{-7} - 8 \cdot 10^{-7}$	50Hz – 5000Hz
Fe-Ni	40000-1000000	0.25-40	0.6-1.6	450	25	$4.8 \cdot 10^{-7} - 5.8 \cdot 10^{-7}$	50Hz – 20000Hz
Fe-Co	1000-80000	30-700	2.4	950	70	$3.5 \cdot 10^{-7}$	1kHz – 100kHz
Ferrites MnZn	500-20000	5-80	0.35-0.8	130-280	-2	0.5 -2	10kHz - 4MHz
Ferrites NiZn	40-300	20-350	0.25-0.8	110-400	-20	$10^3 - 10^7$	0.1MHz – 1GHz
Amorphous Alloys	10000-1000000	0.02-4	0.57-1.8	225-420	0.5-40	$1 \cdot 10^{-6} - 2 \cdot 10^{-6}$	0.4kHz – 250kHz
Powder Alloys	3-550	0.6-4	0.5-1.6	400-770	-2.8-8.2	$100 \cdot 10^{-6} - 1$	1kHz – 100MHz
Nanocrystalline Alloys	500-300000	0.5-3	1.2-1.5	570-600	0.1-2	$0.8 \cdot 10^{-6} - 1.3 \cdot 10^{-6}$	0.4kHz - 150kHz

Table 1: Properties of Soft Magnetic Alloys used in SMPS Converters.

Usually, the power electronics applications for domestic appliances and the LED lighting systems switch at frequencies between $30kHz \div 200kHz$ and transfer power of up to $5kW$. In these applications, the powder cores are primarily used as the DM/CM chokes for EMI filtering, while the ferrites are utilized to convert energy from one level to another. This is because ferrites have low power loss and no thermal aging compared to powder alloys of equivalent parameters [55], [57-59]. Moreover, ferrites are cost-efficient and come with a greater variety of core shapes, allowing for more flexible design and adjustment of the air gap. Therefore, they are considered the preferred magnetic material of choice in this research.

2.4 Loss Mechanisms in Ferrite Magnetic Components.

2.4.1 Winding Loss.

The alternating currents that flow in the windings and the core of the magnetic component generate a magnetic field due to their own currents and also magnetic fields due to all current-carrying conductors in their vicinity. These, in turn, induce an electromotive force that, according to Faraday's law, creates eddy currents in the conductors. The eddy currents oppose penetration of the conductor by the magnetic field and convert electromagnetic energy into heat, generating additional ohmic losses. The eddy-current phenomena can be split into two parts: the skin effect and the proximity effect. The skin effect exists in conductors and is created by the magnetic field of their own time-varying current. The proximity effect, on the other hand, is also due to the magnetic field, but in this case, it is created by the time-varying currents flowing in adjacent conductors. Both of the phenomena are orthogonal to each other and can be considered separately [1-9], [60-68].

The *skin effect* limits the effective cross-sectional area of the conducting wire to a tiny depth, known as the skin depth, near its surface, thereby increasing the effective wire resistance. Explaining the phenomenon, the following current $i(t)$ generates the circular magnetic field $H(t)$ inside and outside of the conductor as shown in Figure 13.

The field generates the eddy currents within the conductor, which flow in the opposite direction to the applied current $i(t)$ in the centre of the wire and in the same

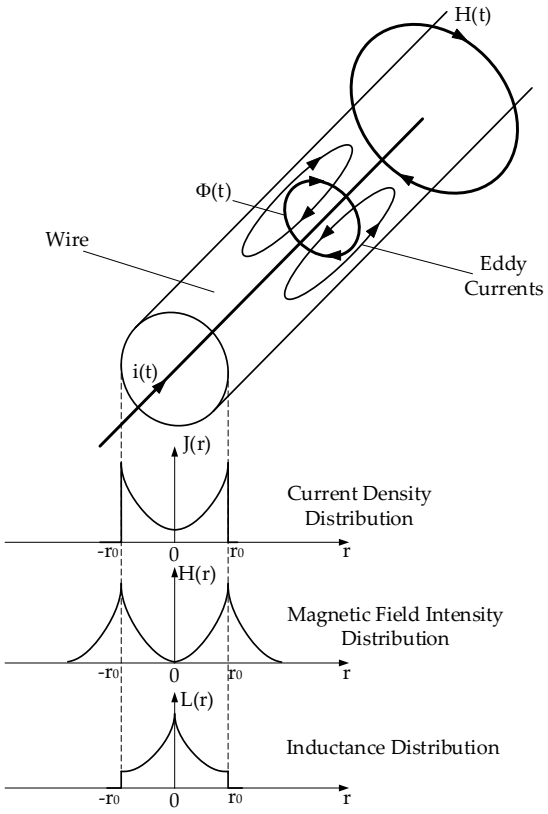

Figure 13: Skin Effect in Round Wire at High Frequencies.

direction near its surface. This results in a nonuniform current distribution, with the net current concentration near the wire surface [2], [4], [60-68].

The *proximity effect* is caused by the time-varying current in conductors, which generates internal and external time-varying magnetic fields that induce eddy currents in nearby conductors of adjacent winding layers in multi-layer inductors and transformers. In this case, each conductor is subject to its own field and the fields generated by other inductors. If the conductor carries its own current, the total eddy current is the sum of the skin and the proximity effect; otherwise, only the proximity effect eddy current is induced. This is due to the orthogonal superposition of these two phenomena, where the skin effect exhibits even symmetry, and the proximity effect exhibits odd symmetry. The proximity effect of the three-layer foil inductor is shown in Figure 14 [2], [4], [60-68].

As shown in Figure 14d, the core is placed inside the windings. Suppose the number of layers increases, starting from the layer adjacent to the core and proceeding outward to the outermost one. In that case, the amount of the current encircled by the

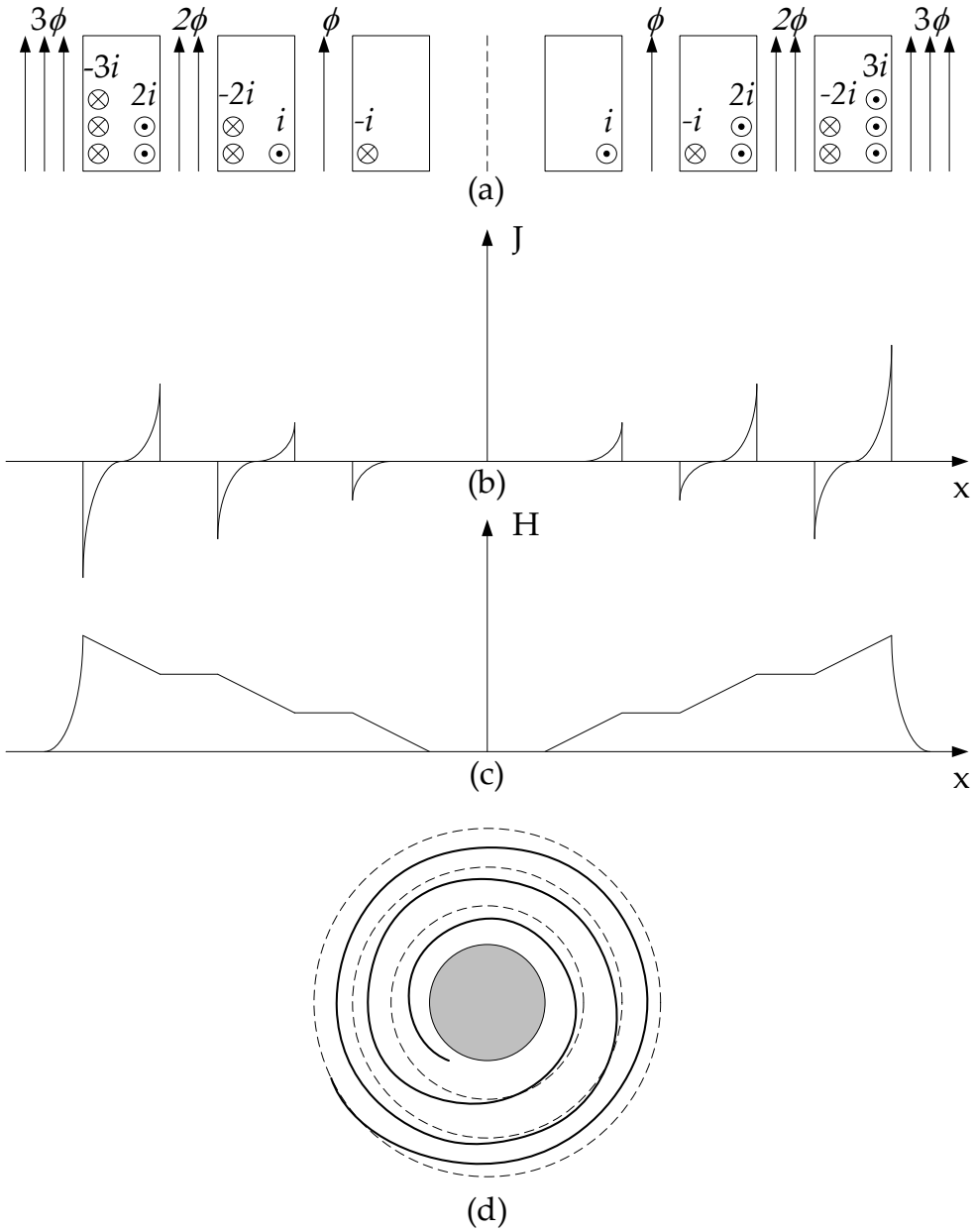

Figure 14: Proximity Effect in Foil Winding Inductor; (**a**) Cross-Section of the Windings; (**b**) Current Density Distribution; (**c**) Magnetic Field Intensity Distribution; (**d**) Top View of the Windings with Highlighted Ampere Contours (dashed lines).

Amperian contour also increases, and with it the flux density. The magnetic flux lines, according to the Lenz right-hand rule, are parallel to the winding layers and normal to the turns and the direction of the current. With the assumption that the core relative permeability is infinite, the magnetic field inside the core is zero. The time-varying current $i(t)$, which is forced to flow through all the layers, is first induced on the outer

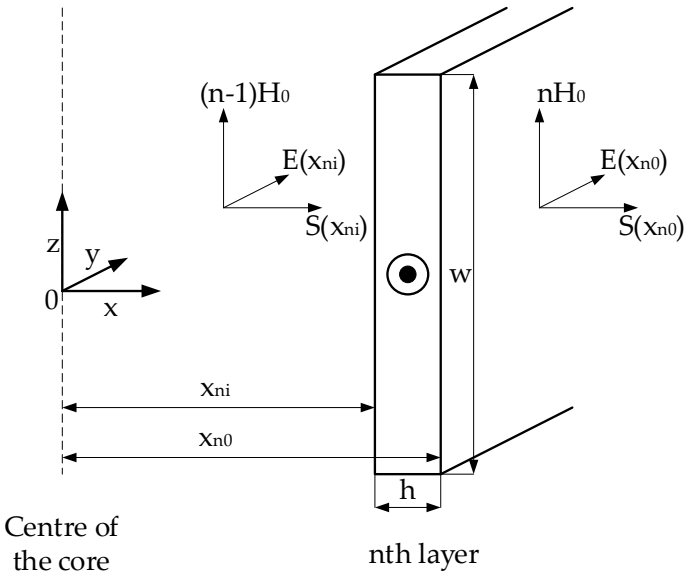

Figure 15: Boundary Conditions at the Foil Winding nth Layer.

surface of the innermost layer. The same current with opposite direction $-i(t)$ is induced on the innermost surface of the adjacent conductor in the second layer. Because the net current is $i(t)$ the current $2i(t)$ must flow on the right surface of the second layer. This rule is applied to all layers, as shown in Figure 14.

The equation, which combines skin and proximity losses into a single solution, is the well-known Dowell's equation. The final form of this equation for sinusoidal excitation can be achieved using cylindrical [62] or Cartesian [4] coordinates, as shown below.

The magnetic field and current density distribution in the foil conductor can be calculated using one-dimensional Maxwell equations:

$$\nabla x\, E = -\mu_0 \cdot \frac{\partial H}{\partial t} \tag{9}$$

$$\nabla x\, H = \sigma E = J \tag{10}$$

Due to the symmetry (see Figure 15) only the y and z coordinates can be used and the equations (9)-(10) can be rewritten as:

$$\frac{dE_y}{dx} = -j\omega\mu_0 H_z \tag{11}$$

$$-\frac{dH_z}{dx} = \sigma_w E_y = J_y \tag{12}$$

Based on the equations (11)-(12) the skin depth can be calculated using the so-called scalar Helmholtz equation for a one-dimensional field distribution in the direction x, which is as follows [2], [4], [62]:

$$\frac{d^2H_z(x)}{dx^2} = j\omega\mu\sigma_w H_Z(x) = \gamma^2 H_z(x) \; for \; x \geq 0 \tag{13}$$

where the complex propagation constant is given by:

$$\gamma = \sqrt{j\omega\mu\sigma_w} = (1+j)\sqrt{\pi\mu\sigma_w f} = \frac{1+j}{\delta_w} \tag{14}$$

and the skin depth δ_w is:

$$\delta_w = \frac{1}{\sqrt{\pi\mu\sigma_w f}} = \sqrt{\frac{\rho_w}{\pi\mu_r\mu_0 f}} \tag{15}$$

$$H_z(x) = H(x) = H_1 e^{\gamma x} + H_2 e^{-\gamma x} \tag{16}$$

This solution can be solved by applying boundary and initial conditions to the left and right surfaces of each winding layer, as depicted in Figure 15.

It is assumed that the core is an ideal one with infinite relative permeability. This implies that the magnetic field intensity in the core is zero, and thus, the magnetic field at the inner (left) surface of the first layer is $H(0) = 0$. Moreover, the magnitude of the magnetic field between layers is assumed to be constant and if the value between the nth and the $(nth + 1)$ layer is considered, it should be calculated on the outer (right) surface of the nth layer. The Ampere's law at this surface is given by:

$$\oint_{Cn} H \cdot dl = ni_l = nI_m \cos(\omega t) \tag{17}$$

The amplitude of the magnetic field intensity between the first and second layers is:

$$H_0 = \frac{I_m}{w} \tag{18}$$

The initial condition for magnetic field intensity at the outer surface of the nth layer is:

$$H(x_{no}) = nH_0 = \frac{nI_m}{w} = H_1 e^{\gamma x_{n0}} + H_2 e^{-\gamma x_{n0}} \tag{19}$$

and similar at the inner surface of the nth layer is:

$$H(x_{ni}) = (n-1)H_0 = \frac{(1-n)I_m}{w} = H_1 e^{\gamma x_{ni}} + H_2 e^{-\gamma x_{ni}} \tag{20}$$

Then, the constants H_1 and H_2 can be calculated as follows:

$$H_1 = H_0 \frac{ne^{-\gamma x_{ni}} - (n-1)e^{-\gamma x_{n0}}}{e^{-\gamma h} - e^{\gamma h}} = H_0 \frac{ne^{-\gamma x_{ni}} - (n-1)e^{-\gamma x_{n0}}}{2\sinh((\gamma h)} \quad (21)$$

$$H_2 = H_0 \frac{(n-1)e^{-\gamma x_{n0}} - ne^{-\gamma x_{ni}}}{e^{\gamma h} - e^{-\gamma h}} = H_0 \frac{(n-1)e^{-\gamma x_{n0}} - ne^{-\gamma x_{ni}}}{2\sinh((\gamma h)} \quad (22)$$

Using equations (21) and (22) in equation (16) yields the magnetic field intensity in the nth layer:

$$H(x) = H_0 \frac{n \cdot sinh[\gamma(x - x_0)] + (n-1)\sinh[\gamma(x_{n0} - x)]}{\sinh(\gamma h)} \quad (23)$$

where $h = x_{n0} - x_{ni}$ is the foil thickness.

Substitution of equation (23) into equation (11) gives the electric field intensity in the nth layer:

$$E(x) = \rho_w \frac{dH(x)}{dx} = H_0 \rho_w \gamma \frac{(n-1)cosh[\gamma(x_{n0} - x)] - n \cdot \cosh[\gamma(x - x_{ni})]}{\sinh(\gamma h)} \quad (24)$$

According to the Poynting theorem, the power flowing into a closed surface S at any point of time is equal to the power dissipated as heat and the energy stored in electric and magnetic fields within the volume V [4], which is expressed for sinusoidal excitation as:

$$\oint_S (E \times H^*) \cdot ds = -\iiint_V (\rho_w |J|^2 + j\omega\epsilon_0 |E|^2 + j\omega\mu_0 |H|^2) dV \quad (25)$$

As depicted in Figure 15, the Poynting vector has a normal component perpendicular only to the left and right surfaces of the foil conductor. Therefore, the complex power of the nth layer can be expressed as [4]:

$$P_{Zn} = w l_T E(x_{ni} H(x_{ni}) - E(x_{n0}) H(x_{n0}) = \frac{\rho_w l_T I_m^2 \gamma}{2w} [\coth(\gamma h) + 2(n^2 - n)\tanh(\frac{\gamma h}{2})] \quad (26)$$

The DC power loss of the nth layer can be expressed as:

$$P_{wDCn} = \frac{\rho_w l_T I_m^2}{2wh} = \frac{\rho_w l_T I_{DC}^2}{wh} \quad (27)$$

The normalized complex power in the nth layer of foil winding is:

$$\frac{P_{Zn}}{P_{wDCn}} = \left(\frac{h}{\rho_w}\right)(1 + j)\left[\coth(\gamma h) + 2(n^2 - n)\tanh\left(\frac{\gamma h}{2}\right)\right] \quad (28)$$

where:

$$\coth(\gamma h) = \frac{\sinh\left(\frac{2h}{\delta_w}\right) - j\sinh\left(\frac{2h}{\delta_w}\right)}{\cosh\left(\frac{2h}{\delta_w}\right) - \cos\left(\frac{2h}{\delta_w}\right)} \tag{29}$$

$$\tanh\left(\frac{\gamma h}{2}\right) = \frac{\sinh\left(\frac{h}{\delta_w}\right) + j\sinh\left(\frac{h}{\delta_w}\right)}{\cosh\left(\frac{h}{\delta_w}\right) + \cos\left(\frac{h}{\delta_w}\right)} \tag{30}$$

The winding resistance of the nth layer can be obtained by rearranging equation (28) as follows:

$$R_{wn} = \frac{Re\{P_{Zn}\}}{P_{wDCn}} R_{wDCn} = R_{wDCn}\left(\frac{h}{\delta_w}\right)\left[\frac{\sinh\left(\frac{2h}{\delta_w}\right) + \sin\left(\frac{2h}{\delta_w}\right)}{\cosh\left(\frac{2h}{\delta_w}\right) - \cos\left(\frac{2h}{\delta_w}\right)} + 2(n^2 - n)\frac{\sinh\left(\frac{h}{\delta_w}\right) - \sin\left(\frac{h}{\delta_w}\right)}{\cosh\left(\frac{h}{\delta_w}\right) + \cos\left(\frac{h}{\delta_w}\right)}\right] \tag{31}$$

The winding resistance of all layers is given by:

$$R_w = \sum_{n=1}^{N_l} R_{wDCn}\left(\frac{h}{\delta_w}\right)\left[\frac{\sinh\left(\frac{2h}{\delta_w}\right) + \sinh\left(\frac{2h}{\delta_w}\right)}{\cosh\left(\frac{2h}{\delta_w}\right) - \cos\left(\frac{2h}{\delta_w}\right)} + 2(n^2 - n)\frac{\sinh\left(\frac{h}{\delta_w}\right) - \sinh\left(\frac{h}{\delta_w}\right)}{\cosh\left(\frac{h}{\delta_w}\right) + \cos\left(\frac{h}{\delta_w}\right)}\right] \tag{32}$$

where:

$$\sum_{n=1}^{N_l}(n^2 - n) = \frac{N_l\left(N_l^2 - 1\right)}{3} \tag{33}$$

and thus:

$$R_w = R_{wDC}\left(\frac{h}{\delta_w}\right)\left[\frac{\sinh\left(\frac{2h}{\delta_w}\right) + \sinh\left(\frac{2h}{\delta_w}\right)}{\cosh\left(\frac{2h}{\delta_w}\right) - \cos\left(\frac{2h}{\delta_w}\right)} + \frac{2(N_l^2 - 1)}{3}\frac{\sinh\left(\frac{h}{\delta_w}\right) - \sinh\left(\frac{h}{\delta_w}\right)}{\cosh\left(\frac{h}{\delta_w}\right) + \cos\left(\frac{h}{\delta_w}\right)}\right] \tag{34}$$

Equation (34) is Dowell's equation for the multilayer foil winding resistance.

This equation can be easily transformed to calculate the high-frequency winding resistance of rectangular, square, round, or Litz wire, as shown in [4].

2.4.2 Core Loss

The core loss of the ferrite-based magnetic components is due to the internal structure of the ferrite material and the characteristics of the applied external magnetic field. In ferrites, the magnetization process is mainly due to the electron spin moment within each atom and spin interactions and their alignments among neighbouring atoms within the crystal grains of the polycrystalline ferrite. The grains create small regions of uniform magnetization, called magnetic domains, in the same direction. Domains of

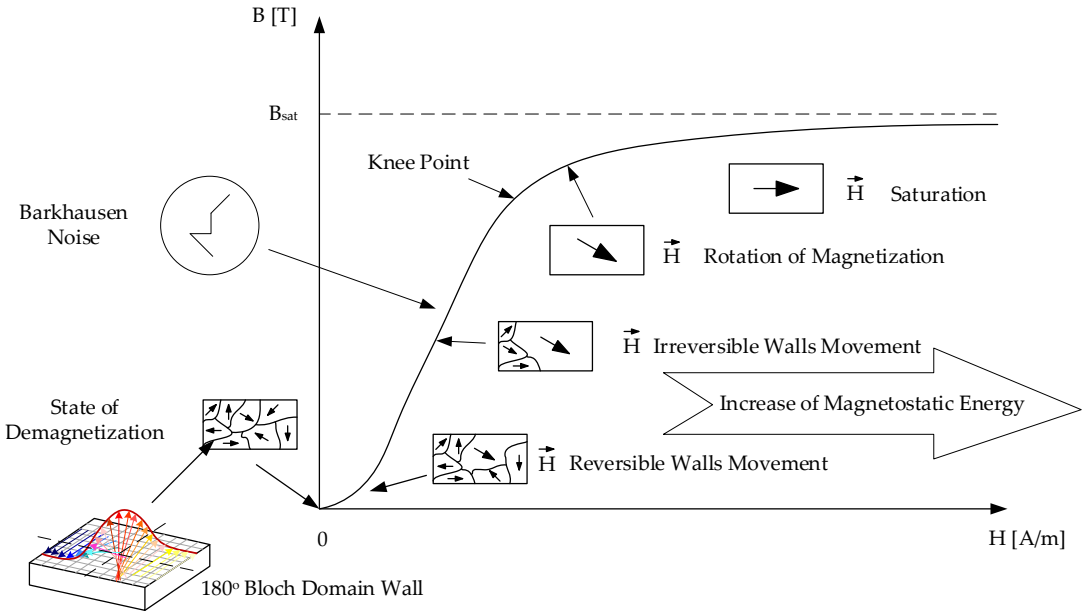

Figure 16: Magnetizing Curve of Ferrite Magnetic Component.

opposite direction of magnetization are separated from each other by the domain walls, as shown in Figure 16. Moreover, the state of local magnetization depends on factors such as grain structure, grain size, presence of impurities, local stress, and the balance of local energy. The local energy depends on [4], [33], [48], [52], [69]:

- magnetostatic energy associated with demagnetizing fields,
- magnetocrystalline energy associated with the anisotropy of crystals,
- exchange energy associated with the interactions between neighbouring magnetic moments,
- magnetoelastic energy associated with the magnetostriction effect,
- domain wall energy associated with the interaction between neighbouring electron spins.

The magnetization process, as shown in Figure 16, can be divided into a few steps. Initially, the magnetic material is fully demagnetized, and the applied external magnetic field is zero. The domains within the material are fully magnetized and randomly oriented, so the net flux measured outside is also zero. If a small external magnetic field is applied, it interacts with the magnetic domains within the material, and the domains attempt to realign with the imposed field. The domains in which the direction of dipoles is close to the applied field grow in size while others diminish. At

this stage, the process is reversible; if the applied magnetic field is removed, the material returns to its original state without any irreversible changes, and the hysteresis phenomenon does not exist. Beyond this point, if the external magnetic field still increases, more and more spinning electrons inside the material align with the external magnetic field resulting in a stronger magnetic flux density. This realignment produces a high relative permeability of the ferromagnetic material; however, the movement of the domain walls becomes irreversible, and if the external magnetic field is removed, the material remains partially magnetized, exhibiting the hysteresis phenomenon.

The movement of particular domain walls in this magnetization stage is detectable as the Barkhausen emission effect, resulting in discontinuities of the magnetic flux density and jumps in the magnetizing characteristics. Finally, suppose the magnitude of the external magnetic field is increased above the knee point. In that case, the movement of domain walls stops, and the magnetization is primarily due to the rotation of the magnetic domains' direction inside the material. The external magnetic field tends to realign all the magnetic domains along its direction. If the magnetic flux density reaches the saturation level, the magnetic material is fully magnetized, becoming a single domain, and all spinning electrons are aligned with the external magnetic field. If magnetization reaches the saturation level, the change in magnetic flux density is smaller than the change in magnetic field intensity, and the relative permeability drops to one, as for an air coil. The saturation causes excessive core loss and localized hot spots due to the nonuniform magnetic flux distribution inside the ferrite core. Moreover, the saturation flux density decreases as the temperature increases.

The effects that contribute to core loss, as well as the most common core loss models, are shown in Figure 17.

The mathematical models are divided into five main approaches: the Rayleigh, the Duhem, the Preisach, the Chua, and the Play, each with numerous variations (not depicted). Because these models involve substantial mathematical analysis, only two of them —the most popular ones, the Jiles-Atherton [33], [70-73] and the Coleman-Hodgdon [70], [74] — will be briefly discussed. The others are left for the reader to explore through self-study using the external literature sources [33], [70], [75-86].

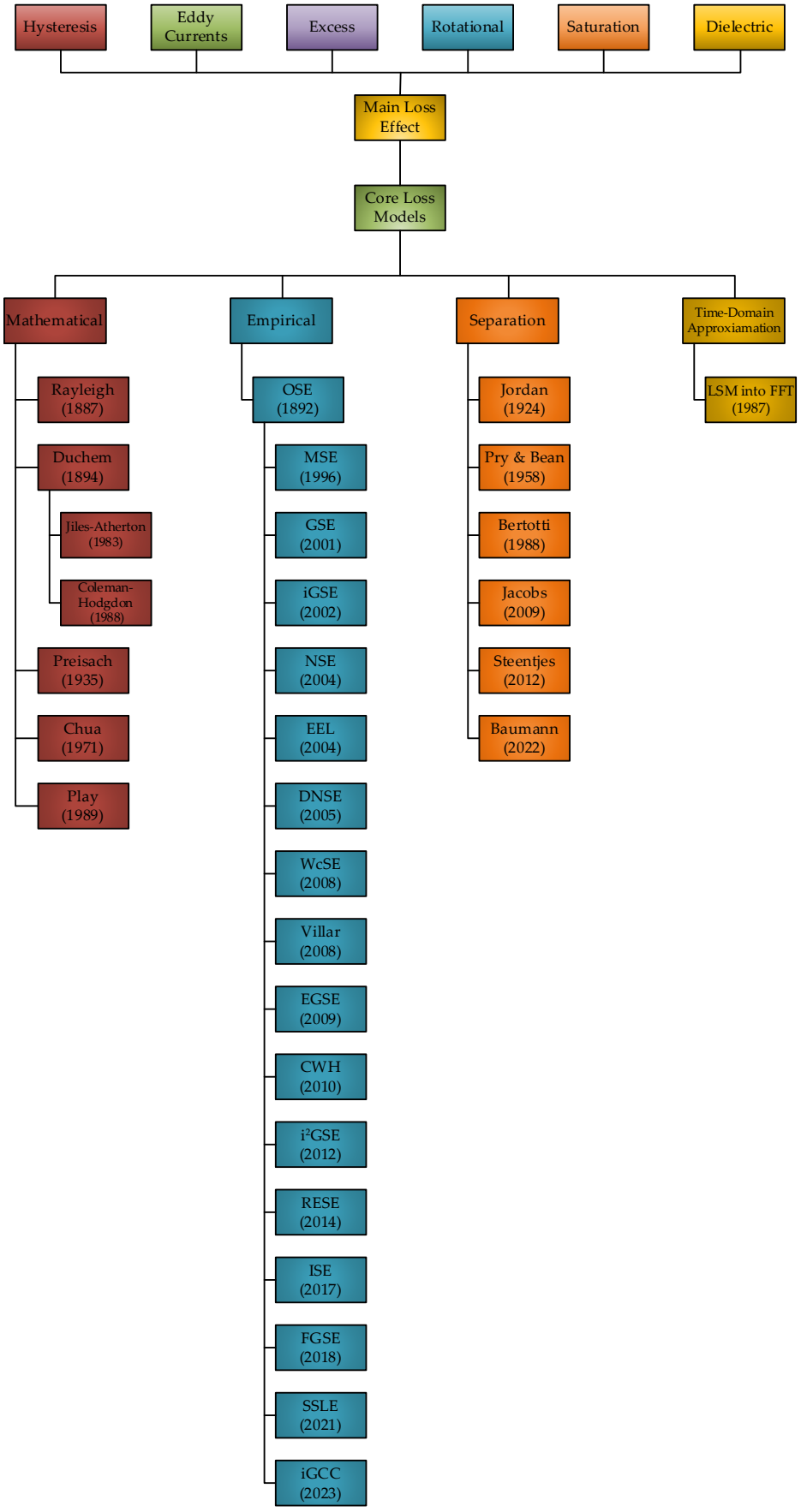

Figure 17: Core Loss Models.

The assumption of the *Jiles-Atherton* core loss model takes into account the real physical aspects of the magnetization process, which contrasts with, for example, the Rayleigh or Preisach approach. The model is based on energy analysis and separates the mechanisms of reversible and irreversible domain wall motions, as well as the pinning of domain walls. The Langevin expression is used to describe the anhysteretic curve and separate the reversible and irreversible domain wall motions. The expression is given by:

$$M_{an}(H_e) = M_s\left(\coth\left(\frac{H_c}{a}\right) - \left(\frac{a}{H_e}\right)\right) \tag{35}$$

where $H_e = H + \alpha M$ is the effective magnetic field intensity taking into account interdomain coupling. The a parameter characterizes the shape of anhysteretic magnetization, while the α parameter is the interdomain coupling coefficient. Suppose the energy dissipation due to the domain wall motions and the domain walls' pinning is taken into account. In that case, the non-reversible motion magnetization changes of the walls are expressed by [33], [70-73]:

$$\frac{dM_{nrev}}{dH} = \frac{1}{k - \alpha(M_{an} - M_{nrev})}(M_{an} - M_{nrev}) \tag{36}$$

where:

$$k = M_{an}(H_c)\left\{\frac{\alpha}{1-c} + \left[\frac{1}{(1-c)\chi_{H_c} - \frac{cdM_{an}(H_c)}{dH}}\right]\right\} \tag{37}$$

is the pinning constant, the c is the initial susceptibility of the magnetization curve, χ_{an} is the differential susceptibility of the anhysteretic curve at the origin, χ_{Hc} is the slope of the hysteresis loop at H_c. The final version of the hysteresis model with the reversible changes $M_{rev} = c(M_{an} - M_{nrev})$ included is given by [33], [70-73]:

$$\frac{dM}{dH} = \frac{M_{an} - M_{nrev}}{k - \alpha(M_{an} - M_{nrev})} + c\left(\frac{dM_{an}}{dH} - \frac{dM_{nrev}}{dH}\right) \tag{38}$$

Some changes have been made to the original equation (38) to account for the directional dependency linked to the rate-independence of the Duhem model and to compensate for some problems with unphysical negative permeability [33], [87-89], as follows:

$$\frac{dM}{dH} = \frac{1}{1+c}\delta_d \frac{M_{an} - M_{nrev}}{k\delta - \alpha(M_{an} - M)} + \frac{c}{1+c}\frac{dM_{an}}{dH} \tag{39}$$

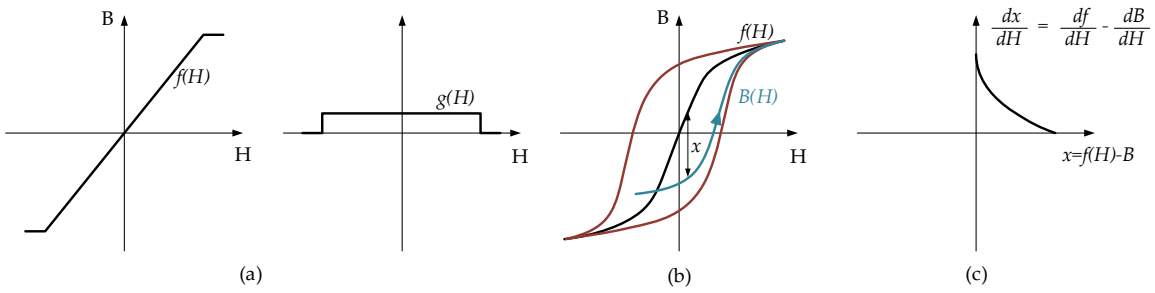

Figure 18: Coleman-Hodgdon Model of Hysteresis; (**a**) the Example of Anhysteretic Curve $f(H)$ and Reversible Function $g(H)$; (**b**) the Hysteresis Curve with Distance x to Anhysteretic Curve $f(H)$; (**c**) the Change of Distance dx/dH.

The difficulty with the Jiles-Atherton model is finding the fitting parameters M_S, α, a, c, k, however, several up-to-date studies have already been done on this subject, and thus these might be of help to define their values [90-93].

The *Coleman-Hodgdon* hysteresis-based core loss model is given by the following equation [33], [94-97]:

$$\frac{dB}{dH} = g(H) \pm \alpha_c (f(H) - B) \tag{40}$$

The anhysteretic curve $f(H)$ describes the hysteresis, the reversible function $g(H)$ describes the drift from the anhysteretic curve, while the parameter α_c is a fitting parameter that differs between the fitting models.

The drift function is reversible and similar to the derivative of the anhysteretic curve $f(H)$. It sets the initial curve and defines how the slope dB/dH drifts away from the anhysteretic function. Moreover, it should be lower than $df(H)/dH$, otherwise, it might stay along the anhysteretic curve and move without the hysteresis.

The second term describes the relationship between the dB/dH slope and the distance x to the anhysteretic curve, which can be expressed as [33], [94-97]:

$$x = f(H) - B \tag{41}$$

The dB/dH slope increases by a factor of $\alpha_C x$ and if the distance x is high enough, the slope dB/dH follows the slope of the anhysteretic curve and the distance stops increasing. This can be expressed by the following equation:

$$\frac{dx}{dH} = \frac{df(H)}{dH} - \frac{dB}{dH} \tag{42}$$

The limiting curves described by the equation (42) are the maximum distances between the hysteresis and the anhysteretic curve.

The examples of the Coleman-Hodgdon model functions are shown in Figure 18. This model will be discussed later in Chapter 3 regarding possible improvements to the state-of-the-art solutions.

The empirical core loss model group is probably the most popular, versatile, and widely used among scientists and engineers for estimating core losses at various excitation signals. All the models within this group derive from the original work of Charles Steinmetz in the late 19th century [98-125].

The *original Steinmetz equation* (OSE) is designed to calculate the average core power loss per unit of volume or unit of mass [102] and is given by:

$$P_{OSE} = k f^{\alpha} B_m^{\beta} \tag{43}$$

The k, α, β are the Steinmetz parameters obtained in the fitting of the double logarithmic core loss characteristics, usually given by the core manufacturers. These parameters depend on the switching frequency f and the maximum magnetic flux density B_m as depicted in the equation. The OSE, despite its simplicity, does not take into account DC signals and is not suitable for non-sinusoidal excitation signals [119], which usually prevail in modern switch-mode power supplies. Moreover, the Steinmetz parameters depend on the temperature [46], [98-100], [103-104].

The *modified Steinmetz equation* (MSE) was introduced to calculate the core losses caused by non-sinusoidal excitation waveforms. This approach assumes that the core loss is directly proportional to the rate of change of the magnetic flux density, dB/dt, a physical parameter that can substitute for the empirical, non-physical parameter of the fundamental magnetization frequency in the OSE. Therefore, the goal of this method is to find the equivalent magnetization frequency, normalized with respect to a sinusoidal case, assuming an average magnetic flux density rate of change [46], [70-73], [98-100], [103-104]. The relationships are as follows:

$$\dot{B} = \frac{1}{\Delta B} \oint \frac{dB}{dt} dB = \frac{1}{\Delta B} \int_0^T \left(\frac{dB}{dt}\right)^2 dt = \Delta B \cdot \frac{\pi^2}{2} \cdot f_{eq} \tag{44}$$

$$f_{eq} = \frac{2}{\Delta B^2 \pi^2} \int_0^T \left(\frac{dB}{dt}\right)^2 dt \tag{45}$$

$$P_{MSE} = \left(k f_{eq}^{\alpha-1} B_m^{\beta}\right) f \tag{46}$$

where: the $\Delta B = B_{max} - B_{min}$, $B_m = \frac{\Delta B}{2}$ and the k, α, β are the parameters taken from the OSE.

Despite the improvement in accuracy over the OSE for non-sinusoidal excitation, the MSE suffers from low accuracy at both low and high duty cycles. The possible cause is the close-to-boundary duty cycles, which introduce a significant change in the distribution of higher harmonics, thereby lowering the fundamental frequency component. This leads to inaccurate results if the original Steinmetz parameters are used [46], [98-101], [111], [115], [119-120].

The *generalized Steinmetz equation* (GSE) has been introduced as another improvement to the MSE. This method assumes that the average specific power loss is proportional to the instantaneous value of the magnetic flux density $B(t)$ and also its rate of change $dB(t)/dt$. The coefficients of the final method formula have been chosen to match the MSE for sinusoidal waveforms, and the formula is given as follows:

$$P_{GSE} = \frac{1}{T}\int_0^T k_1 \left|\frac{dB}{dt}\right|^{\alpha} |B(t)|^{\beta-\alpha} dt \tag{47}$$

$$k_1 = \frac{k}{(2\pi)^{\alpha-1}\int_0^{2\pi} |cos\theta|^{\alpha} |sin\theta|^{\beta} d\theta} \tag{48}$$

where: k, α, β are the Steinmetz coefficients as in the MSE and the θ is the phase angle of the sinusoidal waveform.

The advantage of the GSE over the MSE is its sensitivity to the DC bias and the ability to calculate the core loss at any excitation level. However, its disadvantage is the limitation on accuracy when higher harmonics in the magnetic flux density become significant. In this case, an analytical approach to the hysteresis loss must be taken into account due to the existence of minor loops [46], [98-100], [105], [115].

The *improved generalized Steinmetz equation* (iGSE) was introduced to mitigate the GSE issues, including minor hysteresis loops and higher harmonics in the magnetic flux density. It was assumed that the magnetic flux density is piece-wise linear, which allows for calculating the power loss of the major loop and each minor loop separately. The total loss is assumed to be the weighted average of each loop, where the contribution of each is weighted by the fraction of the total period it occupies. Moreover, the iGSE replaces

the instantaneous magnetic flux density $B(t)$ in the GSE with its peak-to-peak value ΔB. Therefore, the method's formulas can be written as:

$$P_{iGSE} = \frac{1}{T}\int_0^T k_i \left|\frac{dB}{dt}\right|^{\alpha} (\Delta B)^{\beta-\alpha} dt \tag{49}$$

The equation (49) can also be written as:

$$P_{iGSE} = \frac{(k_i \Delta B)^{\beta-\alpha}}{T}\sum_m \int_{t_m}^{t_{m+1}} \left|\frac{dB}{dt}\right|^{\alpha} dt = \frac{(k_i \Delta B)^{\beta-\alpha}}{T}\sum_m \left|\frac{B_{m+1}-B_m}{t_{m+1}-t_m}\right|^{\alpha} (t_{m+1}-t_m) \tag{50}$$

$$k_i = \frac{k}{(2\pi)^{\alpha-1}\int_0^{2\pi}|cos\theta|^{\alpha}2^{\beta-\alpha}d\theta} \tag{51}$$

where: k, α, β are the original Steinmetz parameters, B_m, B_{m+1} are the consecutive amplitudes of the magnetic flux density in each minor loop, t_m, t_{m+1} are the consecutive time intervals of each minor loop. The iGSE core loss calculation method is considered to be more accurate than the OSE, MSE, or GSE, however it still gives some errors when the duty-cycle D takes very low or very high values [46], [98-101], [106], [111], [115], [116].

The *natural Steinmetz extension* (NSE) has been developed independently of the iGSE; however, it is assumed to be identical to it. The main formulas of the NSE are given by:

$$P_{NSE} = \left(\frac{\Delta B}{2}\right)^{\beta-\alpha} \frac{k_N}{T}\int_0^T \left|\frac{dB}{dt}\right|^{\alpha} dt \tag{52}$$

$$k_N = \frac{k}{(2\pi)^{\alpha-1}\int_0^{2\pi}|cos\theta|^{\alpha}d\theta} \tag{53}$$

where: ΔB is the peak-to-peak value of magnetic flux density, k, α, β are the original Steinmetz coefficients [46], [98-99], [107].

The *equivalent elliptical loop* (EEL) method assumes that the magnetic field intensity H can be decomposed into a reversible component H_{rev} and the irreversible component H_{irr}, and thus the hysteresis loss can be expressed as:

$$P_h = \frac{1}{T}\int_0^T (H_{rev} + H_{irr})\frac{dB}{dt}dt = \frac{1}{T}\int_0^T H_{irr}\frac{dB}{dt}dt \tag{54}$$

The reversible component is directly obtained from the B-H curve without the hysteresis loop. It is assumed that the H_{rev} is related to the reactive power in the material and the

H_{irr} is related to the instantaneous hysteresis loss, and thus the instantaneous hysteresis power loss is given by:

$$p_h(t) = H_{irr}\frac{dB}{dt} \tag{55}$$

and thus, the main goal in calculating the power loss is to obtain the H_{irr}. It is done by the introduction of the equivalent elliptical loop (EEL) where H_{irr} is computed by tracing the equivalent elliptical loop of the same area as the hysteresis loop. The loop is described by:

$$B = B_m \sin(\theta) \tag{56}$$

$$H_{irr} = H_m \cos(\theta) \tag{57}$$

The B_m is obtained from the historical record of the magnetic flux density, while the H_m is obtained under the assumption that the core loss calculated in the time domain is the same as in the frequency domain for sinusoidal excitation. The B_m can only be obtained from the stored elliptical loop if all ellipses inside the current ellipse are removed. In the case of a smaller ellipse created by the minor loop, the current ellipse is moved to the list of recorded ellipses, and the new ellipse becomes the current ellipse. The total core loss is then given by:

$$P_{EEL}(t) = |C| \cdot \left|\frac{dB}{dt}\right|^{\alpha} \tag{58}$$

$$C = \pm\frac{1}{C_{\alpha\beta}} k \cdot |B_m \cos(\theta)|^{\beta-\alpha} \tag{59}$$

$$C_{\alpha\beta} = (2\pi)^{\alpha}\frac{2}{\pi}\int_0^{\frac{\pi}{2}} \cos^{\beta}\theta d\theta \tag{60}$$

where k, α, β are the Steinmetz parameters. The EEL does not introduce any additional parameters; however, it suffers from low accuracy at very low and very high duty ratios [46], [111], [121].

The *double natural Steinmetz extension* (DNSE) splits the losses into two parts: the first part is the low-frequency hysteresis loss, and the second part is the high-frequency loss, based on the NSE method. The power split is introduced to mitigate unrealistic values of α parameters for ferrites in the OSE method at high frequencies. The authors assume that at low frequencies, around 20 kHz, the loss corresponds to the "pure" hysteresis, while at high frequencies, around 100 kHz to 500 kHz, the loss is mainly due

to peak-to-peak induction. Moreover, the method assumes the loss dependency on the shape of the waveform. The method of solution is as follows:

$$P_{DNSE} = P_h + P_{NSE} = \gamma f B_m^{\beta_1} + (1-\gamma)\left(\frac{\Delta B}{2}\right)^{\beta_2-\alpha} \frac{k_N}{T}\int_0^T \left|\frac{dB}{dt}\right|^{\alpha} dt \tag{61}$$

where α, β_1, β_2 are the Steinmetz parameters, the k_N is given by equation (53) and the γ is the fitting parameter. The accuracy of the DNSE is not fully verified; however, the authors claim that the method deviation compared to the measured data is not higher than 5% [46], [108].

The *waveform coefficient Steinmetz equation* (WcSE) introduces the concept of the flux waveform coefficient (FWC) to compare the average magnetic flux density under non-sinusoidal excitation to the average of the magnetic flux density under sinusoidal excitation, if the peak magnetic flux density stays the same in both cases. Then, to find the power loss under non-sinusoidal excitation, the OSE is multiplied by this coefficient, as follows:

$$P_{WcSE} = FWC \cdot P_{OSE} = FWC \cdot k f^{\alpha} B_m^{\beta} \tag{62}$$

This approach has the highest accuracy with a duty ratio of $D = 0.5$ and worsens if the duty ratio drifts away from this value. In general, the WcSE does not have any physical meaning [46], [98-99], [109].

The *Villar* core loss model transfers the OSE, MSE, iGSE, EEL, and the WcSE models to the rectangular waveform case with an introduced zero voltage period T_0, a typical output characteristic in most power electronic converters [98], [110-111]. Based on these conditions, the peak magnetic flux density and the zero-voltage period can be expressed as:

$$B_m = \frac{1}{2}\frac{V}{NA}\left(\frac{T}{2} - T_0\right) \tag{63}$$

$$T_0 = \omega\frac{T}{2\pi} \tag{64}$$

where N is the number of turns, A is the area of the core, ω is the zero-voltage period in radians.

The piece-wise linear model (PWL) can be easily used regarding the rectangular waveform case to define the magnetic flux density, which is as follows:

$$B(t) = B_m \begin{cases} -1 + \dfrac{1}{TD}t & 0 < t < \dfrac{T}{2} - T_0 \\ 1 & \dfrac{T}{2} - T_0 < t < \dfrac{T}{2} \\ 1 - \dfrac{1}{TD}\left(t - \dfrac{T}{2}\right) & \dfrac{T}{2} < t < T - T_0 \\ -1 & T - T_0 < t < T \end{cases} \tag{65}$$

where: the duty ratio is $D = 1 - \frac{\omega}{\pi}$.

The PWL expression of the core loss models is given by:

$$P_{OSE} = k f^{\alpha} B_{sq}^{\beta} D^{\beta} \tag{66}$$

$$P_{MSE} = \left(\frac{8}{\pi^2}\right)^{\alpha-1} k f^{\alpha} B_{sq}^{\beta} D^{\beta-\alpha+1} \tag{67}$$

$$P_{iGSE} = 2^{\alpha+\beta} k_i f^{\alpha} B_{sq}^{\beta} D^{\beta-\alpha+1} \tag{68}$$

$$P_{EEL} = \frac{C_{\beta\alpha}}{C_{\alpha\beta}} k f^{\alpha} B_{sq}^{\beta} D^{\beta-\alpha+1} \tag{69}$$

$$P_{WcSE} = \frac{\pi}{4}\left(1 + \frac{\omega}{\pi}\right) k f^{\alpha} B_{sq}^{\beta} D^{\beta} \tag{70}$$

where:

$$C_{\beta\alpha} = 4^{\alpha} \frac{2}{\pi} \int_0^{\frac{\pi}{2}} \cos(\theta)^{\beta-\alpha}\, d\theta \tag{71}$$

$$B_{sq} = \frac{T}{4}\frac{V}{NA} \tag{72}$$

$$\theta = \frac{\pi}{\frac{T}{2} - T_0} t \tag{73}$$

There is no accuracy verification of this method in the external literature; however, the authors claim that the Villar-based WcSE error is not greater than 30%, the EEL error is in the range of 16%-18% and the MSE and iGSE errors are in the range of 10%-12% compared to the measured core power loss.

The *expanded generalized Steinmetz equation* (EGSE) method was developed to address some issues with the GSE model, specifically the frequency dependence of core losses that are not included in the GSE model. It was done by introducing an additional parameter related to the magnetic field frequency dependence as follows:

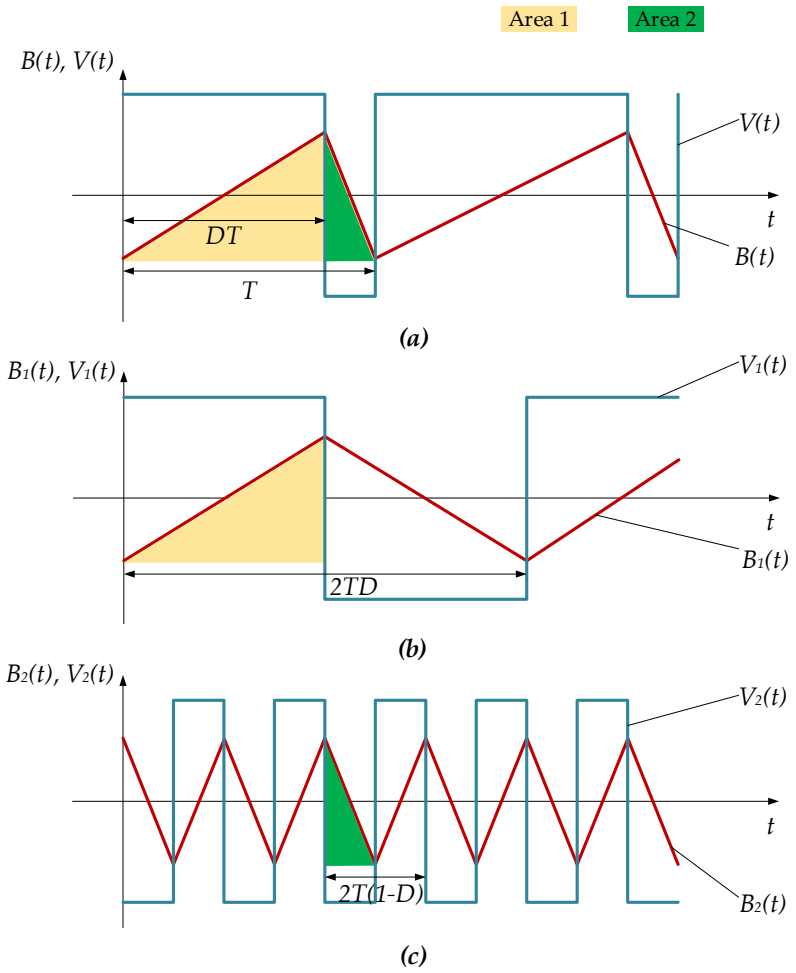

Figure 19: CWH Method - Decomposition of Rectangular Excitation Waveform into Two Pulses; (**a**) Square Excitation Waveform and Trapezoidal Induction Waveform; (**b**) Decomposition into First Pulse; (**c**) Decomposition into Second Pulse.

$$P_{EGSE}(t) = k_2|B|^{\epsilon}\left|\frac{dB}{dt}\right|^{\zeta\left|\frac{dB}{dt}\right|^{\eta}} \tag{74}$$

$$P_{EGSE} = \frac{k_2}{T}\int_0^T |B|^{\epsilon}\left|\frac{dB}{dt}\right|^{\zeta\left|\frac{dB}{dt}\right|^{\eta}} dt \tag{75}$$

$$k_2 = \frac{\sum P_m}{\sum\left(\frac{1}{T}\int_0^T |B|^{\epsilon}\left|\frac{dB}{dt}\right|^{\zeta\left|\frac{dB}{dt}\right|^{\eta}} dt\right)} \tag{76}$$

where: $k_2, \epsilon, \zeta, \eta$ are the fitted parameters and the P_m is the measured average core loss at each point of the loss chart.

The EGSE has been proven for the low-frequency sinusoidal excitations only [99], [112]. The authors of the method claim that its error in core loss prediction is not greater than

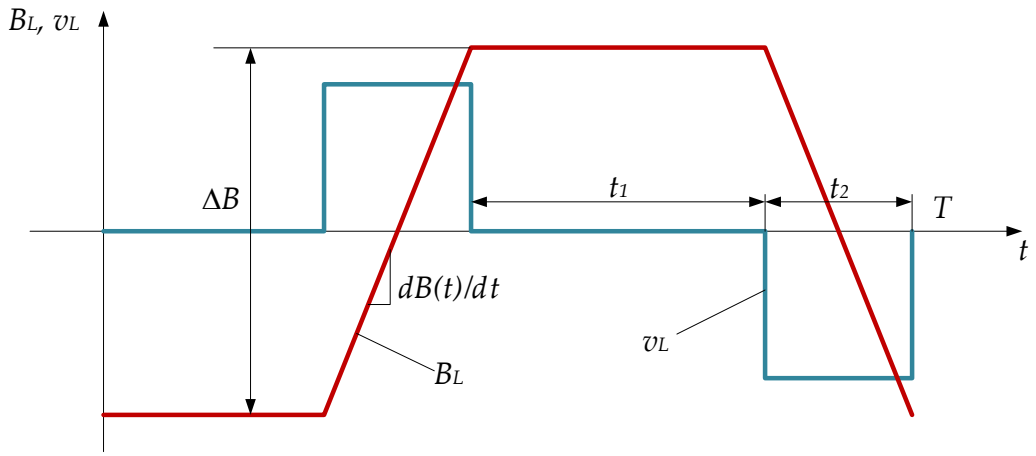

Figure 20: Rectangular Excitation and Trapezoidal Induction Waveforms with Relaxation Period Included.

8.7%; however, the method's accuracy has not been proven in any other scientific literature.

The *composite waveform hypothesis* (CWH) assumes that when a voltage square waveform is applied in a power electronics application, the flux in the core will ramp up or down, depending on whether a positive or negative voltage pulse is applied. The hypothesis has been made that the power loss occurring during each transition depends only on the amplitude and duration of the pulse, and there is no loss during the periods when the voltage is zero, which corresponds to the constant flux situation. Based on this hypothesis, it is possible to decompose each of the rectangular waveforms into a set of two pulses and calculate the power loss associated with each pulse as shown in Figure 19. Then the total power loss per cycle is the sum of the power loss of each cycle. This can be expressed based on the Herbert plot as:

$$P_{CWH} = \frac{1}{T}\left(P_{sqr}\left(\frac{V_1}{N}, t\right)\cdot t_1 + P_{sqr}\left(\frac{V_2}{N}, t\right)\cdot t_2\right) \tag{77}$$

where the P_{sqr} is the power loss of a rectangular waveform of given parameters, V_1/N and V_2/N are the applied voltages per turn in time t_1 and t_2, respectively. The accuracy of the method is not clearly reported by the method authors and by the independent literature [98], [122].

The *improved generalized Steinmetz equation* (i²GSE), as shown in Figure 20, takes into account the core relaxation process during the zero-voltage transition periods when a rectangular excitation waveform is applied. Some of the core loss calculation methods

overlook this phenomenon, which may lead to significant errors in core loss prediction. The relaxation phenomenon itself is related to the change of the core material thermal equilibrium due to the rapidly changing magnetization in the high-frequency or pulsed field applications. The new equilibrium is reached by rearranging the structure of the magnetic domains to achieve the state of the lowest energy. It influences the speed of flux change and thus the shape of the B-H loop, which becomes dependent on the rate of change of the magnetic field. The magnetic relaxation causes a change in magnetization, even if the applied field is constant, and residual energy loss still occurs.

The i²GSE method is an improvement of the iGSE method [106] that adds a component related to the relaxation process of the core loss during transient zero-voltage states. The model is written as:

$$P_{i^2GSE} = \frac{1}{T}\int_0^T k_i \left|\frac{dB}{dt}\right|^{\alpha} (\Delta B)^{\beta-\alpha} dt + \sum_{l=1}^{n} Q_{rl} P_{rl} \tag{78}$$

where: P_{rl} is the time-average power loss density due to the lth of n transients to zero voltage and can be expressed as:

$$P_{rl} = \frac{1}{T} k_r \left|\frac{d}{dt} B(t_-)\right|^{\alpha_r} (\Delta B)^{\beta_r} \left(1 - e^{-\frac{t_1}{\tau}}\right) \tag{79}$$

and the Q_{rl} is the voltage change, which is:

$$Q_{rl} = e^{-q_r \left|\frac{dB(t_+)/dt}{dB(t_-)/dt}\right|} \tag{80}$$

where: $\alpha, \beta, k_i, \alpha_r, \beta_r, k_r, \tau, q_r$ are the material parameters, $dB(t_-)/dt$ is the magnetic flux density change before the switching, $dB(t_+)/dt$ is the magnetic flux density change after switching, t_1 is the zero voltage constant flux time, τ is the relaxation time.

The i²GSE method is considered more accurate than the iGSE method, especially when trapezoidal and triangular induction waveforms are considered. However, its drawback is a complicated measurement and calculation process to obtain the material parameters, which makes the method highly impractical in industry-related projects [46], [98-99], [114].

The *rectangular extension of the Steinmetz equation* (RESE) method is specifically designed for rectangular AC voltages. It is based on the ideal inductor model connected in parallel with the equivalent core loss resistor. The method itself is similar to the WcSE method, introducing the proportionality coefficient between the square and the

sinusoidal waveform core losses. In the WcSE, this coefficient is related to the average value of the magnetic flux density waveform, whereas in the RESE, it is directly related to the measured core loss. To determine the proportionality coefficient, the triangular and sinusoidal magnetic flux densities with the same peak-to-peak values were compared, and the resulting ratio was referred to the equivalent resistor loss at the same excitation signals. The method itself is expressed by the following equation:

$$P_{RESE} = \frac{8}{\pi^2[4D(1-D)]^{\gamma+1}} k f^{\alpha} B_m^{\beta} \tag{81}$$

where: D is the duty ratio, k, α, β are the Steinmetz coefficients, γ is a material-related fitting coefficient.

The drawback of this method is that it requires obtaining a lookup table of the γ coefficients directly from the power loss measurement. Nevertheless, the method is considered to be more accurate than the MSE, GSE, and iGSE methods for rectangular excitation waveforms [46], [99], [115].

The *improved Steinmetz equation* (ISE) combines the CWH and the WcSE method. The CWH assumes that the total core loss can be considered as a sum of two rectangular pulses, as shown in Figure 19. The total area of the original magnetic flux density during the period T is split into two parts, the area A_1 during the DT period and the area A_2 during the $(1-D)T$ period as shown in Figure 19a. The area A_1 becomes a half-period area of a new signal $B_1(t)$ and the area A_2 becomes a half-period of a new signal $B_2(t)$. These two new signals have frequencies $f_1 = \frac{1}{T_1} = \frac{f}{2D}$, $f_2 = \frac{1}{T_2} = \frac{f}{2(1-D)}$ and the same duty cycle of 0.5, respectively. The core loss, according to the CWH, is as follows:

$$P_{ISE(CWH)} = \frac{1}{T}\left(\int_0^{DT} P_{ISE(CWH)}(t)dt + \int_{DT}^{T} P_{ISE(CWH)}(t)dt\right) = DP_{ISE(CWH)1} + (1-D)P_{ISE(CWH)2} \tag{82}$$

where the $P_{ISE(CWH)1}$ and $P_{ISE(CWH)2}$ are the time-average power losses of signals $B_1(t)$ and $B_2(t)$.

The CWH approach is then combined with the WcSE method, which is claimed to have a high accuracy under square wave excitation with a duty cycle of $D = 0.5$. Then the final equation is:

$$P_{ISE} = D\frac{\pi}{4}k_1\left(\frac{f}{2D}\right)^{\alpha_1} B_m^{\beta_1} + (1-D)\frac{\pi}{4}k_2\left(\frac{f}{2(1-D)}\right)^{\alpha_2} B_m^{\beta_2} \tag{83}$$

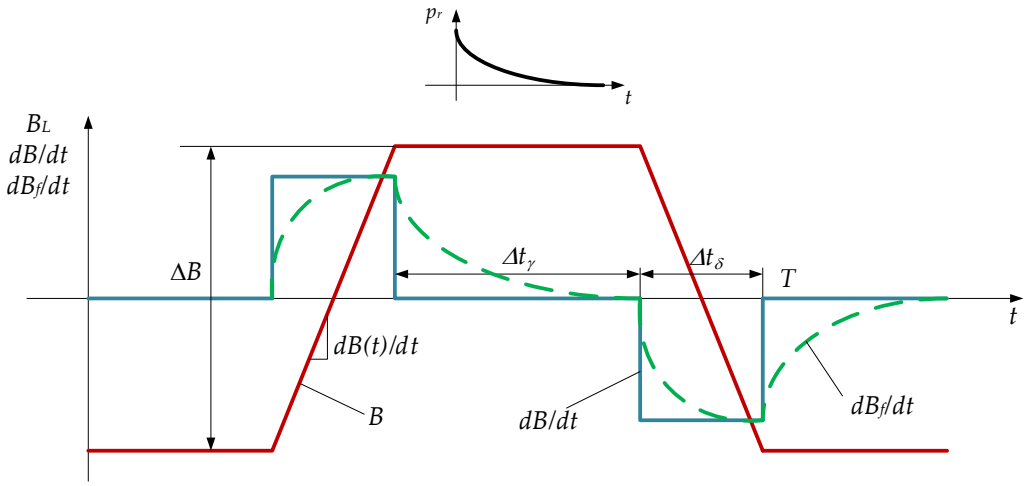

Figure 21: FGSE Method, Magnetic Flux Density (in Red), Derivative of Magnetic Flux Density (in Blue), Filtered Derivative of Magnetic Flux Density (in Green), Relaxation Power Loss During Constant Magnetic Flux Density.

where: $k_1, \alpha_1, \beta_1, k_2, \alpha_2, \beta_2$ are the Steinmetz parameters to be fitted at the corresponding frequencies of $f_1 = \frac{f}{2D}$ and $f_2 = \frac{f}{2(1-D)}$, respectively.

The method incorporates the duty cycle and frequency dependence of the Steinmetz parameters, which can be considered an advantage. The method's accuracy is claimed to be better than the iGSE; however, its accuracy is not clearly verified against other methods [46], [98-99], [109], [116], [122].

The *filtered, improved generalized Steinmetz equation* (FGSE) accounts for power loss during the relaxation period. It splits the core losses into the eddy current loss expressed as:

$$P_{eddy} = k_{eddy} \frac{1}{T} \int_0^T \left(\frac{dB}{dt}\right)^2 dt \tag{84}$$

while the rest of the losses are expressed by the iGSE method.

The energy loss during the relaxation period in the constant B interval can be expressed as the exponential decay, which is:

$$E_{const} = \Delta E \left(1 - e^{-\frac{\Delta t_\gamma}{\tau_r}}\right) \tag{85}$$

where: ΔE is the maximum energy loss and Δt_γ is the duration of an interval with B held constant, and τ_r is the relaxation time. The energy loss increases up to a certain point as the Δt_γ increases until the system reaches an equilibrium in its lowest energy state for a

given field perturbation, which can be modeled as an exponential decay. As shown in Figure 21, the dB/dt is filtered by the first-order transfer function with a time constant τ_f which corresponds to the dB_f/dt waveform and is proportional to the relaxation power loss. This phenomenon is included in the overall model, which is expressed as:

$$P_{FGSE} = \frac{1}{T}\int_0^T \left(k_i \left|\frac{dB}{dt}\right|^{\alpha} (\Delta B)^{\beta-\alpha} + k_f \left|\frac{dB}{dt}\right|^{\alpha_f} \left(\Delta B_f\right)^{\beta_f-\alpha_f} + k_e \left(\frac{dB}{dt}\right)^2 \right) dt \tag{86}$$

where $k_e, k_i, \alpha, \beta, k_f, \alpha_f, \beta_f$ are coefficients to be fitted.

During the Δt_γ the relaxation loss is proportional to the rate of change of filtered magnetic flux density B_f multiplied by the filtered flux density variation. The method is suitable for trapezoidal and triangular induction, and the authors of the method claim that the FGSE is more accurate than the MSE or iGSE method due to the inclusion of relaxation phenomena. The method, however, is not clearly compared against any other methods in the literature [46], [117].

The *Stenglein Steinmetz loss equation* (SSLE) method introduces the calculation of specific power loss per volume $P_{v,spec}$ by means of the effective frequency f_{eff} and the quasi-static energy loss density $E_{v,hyst}$. The quasi-static energy loss comprises the influence of low-frequency magnetic field density swing ΔB, the DC bias B_{dc} and the effective frequency represents the dynamic effects at high frequencies.

This relationship is given by:

$$P_{v,spec} = E_{v,hyst}(\Delta B, B_{dc}) f_{eff} \tag{87}$$

It is assumed that the dynamic effect can be modelled by the second derivative of $B(t)$, yielding the effective frequency for non-sinusoidal excitation as:

$$f_{eff_{nonsin}} = f\left(1 + c\left(\frac{1}{\Delta B}\int_0^T \left|\frac{d^2B(t)}{dt^2}\right| dt\right)^{\gamma}\right) \tag{88}$$

while for sinusoidal excitation it is:

$$f_{eff_{sin}} = f\left(1 + c\left(4\pi f_{eq}\right)^{\gamma}\right) \tag{89}$$

This approach allows for calculating core power loss for arbitrary shapes of $B(t)$ by calculating frequency-independent c and γ coefficients, which can be extracted directly from the manufacturer's characteristics.

The general principle of how to do it is to compare the specific energy loss at sinusoidal excitation with the specific energy loss caused by the non-sinusoidal excitation with the

Loss Model	Additional Steinmetz Parameters	DC Bias	Relaxation Effect	Magnetic Flux Density Excitation Waveform	Accuracy
OSE	No	No	No	Sinusoidal	N/A
MSE	No	No	No	Any Shape	Better than OSE
GSE	No	Yes	No	Any Shape	Better than MSE
iGSE	No	No	No	Any Shape	Better than GSE
NSE	No	No	No	Any Shape	Better than GSE
EEL	No	No	No	Any Shape	Better than MSE
DNSE	Yes	No	No	Any Shape	Not Clearly Identified
WcSE	No	No	No	Any Shape	Not Clearly Identified
Villar	No	No	No	Any Shape	Not Clearly Identified
EGSE	Yes	No	No	Sinusoidal	Not Clearly Identified
CWH	No	No	No	Trapezoidal and Triangular	Not Clearly Identified
i²GSE	Yes	No	Yes	Trapezoidal and Triangular	Better than iGSE
RESE	Yes	No	No	Triangular	Better than MSE, GSE and iGSE
ISE	No	No	Yes	Trapezoidal and Triangular	Better than iGSE
FGSE	Yes	No	Yes	Trapezoidal and Triangular	Better than MSE and iGSE
SSLE	Yes	Yes	No	Any Shape	Not Clearly Identified
iGCC	Yes	No	No	Any Shape	Better than ISE and SSLE

Table 2: Chosen Properties of Empirical Core Loss Calculation Methods.

same ΔB and B_{dc}. The equivalent switching frequency f_{eq} as in equation (89) is calculated assuming that the sinusoidal waveform leads to the same specific energy loss density, yielding:

$$f_{eq} = \frac{1}{4\pi\Delta B}\int_0^T \left|\frac{d^2B(t)}{dt^2}\right| dt \tag{90}$$

So, the specific power loss with the help of equation (90) can be determined as:

$$P_{v,spec} = k f^{\alpha-1}\left(\frac{\Delta B}{2}\right)^{\beta} \tag{91}$$

The method introduces an error of up to 15% between calculation and measurement; however, it is claimed to be more accurate than the iGSE method [123-124].

The *improved generalized composite calculation* (iGCC) method extends the core loss calculation to arbitrary waveforms based on the CWH and the Steinmetz approach.

The extension of the iGCC calculations to the arbitrary waveform is based on the introduction of the time-varying local equivalent frequency, which quantifies the instantaneous rate of change of the magnetic flux density and is expressed as:

$$\widetilde{f(t)} = \frac{1}{2}\frac{\left|\frac{dB}{dt}\right|}{\Delta B} \tag{92}$$

Having the time varying frequency, the arbitrary waveform can be decomposed into many symmetric triangular waveforms, and the iGCC power loss can be calculated using the CWH method as follows:

$$P = \frac{1}{T}\int_0^T P_{sym}\left(\widetilde{f(t)}, \Delta B\right)dt \tag{93}$$

The equation (93) can also be written as a summation for piecewise-linear functions as follows:

$$P = f\sum_{i=1}^{n} P_{sym}\left(\frac{1}{2}\frac{\left|\frac{\Delta B_i}{\Delta_i}\right|}{\Delta B}, \Delta B\right)\Delta t_i \tag{94}$$

If a loss map or an interpolant is available for $P_{sym}(f, \Delta B)$ the iGCC can be directly computed, or alternatively, the losses can be calculated using the frequency-dependent Steinmetz equation for triangular waveforms, which is:

$$P_{sym}(f, \Delta B) = \lambda(f)\Delta B^{\beta(f)} \tag{95}$$

and the total power losses are:

$$P = \frac{1}{T}\int_0^T \lambda\left(\tilde{f}(t)\right)\Delta \mathrm{B}^{\beta(\tilde{f}(t))}dt \tag{96}$$

The method itself combines the features of the ISE method, which provides accuracy at extreme duty cycles, with the applicability over a wide frequency range, and the iGSE to handle arbitrary waveforms. It is claimed that the method introduces a maximum error of 13% compared to the measured data and outperforms the iGSE and the SSLE methods in core loss prediction [124].

The chosen properties of empirical core loss calculation methods are shown in Table 2.

The next approach to the core loss calculation methods is the core loss separation group [126-139].

The general idea of core loss separation methods was first introduced for iron-based materials by Jordan a century ago [126]. The main concept of it is to split the classical hysteresis loss introduced by Steinmetz [102] into two parts: the static hysteresis loss and the dynamic eddy current loss. The hysteresis loss in this case is caused by the friction forces involved in changing the domain walls' alignment and rotation during the

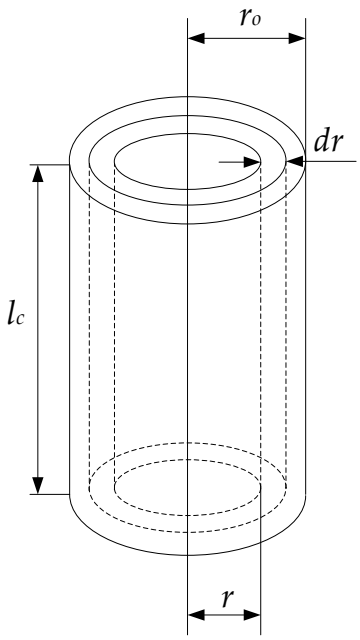

Figure 22: Cylindrical Magnetic Core Cross-Section.

magnetization process [4]. This loss is dissipated as heat and can be expressed for sinusoidal excitation with a parallelogram-based B-H loop as:

$$P_h = f \oint H \cdot dB = 4fH_m B_m sin\alpha = \frac{4fB_m^2}{\mu_r \mu_0} sin\alpha = k_h f B_m^2 \tag{97}$$

Moreover, in ferrites, the time-varying magnetic flux induces a voltage that generates the eddy currents. These currents flow in the core, causing conduction loss due to the core resistance. Considering a cylindrical core as shown in Figure 22 and using Faraday's law, one can get [4]:

$$v_L(t) = \frac{d\lambda(t)}{dt} = NA_c \frac{dB(t)}{dt} \tag{98}$$

The electric field density induced in the cylindrical shell of radius r is given by:

$$E(r,t) = \frac{d\phi(t)}{dt} = \frac{\pi r^2 v_L(t)}{A_c N} \tag{99}$$

where the shell resistance is:

$$R_{sh} = \rho_c \frac{2\pi r}{l_c dr} \tag{100}$$

The instantaneous eddy-current power loss in a shell is:

$$dp_e(r,t) = \frac{E^2(r,t)}{R_{sh}} = \frac{\pi l_c r^3 dr}{2\rho_c}\left(\frac{dB(t)}{dt}\right)^2 \quad (101)$$

and in the entire core:

$$p_e(t) = \int_0^{r_0} dp_e(r,t)dr = \frac{l_c A_c^2}{8\pi\rho_c}\left(\frac{dB(t)}{dt}\right)^2 \quad (102)$$

The time-average eddy current power loss density for sinusoidal excitation is:

$$P_e = \frac{1}{V_c}\frac{1}{T_e}\int_0^T p_e(t)dt = \frac{1}{8\pi\rho_c A_c N^2}\frac{1}{2\pi}\int_0^{2\pi} v_L(\omega t)d(\omega t) = \frac{\pi A_c(\mu_r\mu_0 f N I_{Lm})^2}{4l_c^2\rho_c} = k_{ec}(fB_m)^2 \quad (103)$$

where: V_c is the volume of the core, A_c is the cross-sectional area of the core, N is the number of winding turns, l_c is the magnetic length of the core, ρ_c is the resistivity of the core.

Therefore, the entire core power loss density predicted by Jordan for sinusoidal excitation is as follows:

$$P_c = P_h + P_{ec} = k_h f B_m^2 + k_{ec}(fB_m)^2 \quad (104)$$

The Pry and Bean in [127] recognized that equation (104) is insufficient to accurately describe the power loss in magnetic materials with magnetic domains in their structure. There exists an excess eddy-current loss not described by the classical model because it also depends on the square of the domain walls' velocity. In the magnetic material, the eddy currents are localized at the moving domain walls, where the eddy current density can reach very large values. The domains, which grow in size during the magnetization process, have more widely spaced walls; thus, each wall must move faster to produce a given flux change at a given frequency. Consequently, the total loss increases as the number of domain walls decreases [52]. The drawback of this method is its complexity [52].

The Pry and Bean approach was systematized by Bertotti [69], [128], who introduced the concept of magnetic objects (MO), which describes the large-scale behavior of magnetic domains. The magnetic object corresponds to a group of neighboring interacting domain walls, simplifying the eddy current loss problem to a function of current, frequency, and the material microstructure. As shown in [136], the excess eddy-current loss can be expressed as:

$$p_{exc} = \sqrt{\frac{A\alpha n_0}{\rho}}\left(\frac{dB(t)}{dt}\right)^{3/2} \tag{105}$$

while the average excess eddy current loss for sinusoidal excitation is given by:

$$P_{exc} = 1.75\sqrt{\frac{2\pi A\alpha n_0}{\rho}}(fB)^{3/2} \tag{106}$$

where: α is a numerical constant, n_0 is the statistical distribution of the local coercive fields, A is the core cross-section area, ρ is the core resistivity.

The Bertotti core loss approach can be written as:

$$P_c = P_h + P_{ec} + P_{exc} = k_h f B_m^2 + k_{ec}(fB_m)^2 + k_{exc}(fB)^{3/2} \tag{107}$$

The better curve fitting approach can be obtained if the magnetic flux density of the hysteresis loss is raised to the power of α to be fitted rather than to the power of 2, as follows:

$$P_c = P_h + P_{ec} + P_{exc} = k_h f B_m^{\alpha} + k_{ec}(fB_m)^2 + k_{exc}(fB)^{3/2} \tag{108}$$

Moreover, some scientists disregard the idea of dividing the core loss into hysteresis loss, eddy current loss, and excess loss as being unphysical [52]. The excess loss appears only because the classical eddy-current approach ignores the existence of domains and domain wall motions as the origin of the eddy currents. The magnetization process under DC conditions involves hysteresis loss, which consists of domain wall motion at low fields and domain wall rotation at high fields, being a source of eddy currents and the origin of power loss under DC conditions. Therefore, in all states, the power loss is primarily caused by eddy currents; thus, the power loss separation model is based on false assumptions. Despite objections to the core loss separation model, it is widely accepted among scientists and engineers. The accuracy of the Bertotti method was claimed to be within 10%. However, the test-bench measurement was only performed up to 400 Hz.

Jacobs et al. introduced the rotational and saturation losses to the Bertotti model [33], [129], [133]. Rotational loss occurs in rotating electrical machines and transformers, where the magnetic material can be magnetized by a magnetic field rotating in space. The rotational loss depends on the circular and elliptical magnetization, as well as the direction of rotation, and can be significantly higher than the axial loss.

Except for the rotational losses, Jacobs et al. introduced a higher-order term into the model to account for losses at large fields, which for iron laminations are due to saturation. The equation, which describes the entire power loss, is given by:

$$P_c = P_h + P_{ec} + P_{exc} + P_{sat} = k_h f B_m^{\alpha} + k_{ec}(fB_m)^2 + k_{exc}(fB)^{3/2} + k_{sat}B^{\xi+2}f^2 \quad (109)$$

where the particular components can be expressed as:

$$P_h = k_h\left(1 + \frac{B_{min}}{B_{max}}(r_h - 1)\right)B_{max}^2 f \quad (110)$$

$$P_{ec} = k_{ec}\sum_{n=1}^{\infty}\left|\overrightarrow{B_n}\right|^2(nf)^2 \quad (111)$$

$$P_{exc} = k_{exc}\sum_{n=1}^{\infty}\left|\overrightarrow{B_n}\right|^{1.5}(nf)^{1.5} \quad (112)$$

$$P_{sat} = k_{sat}B^{\xi+2}f^2 \quad (113)$$

Some modifications to the Jacobs approach have been done by Steentjes [130] so that equation (112) can be written to account for the flux distortion and the rotational loss in a more proper way:

$$P_{exc} = k_{exc}\left(1 + \frac{B_{min}}{B_{max}}(r_{exc} - 1)\right)\sum_{n=1}^{\infty}\left|\overrightarrow{B_n}\right|^{1.5}(nf)^{1.5} \quad (114)$$

where: r_h and r_{exc} are the rotational loss factors, $\frac{B_{min}}{B_{max}}$ is the flux distortion factor, $B_n = \sqrt{B_{n,x}^2 + B_{n,y}^2}$ and $B_{n,x}$, $B_{n,y}$ are the amplitudes of the nth harmonic in x and y direction of the rotational field.

The authors in [130] claim that the method's error in the power loss prediction does not exceed 4% compared to the measurement. The disadvantage of this method is that the measurements have been conducted for low frequencies of up to 400 Hz and only for rotating electrical machines.

Recently, Baumann et al. introduced a new core power loss separation model designed explicitly for magnetic cores with large volume and cross-section. The model enables the calculation of two additional loss mechanisms: electrical polarization losses and volume eddy current losses. The proposed model is expressed by the following equation:

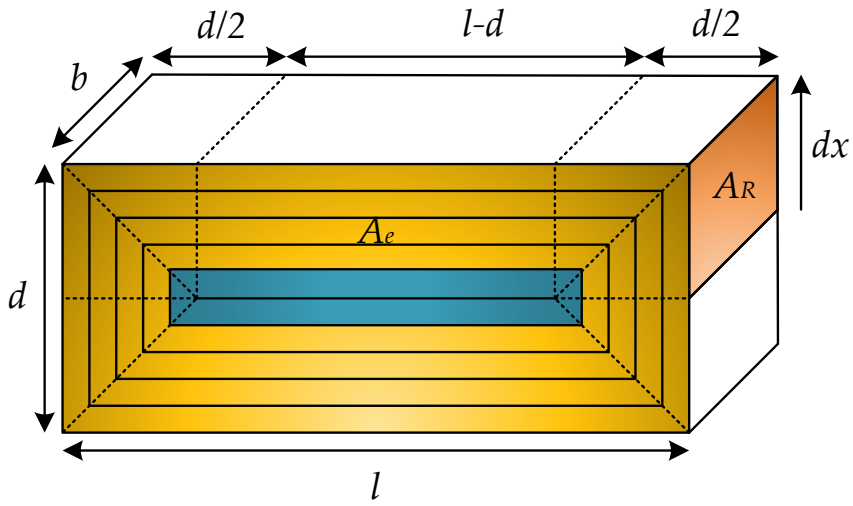

Figure 23: Core Cross-Section with Integration Loops.

$$P_{Baumann} = P_h + P_{eddy,grain} + P_{res} + P_{dielectric} \tag{115}$$

where: P_h is the hysteresis loss due to the change of the magnetic moments in time, $P_{eddy,grain}$ are the eddy-current losses due to non-zero conductivity on the grain-level size, P_{res} are the residual losses are due to the phase shift between the external magnetic field and the oscillating magnetic moments at high frequencies, $P_{dielectric}$ is the dielectric volume loss.

The principle of the method is described with the help of Figure 23 [131]. If sinusoidal magnetic flux density flows across the magnetic cross-section, a voltage is induced, which is:

$$V_{eff} = \frac{\omega B_{max} 2x(l-d+2x)}{\sqrt{2}} \tag{116}$$

The resistance of the concentric loops, as depicted in Figure 23, is:

$$R = \frac{2\rho l}{dA_R(x)} = 2\rho \frac{(l-d)+4x}{bdx} \tag{117}$$

and the power due to the movement of electrons is:

$$dP = \frac{V_{eff}^2}{R} = \frac{4\pi^2 f^2 B_{max}^2 b(l-d+2x)^2 x^2}{\rho(l-d+4x)} dx \tag{118}$$

and thus, the specific loss per unit volume is given by:

$$P_v = \frac{\pi^2 f^2 B_m^2}{16\rho} \cdot \frac{64}{ld} \int_0^{\frac{d}{2}} \frac{2lx^2 - 2dx^2 + 4x^3}{l-d+4x} dx = \frac{\pi^2 f^2 B_m^2}{16\rho} \left[\frac{(l-d)^4}{4ld} \ln \frac{l+d}{l-d} - \frac{(2l-2d)^2}{4} \right] \tag{119}$$

which can be written as:

$$P_v = \frac{\pi^2 f^2 B_m^2 A_e F_G}{16\rho} \tag{120}$$

where:

$$F_G = \frac{(l-d)^4}{4(ld)^2}\ln\frac{l+d}{l-d} - \frac{l^2-4dl+d^2}{2ld} \tag{121}$$

is the geometric factor.

The conductivity and the dielectric polarization losses can be combined into the effective dielectric loss $\epsilon_r^{"}$, which is expressed as:

$$\epsilon_r'' = \epsilon_{dipol}'' + \frac{\sigma}{\epsilon_0 \omega} \tag{122}$$

The effective dielectric loss can be treated as high-frequency conductivity, which is:

$$\sigma_{hf} = \epsilon_0 \omega \epsilon_{dipol}'' + \sigma \tag{123}$$

So, the dielectric loss is given by:

$$P_{dielectric} = \frac{\pi^2 f^2 B_m^2 A_e F_G (\epsilon_0 \omega \epsilon_{dipol}'' + \sigma)}{16} = \frac{\epsilon_0 \pi^3}{8}\left(\epsilon_{dipol}'' + \frac{\sigma}{2\pi f \epsilon_0}\right) f^3 B_m^2 A_e F_G \tag{124}$$

This loss can be split into two parts, the $P_{eddy,volume}$ and P_{dipol}, which are expressed as follows:

$$P_{eddy,volume} = \frac{\epsilon_0 \pi^3}{8}\frac{\sigma}{2\pi f \epsilon_0} f^3 B_m^2 A_e F_G \tag{125}$$

$$P_{dipol} = \frac{\epsilon_0 \pi^3}{8}\epsilon_{dipol}'' f^3 B_m^2 A_e F_G \tag{126}$$

The authors claim that the method has a maximum error of 15% in core loss prediction between calculations and measurements.

Most of the remaining core loss separation models usually modify the coefficients at each separated loss using the methods presented herein. Therefore, it is difficult to name them or distinguish them as being unique; thus, they are not described here in more detail.

The last group of the core loss calculation methods is the time-domain approximation (TDA) group. This method uses the fast Fourier transform (FFT) to calculate the product of the magnetic flux density, magnetic flux intensity, and the phase shift of them at each harmonic, as shown in the following equation:

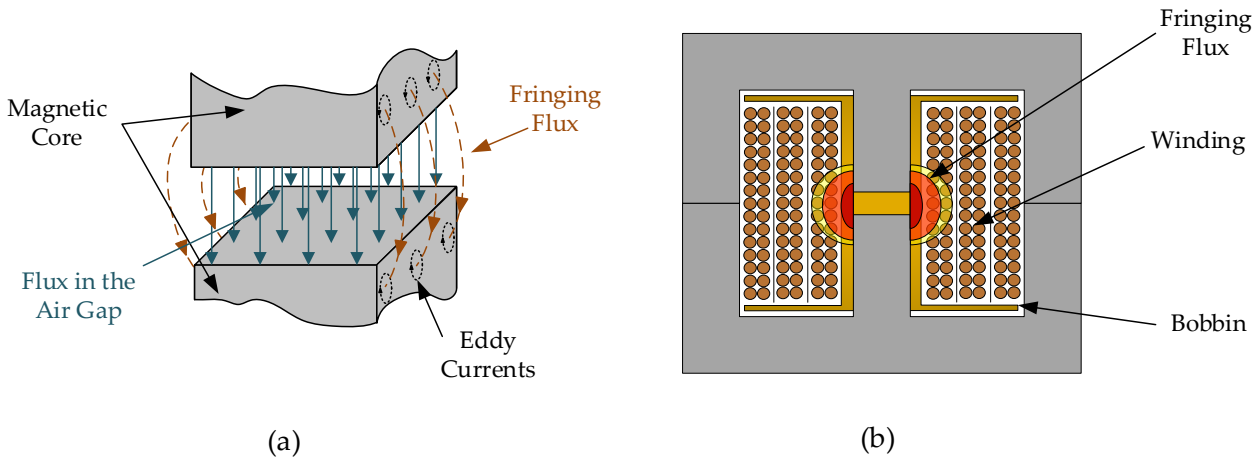

Figure 24: Fringing Flux; (**a**) Around the Air Gap; (**b**) Inside an Inductor with Gapped Core.

$$P_{cFFT} = \sum_{n=1}^{\infty} \pi(fn) B_n H_n sin\phi_n \tag{127}$$

This method can be applied to sinusoidal and non-sinusoidal induction waveforms; however, it is only suitable for linear systems, which is its primary limitation [98], [100], [118], [140-142]. This issue is clearly discussed in [118], where the primary reason is the high nonlinearity of the magnetic flux density, which typically rises to a power greater than 2, introducing significant errors in the harmonic magnitude prediction, especially with square excitation waveforms.

2.4.3 Loss in Gapped Inductors.

The air gap in inductors and transformers is introduced to avoid core saturation, while allowing for higher current levels at the expense of reduced inductance. Moreover, it increases thermal stability and makes permeability and inductance more predictable and effective.

However, the air gap also introduces the fringing field, as shown in Figure 24. The fringing field is created at the moment of passing from the magnetic core to a non-magnetic medium, which is, e.g., air. At this moment, the magnetic lines repel each other bending outwards, and thus the cross-sectional area of the magnetic field and its effective length increase, while the flux density decreases.

Moreover, the fringing flux induces eddy currents in nearby windings and the core, causing a local excess of the power loss, and thus the hot-spots in the vicinity of the

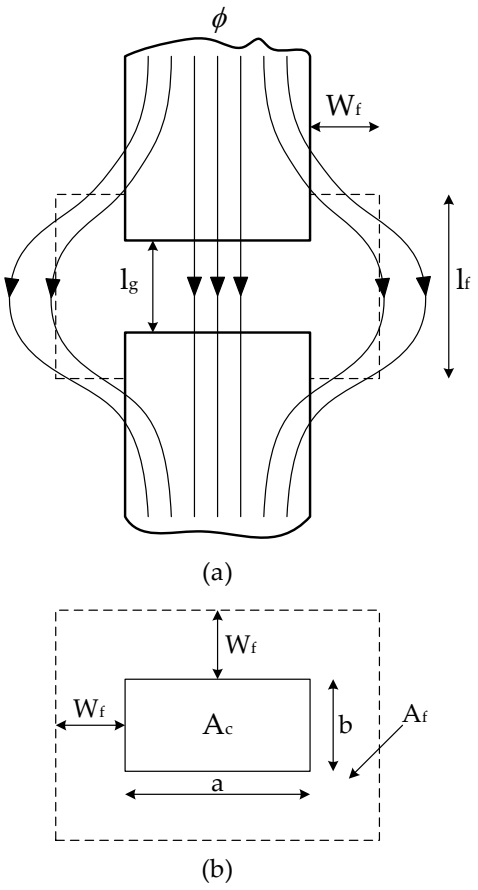

Figure 25: Kazimierczuk's Fringing Flux Calculation Method; (**a**) Flux Distribution Around the Air Gap; (**b**) Cross-Sectional Area of the Core A_C and the Fringing Flux A_f.

gap [1], [4], [143-146]. This phenomenon is particularly important for high-current, high-frequency magnetic components with low core resistivity, such as ribbon laminations, nanocrystalline, or amorphous alloys. For ferrites with high resistivity, however, it can be neglected. Considering the windings, the rule of thumb is to place them at least two gap lengths away from the gap to avoid induction of eddy currents and prevent overheating [4].

The fringing field reluctance shunts the gap reluctance, increasing the inductance. There are a few empirical equations to calculate the fringing factor, e.g., Partridge's given by [4], [146-148]:

$$F_{fringing(Partridge)} = 1 + \frac{al_g}{N_g\sqrt{A_c}}\ln\left(\frac{2w}{l_g}\right) \tag{128}$$

where: l_g it the gap length, N_g is the number of air gaps, w is the width of the core

window, a is the proportionality coefficient. The alternative approach was given by Kazimierczuk in [4] as shown in Figure 25 and is expressed as:

$$F_{fringing(Kazimierczuk)} = 1 + \frac{A_f l_g}{A_c l_f} \tag{129}$$

and by Hurley et al. in [62] as:

$$F_{fringing(Hurley)} = \frac{(a+g)(b+g)}{ab} \tag{130}$$

where: a, b are the dimensions of the rectangular core cross-section, g is the length of the gap.

The gap loss in the core was predicted in [144], [147] for steel laminated cores, which work at the line frequencies, which is:

$$P_{g(core)} = G l_g W_{core} f B_m^2 \tag{131}$$

where: $P_{g(core)}$ is the gap loss, l_g is the gap length, W_{core} is the lamination width, B_m is the peak induction, f is the frequency, G is the numerical constant.

However, the accuracy of this equation has been questioned, claiming that it overestimates the gap loss for amorphous metal cores. It is stated that this loss seems to be insignificant for inductors with very thin laminations and high resistivity [1], [143], [149]. Other works also suggest that the fringing flux has minimal impact on the loss increase caused by the cut cores [1], [143], [150]

This equation was further improved for nanocrystalline cores in [1] as:

$$P_{g(core)} = k_g l_g W_{core}^{1.65} f^{1.72} B_m^2 \tag{132}$$

where: $k_g = 1.68 \cdot 10^{-3}$.

The authors in [1] estimate that the error in the total power loss prediction of the nanocrystalline-based inductor does not exceed 18.1% using equation (132). However, the accuracy of the other methods used to predict winding loss and core loss is not clearly demonstrated or justified.

The gap-fringing field also induces losses in nearby windings. This phenomenon has been thoroughly studied in various works [65], [151-171].

Unfortunately, most of these works are difficult to follow due to the complicated mathematics involved, such as Bessel functions, cylindrical coordinates, and complex solutions, which require calculations of two-dimensional magnetic field intensity. Moreover, in most cases, the gap and fringing field loss are not treated separately but

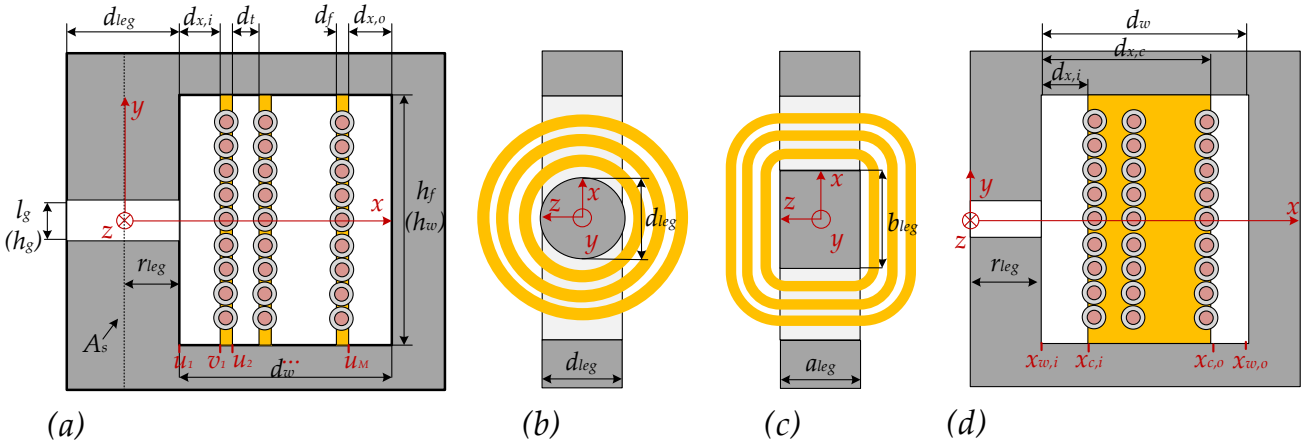

Figure 26: E/ER/ETD Inductor Model for Derivation of Fringing Flux Loss for Foil, Solid Round and Litz Wire; (**a**) 2-D Core Window; (**b**) Top View of ER/ETD Core Used for Length Scaling; (**c**) Top View of E Core Used for Length Scaling; (**d**) Simplified 2-D Core Window Assuming the Windings to be a Unified Conductor Block.

are embedded into the overall proximity losses of the windings. This makes most of these solutions unattractive to design engineers for use in commercial projects.

Recently, Ewald et al. [168-169] introduced a new method for predicting the gap and fringing loss in windings, which appears to be clearly explained and simple enough to be implemented in commercial designs.

The method introduces a set of formulas to calculate the winding loss in gapped inductors for foil, solid round, and Litz wires, taking into account skin, proximity, and fringing losses.

The description of the entire method, due to the excess of material and its complexity, is left to the reader for self-study. Only calculations of the fringing loss will be explained in more detail with the help of Figure 26. Moreover, this approach would also allow the use of other common winding loss calculation methods, such as the Dowell method, to predict winding loss in a classical manner and include fringing loss in the calculations separately.

Considering the inductor with a foil conductor, the method for calculating the gap loss is based on the assumption that the magnetic energy density is stored in the magnetic field.

The model, as shown in Figure 26, is divided into N rectangular conductors and $N + 1$ non-conductive regions. The air gap is placed in the middle of the centre leg.

The idea to calculate the influence of the fringing field and the fringing field-related loss on the windings is to find flux density components of the conducting and non-conductive regions by solving the relationship between the electric field and the magnetic vector potential, which can be written as follows:

$$\vec{J} = \sigma\vec{E} = -j\omega\sigma\left(\vec{A} + \frac{1}{j\omega}\nabla\phi\right) = -j\omega\sigma\vec{F} \tag{133}$$

The $\vec{F}$ is a modified vector potential, which replaces the magnetic vector potential. It can be obtained by solving the Laplace and diffusion equations in non-conductive (NC) and conductive (C) regions, which can be expressed as:

$$\nabla^2\vec{F}^{(NC)} = 0 \tag{134}$$

$$\nabla^2\vec{F}^{(C)} = \gamma^2\vec{F}^{(C)} \tag{135}$$

where: $\gamma^2 = j\omega\sigma\mu$.

The solution to the above is based on the assumption that the current, current density, magnetic vector potential, and the electric potential $\nabla\phi$ have only components in the z-direction, and the magnetic field is perpendicular to the vector potential, having only components in the xy-plane. Moreover, the influence of the air gaps on the magnetic field is modeled as surface current densities, and the core is closed by a high-permeability material. The surface current flows in the opposite direction to the current in the windings. Then the magnetic field around the gap can be decomposed into the spatial Fourier series with only cosine functions due to the strict symmetry of the core window with respect to the x-axis.

The solution to equations (134) and (135) for both non-conductive and conductive regions is given by:

$$F_z = \begin{Bmatrix} C_{m,0}(x-u_m) \\ M_{n,0}e^{-\gamma(x-v_n)} + N_{n,0}e^{\gamma(x-v_n)} \end{Bmatrix} + \sum_{k=1}^{\infty}\begin{Bmatrix} C_{m,k}e^{-p_k(x-u_m} + D_{m,k}e^{p_k(x-u_m)} \\ M_{n,k}e^{-\xi_k(x-v_n)} + N_{n,k}e^{\xi_k(x-v_n)} \end{Bmatrix}\frac{\cos(p_k y)}{p_k} \tag{136}$$

where: ξ_k is the attenuation constant equal to $\xi_k = \gamma^2 + p_k^2$, $p_k = 2\pi k N_g/h_w$, N_g is the number of air gaps. The magnetic flux density for non-conductive and conductive regions is $\vec{B} = \mu\vec{H} = \nabla\times\vec{F}$, and thus the spatial components in x and y direction, which represent the field due to the air gap, are given by:

$$\mu H_x = -\begin{Bmatrix} C_{m,k}e^{-p_k(x-u_m} + D_{m,k}e^{p_k(x-u_m)} \\ M_{n,k}e^{-\xi_k(x-v_n)} + N_{n,k}e^{\xi_k(x-v_n)} \end{Bmatrix} \sin(p_k y)$$
$$\mu H_y = \begin{Bmatrix} C_{m,k}e^{-p_k(x-u_m} + D_{m,k}e^{p_k(x-u_m)} \\ M_{n,k}e^{-\xi_k(x-v_n)} + N_{n,k}e^{\xi_k(x-v_n)} \end{Bmatrix} \cos(p_k y) \quad (137)$$

The calculation of $C_{m,k}, D_{m,k}, M_{n,k}, N_{n,k}$ are solved numerically as shown in [168-169].

The calculation of the losses due to the fringing field of the gap is done based on the Poynting theorem which can be expressed as

$$P = \frac{1}{2}\iiint x\,\vec{E}\vec{J^*}dxdydz \quad (138)$$

Because it is assumed that the electric and the magnetic field do not vary with z-coordinate, the overall losses are obtained by multiplying the losses per unit length P_n' by the conductor length l_n. Therefore, only the per-unit-length losses have to be determined by integrating the Poynting vector over the conductor edges ∂S_n in the xy-plane, with the multiplication by the conductor length. The losses per unit length and conductor with assumptions of scalar magnetic potential can be expressed as:

$$P_n' = -\frac{1}{2}\Re\left\{\frac{\gamma^2}{\mu\sigma}\oint_{\partial S_n} F_z(H_y^*\vec{e_x} - H_x^*\vec{e}_y)d\vec{s_n}\right\} \quad (139)$$

The x-component of the magnetic field at the yokes is forced to zero, and thus equation (139) can be simplified to an integration along both conductor edges in y- direction and is:

$$P_n' = \frac{\omega}{2}\Im\left\{\int_{-\frac{h_w}{2}}^{\frac{h_w}{2}} F_z(v_n + d_f, y)H_y^*(v_n + d_f, y) - F_z(v_n, y)H_y^*(v_n, y)dy\right\} \quad (140)$$

Solving equation (140), the losses per unit length due to the air gap fringing field are given by:

$$P_{n,k}' = \frac{\omega h_w}{\mu\delta}\left(\frac{\zeta_{1,k}}{2p_k^2}\left(|M_{n,k}|^2 e^{-\zeta_2\Delta} + |N_{n,k}|^2 e^{\zeta_2\Delta}\right)\sinh(\zeta_2\Delta) + \frac{\zeta_{2,k}}{2p_k^2}\Re\{M_{n,k}^* N_{n,k}e^{j\zeta_1\Delta}\}\sin(\zeta_1\Delta)\right) \quad (141)$$

where: $\Delta = d_f/\delta$, the skin depth is $\delta = \sqrt{1/\pi f\sigma\mu}$, and the coefficients $\zeta_{1,k} = \left(\left(\frac{p_k^4\delta^4}{4} + 1\right)^{\frac{1}{2}} - \frac{p_k^2\delta^2}{2}\right)$, $\zeta_{2,k} = \left(\left(\frac{p_k^4\delta^4}{4} + 1\right)^{\frac{1}{2}} + \frac{p_k^2\delta^2}{2}\right)$.

The total loss due to the fringing field is given by:

$$P_{f(Foil)} = \sum_{n=1}^{n}\sum_{k=1}^{\infty} l_n P_{n,k}' \quad (142)$$

The additional resistance due to the fringing field can be computed as follows:

$$R_{f(Foil)} = 2P_{f(Foil)}/I_m^2 \tag{143}$$

where: I_m is the amplitude of the applied current.

In a fairly similar manner, Ewald et al. calculate the air gap's influence on the winding loss for solid round and Litz wire [170]. However, in this case, the formulas presented by the authors consider the complete inductor geometry instead of the losses per unit length. Moreover, the formulas do not apply to foil conductors because they act as eddy current shields and must be modelled separately. The calculation of these formulas with the help of Figure 26 is left to the reader for a self-study, and only the final equations describing the resistance due to the fringing field for solid round and Litz wire are given below:

$$R_{f(SolidRound)} = R_{DC}G_R\frac{2\pi h_w}{\mu_0^2 V_{UC}}\sum_{k=1}^{\infty} c_k\left(x_{c,i}, x_{c,o}\right)|C_k|^2 + d_k\left(x_{c,i}, x_{c,o}\right)|D_k|^2 \tag{144}$$

$$R_{f(Litz)} = R'_{DC}G'_R\frac{2\pi h_w}{\mu_0^2 V_{UC}}\sum_{k=1}^{\infty} c_k\left(x_{c,i}, x_{c,o}\right)|C_k|^2 + d_k\left(x_{c,i}, x_{c,o}\right)|D_k|^2 \tag{145}$$

where:

$$R_{DC} = \frac{4N(x_{c,o} + x_{c,i})}{\sigma d^2} \tag{146}$$

$$V_{UC} = \pi h_w(x_{c,o}^2 - x_{c,i}^2) \tag{147}$$

$$G_R = \pi^2 d^2 Re\left\{\frac{\alpha I_1(\alpha)}{I_0(\alpha)}\right\} \tag{148}$$

$$\alpha = (1+j)\frac{d}{2\delta} \tag{149}$$

$$R'_{DC} = \frac{4N(x_{c,o} + x_{c,i})}{\sigma d_s^2 N_s} \tag{150}$$

$$G'_R = \pi^2 d_s^2 N_s Re\left\{\frac{\alpha' I_1(\alpha')}{I_0(\alpha')}\right\} \tag{151}$$

$$\alpha' = (1+j)\frac{d_s}{2\delta} \tag{152}$$

$$C_k = -\frac{2\mu_0 k_\mu N}{p_k h_w(1 - e^{-2p_k d_w})} si\left(p_k\frac{h_g}{2}\right) \tag{153}$$

$$D_k = C_k e^{-2p_k d_w} \tag{154}$$

$$c_k(x_1, x_2) = \left[-\frac{e^{-2p_k(x-u_1)}(2p_k x + 1)}{4}\right]_{x_1}^{x_2} \tag{155}$$

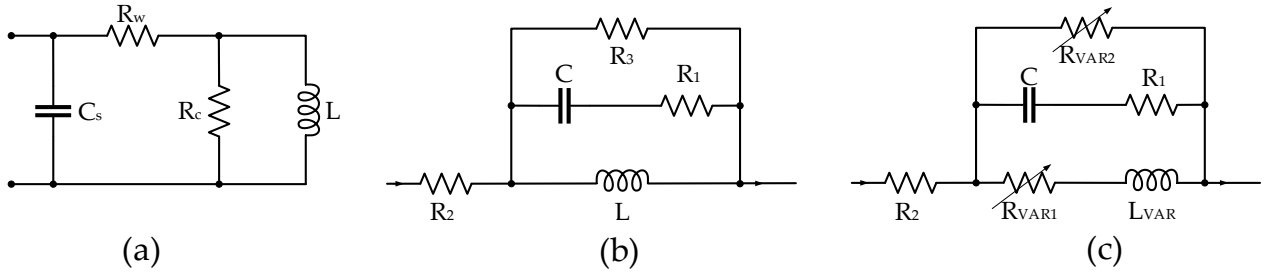

Figure 27: Equivalent Inductor Models; (**a**) Kazimierczuk's Approach; (**b**) Coilcraft Advanced Frequency Domain Approach; (**c**) Coilcraft Impedance Model Approach.

$$d_k(x_1, x_2) = \left[\frac{e^{2p_k(x-u_1)}(2p_k x - 1)}{4}\right]_{x_1}^{x_2} \tag{156}$$

where: $si(x) = \sin(x)/x$, $p_k = 2\pi k N_g/h_w$, I_v is the modified Bessel function of the first kind and the v-th order, δ is the skin depth, σ is the conductivity, d is the diameter of bare solid round wire, d_s is the diameter of a bare strand of the Litz wire, N_g is the total number of air gaps, $N = \sum_{n=1}^{N_{EFC}} N_n$ is the total number of conductors, N_{EFC} is the number of equivalent foil conductors (number of layers), N_n is the number of conductors in each EFC (winding layer), N_s is the number of strands in a bundle, V_{UC} is the volume of the winding. The authors predict that their method can predict winding losses with an error of 10% for solid round and Litz conductors, and with less than 15% error for foil conductors.

2.5 Modelling of Ferrite Inductors.

2.5.1 Circuit Modelling.

The physical power inductor is a complex system that can only be modeled using several discrete RLC components, which approximate its distributed characteristics, as shown in Figure 27 [4], [174-175]. To make it possible, the circuit modelling using simulation programs with integrated circuits emphasis (SPICE) was initially developed to mathematically predict these types of difficult behaviors. This approach significantly speeds up the entire design process because there is no need to build the physical circuit and also allows in non-destructive way to perform several circuit analyses [174-177].

The SPICE models are intended to behave as a virtual representation of the real inductors. Thus, their models must be carefully designed to capture all the appropriate characteristics of the inductor. This imposes challenges and limitations on the modelling.

For instance, small-signal frequency domain models operate within their linear region of operation with low signal excitations and utilize Laplace elements to capture frequency-dependent parameters, such as inductance or resistance. These simulations may be useful for low-current, EMI, or RF designs, but not for high-power applications. Power supplies usually require transient and steady-state time domain simulations with large signal excitations, and the simulation software does not process Laplace elements in the time domain. Moreover, the magnetic components might saturate when exposed to high-level excitation signals, which also needs to be modeled. Therefore, there is no single equivalent SPICE inductor model that captures all AC loss mechanisms and inductor behavior under all conditions.

Besides SPICE circuit modelling, the correct equivalent inductor circuit models are also needed to extract the inductor parameters, such as complex permeability, capacitance, windings, and core resistance, directly from impedance measurements [178-179].

Therefore, in Chapter 3, an improvement to the equivalent inductor models depicted in Figure 27 will be shown. The proposed modifications will enable the accurate estimation of the measured complex permeability and facilitate the integration of the small-signal and large-signal core loss models into a unified model.

2.5.2 Thermal Modelling.

International standards typically limit the maximum operating temperature of magnetic components, which is one of the key factors limiting their size reduction and overall optimization. Moreover, the temperature rise is related to the power loss; thus, a correct thermal model can help verify whether the estimated power loss is accurate and how it is distributed within the magnetic component.

The simplest way to predict a temperature rise of a magnetic component is to use empirical estimations to simplify the one-dimensional heat equations [4], [147], [180-182]. However, these empirical estimations are usually limited to natural convection. The equation introduced by McLyman [4], [147] is given by:

$$\Delta T_{total} = 450\left(\frac{P_{total}}{A_{total}}\right)^{0.826} \tag{157}$$

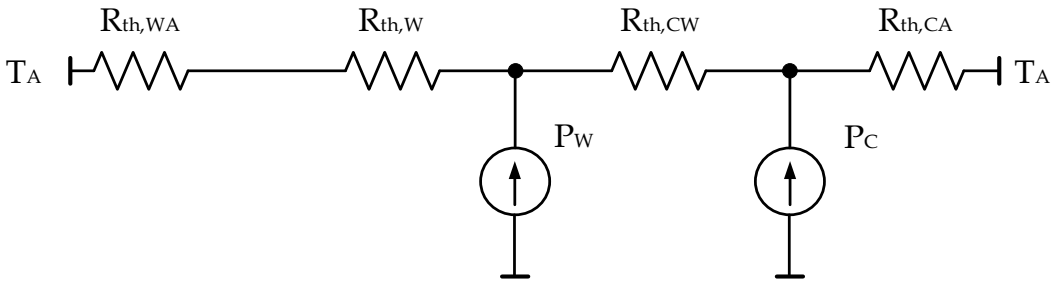

Figure 28: Thermal Model of an Inductor.

where: ΔT is the temperature rise, P_{total} is the total power dissipated by an inductor, A_{total} is the total outer surface are of an inductor which directly dissipates heat to the ambient.

The total temperature rise ΔT_{total} in the equation, can also be considered as a sum of the temperature rise of the external surface to the ambient and also the temperature rise across the component between its surface and its hottest point $\Delta T_{total} = \Delta T_{surface} + \Delta T_{accros}$.

Another empirical equation was introduced by Micrometals [181-182]:

$$\Delta T_{total} = \left(\frac{P_{total}}{A_{total}}\right)^{0.833} \tag{158}$$

Escribano et al. [181] introduced a relationship between inductor temperature rise, its thermal resistance, and its volume, which can be expressed as:

$$\Delta T_{total} = R_{th} P_{total} = \frac{K_{th}}{V^{2/3}} P_{total} \tag{159}$$

where: R_{th} is the thermal resistance of an inductor, K_{th} is the coefficient which depends on the inductor geometry and film coefficient of the outer inductor surface, V is the volume of an inductor.

Another way to simplify the heat equation and predict the inductor temperature rise is to use thermal networks in the form of a thermal ladder, as shown in Figure 28. This can be done using 1-D [4], [183], 2-D [184-185], and 3-D models [186]. This approach has a limitation of being linear, while the boundary conditions considering convection and radiation are not linear. Moreover, in these types of models, the power losses are concentrated at a single point, rather than being physically distributed along solid bodies. The thermal networks could also be complicated in structure and applicable only to one particular inductor design case [180].

2.5.3 FEM Modelling.

Finite element modelling (FEM) is used to comprehensively design and simulate magnetic components in a multi-physics environment. In general, the description of the physical systems is done through partial differential or integral equations. These equations, instead of being solved analytically, which can often be difficult or infeasible, are solved numerically and approximately by the FEM software. This is done by dividing (meshing) the domain of interest into smaller subdomains (finite elements), setting up a relatively simple set of equations for each element at each mesh node, and then gathering these into larger algebraic sets of equations that model the entire simulated system. These equations are then solved numerically by minimizing predefined error functions, during which the solution approaches the optimum as the elements are chosen smaller (i.e., a finer mesh). The FEM approach delivers the most realistic solution with the highest accuracy among circuit and thermal modelling if the simulation parameters, such as material properties and boundary conditions, are correctly defined.

The setup of the FEM simulation is iterative, and each step should be executed in a predefined order, which also might require adaptation and re-execution of earlier steps, which are:

- The relevant FEM software must be chosen, e.g., Ansys Maxwell, for electromagnetic simulation.
- The appropriate solver must be chosen, e.g., magnetostatic, eddy current, or transient, depending on the type of simulation.
- The simulated geometry must be designed in the FEM software itself or imported as a CAD model.
- The relevant materials and materials' properties must be allocated to imported geometrical elements.
- The excitation signals and boundary conditions must be set.
- The solver setting must be defined.
- The geometry must be successfully divided (converged) into smaller volumes (meshing) on which the physics is going to be solved.
- Numerical solution of the resulting model.
- Post-processing of the computed results.

The most popular FEM software for simulating magnetic components is Ansys Maxwell, COMSOL Multiphysics, and CST Studio Suite. This software is typically divided into various simulation solutions within multiphysics suites, allowing users to combine, for example, electromagnetic simulation performed in Ansys Maxwell with thermal simulation in Ansys Icepak to obtain comprehensive simulation results for the same simulated object. The same applies to the COMSOL Multiphysics and CST Studio Suite.

2.6 Summary.

In this chapter, a comprehensive overview of magnetic components used in power electronics has been provided. The importance of power electronics and its magnetic components is evidenced by the number of existing converters and their applications across various industrial branches.

However, the main aim of this chapter is to demonstrate the properties of magnetic components, their loss mechanisms, and the state-of-the-art loss calculation techniques, as well as the possible modelling and simulation techniques to optimize their design.

Based on the overview in Chapter 3, an improved complex permeability measurement and calculation technique will be proposed. These techniques are based on small-signal impedance measurements, an improved inductor model, and iterative approximation curve fitting. This approach may help in the development of improved inductor loss models and universal SPICE models that capture all AC loss mechanisms, which currently do not exist.

Moreover, in Chapter 3, an improved RESE (iRESE) core loss model will be presented. The iRESE unifies the Steinmetz-based core loss model with the small-signal complex permeability model to comprehensively characterize the entire core loss spectrum, regardless of the magnitude of the excitation signals. It also considers the rectangular excitation of signals and the DC bias phenomenon commonly present in the switch-mode power supplies (SMPS), along with the magnetic permeability roll-off near the core saturation level.

Chapter 3

3. Analytical Modelling and Power Loss Calculations of Inductors.

Most of the chapter text is taken from the author's papers [187], [208] and referenced when appropriate.

3.1 Improved Measurement and Calculation Techniques of Complex Permeability.

The inductor optimization process requires verification and improvement in the calculation of several quantities, including winding resistance, core resistance, temperature rise, and power loss, which define the inductor's shape, size, and cost. These quantities depend on each other, so a miscalculation in one might cause significant discrepancies in the others, and thus, they must be carefully studied [187].

The tool commonly used for this purpose is a vector network analyzer (VNA). This relatively affordable device sweeps through frequency ranges, extracting all the necessary information that is further required for the design of an equivalent inductor model. Moreover, the VNA has one significant advantage - it allows measurement in the "off-line" mode, on a stand-alone inductor, which significantly simplifies the method, saving time and resources. However, it should be remembered that this type of inductor analysis is performed using a small-signal technique. Thus, large-signal losses require additional effort in measurements, especially when core loss is considered.

In the model, the inductor equivalent series resistance (ESR), as shown in Figure 29 and Figure 30, consists of embedded information on winding and core resistance. Therefore, an engineer must know both quantities to split the data accurately. The winding resistance is usually calculated using Dowell's equation [4-5]. In contrast, the core resistance depends mostly on the imaginary part of the complex permeability when the applied testing signal is small enough. Unfortunately, the precise estimation of core resistance is not always possible because the core manufacturers' data are subject to significant measurement uncertainties [188]. Moreover, the real inductor itself is a

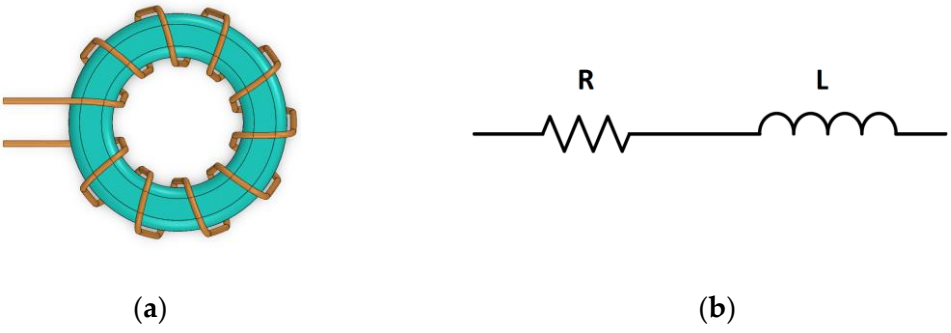

(**a**) (**b**)

Figure 29: (**a**) Toroidal Ferrite Coil and (**b**) its Equivalent Simplified Series Model.

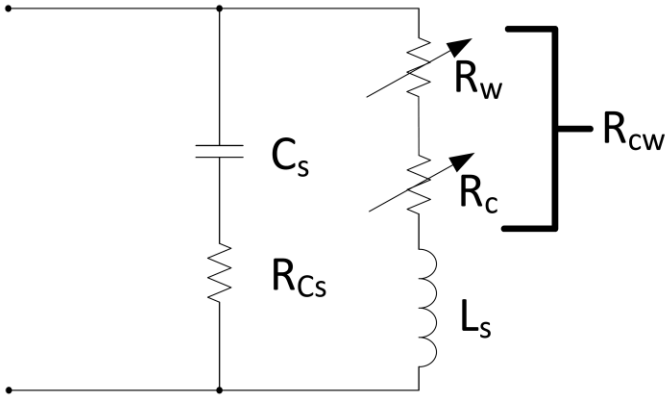

Figure 30: Series Un-Gapped High-Frequency Equivalent Inductor Model.

complex system with many other quantities influencing permeability values. The best way to achieve good convergence in calculations is to obtain the required information directly from the complex permeability measurement, thereby stripping out results from unwanted information.

However, several existing complex permeability measurement and calculation techniques do not fully reveal how complex permeability is measured and fitted, or the fitting is oversimplified [189-195] or overly complicated [196]. The fittings are done based on not fully complete equivalent inductor models with several fitting variables, which can take arbitrary values and do not represent the physical behavior of the inductor [197-198]. This approach cannot yield the valid results necessary for simulation programs with integrated circuit emphasis (SPICE), commonly used in industry to model the behavior of electronic circuits and expedite time-to-market product release [174-175].

This chapter paragraph discusses existing complex permeability measurement and calculation techniques and proposes a new one based on small-signal impedance

measurements, an improved equivalent inductor model, and an iterative approximation curve fitting technique. This enables the relatively accurate estimation of complex permeability values, regardless of inductor size, shape, winding structure, or frequency range. The method is simple and intuitive to process, assuming the frequency dependence of most inductor model components, and thus overcomes some limitations and the complexity of other methods [4], [178], [190], [196-197]. This is significant because it may aid in the development of improved inductor loss models and universal simulation models (e.g., SPICE models) that capture all AC loss mechanisms, which currently do not exist, especially in high-frequency power electronics applications.

3.1.1 Complex Permeability Verification.

The verification of complex permeability values and the characteristics provided by core manufacturers is crucial for inductor power loss and overall optimization [155], [174-179]. This can be successfully done if the inductor model is well-defined, together with all its parasitic components, which influence the inductor impedance measurement. It must be considered that most existing inductor models used in standard power electronic applications are valid for switching frequencies of up to 3 MHz, a range that shall be significantly extended [190].

3.1.1.1 Definition of Inductor Lumped Model and Complex Permeability Values.

Some of the research work [189], [195], [197] and the IEC 62044-2 standard [192] simplify the complex permeability measurement procedure by assuming that the toroidal lumped inductor model, as shown in Figure 29, is only a series combination of resistance and reactance. In the case of an ungapped toroidal core with only one layer of widely spaced windings, this approach may yield valid results. However, it is worth the additional effort to take a step further and refine the model to be even more accurate, incorporating the remaining parasitic components into the overall calculations [187].

The existing high-frequency equivalent inductor models, except for the simplified R-L circuit, consider the inductor's stray capacitance, core resistance, leakage inductance-related components, and the influence of inductor terminals [4], [155], [174-175], [179], [190], [199].

Considering the power inductor, these models can be further simplified as shown in Figure 30, removing all the parasitic components influencing the model until a multi-megahertz switching frequency is in place,

where:

C_s – inductor stray capacitance measured at self-resonance,

R_{c_s} – inductor stray capacitance equivalent series resistance,

L_s – inductor series inductance measured at low frequencies,

R_c – equivalent core series resistance,

R_w – winding resistance,

R_{cw} – core and windings equivalent series resistance.

As reported in [174-175], the inductor lumped model should include the equivalent series resistance of the stray capacitor to make the model more realistic and avoid nonexistent signal spikes if the model is placed in a simulation software.

The capacitor ESR is primarily influenced by the dielectric permittivity of the coating on the winding wires, which is typically made of polyurethane or polyamide resin, and to a lesser extent by the dielectric permittivity of other insulation materials, such as Kapton, Mylar, and others [5]. Usually, the dielectric constant for such materials ranges from 3 to 4 [5], [200-202]. Moreover, the IEC 60317-20 [203] imposes on the enameled winding wires an upper limit for the dielectric loss tangent, which is $300 \cdot 10^{-4}$ at 1MHz frequency. Taking these factors into account, the inductor capacitance ESR (R_{Cs}) can be estimated as:

$$R_{Cs} = \frac{\tan\delta}{\omega \cdot C_s} \tag{160}$$

where:

$\tan\delta$ – dielectric loss tangent, which is assumed to be $300 \cdot 10^{-4}$ for copper-to-copper wire turn,

ω – angular frequency.

The impedance, the real and imaginary parts of the inductor equivalent model shown in Figure 30, can be expressed as:

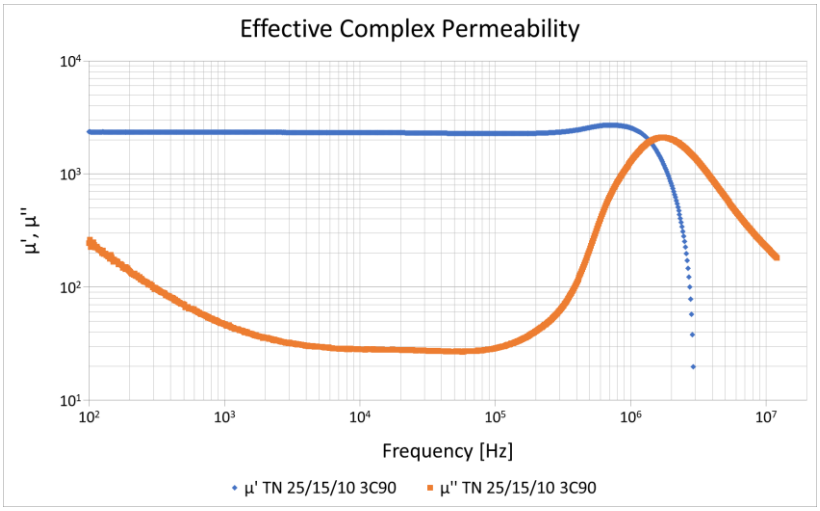

Figure 31: Effective Complex Permeability of TN25/15/10-3F3 Toroidal Core, Blue – Real Part of Complex Permeability, Orange – Imaginary Part of Complex Permeability.

$$r = \frac{\omega^4 L_s^2 C_s^2 R_{Cs} + \omega^2 C_s^2 R_{cw} R_{Cs}(R_{cw} + R_{Cs}) + R_{cw}}{(1 - \omega^2 L_s C_s)^2 + \left(\omega C_s (R_{cw} + R_{Cs})\right)^2} \tag{161}$$

$$x = \frac{\omega^3 L_s C_s (C_s R_{Cs}^2 - L_s) - \omega C_s R_{cw}^2 + \omega L_s}{(1 - \omega^2 L_s C_s)^2 + \left(\omega C_s (R_{cw} + R_{Cs})\right)^2} \tag{162}$$

where:

$R_{cw} = R_w + R_c$

and thus, the effective real and imaginary part of the complex permeability is [192]:

$$\mu_r' = \frac{l_c}{\mu_0 A_c N^2} \cdot \frac{x}{\omega} \tag{163}$$

$$\mu_r'' = \frac{l_c}{\mu_0 A_c N^2} \cdot \frac{r}{\omega} \tag{164}$$

As it is self-evident, the effective complex permeability values depend on the inductor core geometry and winding structure, and thus are unique for each inductor setup [191]. Therefore, the data provided by the core manufacturers is for close-to-ideal inductors and is valid far from the inductor's self-resonance. Otherwise, it may only serve as a basis for the initial estimation of the core magnetic permeability behavior [187]. This assumption will be verified in Chapter 4.

As shown in Figure 31, the imaginary part of the effective complex permeability characteristics bends upwards at low frequencies. This phenomenon is primarily due to the resistance of the inductor windings, and to a lesser extent, to the remaining parasitic RLC elements that the physical inductor is composed of, as shown in Figure 30.

The effective complex permeability model itself represents the physical behavior of a real inductor, where the resistance of the winding wires and other parasites must be included. Therefore, the bending might be removed from the measurement e. g. by a curve fitting [189], because it represents a physical change from the dominance of the core loss to the winding loss [187].

3.1.1.2 Mathematical Verification of Low-Frequency Effective Complex Permeability.

As shown, the measured low-frequency imaginary part of the complex permeability bends upward to higher values. Mathematically, this phenomenon might be explained by the fact that when frequency decreases toward zero (equation (161)), the real part of the inductor impedance tends to the frequency-independent finite value, which is the windings' DC resistance (R_{wDC}). This can be written as:

$$\lim_{\omega \to 0} r = R_{wDC} \tag{165}$$

while, at the same time, the imaginary part of the effective complex permeability tends to infinity:

$$\lim_{\omega \to 0} \mu_r'' = \frac{l_c}{\mu_0 A_c N^2} \cdot \frac{r}{\omega} = \frac{l_c}{\mu_0 A_c N^2} \cdot \frac{R_{wDC}}{\omega} \to \infty \tag{166}$$

The bending indeed exists and is caused by a natural phenomenon, which originates from the inductor lumped model and is an inherent part of the effective complex permeability model itself.

On the other hand, the above phenomenon does not exist if we consider the real part of complex permeability. In this case, the imaginary part of the inductor impedance tends to zero,

$$\lim_{\omega \to 0} x = 0 \tag{167}$$

while the real part of complex permeability tends to a high but finite value, which depends on the inductor's lumped parameters and can be expressed as follows:

$$\lim_{\omega \to 0} \mu_r' = \frac{l_c}{\mu_0 A_c N^2} \cdot \frac{x}{\omega} = \frac{l_c}{\mu_0 A_c N^2} \cdot (-C_s R_{cw}^2 + L_s) \approx \frac{l_c}{\mu_0 A_c N^2} \cdot L_s \tag{168}$$

Based on the characteristic shown in Figure 31 and the mathematical explanation of the low-frequency bending phenomenon, the new iterative approximation curve fitting technique, together with verification of complex permeability characteristics, will be presented next.

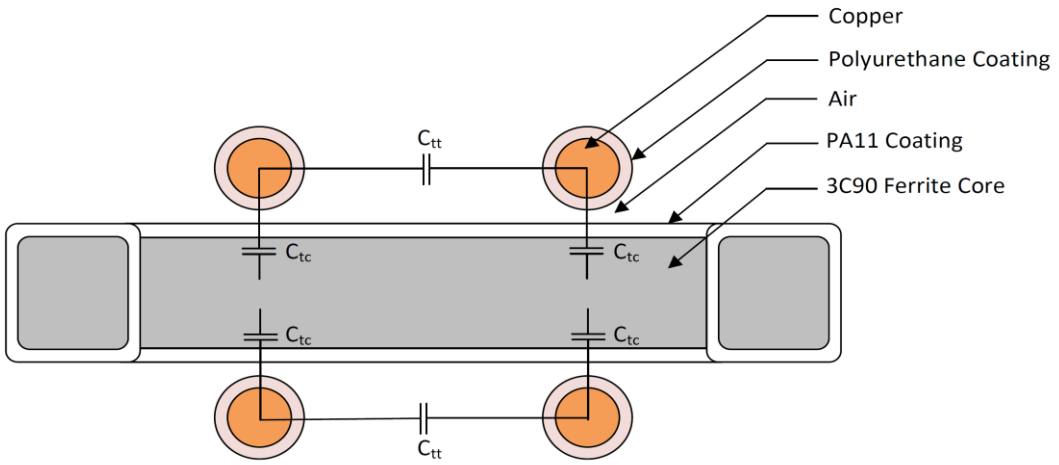

Figure 32: Example of Toroidal Inductor Cross-Section with Highlighted Turn-to-Turn and Turn-to-Core Capacitance.

3.1.1.3 Mapping of Effective Complex Permeability Characteristics based on Inductor Equivalent Model and Iterative Approximation Curve Fitting.

The effective complex permeability curves can be mapped from measurements using an iterative approximation curve-fitting technique based on a series of ungapped equivalent inductor models, as shown in Figure 30. During the fitting process, the samples' impedance should be measured using an impedance or VNA analyzer. The inductance value used in the approximation should be measured at low frequencies (a few tens of kHz at most) and lie within the plateau range of the measured characteristics.

It is suspected that most of the inductor stray capacitance is between wire turns and between wire turns and the core, as shown in Figure 32. Therefore, the dielectric loss tangent of the capacitor ESR is a complex case influenced by the dielectric permittivity of several materials, such as the enameled copper wire coating, the air between the wire and the core, the core coating, and the core material itself [187].

Unfortunately, insufficient research has been conducted on the electrical parameters of such materials, so loss tangent characteristics versus frequency are not commonly available [191], [204]. It is assumed that most of the capacitor ESR loss tangent is due to the ratio of the core imaginary and the real part of complex permittivity, which might sharply increase at high frequencies due to the ferrite material structure itself, core shape, and its dimensional resonance [191], [205].

The approximation itself assumes that the resistance of the inductor windings changes along the frequency range according to the standard Dowell equation [4-5],

[179]. This assumption yields accurate results, especially when the inductor has no distributed or discrete air gaps and consists of a single layer of widely spaced winding turns [187].

The extraction assumes that the measured complex permeability values follow equations (163-164), where r and x come from the impedance measurement. Then the obtained results are compared with estimated ones, which are also calculated with the help of equations (163-164); however, at this time, with r and x coming from equations (161-162), namely [187]:

$$\mu'_{r_{estimated}} = \mu'_{r_{measured}} + \xi_{\mu'_r} \tag{169}$$

$$\mu''_{r_{estimated}} = \mu''_{r\,measured} + \xi_{\mu''_r} \tag{170}$$

$$\xi_{\mu'_r} = \mu'_{r_{measured}} - \mu'_{r_{estimated}} \tag{171}$$

$$\xi_{\mu''_r} = \mu''_{r\,measured} - \mu''_{r_{estimated}} \tag{172}$$

where:

$\mu'_{r_{measured}}$ – real part of effective complex permeability (the measured characteristic),

$\mu''_{r\,measured}$ – imaginary part of effective complex permeability (the measured characteristic),

$\mu'_{r_{estimated}}$ – estimated real part of complex permeability, using equations (162) and (163),

$\mu''_{r_{estimated}}$ – estimated imaginary part of complex permeability, using equations (161) and (164),

$\xi_{\mu'_r}$ – shift between measured and estimated real part of complex permeability characteristic,

$\xi_{\mu''_r}$ – shift between the measured and estimated imaginary part of the complex permeability characteristic.

The fitting variable is the imaginary part of the complex permeability, which is part of the core series resistance (R_c), and is expressed as follows:

$$R_c = \frac{\mu''_{r\,fitted}\mu_0 N^2 A_c \omega}{l_c} \tag{173}$$

The $\mu''_{r\,fitted}$ is the value stripped away from the influence of parasitics and represents the actual core loss. Its value can be obtained during an iterative sweep when the absolute value of the shift given by equation (172) is minimal:

$$\xi_{\mu''_{r_{min}}} = MIN\,|\mu''_{r\,measured} - \mu''_{r_{estimated}}| \tag{174}$$

To get the best fitting results, the series inductance L_s was assumed to be a variable one, which changes along the frequency range following the changes of the measured real part of complex permeability, as such:

$$L_s = \frac{\mu' r_{measured} \mu_0 N^2 A_c}{l_c} \tag{175}$$

It is suspected that the method heavily depends on the inductor stray capacitor ESR (R_{Cs}) value. Unfortunately, there is insufficient data available to confirm or refute this phenomenon and accurately estimate the ESR value across the entire frequency range. The theoretical approach to limit its range and estimate its value will be presented next, while the FEM simulation and test-bench measurement results will be presented in Chapters 4 and 5, respectively.

3.1.2 Estimation of Inductor Stray Capacitor ESR Value.

The ESR of the inductor stray capacitor (R_{Cs}) depends on the dielectric loss tangent (equation (160)) of several materials as shown in Figure 32. As it is suspected, one of the most significant contributors to the ESR is the loss tangent of the core coating and the core itself.

The method presented in this paper utilizes an inductor series equivalent model for the calculations. Additionally, the stray capacitance within the model also includes an ESR in series. The relationship between admittance, complex permittivity, and the loss tangent calculations shall also be done with a series capacitor model, which can be expressed as follows:

$$tan\delta = \frac{\omega \epsilon_r'' + \sigma}{\omega \epsilon_r'} \tag{176}$$

$$Y_s = G_s + j\omega C_s \tag{177}$$

$$\epsilon_r = \epsilon_r' - j\epsilon_r'' \tag{178}$$

$$\epsilon_r' = \frac{C_s d_s}{\epsilon_0 A_s} \tag{179}$$

$$\epsilon_r'' = \frac{G_s d_s}{\omega \epsilon_0 A_s} = \frac{\sigma}{\omega \epsilon_0} \tag{180}$$

where:

ω – angular frequency,

G_s – measured series conductance,

C_s – measured series capacitance,

ϵ_r – series relative complex permittivity,

ϵ_r' – real part of the series complex permittivity,

ϵ_r'' – imaginary part of the series complex permittivity,

σ – material conductivity,

d_s – sample thickness,

A_s – sample cross-section.

The loss tangent does not depend very much on the sample thickness and cross-section, and thus, equation (176) can be simplified to:

$$tan\delta \approx \frac{\epsilon_r''}{\epsilon_r'} = \frac{G_s}{\omega C_s} \tag{181}$$

Moreover, a better understanding of the origin of the inductor's stray capacitance and its ESR requires an investigation of the core resonance phenomena and their influence on the complex permeability values, which will be discussed next.

3.1.3 Influence of Core Natural and Dimensional Resonance on Complex Permeability.

In general, there are at least three factors that contribute to the resonance in Mn-Zn ferrites [48], [206-207], namely:

- resonance due to the windings' stray capacitance and the inductor self-inductance,
- the windings behave as a distributed constant line,
- inherent characteristics of the magnetic material.

As stated in the previous paragraphs, the inductor's stray capacitance and its ESR, which are assumed to be mostly related to the windings, do not appear to impact the inductor's complex permeability characteristics, and the stray capacitance is somehow excluded from the overall calculations. It contradicts what one might expect and suggests that the inductor resonance originates somewhere else.

Moreover, the phenomenon where the winding behaves as a distributed constant line is most pronounced in inductors with multiple turns at multi-megahertz frequencies, in the form of self-repeating resonance.

The resonance phenomenon, which still applies, is the resonance resulting from the inherent characteristics of the magnetic material. In this case, there are two phenomena:

- natural resonance,
- dimensional resonance.

The natural resonance happens to the ferrites with high magnetic permeability due to the resonance of magnetization rotation under the action of the anisotropy field [48],[207].

Above the resonance, the real part of the complex permeability drops along the line known as Snoke's limit.

The Snoke's limit can be calculated as follows [48] [207]:

$$f \cdot \mu_r = \frac{v \cdot B_s}{3 \cdot \pi \cdot \mu_0} \tag{182}$$

$$v = g_e \cdot q_e \cdot \frac{\mu_0}{2 \cdot m_e} \tag{183}$$

where:

$f \cdot \mu_r$ – Snoke's limit in $[MHz]$,

f – switching frequency,

μ_r – relative magnetic permeability,

v – gyromagnetic constant,

B_s – assumed magnetic saturation level of ferrite material,

μ_0 – magnetic permeability of free space,

g_e – electron g-factor,

q_e – electron charge,

m_e – electron mass.

As shown in Figure 31, the change in the real part of the complex permeability characteristics is preceded by an increase in permeability and then followed by a sharp drop. Suppose the drop happens way before Snoke's limit. In that case, it suggests that the magnetic resonance cannot be attributed to the natural resonance, but rather to a second phenomenon related to the shape and dimensions of the inductor core.

For the sake of explanation, in the steady-state at low frequencies, the field inside the core is uniform and in phase with the excitation field provided by the windings,

which represents the quasi-static field assumption. However, as the frequency increases, the field tends to be concentrated at the surface of the core, a phenomenon known as the skin effect, which also applies to conducting materials such as ferrites.

Because of the combined effect of the high resistivity phase of the ferrite grains, and the high permittivity and high permeability at the same time, the excitation field will propagate through the core at a different velocity than in free space. This reduced velocity can be expressed as a product of the wavelength, which is:

$$\lambda = \frac{c}{f\sqrt{\mu_r \epsilon_r}} \tag{184}$$

where:

c – speed of light,

f – switching frequency,

μ_r – ferrite relative permeability,

ϵ_r – ferrite relative permittivity.

In this case, the shorter wavelength causes phase displacement between the magnetic field inside the core and the magnetic field on its surface, and the quasi-static field assumption no longer applies. It causes the net flux linking the windings to be no longer a function of the core cross-sectional area. Moreover, if the dimensions of the core are an integer multiple of the wavelength, the electromagnetic wave will resonate within the core, and the crest of the standing wave will trigger dimensional resonance. If this happens, the net flux linkage of the windings is zero, resulting in a zero apparent inductance [48], [206-207].

The proposed model also assumes that the resonant frequency is almost independent of the number of winding turns, suggesting that the inductor's stray capacitance and its ESR in a given configuration are mostly due to the capacitance and ESR of the core, which will be discussed next. This will be proven in Chapter 4.

3.1.4 Estimation of Inductor Stray Capacitance.

Estimation of the core and the winding capacitances and their ESRs would improve the lumped inductor model and help in the more precise extraction of the complex permeability characteristics.

Theoretical estimation of the winding's capacitance has been done using the method given in [4], namely:

$$C_{tt} = \frac{2\epsilon_0 MLT}{\sqrt{\left(\frac{1}{\epsilon_r}\ln\frac{d_0}{d_i}+1\right)^2 - 1}} \arctan\left(\sqrt{1+\frac{2}{\frac{1}{\epsilon_r}\ln\frac{d_0}{d_i}}}\right) \tag{185}$$

$$C_{s_{nc}} = \frac{C_{tt}}{N-1} \tag{186}$$

$$C_{1,N} = C_{tt} + \frac{C_{1(N-2)}C_{tt}}{2C_{1(N-2)} + C_{tt}} \tag{187}$$

$$C_{s_{wc}} \approx 1.366 C_{tt} \; for \; N \geq 10 \tag{188}$$

$$C_{s_{dc}} \approx 1.366 C_{s_{nc}} = 1.366 \frac{C_{tt}}{N-1} \; for \; N \geq 10 \tag{189}$$

where:

C_{tt} – turn-to-turn capacitance of a single-layer inductor,

N – number of turns,

MLT – mean length of turn,

ϵ_r – relative permittivity,

ϵ_0 – permittivity of free space,

d_0 – winding wire diameter with coating,

d_i – bare winding wire diameter,

$C_{s_{nc}}$ – inductor stray capacitance without a core,

$C_{1,N}$ – inductor stray capacitance with a core and N turns,

$C_{s_{wc}}$ – approximated inductor stray capacitance with a core,

$C_{s_{dc}}$ – approximated inductor stray capacitance with a dummy core,

SRF_{dc} – self-resonant frequency of an inductor with a dummy core,

$C_{s_{dc(meas)}}$ – measured inductor stray capacitance with a dummy core,

L_{dc} – inductance of an inductor with a dummy core.

This method has also been verified in two ways: empirically through finite element method (FEM) analysis and laboratory measurements, as will be shown in Chapters 4 and 5, respectively.

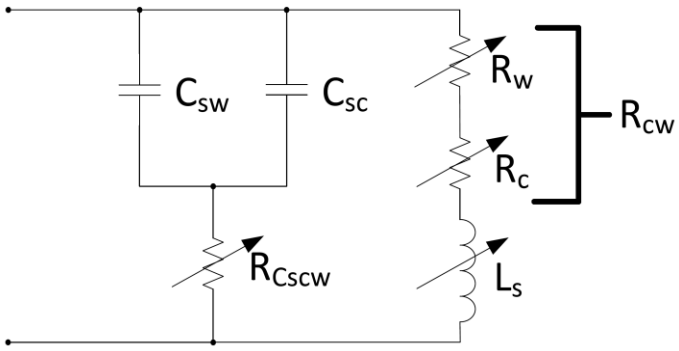

Figure 33: Improved Series Equivalent Inductor Model.

3.1.5 Improved Equivalent Inductor Model.

As it is assumed and will be investigated in subsequent chapters, the inductor's self-resonant frequency depends not only on the windings' capacitance but also on the apparent capacitance of the core.

In the case of the windings' capacitance, it is assumed that in certain inductor configurations, the ferrite core has only a negligible impact on it. Therefore, this capacitance is mostly defined by the coreless turn-to-turn capacitance ($C_{s_{nc}}$) and the capacitance to core coating or bobbin ($C_{s_{wc}}$) (equations (185-189)) [4].

In the case of the core, capacitance exists between core crystal grains due to the high-resistivity phase deposited on the grain boundaries. This causes high effective permittivity [206], which, combined with the ferrite's high permeability, significantly reduces the length of the electromagnetic waves propagating through the core. At certain frequencies, the electromagnetic wave will resonate within the core, triggering dimensional resonance and causing a sharp drop in the real part of the complex permeability. We might refer to the core capacitance as apparent because it is not due to charge storage, but rather to complex resonance-based phenomena that cause winding-core flux decay. Its ESR is also a product of complex phenomena inside the ferrite crystal structure.

Nevertheless, to properly model the inductor, its stray capacitance should be split into two parts: one related to the windings and one related to the core, as shown in Figure 33.

Unfortunately, the relationship between the core and the windings is complex and implicit; thus, there is insufficient scientific evidence regarding the correct

relationship between their ESRs. To keep the model consistent with the obtained data, both ESRs had been combined into one resistance (R_{Cscw}).

The windings' capacitance (C_{sw}) can be estimated using equations (185-189). The core capacitance (C_{sc}) can be estimated by simply subtracting the capacitance obtained from the L-C product at the inductor self-resonant frequency. The combined ESR (R_{Cscw}) of the windings and the core can be obtained using equations (176-181) and the iterative approximation curve fitting technique until the relative fitting error is small (e.g., less than 2%) across the entire frequency range.

3.2 Improved Core Loss Calculations.

The core loss of the ferrite-based magnetic components is usually characterized by the well-known Steinmetz equation and its derivatives. This occurs when the magnitude of the excitation signal is high enough; otherwise, the core loss is defined by the complex permeability. These two models are based on different assumptions; thus, this chapter aims to combine the large- and small-signal core loss models into a single, unified model. Moreover, the chapter paragraph presents improvements to the existing state-of-the-art core loss model, specifically regarding the influence of the switching duty-cycle of rectangular excitation signals and the DC bias [208].

The ferrite-based core loss characteristics provided by the core manufacturers are designed to calculate the average power loss per unit volume or mass. The characteristics are estimated by the well-known original Steinmetz equation (OSE) [102], which is:

$$P_{OSE} = k f^{\alpha} B_m^{\beta} \tag{190}$$

where: *k, a, b* are the Steinmetz coefficients obtained during the fitting of the double logarithmic core loss characteristics given by the core manufacturers, *f* is the switching frequency, and B_m is the amplitude of the magnetic flux density.

Unfortunately, the equation, despite its simplicity, does not account for non-sinusoidal excitation signals, such as rectangular waveforms and their DC bias, a situation that often prevails in modern switch-mode power supplies (SMPS).

As shown in various works, rectangular excitation waveforms have a profound impact on core loss, especially at the minimum and maximum values of the switching duty cycle. Therefore, to address this issue, various core loss models dedicated to the non-sinusoidal excitations have been designed: the MSE [104], GSE [105], iGSE [106],

WcSE [109], i²GSE [114], RESE [115], ISE [116], FGSE [117], SSLE [123]. These models, e.g., assume that the core loss is proportional to the magnetic flux density rate of change (dB/dt) [104-106, 114], the magnetic flux density is piece-wise-linear allowing separate calculations of the power loss of each minor and major B-H loop [106, 114], include the relaxation phenomenon during the zero-voltage transition periods [114, 166-117] and/or DC bias [105, 123]. These models attempt to predict the core loss accurately, but they often suffer from large numbers of hard-to-predict coefficients and overall method complexity.

Therefore, a new core loss model dedicated to rectangular AC voltages, based on the rectangular extension of the Steinmetz equation (RESE) [115] and referred to as an improved RESE (iRESE), is proposed [208].

The iRESE unifies the Steinmetz-based core loss model with the small-signal complex permeability model to comprehensively complete the entire core loss characteristics regardless of the magnitude of the excitation signals. Moreover, it also takes into account the rectangular excitation of signals and the DC bias phenomenon commonly present in the switch-mode power supplies (SMPS), together with the magnetic permeability roll-off near the core saturation level [208].

3.2.1 Review of RESE Based Loss Models.

The RESE model is specifically designed for rectangular AC voltage excitation. It is based on the ideal inductor model connected in parallel with the equivalent core loss resistor, as shown in Figure 34.

It introduces the proportionality coefficient to the OSE that is based on the measured data and serves as a link between the square and the sinusoidal excitation core losses. This coefficient is obtained by comparing the triangular and sinusoidal magnetic flux densities, both with the same peak-to-peak values, and the resulting ratio is referred to as the equivalent resistor loss at the same excitation signal. This gives a “U” shape core loss characteristic as a function of the duty-cycle ratio, a situation commonly encountered in switch-mode power supplies. An example of such characteristics is given in Figure 35.

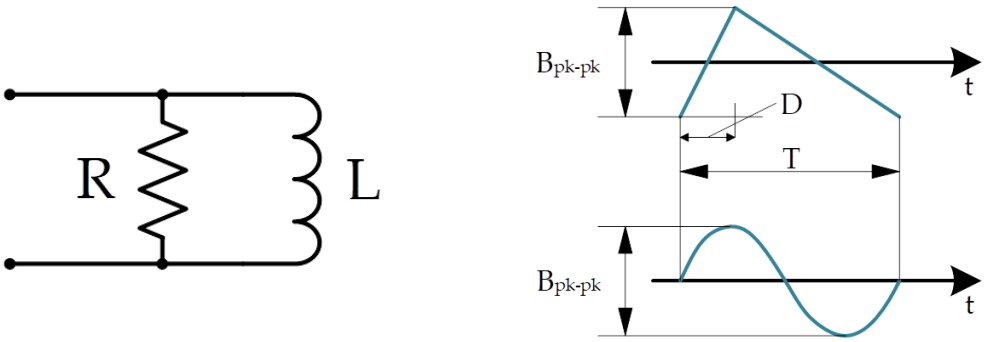

(**a**) (**b**)

Figure 34: RESE; (**a**) Equivalent Core Loss Model; (**b**) Different Induction Waveforms with the Same Peak-to-Peak Values.

The following equation expresses the method itself:

$$P_{RESE} = \frac{8}{\pi^2[4D(1-D)]^{\gamma+1}} k f^{\alpha} B_m^{\beta} \tag{191}$$

where: D is the duty-cycle ratio, k, α, β are the Steinmetz coefficients, γ is the material fitting coefficient.

The primary challenge appears to be verification of the method, particularly due to the precise measurement of power loss versus duty-cycle ratio [115, 209-213]. Typically, this is accomplished through voltage-current measurement using an oscilloscope, known as the two-windings method. This measurement approach, in its standard setup, measures the inductor magnetizing voltage across the inductor's secondary windings and the magnetizing current across the current-sensing resistor

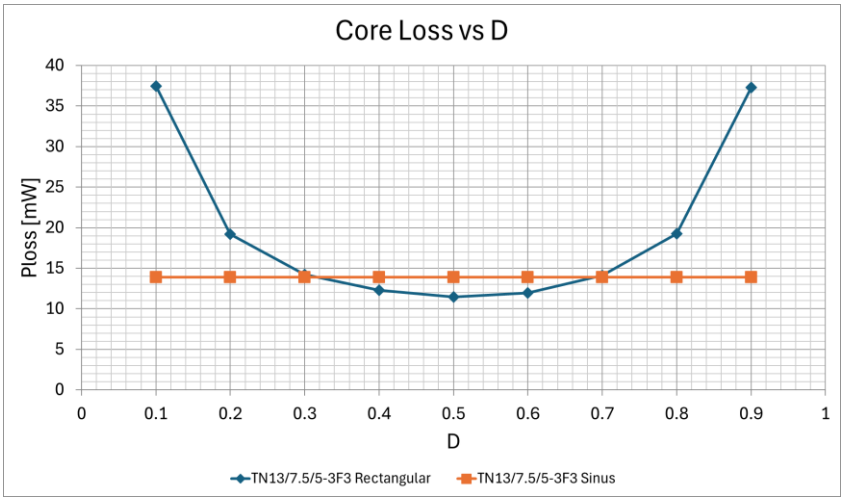

Figure 35: RESE Core Loss for TN13-7.5-5-3F3 @ 200kHz, Bm=25mT, 100°C and Various Duty-Cycles D, Orange – Sinusoidal Excitation, Blue – Rectangular Excitation.

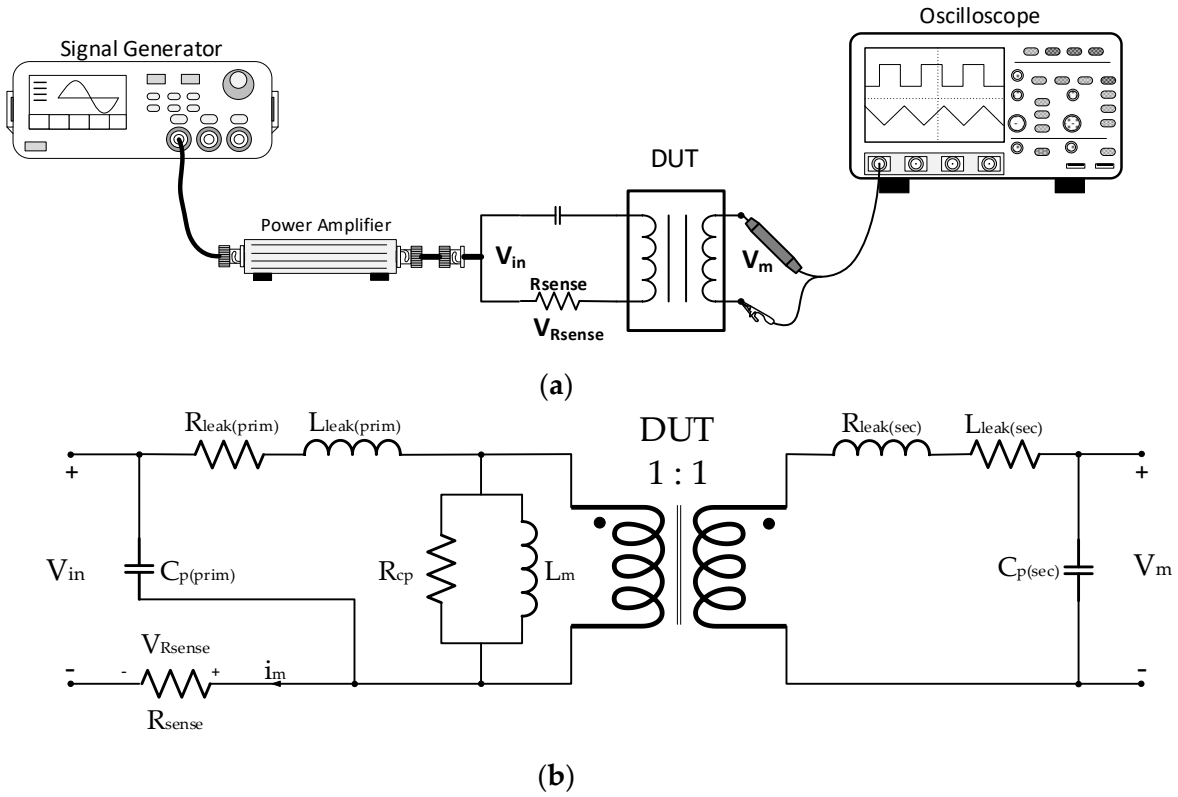

Figure 36: Standard Two-Winding Measurement Method; (**a**) Conceptual Diagram; (**b**) Equivalent Circuit Schematic.

placed on the primary side. This arrangement allows for avoiding the influence of the inductor's winding resistance and parasitics related to the leakage inductance. The core loss is then expressed by:

$$P_c = \frac{1}{R_{sense}} \cdot \frac{1}{T} \int_0^T v_m(t) v_{Rsense}(t) dt \tag{192}$$

The equivalent circuit schematic and equivalent setup are given in Figure 36.

The method can exclude the winding loss and applies to arbitrary excitation waveforms; however, it suffers from the sensitivity to phase discrepancy $\Delta\phi_{sense}$, which is the phase angle difference between the measured voltage v_{Rsense} across the sensing resistor and the magnetizing current i_m flowing through it. This phase discrepancy leads to a core loss measurement error, especially profound at megahertz frequencies [115, 209-211]. The error usually originates from the current sensing resistor's parasitics, voltage probes' frequency and amplitude discrepancies, and the oscilloscope's resolution and sampling rate. Based on the study given in [214], the measurement error applicable to sinusoidal excitations can be expressed as:

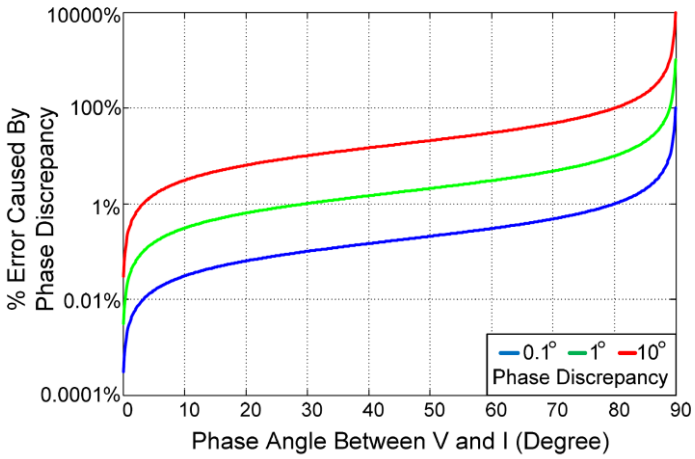

Figure 37: Core Power Loss Measurement Error Versus ϕ_m @ 0.1°, 1° and 10° of Phase Discrepancy $\Delta\phi_{sense}$ [209].

$$\Delta = \tan(\phi_m) \cdot \Delta\phi_{sense} \tag{193}$$

where: ϕ_m is the phase angle difference between the magnetizing voltage v_m and the magnetizing current i_m. Typically, the magnetizing reactance of the tested transformer is significantly higher than the value of the current sense resistor. Therefore, the phase angle between the magnetizing voltage and the magnetizing current is close to 90°. This leads to the situation where the $\tan(\phi_m)$ in equation (193) goes to infinity limit, significantly amplifying variations of phase discrepancy $\Delta\phi_{sense}$, which causes an increase in the measurement error.

A similar relationship also applies to the rectangular excitation signals.

The severity of the measurement error is illustrated in Figure 37 [209], where a 1° phase discrepancy can result in a 100% measurement error near a 90° phase angle.

The mitigation of the core loss measurement error in an almost pure inductive environment was demonstrated in [115, 209, 215-216] by introducing the capacitive and inductive cancellation methods. As the capacitive cancellation is dedicated to the sinusoidal excitations only, and since this work is dedicated to the square excitation signals, the capacitive cancellation will be excluded from the discussion.

The inductive cancellation method applies to any arbitrary waveforms, and the general idea behind it is to introduce a second inductor into the two-winding measurement circuit, as shown in Figure 38.

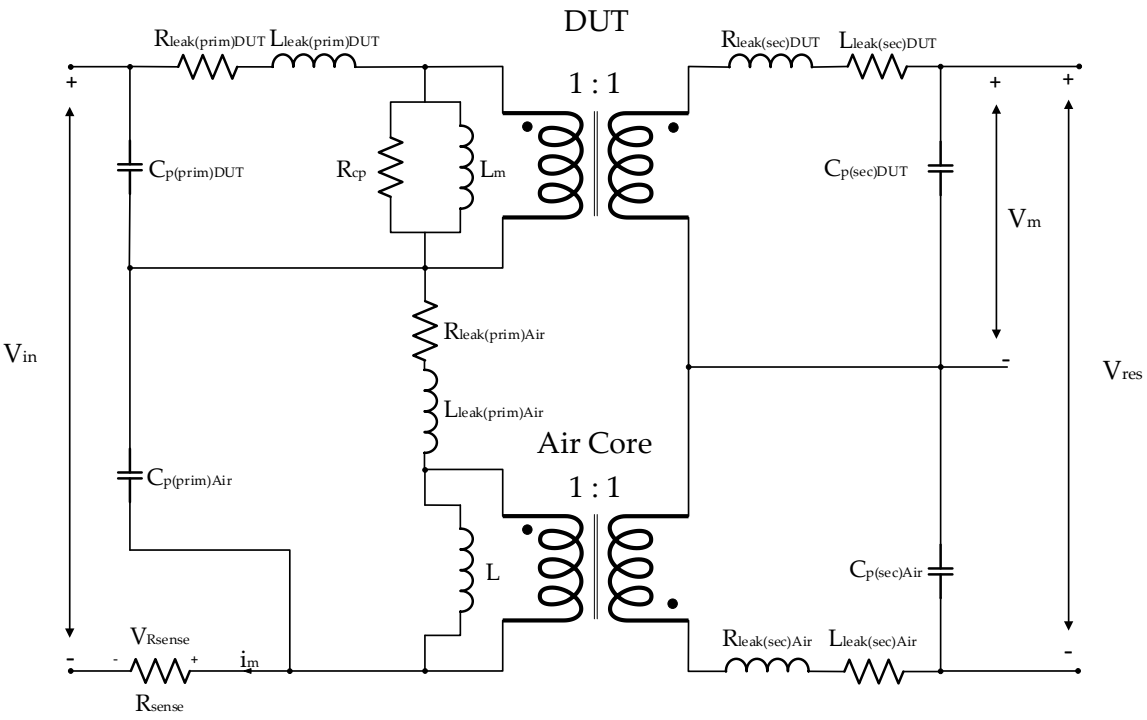

Figure 38: Circuit Diagram of Mu's Inductive Cancellation Method.

The added inductor is placed in such a way that it acts with the inductor under test and the remaining components of the test-bench circuitry, canceling the reactive voltage [209-211, 215-216]. This brings the 90° phase angle between the magnetizing voltage v_m and the magnetizing current i_m near 0°, revealing a purely resistive core loss.

In this case, the equation (192) can be rewritten as:

$$P_c = \frac{1}{R_{sense}} \cdot \frac{1}{T} \int_0^T v_{res}(t) v_{Rsense}(t)\, dt \tag{194}$$

where: v_{res} is the cancellation voltage across the inductive resonant tank.

The measurement error becomes:

$$\Delta = \tan(\phi_{res}) \cdot \Delta\phi_{sense} \tag{195}$$

where: ϕ_{res} is the phase angle between v_{res} and i_m.

In principle, this reactive power cancellation [115, 209-211, 215-216] scheme can be considered as comparing a reference air transformer core loss with the core loss under test. If the reactive power is cancelled during resonance, the power loss difference between the two is the core loss of the inductor under test.

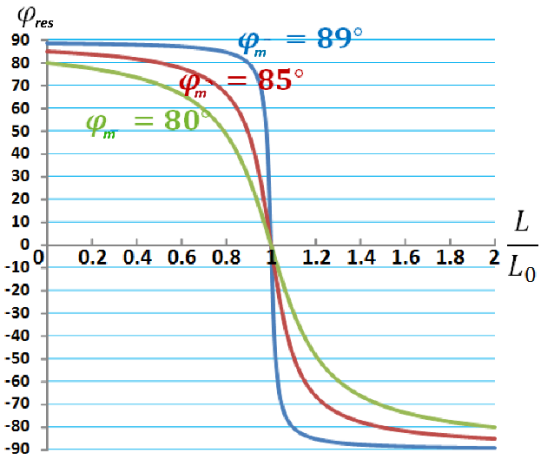

Figure 39: Relation Between ϕ_{res} and Cancellation Inductance L with Three Different Values of ϕ_m [210].

Despite the method's accuracy and simplicity, it suffers from sensitivity to the cancellation inductance value. If the cancellation inductance does not perfectly match the inductance of the tested core, a significant jump in ϕ_{res} occurs, leading to meaningful measurement errors, as shown in Figure 39 [210-211].

This makes the method impractical both industrially and technically, as inductance trimming might be very challenging and time-consuming. The relationships between the critical inductance L_0, the magnetizing inductance L_m and the reference inductance L to achieve perfect cancellations for sinusoidal excitation is given by [210-211]:

$$L_0 = L_m \cdot \frac{R_{cp}^2}{R_{cp}^2 + (\omega L)^2} \tag{196}$$

$$\phi_{\text{res}} = \arctan\left[\left(1 - \frac{\text{L}}{\text{L}_0}\right) \cdot \tan(\phi_m)\right] \tag{197}$$

Furthermore, Mu's method suffers from one more disadvantage. Because the tested cores usually have high magnetic permeability, it is difficult to build a matching air or low core loss transformer. It requires a large number of turns, which introduces significant and undesired winding capacitance and other parasitic elements in the measurement. Therefore, the method is suitable only for low-inductance inductors.

The improvement to the Mu's cancellation method, known as the partial cancellation method, was introduced by Hou et al. in [210-211].

The Hou's method eases the constraints on matching the magnetizing inductance of the core under test with the critical inductance of the reference air transformer by

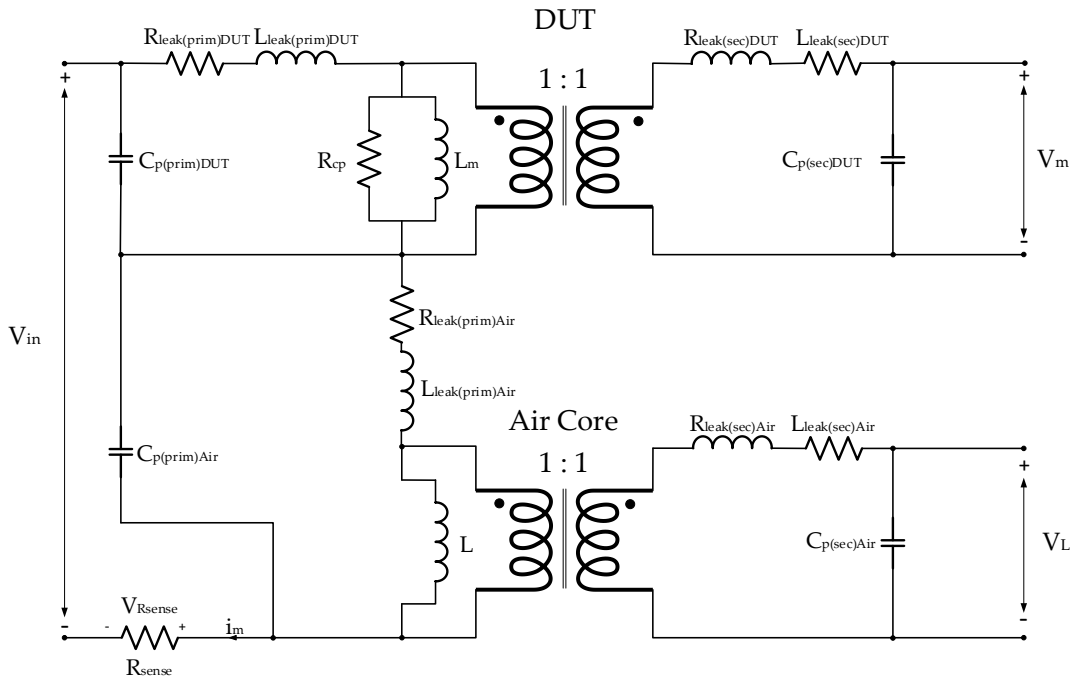

Figure 40: Circuit Diagram of Hou's Inductive Partial Cancellation Method.

introducing the cancellation factor k. The cancellation factor compensates for the mismatch between L_m and L as in Figure 38, therefore, an exact matching between L_m and L is not necessary. The conceptual circuit diagram for this method is given in Figure 40.

In this method, it is assumed that there are three sources of discrepancies during the core loss measurement: (i) $\Delta\phi_{im}$ the phase discrepancy between the measured voltage across the sensing resistor v_{Rsense} and the real magnetizing current flowing through it i_m, (ii) $\Delta\phi_m$ the phase discrepancy between the measured v_m' and real v_m, and (iii) $\Delta\phi_L$ the phase discrepancy between the measured v_L' and real v_L.

Considering the sinusoidal excitation, the cancellation of the $\Delta\phi_{im}$ (if $\Delta\phi_m = \Delta\phi_L = 0$) can be done by the introduction of the cancellation factor k, which is:

$$k = \frac{V_L}{V_m \cdot sin\phi_m} \tag{198}$$

where: ϕ_m is the phase difference between the magnetizing current i_m and the magnetizing voltage v_m.

Then the core loss can be calculated as follows:

$$P_c = \frac{1}{R_{sense}} \cdot \frac{1}{T} \int_0^T v_m v_{Rsense} dt - \frac{1}{k} \cdot \frac{1}{R_{sense}} \cdot \frac{1}{T} \int_0^T v_L v_{Rsense} dt \tag{199}$$

Because the $V_m \cdot sin\phi_m$ cannot be directly calculated, the phase disturbance needs to be introduced to the voltage across the sensing resistor, giving:

$$k = \frac{\int_0^T v_L v'_{Rsense} dt - \int_0^T v_L v_{Rsense} dt}{\int_0^T v_m v'_{Rsense} dt - \int_0^T v_m v_{Rsense} dt} \tag{200}$$

The perturbation cannot be too big or too small; the suggested optimum is $\Delta\phi'_{im} = 1°$.

The remaining phase discrepancies $\Delta\phi_m$ and $\Delta\phi_L$ can be calculated assuming that the $\Delta\phi_{im}$ compensate during the calculation process [210-211]. In this case, it can be written:

$$\frac{1}{R_{sense}} \cdot \frac{1}{T} \int_0^T v'_m v_{Rsense} dt - \frac{1}{k} \cdot \frac{1}{R_{sense}} \cdot \frac{1}{T} \int_0^T v'_L v_{Rsense} dt = P_c + V_m \cdot sin\phi_m \cdot I_m \cdot (\Delta\phi_m - \Delta\phi_L) \tag{201}$$

where: v'_m and v'_L are the measured voltages.

There exists a measurement error due to the remaining phase discrepancy $\Delta\phi_m - \Delta\phi_L$. It is caused by the phase mismatch between the two voltage probes measuring v_m and v_L. This can be eliminated by measuring the same voltage with both of the probes and then calculating an integral $\frac{1}{R_{sense}} \cdot \frac{1}{T} \int_0^T v'_m v_{Rsense} dt$ for each of them. The results should be adjusted by a deskew function in the oscilloscope until the calculated integrals show the same value.

Considering the rectangular excitation waveforms, the cancellation factor is given by [115, 209-211]:

$$k = \frac{V_{L(pk-pk)}}{V_{m(pk-pk)}} \tag{202}$$

where: $V_{L(pk-pk)}$ and $V_{m(pk-pk)}$ are the peak-to-peak values of V_L and V_m, respectively.

The work of Mu [115, 209, 215-216] and Hou [210-211] was further extended by Sanusi et al. in [212] by adding to the original methodology a study on DC bias magnetization in linear region and also by Rasekh et al. in [213] by introducing an offline compensation of phase discrepancy using offline impedance sweep and the FFT analysis.

The area for improvement in Hou's models is to extend core loss calculations into the near-saturation non-linear region and also add the losses existing in the small-signal domain by combining the complex permeability small-signal model with the large-signal Steinmetz-based model. This results in one unified and comprehensive core loss model in all signal domains [208].

3.2.2 Review of Small and Large Signal Core Resistance Calculation Methodologies.

There are two concurrent core resistance calculation methodologies: (i) the small-signal core resistance calculation method, which is based on the complex permeability values, and (ii) the large signal core resistance calculation method based on the Steinmetz equation, which depends on the magnitude of the excitation signal.

3.2.2.1 Small-Signal Core Resistance.

The small-signal series core resistance of an inductor is given by [4, 178]:

$$R_c = Re\left(j\omega \cdot \frac{N^2}{\frac{l_C}{A_c \mu_r^* \mu_0} + R_g} \right) \tag{203}$$

where: A_c is the effective cross-section of a magnetic core, N is the number of winding turns, l_c is the effective magnetic length of the core, μ_0 is the magnetic permeability of the free air, ω is the angular frequency, R_g is the air gap reluctance, $\mu_r^* = \mu_r' - j\mu_r"$ is the complex magnetic permeability.

Regarding the gapless inductor, equation (203) becomes:

$$R_c = \frac{\mu_r'' \mu_0 N^2 A_c \omega}{l_c} \tag{204}$$

where: μ_r'' is the imaginary part of the complex permeability.

According to the IEC 62044-2 [192], the small signal imaginary part of the complex permeability of an inductor under test is given by equation (164), where the impedance measurement is done at a testing signal not exceeding $B_m = 0.25\ [mT]$.

However, as shown in Figure 30, an inductor is a complex system [4, 178, 187, 208]; therefore, the real part of the impedance measurement is, in fact, a combination of many variables coming from the inductor's parasitics.

The relation expressing this variables' mix is given by equation (161).

Thus, the best way to extract the core resistance from this complex equation is to use an iterative approximation curve fitting as shown in [187], which takes into account all the variables seen in Figure 30.

Another approach to calculating the core resistance is to measure the core parallel resistance R_{cp} of an inductor at a self-resonant frequency and then transfer it to the series

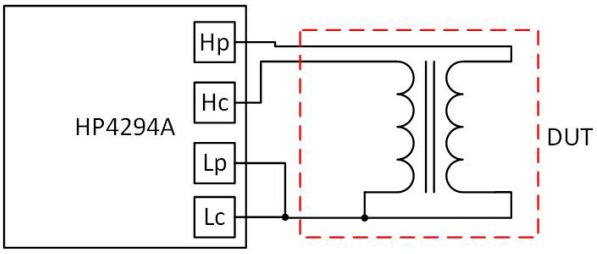

Figure 41: Two-Winding Small-Signal Core Resistance Measurement using HP4294A Impedance Analyzer [178].

one as follows [4, 178]:

$$R_c = \frac{(\omega L)^2 \cdot R_{cp}}{(\omega L)^2 + R_{cp}} \tag{205}$$

The inductor core parallel resistance R_{cp} is constant and well-defined at inductor self-resonance; however, the inductance L seen by the impedance analyzer changes along the frequency range, depends on the magnitude of the testing signal and is also a complex function of the inductor reactance and its parasitic variables [4, 187], which is given by equation (162).

Therefore, the approach using equation (205) must also be carefully examined, as many factors influence the result, and an iterative approximation may also be involved in the calculations.

The fastest and probably one of the most accurate methods for calculating core resistance is to use an advanced impedance analyzer, such as the Agilent/HP 4294A. The measurement in this case is performed using a standard two-winding, four-terminal method, as shown in Figure 36 and Figure 41 [178], respectively.

This type of impedance analyzer precisely measures impedance, even when testing high-Q materials, where the phase difference between the magnetizing current and the magnetizing voltage is very close to 90°, as discussed at the beginning of paragraph 3.2.

3.2.2.2 Large-Signal Core Resistance.

In general form, the ohmic power loss can be expressed as:

$$P = I_{rms}^2 R \tag{206}$$

where: I_{rms} is the RMS value of the current, and R is the resistance.

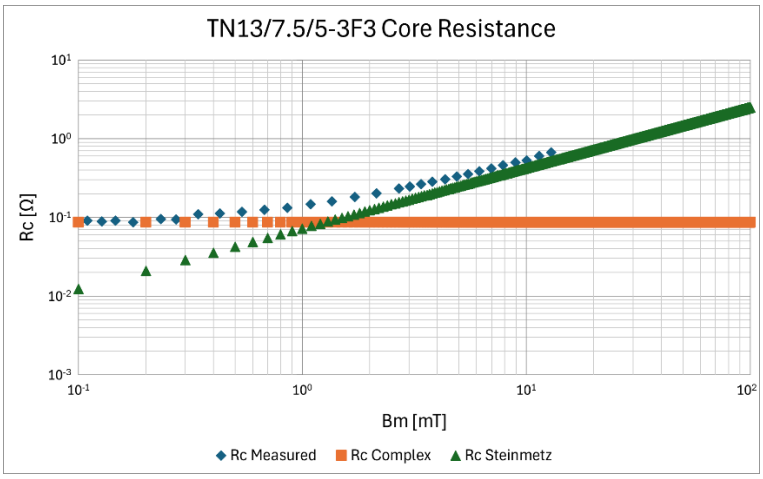

Figure 42: Characteristics of the Core Resistance R_c vs. Magnetic Flux Density B_m @ 200 kHz for TN13/7.5/5-3F3 with a 3 Turns Bifilar Winding, Green - Based on the Steinmetz Model, Orange – Based on the Complex Permeability Model, Blue – Measured Characteristics.

Regarding the core loss, equation (206) can be reformulated into:

$$P_c = \frac{\hat{I}_m^2 R_c}{2} \tag{207}$$

where: $\hat{I}_m$ is the amplitude of the core magnetizing current and R_c is the core resistance.

On the other hand, the core power loss can be expressed using equation (190), yielding:

$$P_c = V_e k f^{\alpha} B_m^{\beta} \tag{208}$$

where: V_e is the effective volume of the core.

Thus, the core resistance is given by:

$$R_c = 2V_e k f^{\alpha} B_m^{\beta} \hat{I}_m^{-2} \tag{209}$$

and adding temperature adjustment, it becomes:

$$R_c = 2V_e k f^{\alpha} B_m^{\beta} \hat{I}_m^{-2} (\xi_1 T^2 - \xi_2 T + \xi_3) \tag{210}$$

where: T is the temperature, ξ_1, ξ_2, ξ_3 are the temperature fitting coefficients.

As shown in Figure 42, the small- and large-signal core loss models exhibit completely different characteristics, which are neither complementary nor intersecting.

Therefore, an educated choice is to find a characteristic that reflects a real behavior of the core loss regardless of the magnitude of the excitation signal, as will be shown in the following paragraph of this work.

3.2.3 Proposed Core Loss Calculation Methodology.

The proposed core loss calculation methodology is not intended to alter or dispute the core loss measurement approach proposed by Mu et al. [115, 209,215-216] and Hou et al. [210-211]. This is because their methodologies have already been proven to be feasible and accurate [212-213]. In this work, Hou's measurement method is used to calculate the core loss. However, the new method, referred to here as the improved RESE (iRESE), is rather an extension of the RESE model, pushing it into small and near-saturation large-signal domains for both sinusoidal and non-sinusoidal excitation signals, including a DC bias magnetization [208].

The knowledge about the core loss and the complex permeability in the small-signal domain can be used, e.g., in the design of the low-noise magnetic shielding [189], while the near-saturation operation is often used in SMPS as a trade-off between magnetic component efficiency, cost, and size [217], or it can also be used for an application-specific solution, such as inrush current limiters [218].

The proposed methodology is assumed to be modular, meaning that its modules or steps can be used independently whenever the application involves sinusoidal or rectangular excitation signals.

The iRESE modular flowchart is given in Figure 43. It is divided into five significant steps, which will be presented subsequently [208].

STEP I:

The DC bias of the applied excitation signal levels off at the operating point, where the induction signal swings between its maximum and minimum values. If one of these extremes lies beyond the linear region of the B-H characteristics, then the magnetic permeability roll-off occurs. The same situation happens if the magnitude of the excitation signal without a DC bias is high enough to exceed the B-H linear region.

This phenomenon affects the swing magnitude of the magnetic flux density at given field intensity values, pre-magnetizes the core, and thus increases the core loss.

The reversible permeability for sinusoidal excitations can be calculated using a method introduced by Esguerra et al. in [219-224]. The method is based on the Coleman-Hodgdon hysteresis model [70, 73, 95, 96], which is given by:

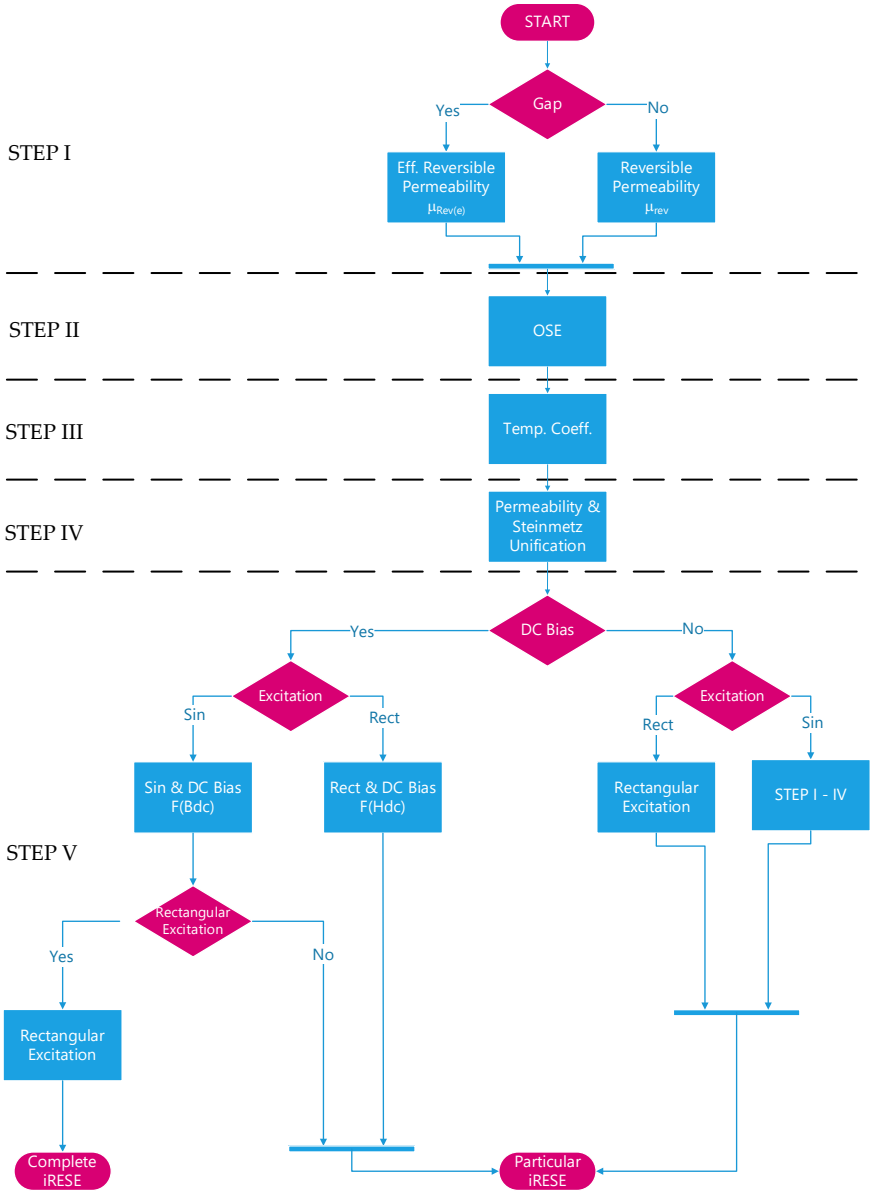

Figure 43: iRESE Modular Flowchart of the Proposed Core Loss Calculation Method, Decision Blocks in Red, Action Blocks in Blue.

$$\frac{dH}{dB} = \pm\alpha\left(\frac{dB}{dt}\right)(f(B) - H) + g(B) \tag{211}$$

where: $f(B)$ and $g(B)$ are the material functions, $f(B)$ is the anhysteretic curve describing the hysteresis, $g(B)$ is the reversible function describing the drift from the anhysteretic curve, and α is the fitting parameter.

The method assumes that there is no need to define arbitrary $f(B)$ and $g(B)$ functions, but instead, an accurately measured major hysteresis loop can be used as a solution to equation (211) and the minor hysteresis loops.

The empirical fit functions, which describe the lower and upper branches of the major hysteresis loop, are given by:

$$H_L(B) = \frac{B}{\mu_0 \mu_c} \cdot \frac{1}{1 - \left(\frac{B}{B_{sat}}\right)^a} + H_c \tag{212}$$

$$H_U(B) = \frac{B}{\mu_0 \mu_c} \cdot \frac{1}{1 - \left(\frac{B}{B_{sat}}\right)^b} - H_c \tag{213}$$

where: H_L is the lower branch of the B-H curve, H_U is the upper branch of the B-H curve, B_{sat} is the assumed saturation of the magnetic flux density, H_c is the coercive magnetic field intensity, a, b are the fitting coefficients and $a \approx b$, μ_c is the magnetic permeability near the coercive magnetic field intensity, μ_0 is the magnetic permeability of the free space.

Then the anhysteretic curve can be described as:

$$H(B) = H_L(B) - H_c \left(1 - \frac{B}{B_{sat}}\right)^\tau \tag{214}$$

$$\tau = \alpha_0 B_{sat} \tag{215}$$

$$\alpha_0 = \frac{1}{\mu_0 H_c}\left(\frac{1}{\mu_i} - \frac{1}{\mu_c}\right) \tag{216}$$

where: μ_i is the initial magnetic permeability.

The reversible permeability for an ungapped core can be calculated as follows:

$$\mu_{rev} = \frac{1}{\mu_0} \cdot \frac{dB}{dH} = \frac{1}{\mu_0} \cdot \left(\frac{dH}{dB}\right)^{-1} \tag{217}$$

Using equations (212-216) and substituting them into equation (217) gives:

$$\mu_{rev} = \left(\frac{1 + (a-1)\left(\frac{B}{B_{sat}}\right)^a}{\left[1 - \left(\frac{B}{B_{sat}}\right)^a\right]^2} \frac{1}{\mu_c} + \frac{1}{\left(1 - \frac{B}{B_{sat}}\right)\left(1 - \frac{B}{B_{sat}}\right)^{-\alpha_0 B_{sat}}} \left(\frac{1}{\mu_i} - \frac{1}{\mu_c}\right) \right)^{-1} \tag{218}$$

and with some empirical modifications, the equation (218) becomes:

$$\mu_{rev} = \left(\frac{1 + (a-1)\left(\frac{B}{B_{sat}}\right)^a}{\left[1 - \left(\frac{B}{B_{sat}}\right)^a\right]^2} \frac{1}{\mu_c} + \frac{1}{\left(1 - \frac{B}{B_{sat}}\right)\left[2 - \left(1 - \frac{B}{B_{sat}}\right)^{-\alpha_0 B_{sat}}\right]} \left(\frac{1}{\mu_i} - \frac{1}{\mu_c}\right) \right)^{-1} \tag{219}$$

The magnetic flux density values at a given magnetic field intensity regarding a DC bias give an anhysteretic magnetization curve described by:

$$H_{dc} = \frac{1}{\mu_0 \mu_c} \cdot \frac{B_{dc}}{1 - \left(\frac{B_{dc}}{B_{sat}}\right)^a} \tag{220}$$

Considering the gapped inductor, the effective reversible permeability can be expressed as follows:

$$\mu_{rev(e)} = \frac{\mu_{rev}}{1 + \frac{\mu_{rev} \cdot l_g}{l_c}} = \frac{1}{\frac{1}{\mu_{rev}} + \frac{l_g}{l_c}} \tag{221}$$

where: l_g is the length of the air gap.

The effective magnetic field intensity at any $\mu_{rev(e)}$ is given by:

$$H_{dc(e)} = H_{dc} + \frac{1}{\mu_{rev(e)} \mu_0} \cdot B_{dc(e)} \tag{222}$$

The above considerations regard the sinusoidal excitations. Unfortunately, the reversible permeability and the B-H characteristics are not well-defined by any models [70] for rectangular excitation signals when saturation occurs. Therefore, in this case, the permeability roll-off must be calculated iteratively, step by step, at any given operating point. It also refers to the DC bias operating point. Empirically, the proposed method follows the lower B-H branch if the DC bias is positive.

As it was described in paragraph 3.2 (Equation (199)), Hou's method [210-211] cancels the reactive power by comparing a reference air transformer core loss with the core loss under test. However, this is only valid in the linear region of the B-H characteristics. If saturation happens, e.g., in the case of a DC bias the relationships $\frac{1}{R_{sense}} \cdot \frac{1}{T}\int_0^T v_m v_{Rsense} dt$ and $\frac{1}{k} \cdot \frac{1}{R_{sense}} \cdot \frac{1}{T}\int_0^T v_L v_{Rsense} dt$ do not change proportionally, introducing an error in the reactive power cancellation. This is because the voltage v_L depends on linear coreless inductance and its permeability, while the voltage v_m drops non-linearly as the magnetic permeability rolls off. Therefore, an additional proportionality factor, which compensates for this phenomenon, must be introduced into equation (199), yielding:

$$P_c = \frac{1}{R_{sense}} \cdot \frac{1}{T}\int_0^T v_m v_{Rsense} dt - \frac{1}{\sigma} \cdot \frac{1}{\eta} \cdot \frac{1}{k} \cdot \frac{1}{R_{sense}} \cdot \frac{1}{T}\int_0^T v_L v_{Rsense} dt \tag{223}$$

where: $\sigma = \frac{\mu_{rev}}{\mu_r}$ is the proportionality factor taking into account small-signal magnetic permeability roll-off near saturation due to DC bias, μ_{rev} is the small-signal reversible permeability value, μ_r is the initial small-signal permeability value measured in the

linear region, $\eta = \frac{\mu_{rev(a)}}{\mu_{r(a)}}$ is the proportionality factor taking into account large-signal magnetic permeability roll-off near saturation, $\mu_{rev(a)}$ is the large-signal reversible permeability value, $\mu_{r(a)}$ is the initial large-signal permeability value measured in the linear region near H_c.

STEP II – IV:

As stated in [188], the core manufacturers' data, as found in the cores' datasheets, is subject to significant uncertainties. Therefore, the first step in the proposed methodology is to verify the original Steinmetz equation coefficients using the measuring method given by Hou et al. [210-211] under sinusoidal excitations.

This should give the following relationship:

$$P_c = V_e k f^{\alpha} B_m^{\beta} (\xi_1 T^2 - \xi_2 T + \xi_3) \tag{224}$$

However, as it will be shown in the test-bench verification (Chapter 4) this relationship would be better fitted with the fifth-degree polynomial regarding core loss temperature dependency, yielding:

$$P_c = V_e k f^{\alpha} B_m^{\beta} \cdot \left(\sum_{n=0}^{5} \xi_n T^n \right) \tag{225}$$

As shown in Figure 42, the transition point between small and large excitation signals causes the Steinmetz characteristics to bend horizontally. Because of the complexity, this non-linear behavior can be fitted by adding to the equation (225) a ninth-degree polynomial, giving:

$$P_c = V_e k f^{\alpha} \left(B_m^{\beta} + \sum_{i=0}^{9} \chi_i B_m^i \right) \cdot \left(\sum_{n=0}^{5} \xi_n T^n \right) \tag{226}$$

where: χ_i are the fitting coefficients of a ninth-degree polynomial regarding magnetic flux density, ξ_n are the fitting coefficients of the fifth-degree polynomial regarding temperature dependency.

STEP V:

According to Figure 43 there are a few scenarios regarding this step, namely:

1. If there is a sinusoidal excitation and a DC bias, then equation (226) becomes:

$$P_c = V_e k f^{\alpha} \left(B_m^{\beta} + \sum_{i=0}^{9} \chi_i B_m^i \right) \cdot \left(\sum_{n=0}^{5} \xi_n T^n \right) \cdot F(B_{dc}) \tag{227}$$

where: $F(B_{dc}) = \sum_{j=0}^{4} \zeta_j B_{dc}^j$ is the sinusoidal excitation and a DC bias magnetization function obtained with the help of equations (211-222), ζ_j are the fitting coefficients. This equation is purely dedicated to sinusoidal excitations with a DC bias.

2. If the rectangular excitation takes place, the corresponding relationship can be added to equation (227), giving:

$$P_c = V_e \frac{8}{\pi^2 \left(4D(1-D)\right)^{\gamma}} \cdot k_1 f^{\alpha} \left(B_m^{\beta} + \sum_{i=0}^{9} \chi_i B_m^i \right) \cdot \left(\sum_{n=0}^{5} \xi_n T^n \right) \cdot F(B_{dc}) \tag{228}$$

where: $k_1 = \delta k, \delta, \gamma$ are the function fitting coefficients @ $B_{dc} = 0$.

The equation (228) can be used to calculate the core loss at rectangular excitation signals if the DC bias and the characteristics from STEP V.1 are known. This equation represents the complete iRESE model.

3. If there is a rectangular excitation without a DC bias, the equation (226) changes as follows:

$$P_c = V_e \frac{8}{\pi^2 \left(4D(1-D)\right)^{\gamma_1}} \cdot k_2 f^{\alpha} \left(B_m^{\beta} + \sum_{i=0}^{9} \chi_i B_m^i \right) \cdot \left(\sum_{n=0}^{5} \xi_n T^n \right) \tag{229}$$

where: $k_2 = \delta_1 k, \delta_1, \gamma_1$ are the function fitting coefficients.

4. If rectangular excitation comes together with a DC bias, the DC bias is added to the rectangular core loss with the assumption that the duty ratio of the signals equals $D = 0.5$. Because a complex relationship exists between B and H near the core saturation region the DC magnetization function to be added is rather a function of H_{dc} than B_{dc} as in equations (227-228), yielding:

$$P_c = V_e \frac{8}{\pi^2 \left(4D(1-D)\right)^{\gamma_1}} \cdot k_2 f^{\alpha} \left(B_m^{\beta} + \sum_{i=0}^{9} \chi_i B_m^i \right) \cdot \left(\sum_{n=0}^{5} \xi_n T^n \right) \cdot F(H_{dc}) \tag{230}$$

where: $F(H_{dc}) = \sum_{j=0}^{4} \epsilon_j H_{dc}^j$ is the DC bias magnetization function, ϵ_j are the fitting coefficients.

As is evident, the proposed iRESE method comprehensively and in a modular manner deals with sinusoidal and rectangular excitation signals, with or without a DC bias. In the next chapter, the assumptions given above will be evaluated through test-bench measurements.

3.3 Summary.

As stated, several existing complex permeability measurement and calculation techniques do not fully reveal how complex permeability is measured and fitted, or the fitting is oversimplified [189-195], [197], or overcomplicated [196]. Moreover, these techniques are often based on mathematical approximations and incomplete equivalent inductor models, where several fitting variables are adjusted simultaneously, taking on arbitrary values [197-198]. This approach cannot lead to valid results and does not accurately represent the physical behavior of the inductor needed for SPICE-based simulation software commonly used in industry [174-175].

The proposed method addresses this issue by implementing an iterative approximation curve-fitting technique. This technique is based on the inductor series equivalent model, with only one fitting variable, assuming that the inductance and the other quantities change along the frequency range according to the measured inductor impedance. This change and the model represent the physical behavior of an inductor, and only one fitting variable ensures high fitting accuracy without the possibility of assigning arbitrary values to other quantities, which would otherwise be fitted. This allows accurate estimation of complex permeability regardless of inductor size, shape, winding structure or frequency range.

The chapter also introduces an improved rectangular extension of the Steinmetz equation (iRESE) core loss calculation method [208].

The iRESE unifies the Steinmetz-based core loss model with the small-signal complex permeability model to comprehensively complete the entire core loss characteristics regardless of the magnitude of the excitation signals.

The unification of both models seems to be imminent both: (i) because that is how the inductor actually behaves and (ii) because the single model can be used in both small and large-signal domains, which was not possible before.

Moreover, it also considers the rectangular excitation of signals and the DC bias phenomenon commonly present in the switch-mode power supplies (SMPS), along with the magnetic permeability roll-off near the core saturation level.

The model is also structured to be modular, meaning that each part can be used separately according to the intended application. This unique approach provides

engineers and scientists with all the required information at once regarding core loss, as well as the flexibility to choose the approach depending on the application they are working on.

The method also discusses the nonlinearity of the inductor magnetizing current and its impact on the core losses in the small-signal domain. Thus, with an extra effort, the method can also be applied to the SPICE modelling and simulation, which is required by the industry for fast and precise estimation of the magnetic components' core loss.

The proposed model has five degrees of freedom regarding the core loss in the ferrite materials and includes dependency on: (i) the magnitude of the magnetic flux density, (ii) frequency of the excitation, (iii) temperature variations, (iv) the shape of the excitation signal, and (v) DC bias.

The method is applicable but not limited to SMPS applications and can also be applied to any other arbitrary applications affected by DC bias and rectangular excitation waveforms, such as electric vehicle inverters and wireless power transfer systems [208].

Chapter 4

4. Test-Bench Measurements and Verification.

This chapter experimentally verifies the assumptions and claims made in Chapter 3. Most of the chapter text is taken from the author's papers [187], [208] and referenced when appropriate.

4.1 Experimental Verification of Inductor Complex Permeability Values.

The experimental verification of inductor complex permeability was done using a Bode 100 VNA from "Omicron Lab" together with a homemade impedance adapter similar to the B-WIC test fixture at 0dBm testing signal strength, as shown in Figure 44. The test prototypes were built with commercially available cores and winding wires. The inductors' physical parameters are shown in Table 3, while the test results are shown in Figure 45a-f and the inductors themselves in Figure 46a-c, respectively, where:

A_c – core cross-section area,

l_c – length of magnetic path,

N – number of turns,

Gap – length of the air gap,

t – distance between two adjacent winding turns,

SRF – inductor self-resonant frequency,

L – inductance measured at approximately 10kHz,

C_s – inductor stray capacitance at self-resonant frequency,

d – winding wire diameter.

Sample No.	Core Type	Core Material	A_c [mm²]	l_c [mm]	N [-]	Gap [mm]	t [mm]	SRF [MHz]	L [µH]	C_s [pF]	d [mm]
Sample 1	TN 10/6/4	3C90	7.8	24.1	10	N/A	2.5	9.907	103.78	2.48	0.28
Sample 2	TN 20/10/7	3C90	33.6	43.6	10	N/A	4.7	2.814	234.17	13.65	0.75
Sample 3	TN 25/15/10	3C90	48.9	60.2	10	N/A	6.3	2.954	237.23	12.49	0.75
Sample 4	TX 58/41/18	3E25	152	152	10	N/A	15.6	1.262	574.60	27.64	0.75
Sample 5	ETD 44/22/15	3C90	173	103	10	N/A	3.2	2.365	331.23	13.67	0.75
Sample 6	ETD 44/22/15	3C90	173	103	10	1.3	3.2	27.663	21.17	1.56	0.75

Table 3: Physical Parameters of Inductors used for Complex Permeability Measurements.

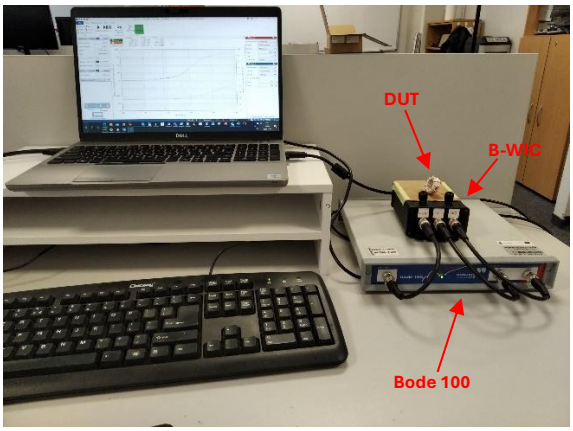

Figure 44: Complex Permeability Test-Bench Setup.

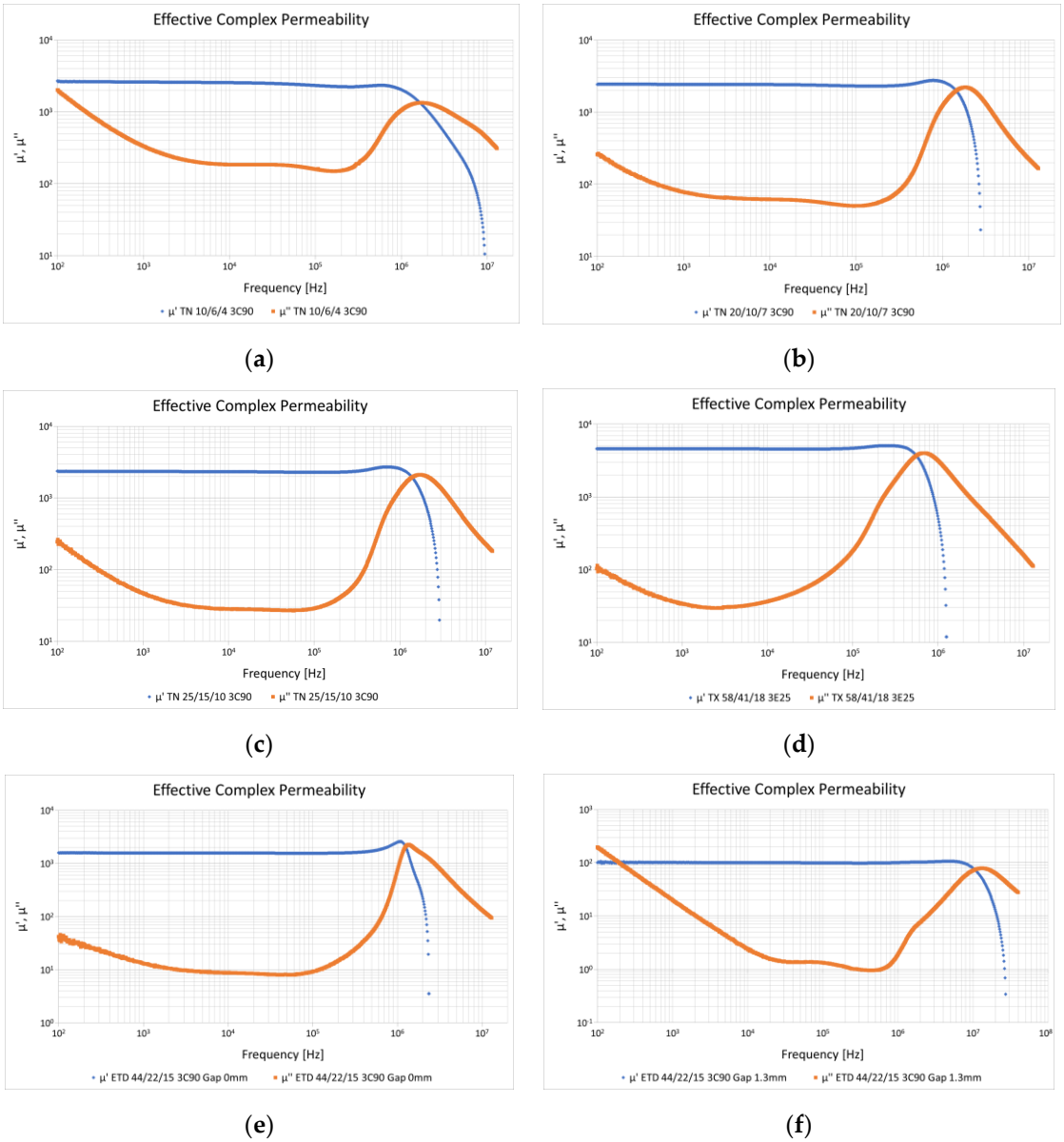

Figure 45: Effective Complex Permeability Plots, Blue – Real Part of Complex Permeability, Orange – Imaginary Part of Complex Permeability, (**a**) Sample 1; (**b**) Sample 2; (**c**) Sample 3; (**d**) Sample 4; (**e**) Sample 5; (**f**) Sample 6.

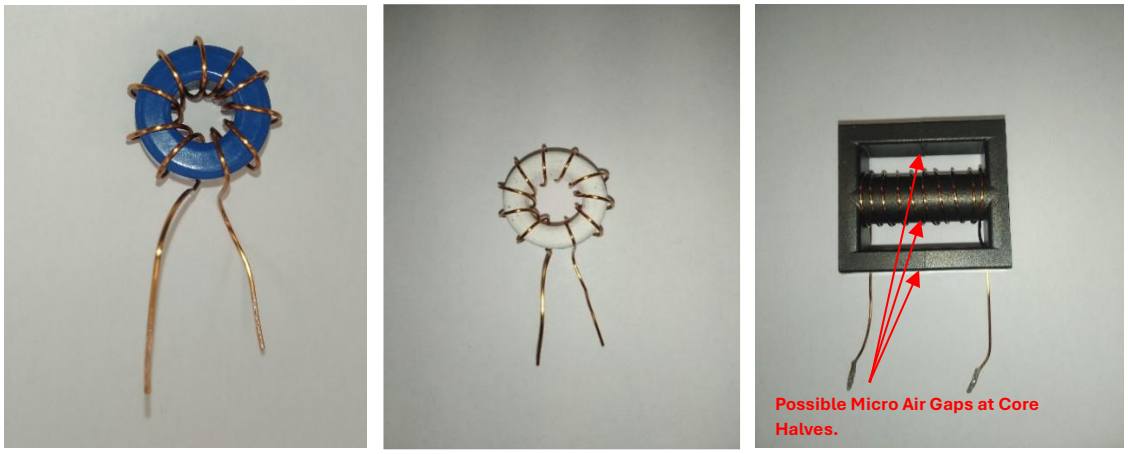

(**a**) (**b**) (**c**)

Figure 46: Structure of Sample 2, Sample 3 and Sample 5; (**a**) Sample 2 used in Verification of Complex Permeability Characteristics; (**b**) Sample 3 used in Verification of Complex Permeability Characteristics; (**c**) Sample 5 with Possible Micro Air Gaps Affecting Complex Permeability Values.

The testing signal strength as per IEC 62044-2 was chosen so as not to exceed $B_{max} = 0.25\ mT$.

As shown in Figure 45a-f, the core shape and the windings' structure impact the complex permeability values as predicted. This makes the permeability characteristics unique for each inductor, especially near the inductor's self-resonant frequency.

The imaginary part of the effective complex permeability characteristics bends upwards at low frequencies. Indeed, this phenomenon is primarily due to the resistance of the inductor windings, and to a lesser extent, to the remaining parasitic RLC elements that the physical inductor is composed of and can be removed from the measurement, e.g., by curve fitting [189], as predicted.

The possible cracks in core material or small air gaps not visible to the naked eye, which, e.g., exist at the joints of core halves, might significantly decrease the complex permeability, and thus the inductance of an inductor itself (Figure 45e, Figure 46c).

The above is even more self-evident if the gapped inductor is considered. The influence of the gap, and thus its resistance and the resistance of the fringing field, dominates, significantly decreasing the values of the real and imaginary parts of the complex permeability characteristics (Figure 45f).

The low-frequency bending phenomenon will be investigated in the following paragraph.

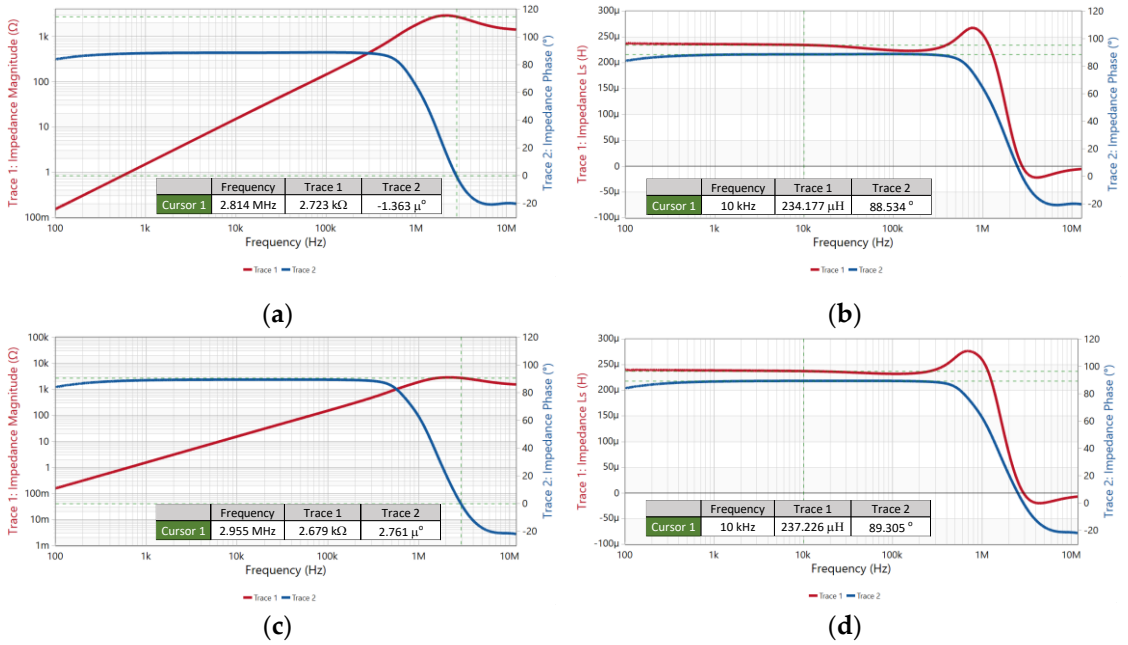

Figure 47: Sample 2 and Sample 3 Impedance Plots; (**a**) Sample 2 Impedance Plot, Red – Impedance Magnitude, Blue – Impedance Phase; (**b**) Sample 2 Inductance Plot, Red – Inductance Value, Blue – Impedance Phase; (**c**) Sample 3 Impedance Plot, Red – Impedance Magnitude, Blue – Impedance Phase; (**d**) Sample 3 Inductance Plot, Red – Inductance Value, Blue – Impedance Phase.

4.1.1 Test-Bench Verification of Complex Permeability based on Inductor Equivalent Model and Iterative Approximation Curve Fitting.

The measured complex permeability curves can be verified using an iterative approximation curve fitting technique based on a series, ungapped equivalent inductor model (Figure 30). The inductors selected for the fitting are Sample 2 and Sample 3, both with ferrite cores made of 3C90 material from Ferroxcube and wound with 10 turns of widely spaced, 0.75 mm in diameter, enameled copper wire (Figure 46a-b). The average space between adjacent winding wires was assumed to be 4.7mm for Sample 2 and 6.3 mm for Sample 3 (Table 3). During the fitting process, the samples' impedance was measured from 100 Hz to 13 MHz using a Bode 100 VNA (Figure 47a-d). The inductance measurement was performed at a frequency of approximately 10 kHz, which falls within the plateau range of the measured characteristics. It is suspected that most of the inductor stray capacitance is between wire turns and between wire turns and the core (Figure 32).

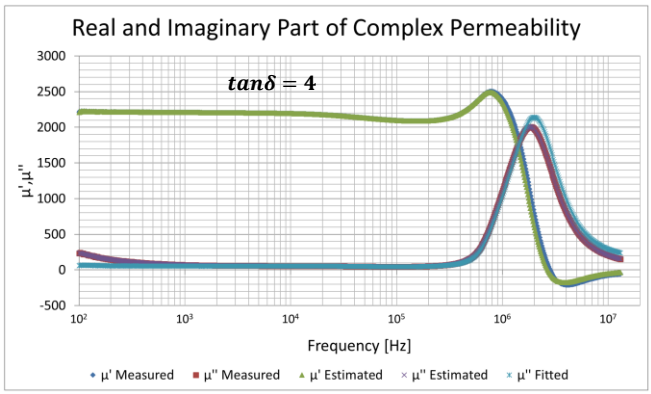

Figure 48: Sample 2 Real and Imaginary Part of Complex Permeability: Dark Blue – Real Part of Measured Characteristic, Green – Real Part of Estimated Characteristic, Dark Red – Imaginary Part of Measured Characteristic, Purple – Imaginary Part of Estimated Characteristic, Light Blue – Imaginary Part of Fitted Characteristic.

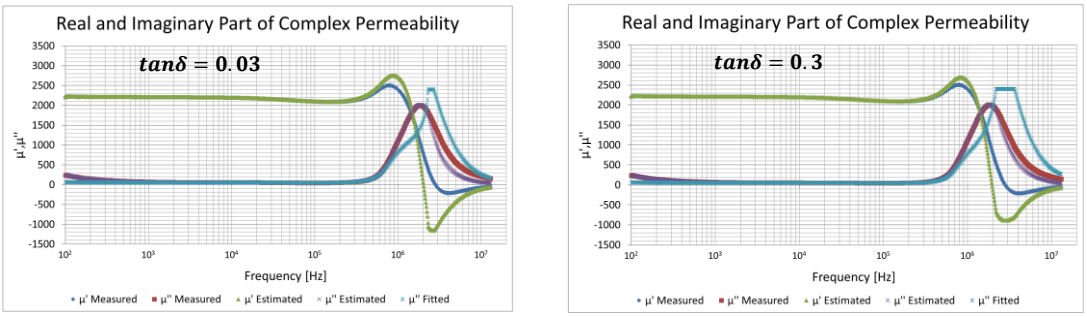

(**a**) (**b**)

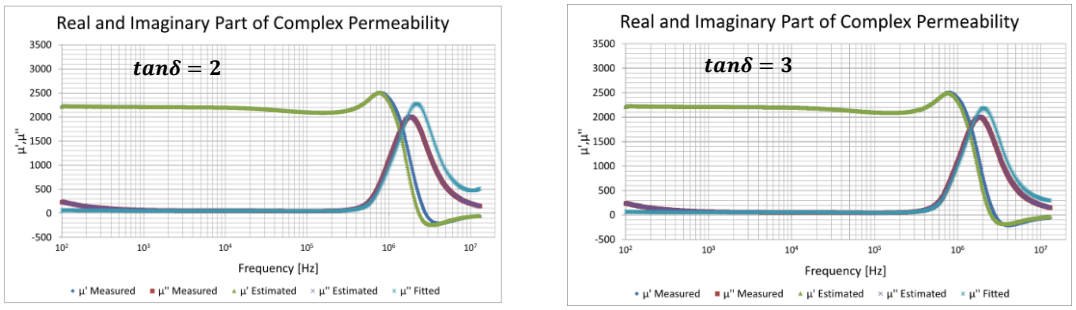

(**c**) (**d**)

Figure 49: Sample 2 Fitting Convergence Depending on Loss Tangent Value, Dark Blue – Real Part of Measured Characteristic, Green – Real Part of Estimated Characteristic, Dark Red – Imaginary Part of Measured Characteristic, Purple – Imaginary Part of Estimated Characteristic, Light Blue – Imaginary Part of Fitted Characteristic; (**a**) Loss Tangent 0.03; (**b**) Loss Tangent 0.3; (**c**) Loss Tangent 2; (**d**) Loss Tangent 3.

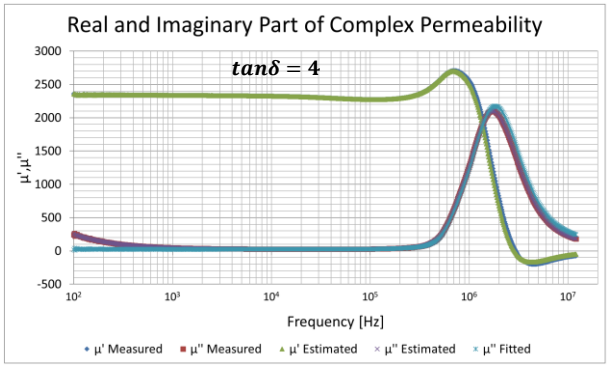

Figure 50: Sample 3 Real and Imaginary Part of Complex Permeability: Dark Blue – Real Part of Measured Characteristic, Green – Real Part of Estimated Characteristic, Dark Red – Imaginary Part of Measured Characteristic, Purple – Imaginary Part of Estimated Characteristic, Light Blue – Imaginary Part of Fitted Characteristic.

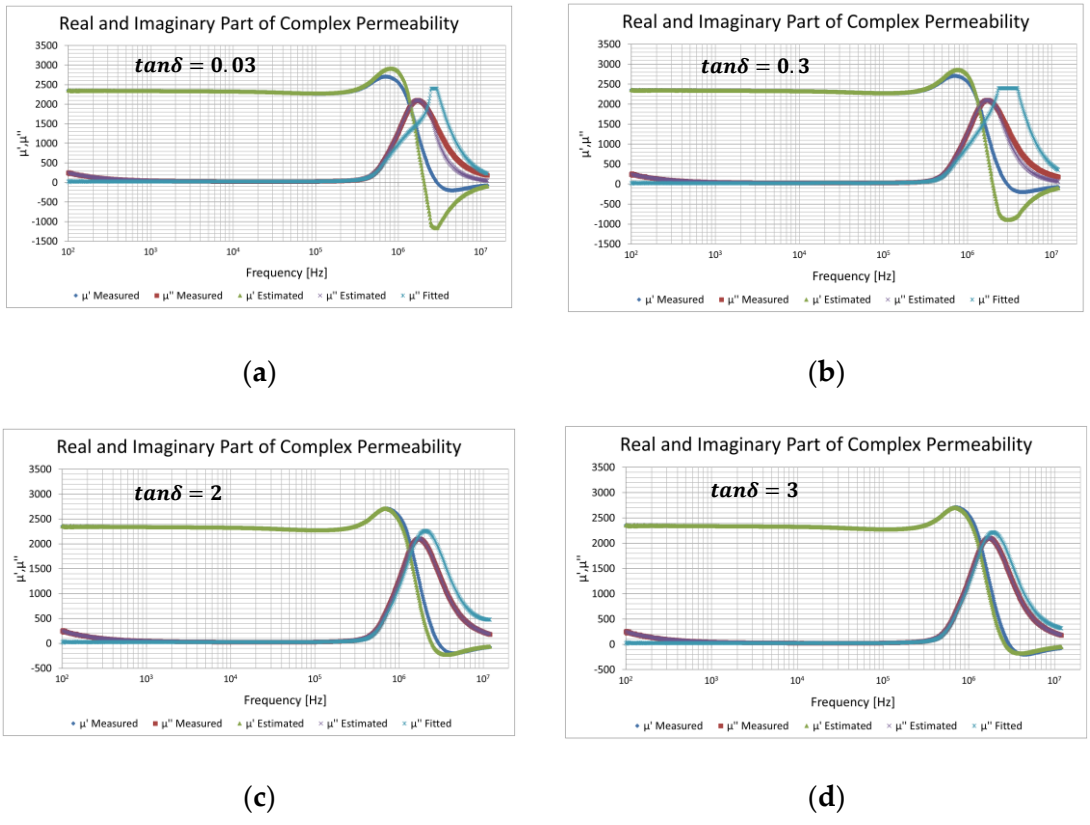

Figure 51: Sample 3 Fitting Convergence Depending on Loss Tangent Value, Dark Blue – Real Part of Measured Characteristic, Green – Real Part of Estimated Characteristic, Dark Red – Imaginary Part of Measured Characteristic, Purple – Imaginary Part of Estimated Characteristic, Light Blue – Imaginary Part of Fitted Characteristic; (**a**) Loss Tangent 0.03; (**b**) Loss Tangent 0.3; (**c**) Loss Tangent 2; (**d**) Loss Tangent 3.

Based on the complex permeability curve fitting results, it was assumed that the loss tangent is equal to 4 across the entire frequency range. This assumption does not affect low-frequency calculations but allows reasonably good curve-fitting results close to and above the inductor's self-resonance.

The $\mu''_{r\,fitted}$ value was obtained during an iterative sweep, specifically a sweep from 1 to 2400 with a step size of 1.

As can be seen in the plots (Figure 48, Figure 49a-d, Figure 50, Figure 51a-d), the fitted values of the imaginary part of complex permeability flatten out at low frequencies, being stripped away from the influence of winding resistance, as predicted in [189]. The estimated and measured complex permeability characteristics align at higher frequencies, suggesting that they are closely fitted. The relative fitting error between $\mu''_{r_{measured}}$ and $\mu''_{r_{estimated}}$ does not exceed 2% for the loss tangent greater than 2 for both of the testing samples. This demonstrates that the inductor model accurately represents reality, and the proposed method appears to be correct.

The method heavily depends on the inductor stray capacitor ESR (R_{Cs}) value (Figure 49a-d, Figure 51a-d). Unfortunately, there is insufficient data available to prove or disprove this phenomenon and to clearly estimate the ESR value across the frequency range. The approach to limit its range and estimate its value will be shown next.

4.1.2 Test-Bench Estimation of Inductor Stray Capacitor ESR Value.

The ESR of the inductor stray capacitor (R_{Cs}) depends on the dielectric loss tangent (equation (160)) of several materials (Figure 32). As it is suspected, one of the biggest contributors to the ESR is the loss tangent of the core coating and the core itself. In order to verify this, a homemade testing fixture has been developed (Figure 52a-b).

The test fixture features a set of two electrodes positioned on adjustable arms to fit between toroidal cores with an external diameter of up to 25 mm. During the test, a sample is placed between electrodes and its admittance is measured.

In the method presented in this paper, calculations are performed using an inductor series equivalent model, as outlined in equations (176-181).

During the measurement, the inductor core, together with its coating, is placed between electrodes, and its impedance is measured using a Bode 100 VNA. Before measurement, to minimize any possible measurement error, the short, open, and load

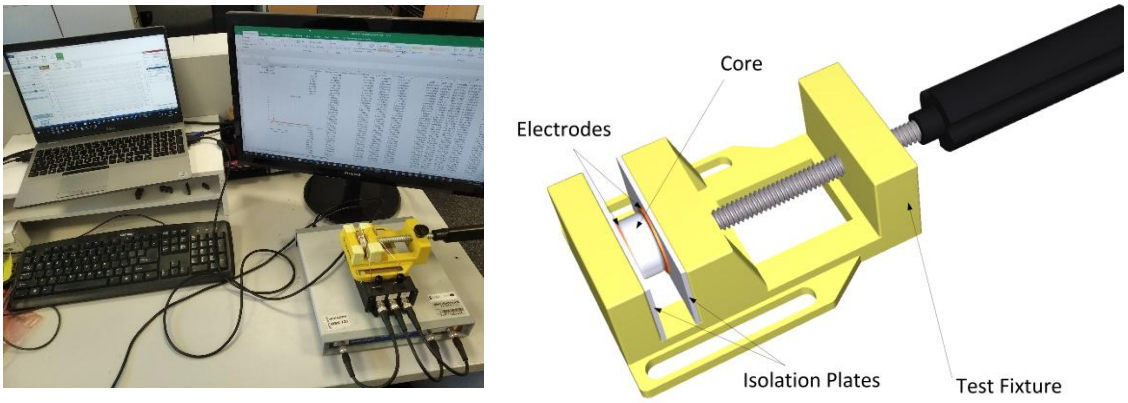

(**a**) (**b**)

Figure 52: Complex Permittivity Test-Bench;(**a**) Test-Bench; (**b**) Test Fixture.

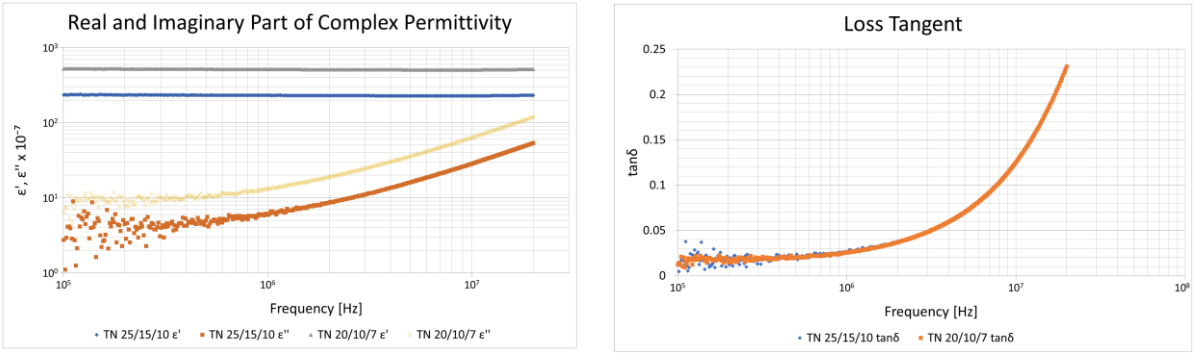

(**a**) (**b**)

Figure 53: Coating-to-Core Permittivity and Loss Tangent Characteristics; (**a**) Real and Imaginary Parts of Complex Permittivity: Grey—Real Part of Sample 2; Yellow—Imaginary Part of Sample 2; Blue—Real Part of Sample 3; Orange—Imaginary Part of Sample 3; (**b**) Loss Tangent: Orange—Sample 2; Blue—Sample 3.

compensation is performed. Fortunately, the loss tangent is not directly dependent on the sample size and shape except for the effect of dimensional resonance (equations (176-180)). This phenomenon [191], [205] in this particular case depends on more than the influence of the granular structure of the 3C90 ferrite, and this will be discussed later in this chapter.

The test results show (Figure 53a-b) that the loss tangent of the polyamide 11 (PA11) dielectric coating to 3C90 ferrite core for both samples (Sample 2 and Sample 3) can reach up to 0.048 at inductor self-resonant frequency and up to 0.16 at 13MHz, which

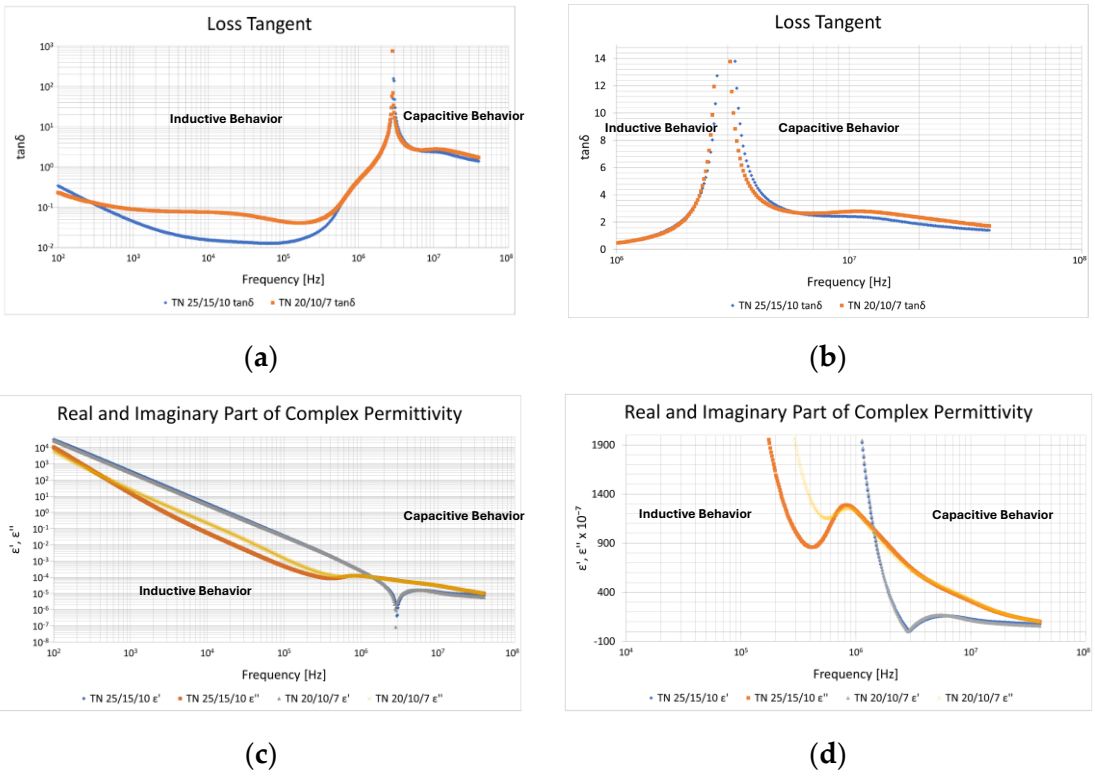

Figure 54: Sample 2 and Sample 3 Loss Tangent and Complex Permittivity Characteristics; (**a**) Loss Tangent, Orange – Sample 2, Blue – Sample 3; (**b**) Loss Tangent – Zoom at Self-Resonant Frequency, Orange – Sample 2, Blue – Sample 3; (**c**) Real and Imaginary Part of Complex Permittivity: Gray – Real Part of Sample 2, Yellow – Imaginary Part of Sample 2, Blue – Real Part of Sample 2, Orange – Imaginary Part of Sample 3; (**d**) Real and Imaginary Part of Complex Permittivity Zoom at Self-Resonant Frequency: Gray – Real Part of Sample 2, Yellow – Imaginary Part of Sample 2, Blue – Real Part of Sample 2, Orange – Imaginary Part of Sample 3.

is the end of the complex permeability measured range. The 0.16 value sets the lower limit for the sought loss tangent. This value, even though expected, is surprisingly low and far from the assumed 4. In fact, a toroidal inductor has a relatively complex structure, and thus, the loss tangent mechanism might originate somewhere else.

One of the ways to figure this out is to look at the inductor's behavior at and beyond its self-resonant frequency, where the inductor becomes a capacitor, and the complex permittivity defines its value and the value of the loss tangent with regard to the whole inductor.

The impedance sweeps of Samples 2 and 3 were performed again from 100 Hz to 40 MHz, and the inductor admittance, complex permittivity, and loss tangent were calculated using equations (176-180) (Figure 54a-d). In this case, we do not know the exact value of the capacitor's thickness and cross-section, due to the non-obvious

capacitor structure, which is, in fact, a toroidal inductor. The loss tangent does not depend significantly on the sample thickness and cross-section; therefore, equation (176) can be simplified to equation (181), as discussed in Chapter 3.

The characteristics show an exponential decay of the loss tangent, ranging from approximately 753 for Sample 2 and 156 for Sample 3 at the inductor self-resonant frequency to approximately 2.7 for Sample 2 and 2.3 for Sample 3 at 13 MHz. The sought loss tangent value lies somewhere between these extremes, and if we include the value from the previous measurement, the possible loss tangent range starts from 0.16 to 753 for sample 2 and 0.16 to 156 for sample 3.

Because the equivalent inductor model beyond self-resonant frequency consists of two parallel branches of a series R-C connection, it is difficult to distinguish the exact value of the inductor stray capacitor ESR (R_{Cs}) directly from the measurement of the overall capacitive inductor admittance/impedance. The loss tangent range does not give us an exact answer to what the loss tangent is, but it narrows the possible choice.

The calculations and test-bench results show that the best-fitting results are obtained with the peak loss tangent values at inductor self-resonance. It suggests that the stray capacitance has only a negligible impact on the complex permeability values in the method presented herein.

A better understanding of the origin of inductor stray capacitance and its ESR requires an investigation of core resonance phenomena and their influence on complex permeability values, which will be presented next.

4.1.3 Test-Bench Verification of the Influence of Core Natural and Dimensional Resonance on Complex Permeability.

As it was stated in Chapter 3, there are at least three factors which contribute to the resonance in Mn-Zn ferrites [48], [206-207], namely:

- resonance due to the windings' stray capacitance and the inductor self-inductance,
- the windings behave as a distributed constant line,
- inherent characteristics of the magnetic material.

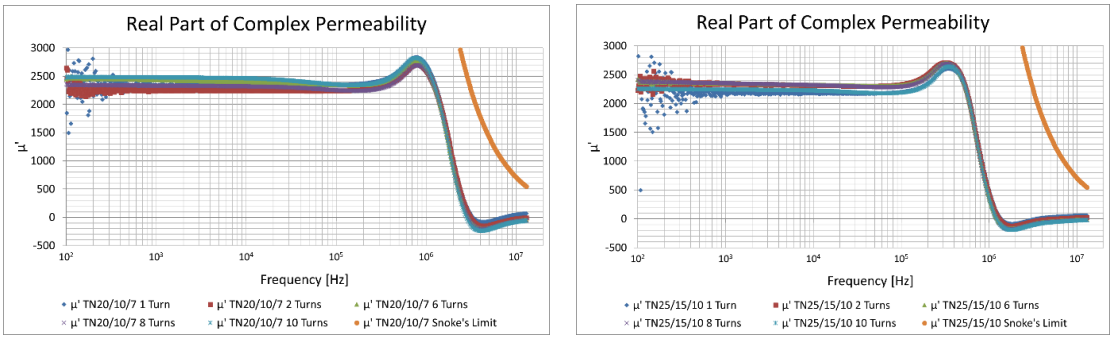

(**a**) (**b**)

Figure 55: Sample 2 and Sample 3 Real Part of Complex Permeability Characteristics at Different Number of Turns and Snoke's Limit; (**a**) Sample 2, Blue – 1 Turn, Red – 2 Turns, Green – 6 Turns, Violet – 8 Turns, Light-Blue 10 Turns, Orange – Snoke's Limit; (**b**) Sample 3, Blue – 1 Turn, Red – 2 Turns, Green – 6 Turns, Violet – 8 Turns, Light-Blue 10 Turns, Orange – Snoke's Limit.

As stated, the inductor's stray capacitance and its ESR, which are assumed to be mostly related to the windings, do not appear to impact the inductor's complex permeability characteristics, and the stray capacitor is somehow excluded from the overall calculations. It contradicts what one might expect and suggests that the inductor resonance originates somewhere else.

Moreover, the phenomenon where the winding behaves as a distributed constant line is most pronounced in inductors with multiple turns at multi-megahertz frequencies, in the form of self-repeating resonance. This phenomenon is not visible in Figure 47a-d, so it shall also be excluded.

The resonance phenomenon, which still applies, is the resonance resulting from the inherent characteristics of the magnetic material. In this case, there are two phenomena:

- natural resonance,
- dimensional resonance.

The natural resonance happens to the ferrites with high magnetic permeability due to the resonance of magnetization rotation under the action of the anisotropy field [48], [206-207].

Above the resonance, the real part of the complex permeability drops along the line known as Snoke's limit.

Sample No.	MLT [mm]	d_i [mm]	d_0 [mm]	ε_r [-]	N [-]	L_{dc} [nH]	SRF_{dc} [MHz]	C_{tt} [pF]	C_{swc} [pF]	C_{snc} [pF]	C_{sdc} [pF]	$C_{sdc(meas)}$ [pF]
Sample 2	34.5	0.75	0.775	4	10	211	305	7.18	9.80	0.80	1.09	1.29
Sample 3	42.0	0.75	0.775	4	10	328	236	8.74	11.93	0.97	1.33	1.39

Table 4: Dummy Core-Based Sample 2 and Sample 3 Parameters.

As shown in Figure 55a-b, the change of the real part of complex permeability characteristics for Sample 2 and Sample 3 is preceded by the permeability increase and then followed by its sharp drop. The drop happens way before Snoke's limit, which suggests that the magnetic resonance cannot be attributed to the natural resonance but rather to the second phenomenon, which is related to the shape and dimensions of the inductor core.

As mentioned, the phenomenon of dimensional resonance is clearly visible in Figure 55a-b, where the real part of the complex permeability increases just below the resonant frequency and then sharply drops above the resonance way before Snoke's limit. The characteristics indicate that the resonant frequency is almost independent of the number of winding turns, suggesting that the inductor's stray capacitance and its ESR in a given configuration are primarily due to the capacitance and ESR of the core, which will be discussed in the next paragraph.

4.1.4 Test-Bench Verification of Inductor Stray Capacitance.

This method has been verified in two ways: empirically through laboratory measurements and by finite element method (FEM) analysis, as will be shown in Chapter 5.

In the laboratory measurement, the inductors' windings have been wound on the acrylonitrile butadiene styrene (ABS) dummy cores with assumed relative permeability (μ_r) equal to 1. This approach would allow for keeping the turns properly structured without the influence of the ferrite core and with a negligible impact on the windings' capacitance by the non-magnetic dummy core. The parameters of the dummy cores are given in Table 4.

Initially, the self-inductance of the windings was measured at approximately 5 MHz, which corresponds to the plateau region of the impedance phase and a phase shift of approximately 90 degrees (Figure 56a-b). Then, the windings' self-resonant frequency

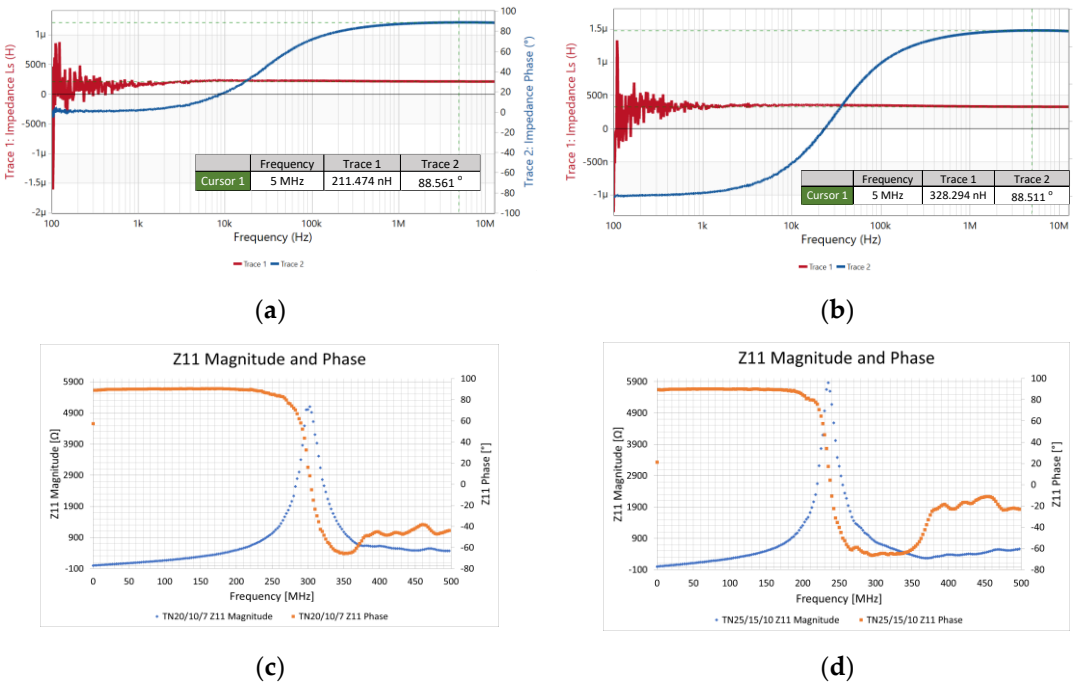

Figure 56: Sample 2 and Sample 3 width ABS Dummy Core; (**a**) Sample 2 Inductance Value measured at 5 MHz, Red – inductance Value, Blue – Impedance Phase; (**b**) Sample 3 Inductance Value Measured at 5 MHz, Red – Inductance Value, Blue – Impedance Phase; (**c**) Sample 2 Imaginary Part of Z_{11} Impedance with Visible Resonant Transition, Blue – Impedance Value, Orange – Impedance Phase; (**d**) Sample 3 Imaginary Part of Z_{11} Impedance with Visible Resonant Transition, Blue – Impedance Value, Orange – Impedance Phase.

was captured using an HP8753E VNA (Figure 56c-d) with the 1-port method. The measured winding capacitance is simply a product of the inductor's self-resonant frequency and the value of inductance, which is:

$$C_{s_{dc(meas)}} = \frac{1}{(2\pi SRF_{dc})^2 \cdot L_{dc}} \tag{231}$$

The empirical results show that the winding capacitance wound on the non-magnetic dummy core shall be considered as an interwinding capacitance between wire windings themselves (equation (186)); however, taking into account a slight increase of the capacitance due to the presence of a core material with certain permittivity (equation (189)). Moreover, the results show that the method given in [4] gives consistent results with a relative discrepancy between C_p (Table 3) and C_{swc} (Table 4) to be 28.2% for sample 2 and 4.4% for Sample 3. Even better results are obtained for the inductors with the dummy cores, with a discrepancy between C_{sdc} and $C_{sdc(meas)}$ to be 15.5% for Sample 2 and 4.3% for Sample 3 (Table 4).

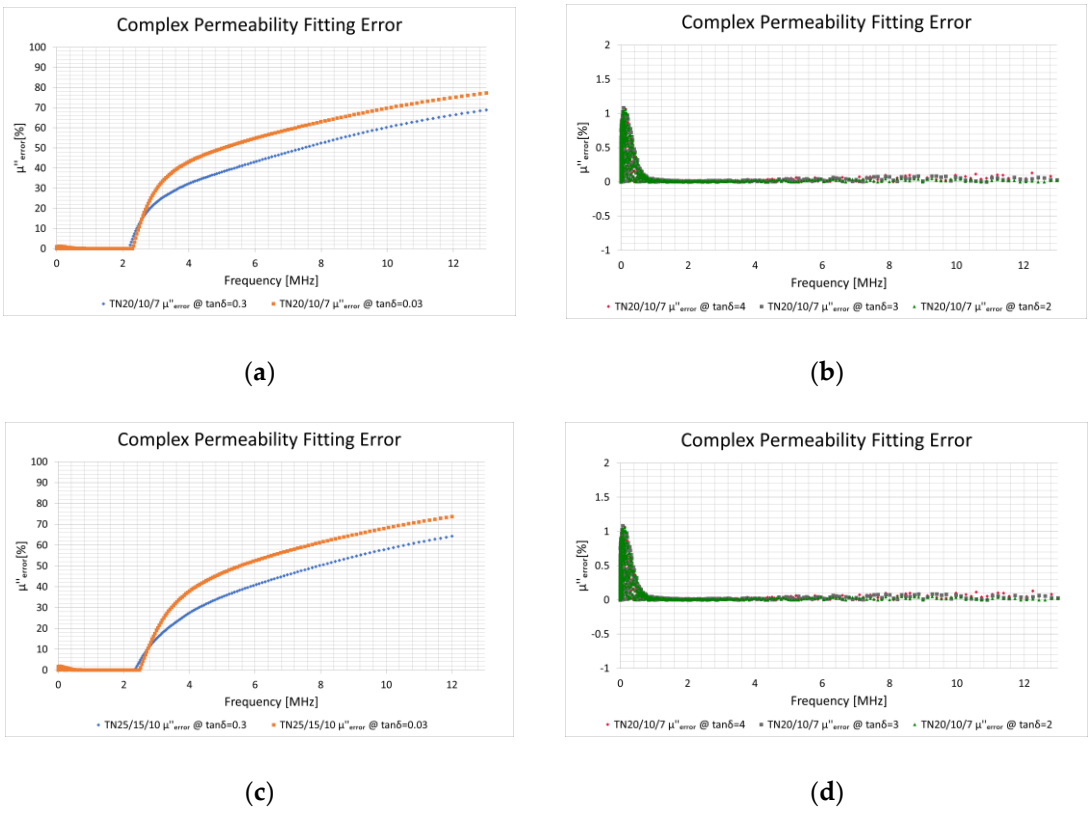

Figure 57: Relative Fitting Error Between $\mu''_{r_{measured}}$ and $\mu''_{r_{estimated}}$; (**a**) Sample 1, Orange - $tand\delta = 0.03$, Blue $tan\delta = 0.3$; (**b**) Sample 1, Green - $tand\delta = 2$, Grey - $tand\delta = 3$, red - $tand\delta = 4$; (**c**) Sample 2, Orange - $tand\delta = 0.03$, Blue $tan\delta = 0.3$; (**d**) Sample 2, Green - $tand\delta = 2$, Grey - $tand\delta = 3$, Red - $tand\delta = 4$.

The results show that, if the inductor stray capacitor ESR loss tangent is correctly defined (in case of Sample 2 and Sample 3 are set above 2), then it is possible to obtain a relative fitting error less than 2% along the entire frequency range (Figure 57a-d).

4.2 Experimental Verification of the iRESE Method.

The test-bench measurement and verification of the iRESE method have been done on three toroidal inductors using cores made by Ferroxcube. These are: TN10/6/4-3C90 - Sample 7, TN10/6/4-3C94 - Sample 8, and TN13/7.5/5-3F3 -Sample 9, wound with three turns of bifilar winding made of DNE 0.65 copper wire as shown in Figure 58a-c. The air core transformer was constructed using a TN58/18/9 – Air Trafo non-magnetic core made of ABS plastic, featuring 10 turns of bifilar winding made from DNE 0.65 mm copper wire, as shown in Figure 58d.

The switching frequencies of the testing setup have been chosen to be 100 kHz, 200 kHz, and 300 kHz, respectively, which are typical values for modern SMPSs and also

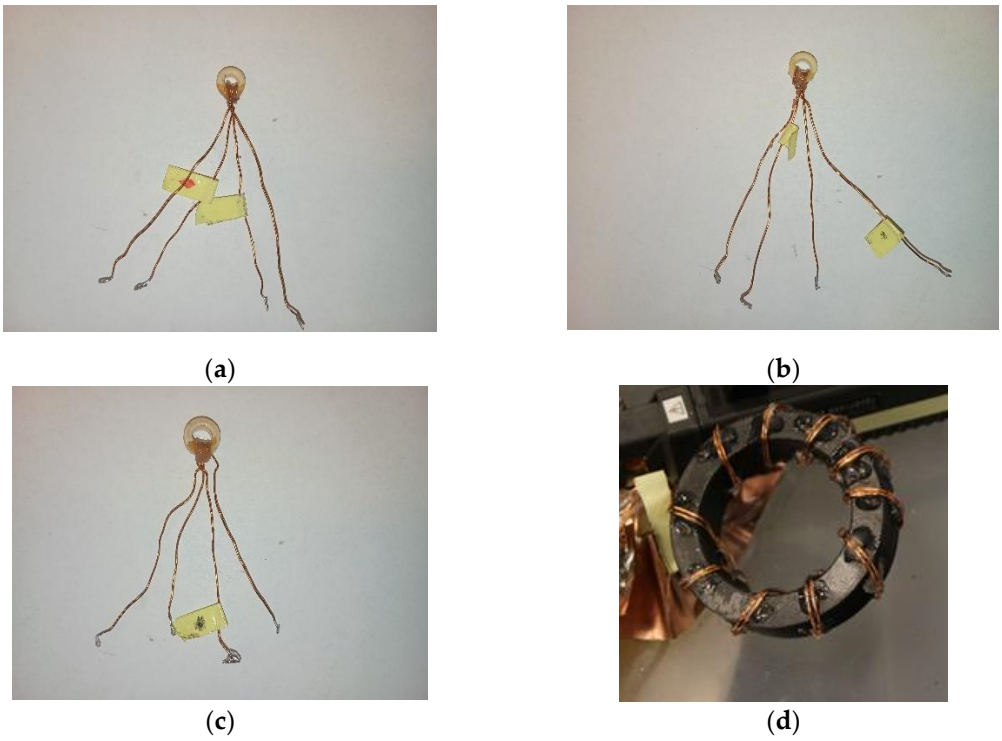

(a) (b) (c) (d)

Figure 58: Structure of the Inductors under Test; (**a**) Sample 7; (**b**) Sample 8; (**c**) Sample 9; (**d**) Air Trafo.

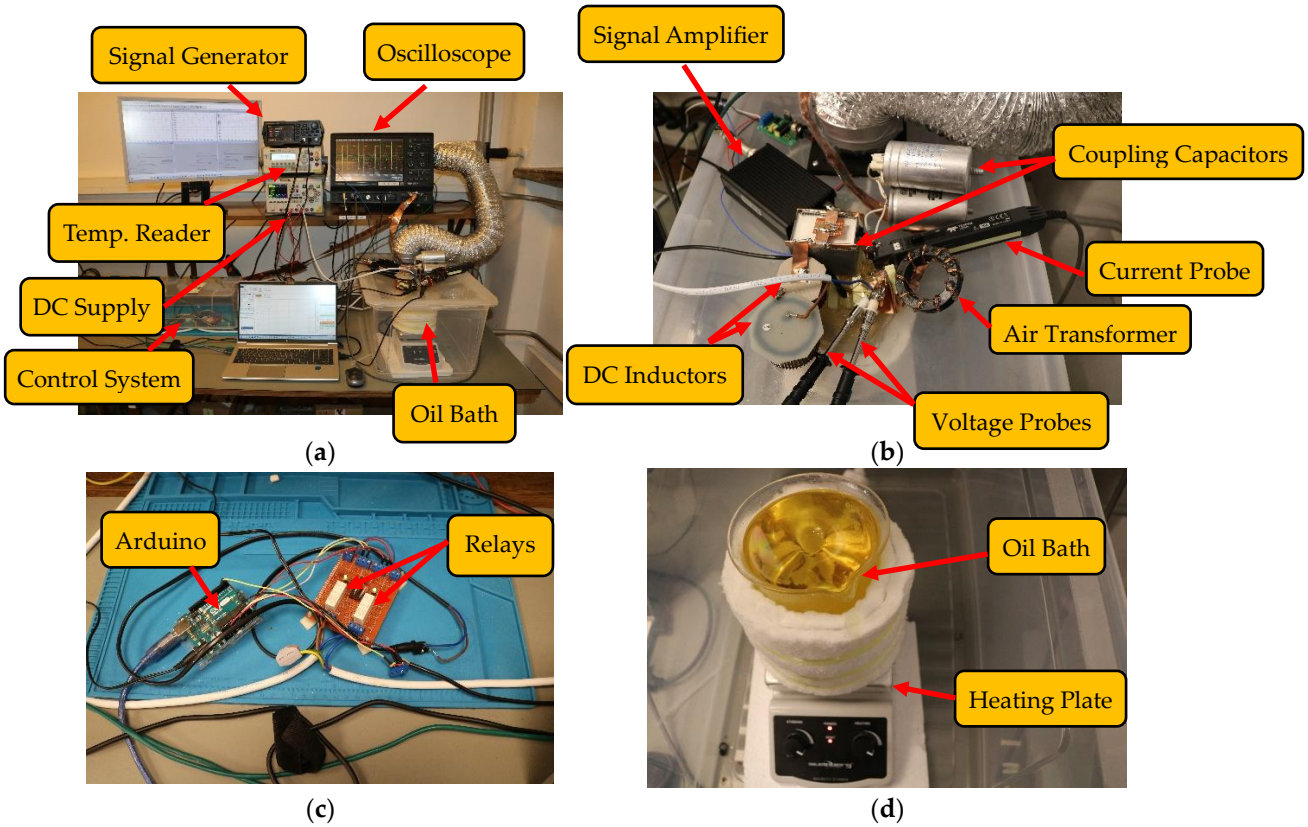

(a) (b) (c) (d)

Figure 59: Test-Bench Setup; (**a**) Entire Test-Bench View; (**b**) Zoom on Test-Bench Circuitry; (**c**) View on Arduino-Based Oil-Batch Temperature Control; (**d**) Oil-Bath Stirred and Heated up by Steinberg Magnetic Stirrer.

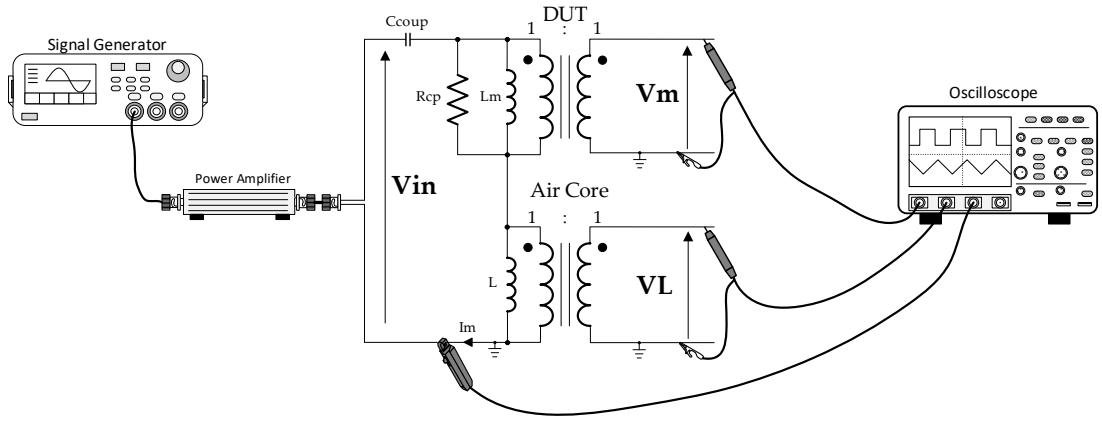

Figure 60: Simplified Test-Bench Measurement System.

the recommended values by the core manufacturers for each of the tested core materials.

The main test-bench setup is shown in Figure 59a-d. It consists of a 12-bit LeCroy HDO6104-MS 1 GHz oscilloscope, a Rigol DG992 SiFi II 2-channel 100 MHz arbitrary signal generator, a Rigol DM3068 digital multimeter, a Rigol DP832A programmable DC power supply, and an FPA301-20W 10 MHz function generator amplifier. The voltage signals were measured using two TESTEC TT-LX 312 voltage probes, while the LeCroy CP031A current probe measured the current.

As shown in Figure 59d, the inductors under test were submerged in an oil bath to heat them to the required temperature and then maintained at this temperature. Moreover, the oil bath has been further encapsulated within a plastic container for additional temperature insulation, fume removal, and to facilitate a close setup of the remaining circuitry to the inductor, as shown in Figure 59b. The temperature control has been implemented using an Arduino platform, along with a set of relays, as shown in Figure 59c. The Arduino used a DS18B20 sensor to monitor and adjust temperature variations, and it was synchronized with a K-type thermocouple used by the Rigol DM3068 as a reference. This setup allowed for keeping the constant temperature within $\pm 2°C$. The circuit schematic of the test bench is shown in Figure 60.

As can be seen in Figure 60, instead of using a current sensing resistor that might introduce significant phase discrepancy between the primary magnetizing current i_m and the secondary side magnetizing voltage V_m of the inductor under test, the LeCroy CP031A current probe has been used. The current probe features a 1 mA/Div sensitivity,

an amplitude accuracy of ±1% of reading, a measurement range of up to 30 A, and a 100 MHz bandwidth, which outperforms any current sensing resistor measurement methodology. Moreover, to limit the possible phase discrepancy between the primary magnetizing current i_m and the inductor secondary side magnetizing voltage V_m the current probe has been deskewed with the voltage probes using the LeCroy DCS015 deskewing fixture.

The voltage probes themselves have been deskewed amplitude-wise and phase discrepancy-wise by measuring the same voltage of 2 V peak-to-peak value with 50 ns rising/falling slopes and 50% duty-cycle ratio at 500 kHz switching frequency using both: (i) Rigol DG992 SiFi II signal generator, and (ii) as described in section 2 by measuring the same voltage and then calculating an integral $\frac{1}{T}\int_0^T v_m' i_m dt$ for each of them. The results were adjusted using deskew functions in the oscilloscope until the calculated integrals showed the same value.

The coupling capacitor C_{coup} has been chosen as a set of capacitors connected in parallel to maintain a constant DC blocking value at various excitation levels and limit the parasitic resistance introduced by it to below 100 mΩ at switching frequencies ranging from 100 kHz to 300 kHz.

The values of the inductor under test and the air core transformer inductances have been chosen as a trade-off between the measurement accuracy and the limitation of the switching noise introduced by the inductors' inductances themselves, as well as

Description	Core	Material	N	L_{prim} [µH]	L_{sec} [µH]	L_{leak_prim} [nH]	L_{leak_sec} [nH]	R_{leak_prim} [mΩ]	R_{leak_sec} [mΩ]	C_{inter_wind} [pF]	R_{cp} [Ω]	f_{res} [MHz]
Sample 7	TN10/6/4	3C90	3	8.184	8.058	239.665	238.684	23.727	17.093	14.751	107.427	16.492
Sample 8	TN10/6/4	3C94	3	9.719	9.751	249.976	236.226	13.048	12.855	12.903	111.939	11.543
Sample 9	TN13/7.5/5	3F3	3	9.736	9.620	172.545	183.281	11.306	10.078	12.454	128.580	8.201
Air Trafo	TN58/18/9	Air	10	0.476	0.476	395.626	371.912	24.617	29.967	25.676	-	100

Table 5: Parameters of Inductors under Test and Air Core Transformer @ 25 °C and 10 kHz.

Description	Core	Material	N	L_{prim} [µH]	L_{sec} [µH]	L_{leak_prim} [nH]	L_{leak_sec} [nH]	R_{leak_prim} [mΩ]	R_{leak_sec} [mΩ]	C_{inter_wind} [pF]	R_{cp} [Ω]	f_{res} [MHz]
Sample 7	TN10/6/4	3C90	3	18.376	18.307	189.042	191.497	21.881	22.56	78.647	150.708	4.800
Sample 8	TN10/6/4	3C94	3	11.708	11.288	182.671	199.912	23.270	21.437	95.059	148.843	7.368
Sample 9	TN13/7.5/5	3F3	3	17.931	17.878	196.525	171.681	26.126	24.991	27.125	171.068	4.722
Air Trafo	TN58/18/9	Air	10	-	-	-	-	-	-	-	-	-

Table 6: Parameters of Inductors under Test and Air Core Transformer @ 100 °C and 10 kHz.

their parasitic capacitances. The further limitation of the switching noise has been done by the limitation of the square waveform excitation signal slew rate to 50 ns on both signal edges. The detailed parameters of the tested inductors and air-core transformer have been obtained using a Bode 100 impedance analyzer and are presented in Table 5 at 25 ˚C/10kHz and in Table 6 at 100 ˚C/10kHz, where: L_{prim} – primary side inductance with secondary side open, L_{sec} – secondary side inductance with the primary side open, L_{leak_prim} – primary side leakage inductance with secondary side shorted, L_{leak_sec} – secondary side leakage inductance with the primary side shorted, R_{leak_prim} – primary side leakage resistance with secondary side shorted, R_{leak_sec} – secondary side leakage resistance with the primary side shorted, C_{inter_wind} – interwinding capacitance with primary and secondary sides shorted, R_{cp} – core resistance measured as the value of impedance at inductor self-resonance, f_{res} – frequency at inductor self-resonance.

Moreover, the further reduction of any unwanted noise or floating potential has been achieved by connecting the oscilloscope, the signal generator, the DC power supply, the primary and secondary sides of the inductors under test, and the air transformer to the same ground plane, as shown in Figure 59 and Figure 60, respectively.

All data processing is performed in the LTspice simulator.

4.2.1 Reversible Permeability Measurement.

STEP I

The calculations start with establishing small- and large-signal reversible permeability roll-off required to estimate the σ and η coefficients shown in equation (223). These coefficients will be used to adjust the OSE calculations when the excitation signal goes into the non-linear region.

First, the B-H characteristics of each of the inductors must be measured at $25°C$ and $100°C$, respectively. Because the anhysteretic curve is assumed to be frequency invariant, the calculations are based solely on the B-H curves captured at 100 kHz. As shown in Figure 61a-c, the lowest testing frequency corresponds to lower inductor impedance, resulting in higher magnetic field intensity values and more pronounced saturation effects. The characteristics reach different values at the far ends of negative and positive. This is due to the FPA301-20W signal amplifier's limitations, as it operates beyond its nominal range under these conditions. The small jump visible in the

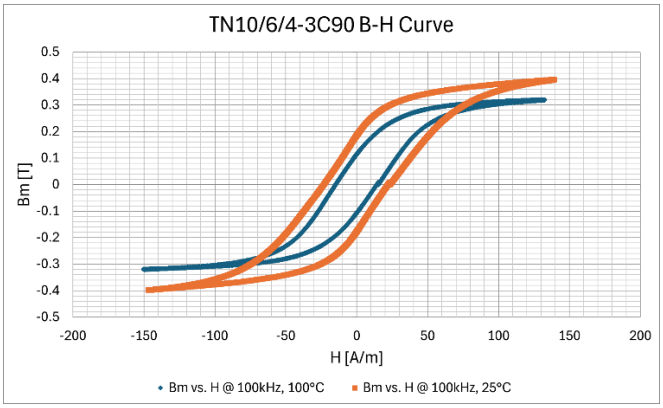

(**a**)

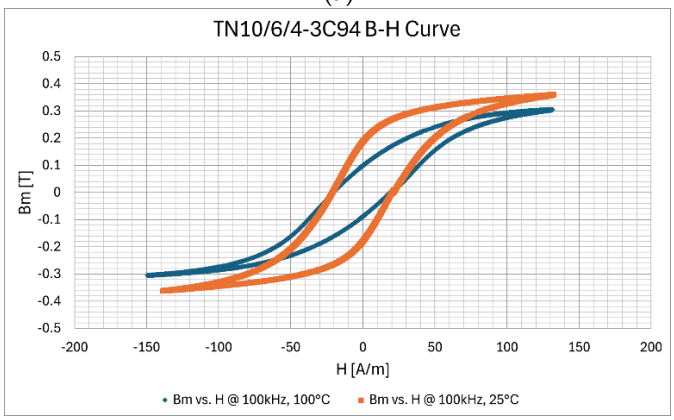

(**b**)

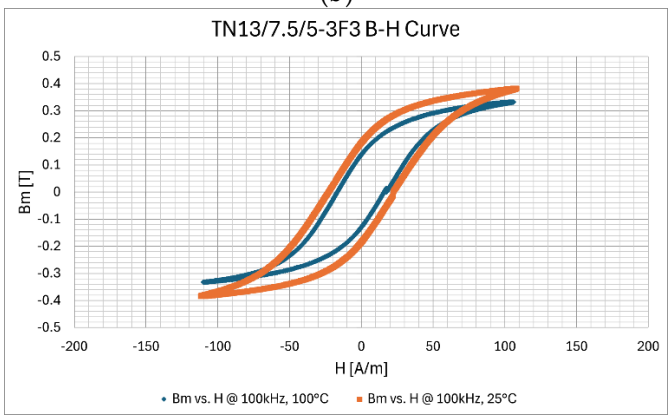

(**c**)

Figure 61: B-H Characteristics @ 100 kHz; (**a**) Sample 7, Orange - @ 25˚C, Blue – @ 100˚C; (**b**) Sample 8, Orange - @ 25˚C, Blue - @ 100˚C; (**c**) Sample 9, Orange - @ 25˚C, blue - @ 100˚C.

characteristics near the positive coercive field value is attributed to the reset of the voltage integral in LTspice.

The calculations of reversible permeability were split into two parts. The small-signal reversible permeability μ_{rev} is used to adjust calculations during DC bias premagnetization and is based on the approach by Esguerra et al. [219-223]. The large-

Description	μ_c	μ_i	a	α_0	B_{sat} [T]
Sample 7	5627	2120	3.1848	10.05	0.48
Sample 8	7236	2639	1.84	9.06	0.46
Sample 9	6464	1963	2.83	12.84	0.51

Table 7: Esguerra et al. Fitted Coefficients @ 25˚C.

Description	μ_c	μ_i	a	α_0	B_{sat} [T]
Sample 7	6778	5070	3.22	2.56	0.36
Sample 8	4187	3235	3.73	2.69	0.37
Sample 9	6939	3975	2.89	4.86	0.41

Table 8: Esguerra et al. Fitted Coefficients @ 100˚C.

signal reversible permeability $\mu_{rev(a)}$ adjusts the calculations if the excitation signal reaches the B-H curve non-linear region, and is based on an iterative approach, measuring the changes of B and H along the B-H curve at each adjacent step, where the B-H curve measurement was performed. The fitting coefficients for the Esguerra et al. approach at 25˚C and 100˚C are given in Table 7 and Table 8, respectively, where: μ_c – is a large-signal permeability measured at the coercive field, μ_i – is an initial small-signal permeability measured by Bode 100 @ 10 kHz, a, α_0, B_{sat} – are the fitting coefficients.

In general, the relative values of both permeability roll-offs exhibit similar behavior at 100 °C, as shown in Figure 62a-c.

Because calculations of the original Steinmetz equation (OSE) involve temperature adjustments, knowledge of the change in the large-signal relative permeability roll-off with temperature is also required. This is illustrated in Figure 63a-c for 25˚C and 100˚C, respectively. The difference between these values is linearly interpolated in calculations.

Having the above data already analyzed, it is now possible to estimate the σ and η shown in equation (223) and go to STEP II-IV.

4.2.2 Estimation of Original Steinmetz Equation Coefficients.

STEP II-III

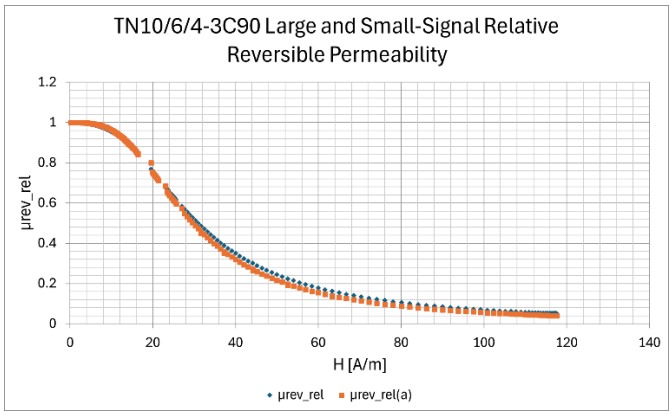

(**a**)

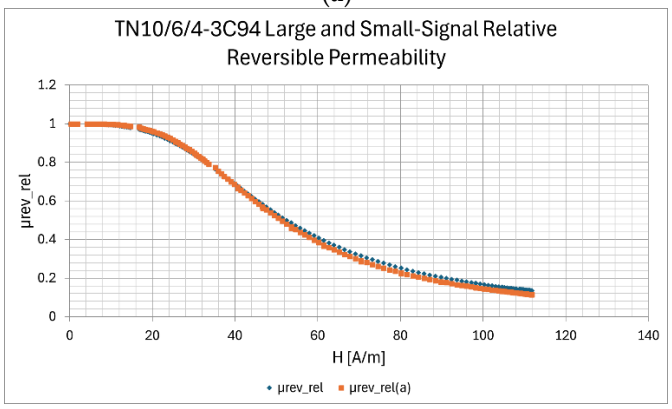

(**b**)

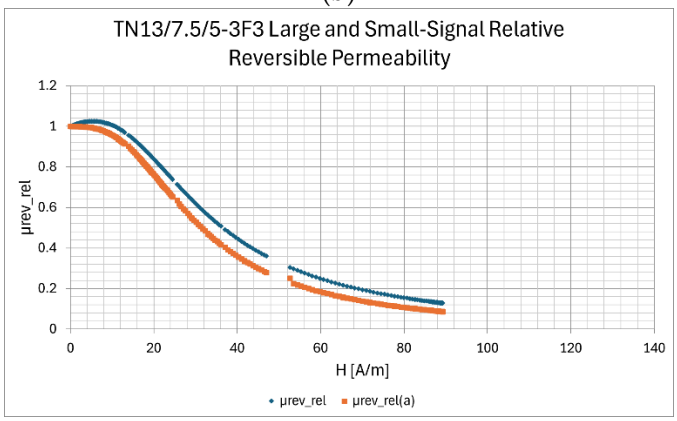

(**c**)

Figure 62: Small $\mu_{rev_{rel}}$ and Large-Signal $\mu_{rev_{rel(a)}}$ Relative Reversible Permeability Characteristics @ 100 kHz and 100°C: (**a**) Sample 7, Orange – Large Signal Relative Reversible Permeability, Blue – Small Signal Relative Reversible Permeability; (**b**) Sample 8, Orange – Large Signal Relative Reversible Permeability, Blue – Small Signal Relative Reversible Permeability; (**c**) Sample 9, Orange – Large Signal Relative Reversible Permeability, Blue – Small Signal Relative Reversible Permeability.

The core power loss and the coefficients describing the OSE equation have been measured at $100°C$, placing the inductors under test in the heated oil bath. The value of the magnetic flux density was extracted from the V_m inductor voltage of sinusoidal shape

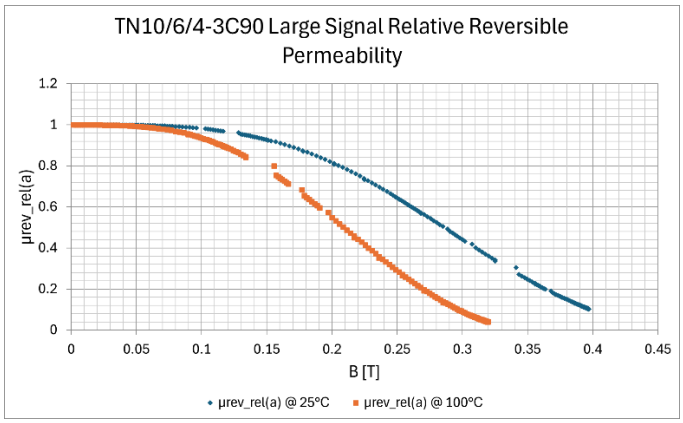

(**a**)

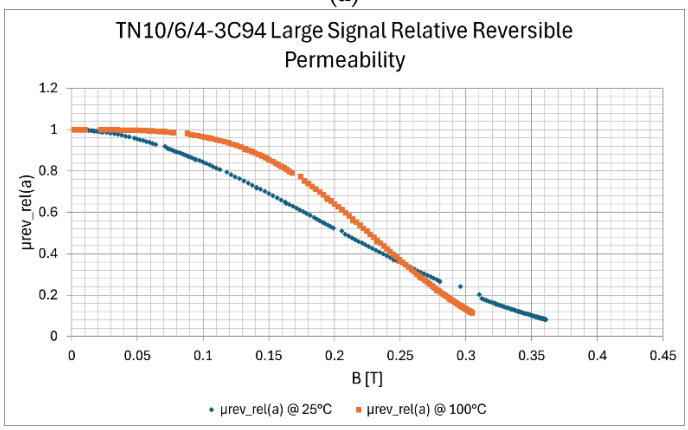

(**b**)

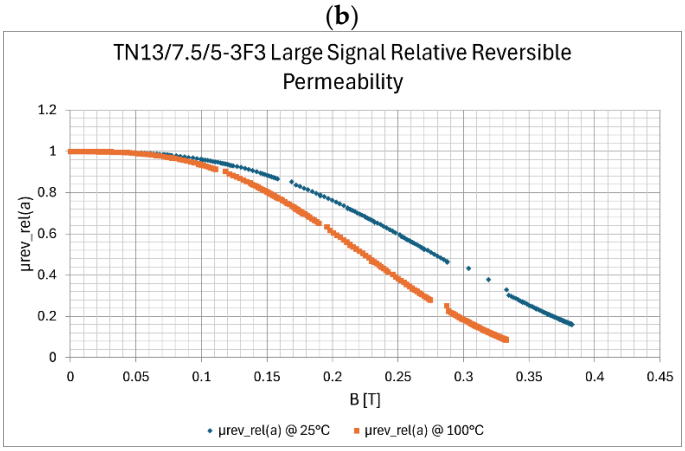

(**c**)

Figure 63: Large Signal Reversible Permeability $\mu_{rev\_rel(a)}$ Characteristics @ 100 kHz: (**a**) Sample 7, Blue – Large Signal Relative Reversible Permeability @ 25°C, Orange – Large Signal Relative Reversible Permeability @ 100°C; (**b**) Sample 8, Blue – Large Signal Relative Reversible Permeability @ 25°C, Orange – Large Signal Relative Reversible Permeability @ 100°C; (**c**) Sample 9, Blue – Large Signal Relative Reversible Permeability @ 25°C, Orange – Large Signal Relative Reversible Permeability @ 100°C.

by integration of the measured signal in LTspice. The switching frequencies were set to 100 kHz, 200 kHz, and 300 kHz, respectively.

At this stage, there is no DC component in the excitation signals, and thus, the σ

coefficient was set to 1.0, while the η coefficient was set accordingly to the amplitude of the magnetic flux density and the reversible permeability change as shown in Figure 63a-c. The coefficient fitting was performed using the Excel Solver and the least squares method.

The STEP III was conducted in a similar manner, where the temperature of the tested inductors was swept from 25 °C to 120 °C at magnetic flux densities of 100 mT at 100 kHz and 50 mT at 200 kHz and 300 kHz, respectively. The fitting of a fifth-degree polynomial was performed using the OriginLab software this time.

The power loss measurement results are shown in Figure 64a-f, overlaid on the power loss characteristics taken directly from the manufacturer's datasheets for reference. The fitting coefficients are shown in Table 9, Table 10, and Table 11, respectively, where: f_s is the switching frequency.

As shown in Figure 64a-f, the data obtained from the manufacturers' datasheets and the test-bench measurements are consistent for 3C90 and 3F3 but differ significantly for 3C94. It is likely due to high material spreads during the manufacturing process, highlighting the importance of material verification before mass-producing of any magnetic components. This should mainly involve Monte-Carlo analysis.

Description	f_s [kHz]	k	α	β	ξ_5	ξ_4	ξ_3	ξ_2	ξ_1	ξ_0
Sample 7	100	0.791	1.529	2.629	-2.45E-9	8.91E-7	-1.20E-4	0.0076	-0.25586	5.515
	200	0.904	1.504	2.525	-1.94E-9	7.29E-7	-1.02E-4	0.0068	-0.23982	5.322
	300	0.970	1.485	2.393	-2.18E-9	8.40E-7	-1.21E-4	0.0083	-0.27899	5.234

Table 9: Sample 7 OSE and Temperature Fitting Coefficients.

Description	f_s [kHz]	k	α	β	ξ_5	ξ_4	ξ_3	ξ_2	ξ_1	ξ_0
Sample 8	100	0.848	1.581	2.761	-6.01E-10	2.30E-7	-3.20E-5	0.00227	-0.09287	2.644
	200	0.810	1.540	2.508	-5.91E-10	2.11E-7	-2.80E-5	0.00195	-0.0823	2.418
	300	0.838	1.533	2.461	-3.49E-10	1.06E-7	-1.09E-5	6.01E-4	-0.02716	1.553

Table 10: Sample 8 OSE and Temperature Fitting Coefficients.

Description	f_s [kHz]	k	α	β	ξ_5	ξ_4	ξ_3	ξ_2	ξ_1	ξ_0
Sample 9	100	0.811	1.547	2.704	-2.51E-9	8.77E-7	-1.12E-4	0.00681	-0.22914	5.049
	200	0.709	1.571	2.769	-2.54E-9	8.87E-7	-1.15E-4	0.00729	-0.25979	5.875
	300	0.826	1.503	2.421	-2.27E-9	8.18E-7	-1.10E-4	0.00703	-0.23142	4.443

Table 11: Sample 9 OSE and Temperature Fitting Coefficients.

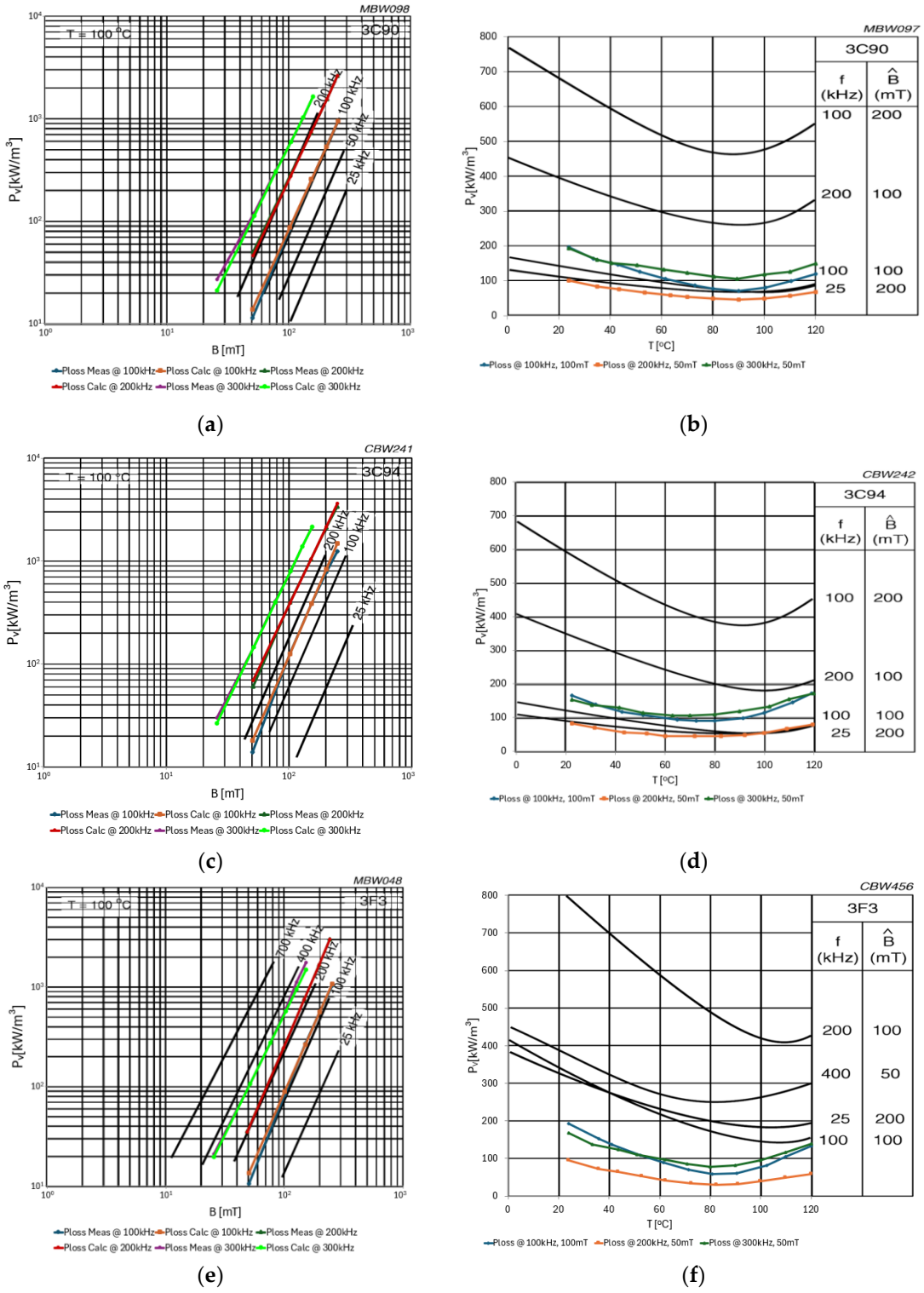

Figure 64: Fitting of Large-Signal Core Loss Characteristics under Sinusoidal Excitation Versus Magnetic Flux Density @ 100°C and Versus Temperature: (**a**) Sample 7 P_v vs. B_m @ 100°C, Blue – Measured Characteristics @ 100 kHz, Orange – Fitted Characteristics @ 100 kHz; Dark Green – Measured Characteristics @ 200 kHz, Red – Fitted Characteristics @ 200 kHz, Purple – Measured Characteristics @ 300 kHz, Light Green – Fitted Characteristics @ 300 kHz; (**b**) Sample 7 P_v vs. T, Blue - @ 100 kHz and 100 mT Signal Swing, Orange - @ 200 kHz and 50 mT Signal Swing, Green - @ 300 kHz and 50 mT Signal Swing; (**c**) Sample 8 P_v vs. B_m @ 100°C, Blue – Measured Characteristics @ 100 kHz,

Orange – Fitted Characteristics @ 100 kHz; Dark Green – Measured Characteristics @ 200 kHz, Red – Fitted Characteristics @ 200 kHz, Purple – Measured Characteristics @ 300 kHz, Light Green – Fitted Characteristics @ 300 kHz; (**d**) Sample 8 P_v vs. T, Blue - @ 100 kHz and 100 mT Signal Swing, Orange - @ 200 kHz and 50 mT Signal Swing, Green - @ 300 kHz and 50 mT Signal Swing; (**e**) Sample 9 P_v vs. B_m @ 100°C, Blue – Measured Characteristics @ 100 kHz, Orange – Fitted Characteristics @ 100 kHz; Dark Green – Measured Characteristics @ 200 kHz, Red – Fitted Characteristics @ 200 kHz, Purple – Measured Characteristics @ 300 kHz, Light Green – Fitted Characteristics @ 300 kHz; (**f**) Sample 9 P_v vs. T, Blue - @ 100 kHz and 100 mT Signal Swing, Orange - @ 200 kHz and 50 mT Signal Swing, Green - @ 300 kHz and 50 mT Signal Swing.

4.2.3 Unified Small and Large-Signal Core Loss Model Measurements.

STEP IV

As stated in [178] and Chapter 3 of this dissertation, there are two concurrent core loss models, depending on the magnitude of the excitation signals that exclude one another. As shown in Figure 42, the large-signal OSE model smoothly transitions to the small-signal complex permeability model at low levels of excitation, and the core resistance characteristics flatten out. So, the unification of both models seems to be imminent both: (i) because that is how the inductor really behaves and (ii) because the single model can be used in both small and large-signal domains, which was not possible before, helping, e.g., in the design of the low-noise magnetic shielding [189].

The core resistance characteristics extraction procedure was performed using a Bode 100 impedance analyzer. To do so, the impedance of the tested inductor was measured at various levels of excitation signals ranging from 0.1 mT to 20mT. During the measurement, the voltage and current were captured using the TESTEC TT-LX 312 and the LeCroy CP031 probes. The voltage probe was connected to the secondary side of the tested inductor to avoid introducing any unwanted parasitic effects at the primary side during measurement.

The real part of the impedance measurement consists of core resistance, winding resistance, and a combination of other parasitic effects, which were discussed in Chapter 3. Therefore, the core resistance must be separated from the remaining unwanted components. Regarding the inductors that are wound with several winding turns, the winding resistance is affected by the magnetic field existing around the core [178]. Thus, the separation process can be performed using the Dowell equation, aided by the small

signal inductor model and the complex permeability iterative approximation method, as shown in [187].

However, in the case of the tested inductors, the real part of the impedance measurement is mainly affected by the resistance of the winding wires and the soldering joints because, as shown in Figure 58a-c, only a small portion of the windings is wound around the core. The structure of the windings is designed in this manner because the inductor must be submerged sufficiently deep into the oil bath while also being connected to the remaining testing circuitry, as shown in Figure 59a-d. Moreover, three turns of bifilar windings are a trade-off between the magnetic field distribution around the core and the limitation of significant inductance introduced into the switching circuitry, which helps avoiding unwanted oscillations during switching.

Therefore, instead of using the method described in [187], it was assumed that the winding resistance can be measured on a dummy core of equivalent size, made of ABS plastic and wound with equivalent winding wire. This resistance is then subtracted from the real part of the measured impedance, giving the core resistance only. Examples of the results for 100 kHz, 200 kHz, and 300 kHz are shown in Figure 65a-c.

As one might expect, the transition between the small- and large-signal core resistance models does not occur smoothly as presented in Figure 65a-c. The visible deviation from that can be seen in Figure 66.

The reason for that might be a complex case. First, the Steinmetz core loss model is simplified by a straight line in the linear domain up to 300mT. This model is typically fitted with a certain level of accuracy, as shown in paragraph 4.2.2. Initially, this introduces some deviations in the prediction of the characteristics' slope at different excitation levels. Second, the Steinmetz model might not be a straight line after all, but rather a segmented one, as shown in the ferrite magnetic design tool provided by TDK [224]. In this case, the measured core loss is not tangential to the Steinmetz-based predicted values due to dispersion in the characteristics slope estimation. Third, in the equation (225) repeated here for convenience:

$$R_c = 2V_e k f^{\alpha} B_m^{\beta} \hat{I}_m^{-2} \left(\sum_{n=0}^{5} \xi_n T^n \right) \tag{232}$$

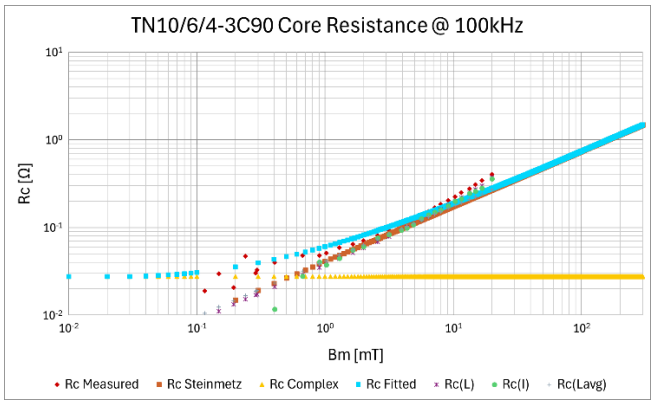

(**a**)

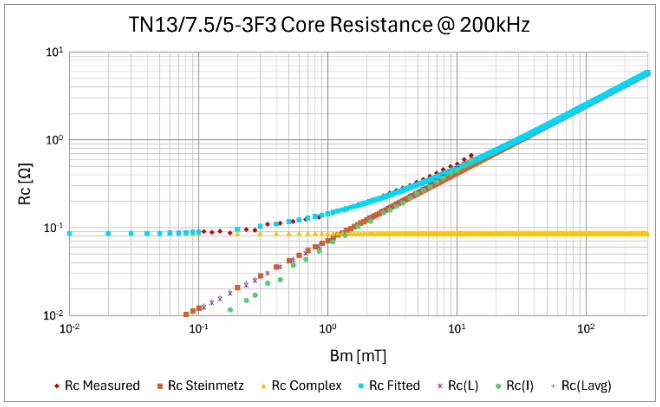

(**b**)

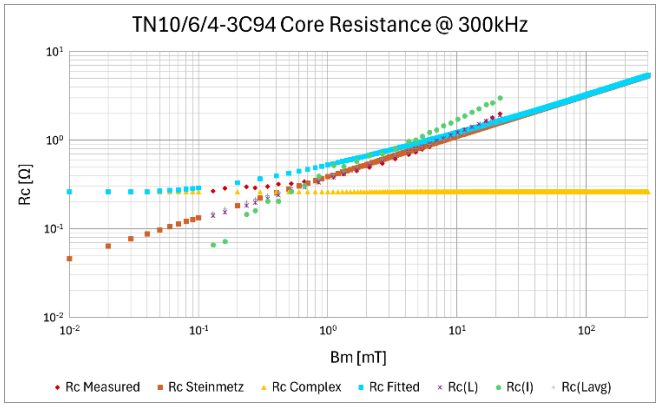

(**c**)

Figure 65: Core Resistance Measurement and Fitting; (**a**) Sample 7 @ 100 kHz; (**b**) Sample 9 @ 200 kHz; (**c**) Sample 8 @ 300 kHz; Red – Measured Core Resistance, Orange – Core Resistance Based on Steinmetz Model, Yellow – Core Resistance Based on Complex Permeability Model, Blue – Fitted Core Resistance Combining Small and Large-Core Resistance Model, Violet – Core Resistance Based on Measured Inductance Value, Green – Core Resistance Based on Measured Current, Gray – Core Resistance Based on Average Inductance Value.

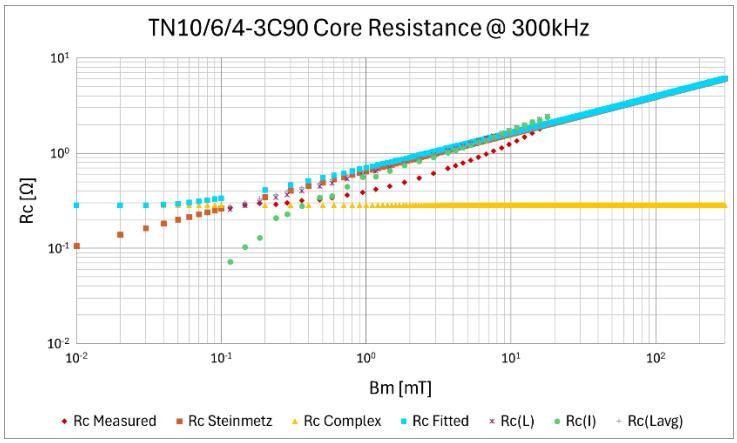

Figure 66: Sample 7 Core Resistance Measurement and Fitting @ 300 kHz, Red – Measured Core Resistance, Orange – Core Resistance Based on Steinmetz Model, Yellow – Core Resistance Based on Complex Permeability Model, Blue – Fitted Core Resistance Combining Small and Large-Core Resistance Model, Violet – Core Resistance Based on Measured Inductance Value, Green – Core Resistance Based on Measured Current, Gray – Core Resistance Based on Average Inductance Value.

the core resistance is a function of two variables: the B_m and the I_m while the I_m does not exist in the original Steinmetz core loss prediction. Therefore, the I_m was measured during the Bode 100 impedance sweep and introduced to the model. This results in the $R_c(I_m)$ characteristic shown in Figure 65a-c and Figure 66, respectively. It can be seen that this characteristic more closely follows the measured values of R_c at higher excitation signals. Additionally, the equation (232) can be rewritten in the linear region to:

$$R_c = 2V_e k f^{\alpha} B_m^{\beta} \left(\frac{B_m N A_c}{L}\right)^{-2} \left(\sum_{n=0}^{5} \xi_n T^n\right) \tag{233}$$

where: N – is a number of winding turns, A_c – is an effective cross-sectional area of the magnetic core, L – is the inductance. In this case, the values of L can be directly taken from the impedance measurement. This approach gives the most consistent results compared to the measured characteristics. Fourth, as previously stated, the winding resistance was measured on a dummy core and assumed to be invariant to the excitation level. Moreover, the inductor parasitics, which contribute to the real and imaginary parts of the impedance, were also neglected. This may also be a cause of the small-signal core resistance characteristics bending phenomenon, which existing core loss models do not predict.

Finally, the impedance analyzer used for the measurements has a limited range of excitation signal amplitudes. At the current setup of the tested inductors and the assumed switching frequencies, it can reach only 20 mT. Therefore, some simplifications were necessary regarding the core resistance fitting procedure. It was then assumed that the value of inductance in equation (233) is an average one, being the mean value of all inductances measured by the impedance analyzer. This is represented by $R_c(L_{avg})$ characteristics shown in Figures 65a-c and Figure 66, respectively. Unifying the small and large-signal core loss model equation (233) becomes:

$$R_c = 2V_e k f^{\alpha} \left(B_m^{\beta} + \sum_{i=0}^{9} \chi_i B_m^i \right) \left(\frac{B_m N A_c}{L_{avg}} \right)^{-2} \left(\sum_{n=0}^{5} \xi_n T^n \right) \tag{234}$$

where χ_i – are the fitting coefficients of the ninth-degree polynomial used to combine small and large signal core loss characteristics. The values of L_{avg} are given in Table 12.

The $\left(\frac{B_m N A_c}{L_{avg}}\right)^{-2}$ expression can now be treated as a constant, allowing the transformation of the core resistance given by equation (234) back to the core loss given by equation (226).

The values of the ninth-degree polynomial are given in Table 13, Table 14 and Table 15, respectively, while the fitted $R_C\ Fitted$ characteristics are shown in Figure 65a-c and Figure 66, respectively. The fitting was performed using OriginLab software.

4.2.4 Rectangular and Sinusoidal Excitations with a DC Bias.

STEP V

As stated in Chapter 3, there are a few scenarios possible in this step, namely:

4.2.4.1 Sinusoidal Excitation with a DC Bias – STEP V.1.

The DC bias was introduced into the test bench by adding a DC voltage source in series with a 1 mH inductor [115, 209, 210, 211, 215, 216]. The inductor transfers the DC bias voltage into the DC bias current used in the premagnetization of the core. The modified test-bench circuit schematic is shown in Figure 67.

The added inductor has a self-resonance frequency of 1.3 MHz, which is sufficiently high to maintain stable inductance at the test switching frequencies.

Description	f_s [kHz]	Sample 7	Sample 8	Sample 9
L_{avg} [μH]	100	7.497	8.672	8.365
	200	7.454	8.741	8.467
	300	7.623	7.622	8.749

Table 12: The Average Value of Inductance During Small- and Large-Signal Core Resistance Fitting.

Description	f_s [kHz]	χ_9	χ_8	χ_7	χ_6	χ_5	χ_4	χ_3	χ_2	χ_1	χ_0
Sample 7	100	-725.08	1025.98	-609.21	197.11	-37.45	4.17	-0.25239	0.00638	2.22E-8	-1.70E-13
	200	-733.34	1020.17	-595.92	189.24	-35.24	3.84	-0.22725	0.00561	1.43E-7	-8.50E-13
	300	-599.28	847.12	-503.48	162.89	-30.94	3.45	-0.20846	0.00527	2.47E-7	-1.19E-12

Table 13: Sample 7 Ninth-Degree Polynomial Coefficients.

Description	f_s [kHz]	χ_9	χ_8	χ_7	χ_6	χ_5	χ_4	χ_3	χ_2	χ_1	χ_0
Sample 8	100	-631.83	879.29	-513.85	163.25	-30.42	3.32	-0.1964	0.00486	2.55E-8	-1.69E-13
	200	-733.34	1020.17	-595.93	189.24	-35.24	3.84	-0.22725	0.00561	1.43E-7	-8.50E-13
	300	-1708.83	2414.73	-1434.67	464.00	-88.12	9.82	-0.59329	0.015	1.67E-7	-8.71E-13

Table 14: Sample 8 Ninth-Degree Polynomial Coefficients.

Description	f_s [kHz]	χ_9	χ_8	χ_7	χ_6	χ_5	χ_4	χ_3	χ_2	χ_1	χ_0
Sample 9	100	-249.76	351.26	-207.63	66.79	-12.61	1.39	-0.08386	0.00211	2.78E-8	-1.66E-13
	200	-587.67	829.69	-492.48	159.12	-30.19	3.36	-0.2028	0.00512	1.55E-8	-9.35E-14
	300	-206.99	287.06	-167.11	52.86	-9.80	1.06	-0.06253	0.00153	2.63E-7	-1.42E-12

Table 15: Sample 9 Ninth-Degree Polynomial Coefficients.

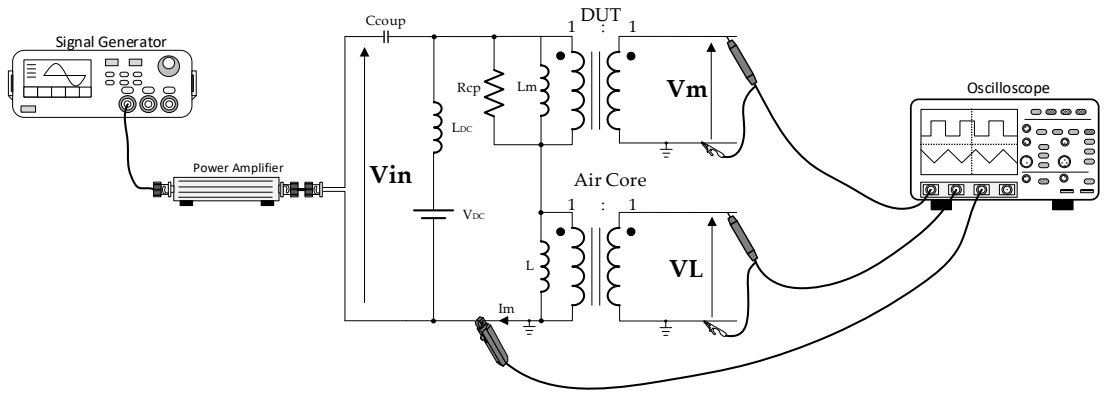

Figure 67: Test-Bench Measurement System with Added DC Bias Source.

Because the DC premagnetization is done by the introduction of a DC bias current, the core loss of the tested inductors with the DC premagnetization is a function of the magnetic field strength $P_c \cdot F(H_{dc})$ rather than a function of the magnetic flux density $P_c \cdot F(B_{dc})$. So, the sinusoidal $P_c \cdot F(H_{dc})$ is transferred into the $P_c \cdot F(B_{dc})$ to get a function of only one variable B as in equation (227). This is achieved using an iterative approximation curve fitting method similar to that described in [187], with coefficients

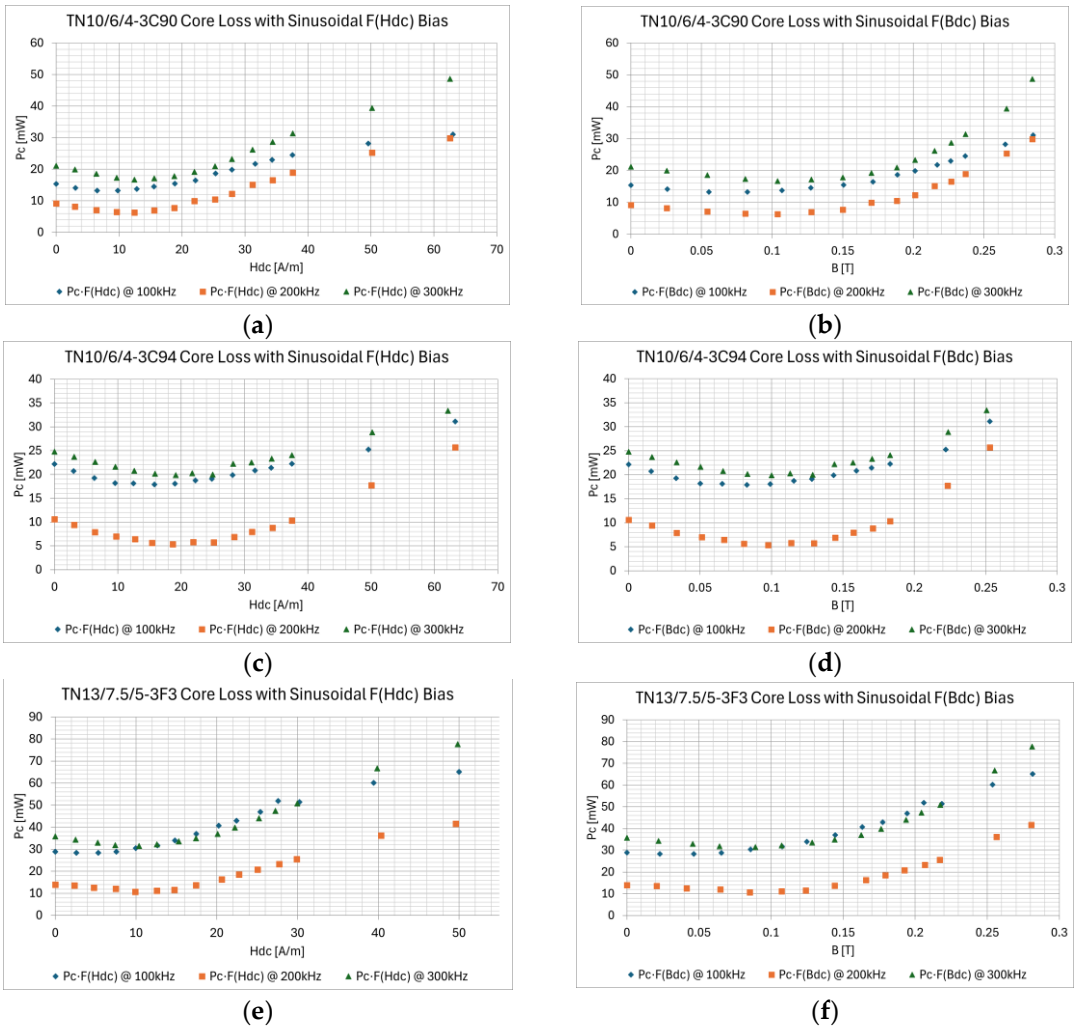

Figure 68: Core Loss with Sinusoidal Excitation and DC Bias Premagnetization; (**a**) Sample 7 $P_C \cdot F(Hdc)$, Blue - @ 100 kHz & $B_m = 100mT$, Orange - @ 200 kHz & $B_m = 50mT$, Green - @ 300 kHz & $B_m = 50mT$; (**b**) Sample 7 $P_C \cdot F(Bdc)$, Blue - @ 100 kHz & $B_m = 100mT$, Orange - @ 200 kHz & $B_m = 50mT$, Green - @ 300 kHz & $B_m = 50mT$; (**c**) Sample 8 $P_C \cdot F(Hdc)$, Blue - @ 100 kHz & $B_m = 100mT$, Orange - @ 200 kHz & $B_m = 50mT$, Green - @ 300 kHz & $B_m = 50mT$; (**d**) Sample 8 $P_C \cdot F(Bdc)$, Blue - @ 100 kHz & $B_m = 100mT$, Orange - @ 200 kHz & $B_m = 50mT$, Green - @ 300 kHz & $B_m = 50mT$; (**e**) Sample 9 $P_C \cdot F(Hdc)$, Blue - @ 100 kHz & $B_m = 100mT$, Orange - @ 200 kHz & $B_m = 50mT$, Green - @ 300 kHz & $B_m = 50mT$; (**f**) Sample 9 $P_C \cdot F(Bdc)$, Blue - @ 100 kHz & $B_m = 100mT$, Orange - @ 200 kHz & $B_m = 50mT$, Green - @ 300 kHz & $B_m = 50mT$.

provided in Table 8. The measurement results are given in Figure 68a-f. The magnetic flux density swing was set to: B_m = 100 mT at 100 kHz, Bm = 50 mT at 200 kHz and 300 kHz, respectively.

During the test-bench measurements, the σ coefficient, as shown in the equation (223) is calculated based on the characteristics given in Figure 62a-c, while the η coefficient depends on the magnitude of the magnetic flux density swing and is based

Description	f_s [kHz]	ζ_4	ζ_3	ζ_2	ζ_1	ζ_0
Sample 7	100	-370.118	199.123	-5.470	-2.5174	1.0098
	200	-186.883	232.729	-10.233	-4.0389	0.9487
	300	99.271	66.133	-3.080	-2.4056	0.9731

Table 16: Sample 7 $P_c \cdot F(B_{dc})$ Fourth-Degree Polynomial Coefficients.

Description	f_s [kHz]	ζ_4	ζ_3	ζ_2	ζ_1	ζ_0
Sample 8	100	684.753	-354.010	78.725	-6.8433	1.0029
	200	150.945	83.041	25.125	-8.408	1.0161
	300	-148.965	80.326	7.861	-3.3445	0.9999

Table 17: Sample 8 $P_c \cdot F(B_{dc})$ Fourth-Degree Polynomial Coefficients.

Description	f_s [kHz]	ζ_4	ζ_3	ζ_2	ζ_1	ζ_0
Sample 9	100	-449.625	188.253	1.674	-0.7833	1.0291
	200	-1136.548	667.751	-71.603	-0.4124	0.9818
	300	-224.727	179.503	-12.493	-1.4470	1.0019

Table 18: Sample 9 $P_c \cdot F(B_{dc})$ Fourth-Degree Polynomial Coefficients.

on the characteristics shown in Figure 62a-c and Figure 63a-c, respectively. Fitting coefficients are given in Table 16, Table 17, and Table 18, respectively.

The characteristics fitting was done using an Excel Solver.

4.2.4.2 Rectangular Excitation with a DC Bias – STEP V.2.

If rectangular excitation occurs, the corresponding core loss is calculated using Equation (228). The measured power loss characteristics are shown in Figure 69a-c. During the core loss measurement, the duty cycle was swept from 0.1 to 0.9 at corresponding magnetic flux densities and switching frequencies, which were Bm = 100 mT at 100 kHz, Bm = 50 mT at 200 kHz, and Bm = 50 mT at 300 kHz, respectively. The σ coefficient was set to 1.0 because there is no DC bias and the η according to the amplitude of magnetic flux density swing as shown in Figure 62a-c and Figure 63a-c, respectively. The measurement was done at 100 °C.

The fitting coefficients of the function described by equation (228) are given in Table 19. They were estimated with the assumption that the $B_{dc} = 0$, and the fitting itself was done using an Excel Solver.

The example of captured waveforms in LTspice format for Sample 7 at 300 kHz and duty-cycles of $D = 0.5$ and $D = 0.1$ are shown in Figure 70a-b, respectively.

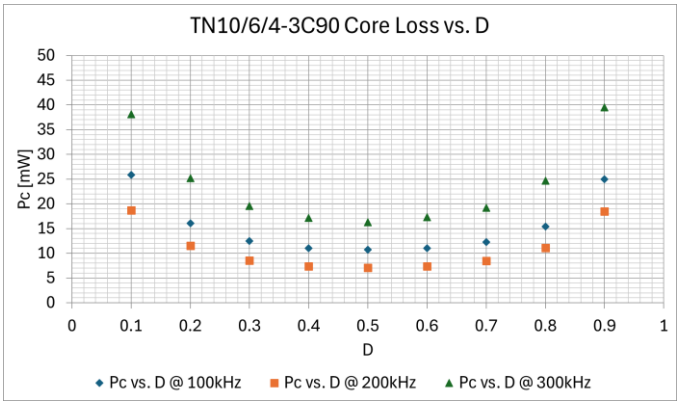

(**a**)

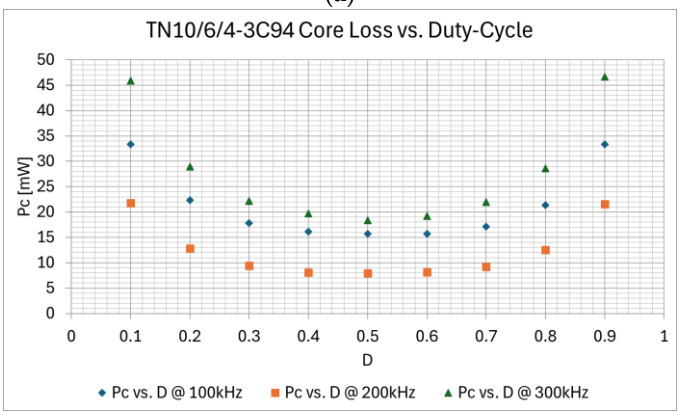

(**b**)

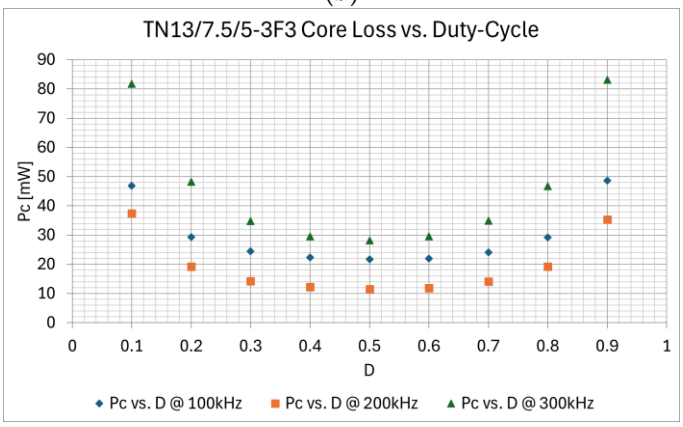

(**c**)

Figure 69: Core Loss under Rectangular Excitation; (**a**) Sample 7, Blue - @ 100 kHz, Bm=100 mT, Orange - @ 200 kHz, Bm=50 mT, Green - @ 300 kHz, Bm=50 mT; (**b**) Sample 8, Blue - @ 100 kHz, Bm=100 mT , Orange - @ 200 kHz, Bm=50 mT , Green - @ 300 kHz, Bm=50 mT; (**c**) Sample 9, Blue - @ 100 kHz, Bm=100 mT , Orange - @ 200 kHz, Bm=50 mT , Green - @ 300 kHz, Bm=50 mT.

4.2.4.3 Rectangular Excitation without a DC Bias – STEP V.3.

If there is no DC bias and a rectangular excitation occurs, the core loss is expressed by Equation (229). The same power loss characteristics as shown in Figure 69a-c apply. The fitting coefficients are given in Table 20.

Description	f_s [kHz]	γ	δ
Sample 1	100	0.8465	0.8512
	200	0.9226	0.9771
	300	0.8205	0.9794
Sample 2	100	0.7525	0.8510
	200	0.9847	0.9209
	300	0.8751	0.9401
Sample 3	100	0.7947	0.9028
	200	1.1165	1.0270
	300	1.0206	1.0089

Table 19: Complete iRESE Model Fitting Coefficients STEP V.2.

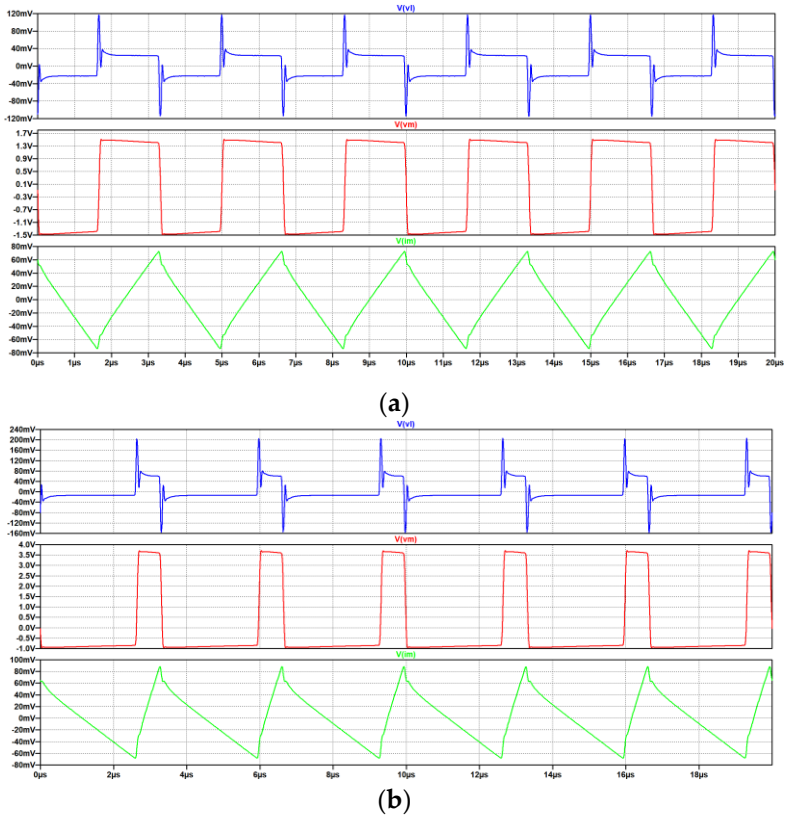

Figure 70: Sample 7 Measured Waveforms Captured for Square Excitation Signal @ 300 kHz and 100°C, $V(vl)$ (Blue) – Voltage at the Secondary Winding of Air Transformer, $V(vm)$ (Red) – Voltage at the Secondary Output of Tested Inductor, $V(im)$ (Green) – Magnetizing Current at Primary Side; (**a**) $D = 0.5$; (**b**) $D = 0.1$.

As might be expected, the fitting coefficients in Table 20 have almost the same values as the coefficients given in Table 19 at $B_{dc} = 0$. The slight differences come from the fitting of the $F(B_{dc})$ function, which is expected.

4.2.4.4 Rectangular Excitation with a DC Bias – STEP V.4.

If rectangular excitation comes together with the DC bias, the DC bias is added to the core loss with the assumption that the duty-ratio of the signals equals $D = 0.5$.

Description	f_s [kHz]	γ_1	δ_1
Sample 1	100	0.8465	0.8596
	200	0.9226	0.9271
	300	0.8205	0.9531
Sample 2	100	0.752	0.8535
	200	0.9847	0.9365
	300	0.8751	0.9401
Sample 3	100	0.7947	0.9028
	200	1.1165	1.0270
	300	1.0206	1.0109

Table 20: Rectangular Excitation Fitting Coefficients without a DC Bias – STEP V.3.

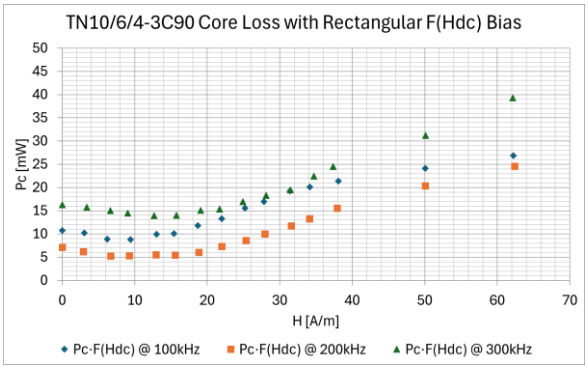

(**a**)

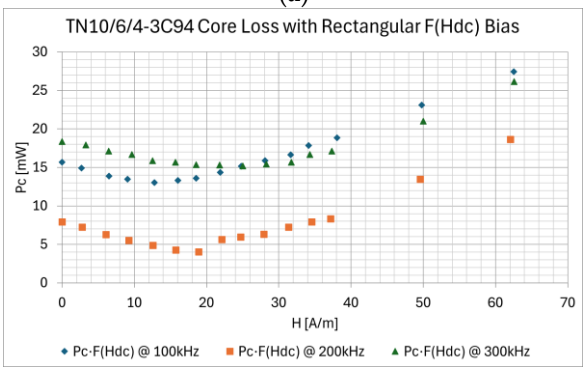

(**b**)

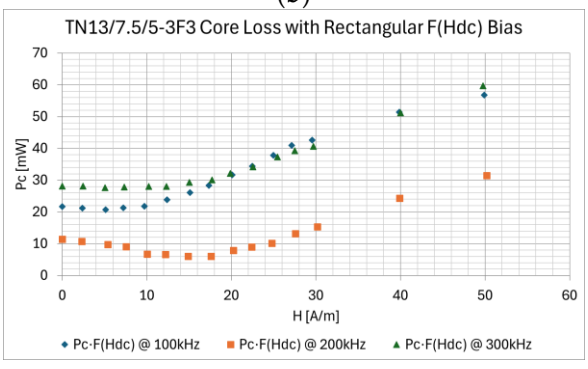

(**c**)

Figure 71: Core Loss under Rectangular Excitation with DC Bias; (**a**) Sample 7, Blue - @ 100 kHz, Bm=100 mT, Orange - @ 200 kHz, Bm=50 mT, Green - @ 300 kHz, Bm=50 mT; (**b**) Sample 8, Blue - @ 100 kHz, Bm=100 mT, Orange - @ 200 kHz, Bm=50 mT, Green - @ 300 kHz, Bm=50 mT; (**c**) Sample 9, Blue - @ 100 kHz, Bm=100 mT, Orange - @ 200 kHz, Bm=50 mT, Green - @ 300 kHz, Bm=50 mT.

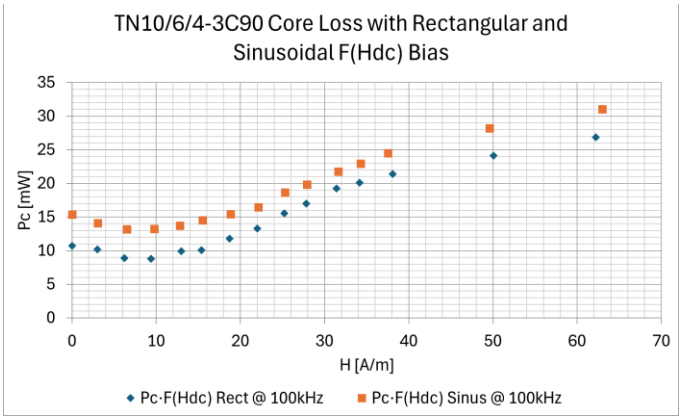

Figure 72: Sample 7 Core Loss under DC Bias @ 100 kHz and Bm=100 mT, Blue – Rectangular Excitation, Orange – Sinusoidal Excitation.

Since a complex relationship exists between B and H near the core saturation region, if rectangular excitation takes place, the DC magnetization function to be added is left as a function of H_{dc} than B_{dc} as in equations (227-228).

The power loss characteristics are shown in Figure 71a-c.

In these measurements, the σ coefficient of equation (223) was set according to the DC value of the magnetic field strength H, while the η coefficient was set according to the peak of the magnetic flux density swing B_m as shown in Figure 62a-c and Figure 63a-c, respectively.

Description	f_s [kHz]	ϵ_4	ϵ_3	ϵ_2	ϵ_1	ϵ_0
Sample 7	100	1.15E-06	-0.0001627	0.007439	-0.08603	1.0606
	200	1.15E-06	-0.0001679	0.008528	-0.11997	1.1115
	300	6.07E-08	-0.0000184	0.001820	-0.03518	1.0186

Table 21: Sample 7 $P_c \cdot F(H_{dc})$ Fourth-Degree Polynomial Coefficients.

Description	f_s [kHz]	ϵ_4	ϵ_3	ϵ_2	ϵ_1	ϵ_0
Sample 8	100	1.00E-6	-0.0001296	0.0056645	-0.08053	1.1350
	200	1.00E-6	-0.0001325	0.0064732	-0.10974	1.1437
	300	-1.72E-08	2.94E-08	0.0004832	-0.02038	1.0186

Table 22: Sample 8 $P_c \cdot F(H_{dc})$ Fourth-Degree Polynomial Coefficients.

Description	f_s [kHz]	ϵ_4	ϵ_3	ϵ_2	ϵ_1	ϵ_0
Sample 9	100	1.15E-06	-0.0001478	0.0062136	-0.05208	1.0729
	200	1.15E-06	-0.0001458	0.0074738	-0.12003	1.1337
	300	6.07E-08	-0.0000214	0.0018027	-0.02333	1.0186

Table 23: Sample 9 $P_c \cdot F(H_{dc})$ Fourth-Degree Polynomial Coefficients.

The peak of the magnetic flux swing (the variable component) was set as in previous cases, as follows: Bm = 100 mT at 100 kHz, Bm = 50 mT at 200 kHz and 300 kHz, respectively.

Moreover, there may be some differences in results regarding the functions described by equations (228) and (230). This is because, as shown in Figure 35, the losses excited by the rectangular signal at a duty ratio of 0.5 are lower than the losses excited by the sinusoidal signal at the same amplitude of the magnetic flux density. An example of this phenomenon is shown in Figure 72. The fitting coefficients are shown in Table 21, Table 22, and Table 23, respectively.

The fitting results are not shown in any of the Figures because they match well the measured characteristics and would not be clearly visible on the graphs.

The cancellation factor k introduced in Chapter 3 and shown in equation (223) in all measurements regarding sinusoidal and rectangular excitations was calculated according to equation (200). It was done by the introduction of 1° perturbation into i_m signal because this method: (i) introduces only a 1% discrepancy to the measurements described in paragraph 4.2.4.2 and paragraph 4.2.4.3, and (ii) solves the problem with perturbed v_L signal at high DC bias values, which would otherwise be introduced into calculations using equation (202).

4.3 Summary.

In this chapter, the test-bench laboratory measurements regarding the core complex permeability, as well as the iRESE core loss calculation technique, have been performed.

The results show that the imaginary part of the effective complex permeability characteristics bends upwards at low frequencies. This phenomenon is primarily due to the resistance of the inductor windings and, to a lesser extent, to the remaining parasitic RLC elements that the physical inductor is composed of and can be removed from the measurement, e.g., by curve fitting [189], as predicted.

The possible cracks in core material or small air gaps not visible to the naked eye, which, e.g., exist at the joints of core halves, significantly decrease the complex permeability, and thus the inductance of an inductor itself (Figure 45e, Figure 46c).

The above is even more self-evident if the gapped inductor is considered. The influence of the gap, and thus its resistance and the resistance of the fringing field, dominates, significantly decreasing the values of the real and imaginary parts of the complex permeability characteristics (Figure 45f).

The low frequency bending phenomenon has been investigated using an equivalent inductor model and an iterative approximation curve fitting technique.

As can be seen in the plots (Figure 48, Figure 49a-d, Figure 50, Figure 51a-d), the fitted values of the imaginary part of complex permeability flatten out at low frequencies, being stripped away from the influence of winding resistance, as predicted in [189]. The estimated and measured complex permeability characteristics align at higher frequencies, suggesting that they are closely fitted. The relative fitting error between $\mu''_{r_{measured}}$ and $\mu''_{r_{estimated}}$ does not exceed 2% for a loss tangent greater than 2 for both testing samples. This proves that the inductor model accurately matches reality, and the proposed method appears to be correct.

However, the method heavily depends on the inductor stray capacitor ESR (R_{Cs}) value (Figure 49a-d, Figure 51a-d). Unfortunately, there is insufficient data available to either prove or disprove this phenomenon and to estimate the ESR value across the entire frequency range accurately. The approach to limit its range has been achieved by investigating the inductor's stray capacitance value, its ESR, and the origin of its resonance.

The range of the inductor stray capacitor ESR has been defined. Its value does not provide an exact answer to what the loss tangent is, but it narrows down the possible choices.

The calculations and test-bench results indicate that the best-fitting results are obtained with peak loss tangent values at the inductor's self-resonance frequency. It suggests that the stray capacitance has only a negligible impact on the complex permeability values in the method presented herein.

A better understanding of the origin of inductor stray capacitance and its ESR requires investigation of core resonance phenomena and their influence on complex permeability values, which has also been done.

As shown in Figure 55a-b, the change in the real part of the complex permeability characteristics for the samples under test is preceded by an increase in permeability and then followed by a sharp drop. The drop happens way before Snoke's limit, which suggests that the magnetic resonance cannot be attributed to the dimensional resonance.

The characteristics indicate that the resonant frequency is almost independent of the number of winding turns, suggesting that the inductor's stray capacitance and its ESR in a given configuration are mostly due to the capacitance and ESR of the core.

The empirical results show that the winding capacitance wound on the non-magnetic dummy core shall be considered as an interwinding capacitance between wire windings themselves (equation (186)), however, taking into account a slight increase of the capacitance due to the presence of a core material with certain permittivity (equation (189)). Moreover, the results show that the method given in [4] gives consistent results with a relative discrepancy between C_p (Table 3) and C_{swc} (Table 4) to be 28.2% for Sample 2 and 4.4% for Sample 3. Even better results are obtained for the inductors with the dummy cores, with a discrepancy between C_{sdc} and $C_{sdc(meas)}$ to be 15.5% for Sample 2 and 4.3% for Sample 3 (Table 4).

The results show that, if the inductor stray capacitor ESR loss tangent is correctly defined (in case of Sample 2 and Sample 3 are set above 2), then it is possible to obtain a relative fitting error less than 2% along the entire frequency range (Figure 57a–d).

Regarding the iRESE method, the measurements and fittings have been performed in five distinct steps, as described in Chapter 3 of this work.

In STEP I, the complex permeability roll-off has been measured and split into two parts: the small-signal reversible permeability μ_{rev} used to adjust calculations during DC bias premagnetization and the large signal reversible permeability $\mu_{rev(a)}$ used in the calculations if the excitation signal reaches the B-H curve nonlinear region.

Because calculations of the original Steinmetz equation (OSE) involve temperature adjustments, knowledge of the change in the large-signal relative permeability roll-off with temperature is also required. Therefore, the reversible permeability values between 25˚C and 100˚C have been linearly interpolated to estimate the σ and η shown in equation (223).

In STEP II and STEP III, the original Steinmetz equation coefficients have been measured at $100°C$, placing the inductors under test in the heated oil bath.

As shown in Figure 64a-f, the data obtained from the manufacturers' datasheets and the test-bench measurements are consistent for 3C90 and 3F3 but differ significantly for 3C94. It is likely due to high material spreads during the manufacturing process, highlighting the importance of material verification before mass-producing any magnetic components.

In STEP IV, a unification between small- and large-signal core loss models has been performed.

As one might expect, the transition between the small- and large-signal core resistance models does not always occur smoothly as presented in Figure 66.

The reason for that is a complex case, which was revealed in this chapter and might be due to the (i) simplification of the Steinmetz model as a straight line; (ii) the actual segmentation of the core loss characteristics as shown by TDK [224]; (iii) the lack of the magnetizing current I_m and its nonlinear impact on measurements in the original Steinmetz core loss predictions; (iv) the influence of parasitic components, the real inductor model is made of; (v) simplification of the model by introduction of the average inductance L_{avg} to an easy transition between core resistance and core loss. The bending phenomenon will be further investigated in Chapter 6 of this dissertation.

In STEP V, measurements and fittings were performed for various scenarios of sinusoidal and rectangular excitation signals. This is a unique approach that provides engineers and scientists with all the required information at once regarding core loss, as well as the flexibility to choose the approach depending on the application they are working on.

Additionally, with extra effort, the method can also be applied to SPICE modelling and simulation, which will be presented in Chapter 5.

Chapter 5

5. FEM and Circuit Simulation.

This chapter, through modelling and simulation, verifies the assumptions and claims made in Chapters 3 and 4, respectively. Most of the chapter text is taken from the author's papers [187], [208], and referenced when appropriate.

5.1 FEM Modelling and Simulation of Inductor Stray Capacitance.

The estimation of the inductor's stray capacitance and self-inductance has also been performed using FEM simulation carried out in Ansys Q3D. The 3D models were created in SolidWorks and then transferred into Ansys Suite. In the simulation, the frequency range has been set from 100 Hz to 6 MHz, which is twice the self-resonant frequency of Samples 2 and Sample 3. The permeability, permittivity, and conductivity for both 3C90 and ABS cores have been assumed to be constant to exclude any possible core natural or dimensional effects. The values of the inductors' inductance and stray capacitance have been measured at 10kHz in the case of the ferrite core and at 5MHz in the case of the ABS core, which, as previously assumed, is the inductors' inductance plateau region. Additionally, a 1mm spacing between the windings and the core has been added for both samples to account for the stiffness of the copper wire and its bending curvature around the core (Figure 46a-b).

The results show (Table 24, Figure 73a-f) that the discrepancy between the theoretical prediction of the windings' stray capacitance if a dummy core is used ($C_{s_{cd}}$) and the FEM simulation ($C_{s_{FEM}}$) is almost negligible with a relative error of 0.9% for Sample 2 and 1.53% for Sample 3. Moreover, the simulation shows that the 3C90 magnetic core with a high permittivity of 10^5, with a high permeability of 2400 and relatively high conductivity of 4, has only a negligible impact on the windings' capacitance, increasing its value by only 17.3% for Sample 2 and by 17.6% for Sample 3. This suggests that the resonant frequency seen in the impedance characteristics of Sample 2 and Sample 3 (3C90 core based), and thus the overall equivalent stray

Sample No.	Core Material	MLT [mm]	d_i [mm]	N [-]	ε_r [-]	μ_r [-]	σ [S/m]	$L_{(FEM)}$ [nH]	$C_{s(FEM)}$ [pF]
Sample 2	ABS	34.5	0.75	10	4	1	$6.25x10^{-18}$	257.3	1.10
Sample 3	ABS	42.0	0.75	10	4	1	$6.25x10^{-18}$	290.7	1.31
Sample 2	3C90	34.5	0.75	10	10^5	2400	4.00	$228.9x10^3$	1.29
Sample 3	3C90	42.0	0.75	10	10^5	2400	4.00	$253.7x10^3$	1.54

Table 24: Ansys Q3D FEM Simulation Parameters and Results for Sample 2 and Sample 3.

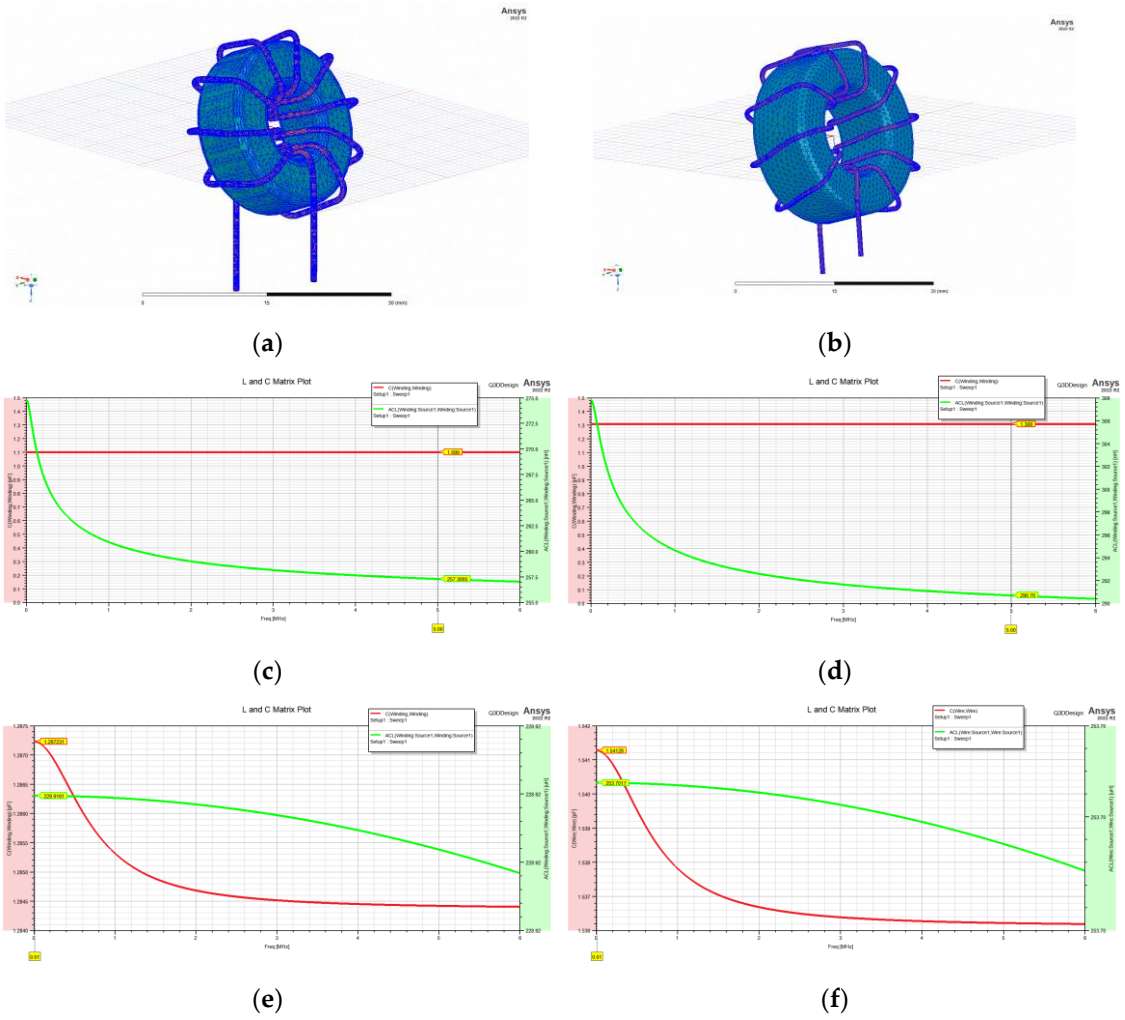

Figure 73: Ansys Q3D FEM RLC Parasitic Extraction of Sample 2 and Sample 3; (**a**) Sample 2 3D Model with Mesh Shown; (**b**) Sample 3 3D Model with Mesh Shown; (**c**) Sample 2 L-C Characteristics with Dummy Core, Red – Stray Capacitance, Green - Inductance; (**d**) Sample 3 L-C Characteristics with Dummy Core, Red – Stray Capacitance, Green – Inductance; (**e**) Sample 2 L-C Characteristics with 3C90 Core, Red – Stray Capacitance, Green – Inductance; (**f**) Sample 3 L-C Characteristics with 3C90 Core, Red – Stray Capacitance, Green – Inductance.

capacitance of the inductor, is mostly due to the dimensional resonance of the core and is associated with this phenomenon as stated in Chapters 3 and Chapter 4, respectively.

5.2 iRESE Core Loss Circuit Simulation.

The obvious choice for modelling and simulation of core loss in ferrites is to use finite element method simulators such as Ansys Maxwell or CST Studio. However, the two-winding oscilloscope-based core loss measurement described in Chapters 3 and 4 involves placing a 3D meshed model into a switching simulator and carrying out the simulation in the time domain. In Ansys Maxwell, this can be achieved through the internal transient solver or via co-simulation in Ansys Simplorer. Unfortunately, the time duration of such a simulation is very time-consuming, which makes this approach impractical, if not impossible.

The alternative to the above is the Simulation Programs with Integrated Circuit Emphasis (SPICE). This type of simulator, such as LTspice, is dedicated to circuit simulations and can, within a reasonable accuracy and time frame, complete the core loss measurements if the circuit model is well-defined.

Regarding the iRESE core loss methodology, the inductor test-bench schematic, including all parasitic components, is shown in Figure 74. The values of these components are listed in Table 25, Table 26, and Table 27, respectively, for a temperature of 100 °C and the selected switching frequency.

To complete the model, the capacitances of the voltage probes, the insertion impedance of the current probe, the impedance of the coupling capacitor, and the internal impedance of the signal amplifier are also introduced into the schematic.
The capacitance of the TESTEC TT-LX 312 voltage probe with 1X divider is 47pF, while the insertion impedance of the CP031A current probe at 300kHz is only 12mΩ. The coupling capacitor impedance is less than 100mΩ at 300kHz, and the internal resistance of the signal amplifier R_{Vin} is 0.8Ω. The coupling capacitor value is 185 μF. Based on impedance analyzer measurements, it was estimated that the air core transformer's self-resonant frequency is around 100 MHz (far beyond the Bode 100 measurement range), and thus its capacitance is estimated to be roughly 5 pF.

As can be seen in Figure 65a-c and Figure 66, the measured core resistance does not form a straight line but curves upward. This is because it is a function of two variables: the B_m and the I_m while the I_m does not exist in the original Steinmetz core

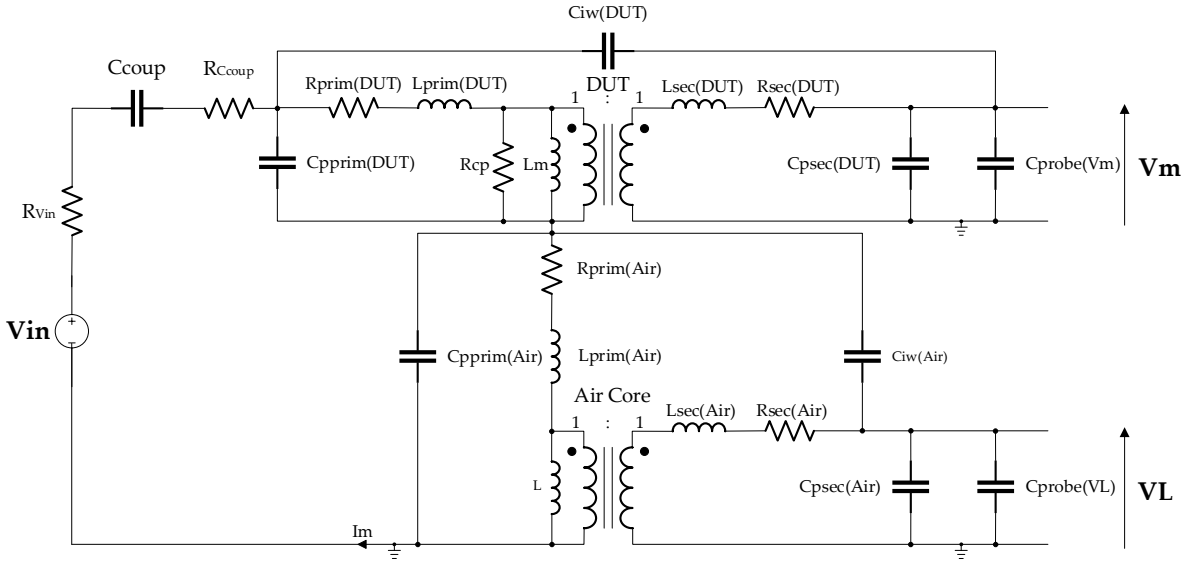

Figure 74: Inductor Test-Bench Schematic used in LTspice Simulation, Including Parasitic Components.

Description	L_{prim} [µH]	L_{sec} [µH]	L_{leak_prim} [nH]	L_{leak_sec} [nH]	R_{leak_prim} [mΩ]	R_{leak_sec} [mΩ]	C_{inter_wind} [pF]	R_{cp} [Ω]	f_{res} [MHz]
Sample 7	18.568	18.548	182.694	184.247	25.784	26.471	24.220	150.708	4.800
Sample 8	11.841	11.414	175.229	189.403	27.772	25.497	18.526	148.843	7.368
Sample 9	18.216	18.140	188.149	166.297	31.611	29.845	20.270	171.068	4.722
Air Trafo	0.487	0.489	314.881	304.308	42.556	39.001	25.388	-	100

Table 25: LTspice Simulation Parameters of Samples and Air Core Transformer @ 100˚C and 100kHz.

Description	L_{prim} [µH]	L_{sec} [µH]	L_{leak_prim} [nH]	L_{leak_sec} [nH]	R_{leak_prim} [mΩ]	R_{leak_sec} [mΩ]	C_{inter_wind} [pF]	R_{cp} [Ω]	f_{res} [MHz]
Sample 7	18.262	18.288	179.118	180.666	33.078	33.402	23.667	150.708	4.800
Sample 8	12.002	11.640	170.801	185.170	35.615	33.457	17.789	148.843	7.368
Sample 9	18.910	18.825	183.873	161.853	39.330	37.527	19.977	171.068	4.722
Air Trafo	0.479	0.482	303.155	293.115	55.424	59.593	25.370	-	100

Table 26: LTspice Simulation Parameters of Samples and Air Core Transformer @ 100˚C and 200kHz.

Description	L_{prim} [µH]	L_{sec} [µH]	L_{leak_prim} [nH]	L_{leak_sec} [nH]	R_{leak_prim} [mΩ]	R_{leak_sec} [mΩ]	C_{inter_wind} [pF]	R_{cp} [Ω]	f_{res} [MHz]
Sample 7	17.519	17.548	176.027	177.572	40.202	40.539	23.436	150.708	4.800
Sample 8	11.867	11.532	167.261	181.697	43.284	41.182	17.572	148.843	7.368
Sample 9	19.089	18.991	181.120	159.157	46.980	44.943	19.873	171.068	4.722
Air Trafo	0.474	0.477	295.656	285.495	70.129	75.881	25.262	-	100

Table 27: LTspice Simulation Parameters of Samples and Air Core Transformer @ 100˚C and 300kHz.

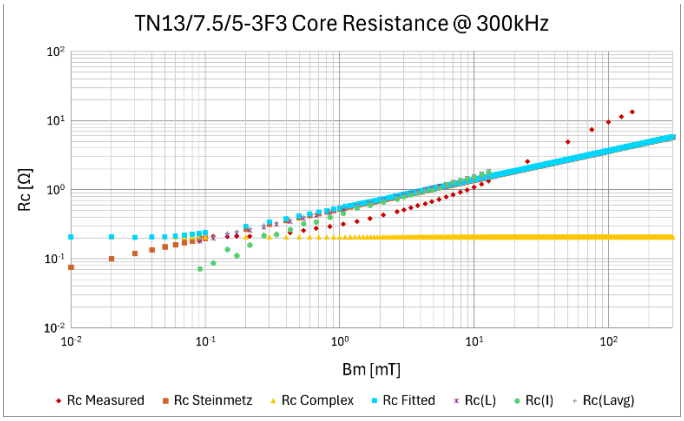

Figure 75: Sample 9 Core Resistance Measurement and Fitting @ 300 kHz, Red – Measured Core Resistance, Orange – Core Resistance based on Steinmetz Model, Yellow – Core Resistance based on Complex Permeability Model, Blue – Fitted Core Resistance Combining Small- and Large-Core Resistance Model, Violet – Core Resistance based on Measured Inductance Value, Green – Core Resistance based on Measured Current, Gray – Core Resistance based on Average Inductance Value.

loss prediction. Therefore, the I_m was measured during a Bode 100 impedance sweep and also during large-signal measurements and was then introduced to the model.

This results in the $R_c(I_m)$ characteristics, which are shown in Figure 65a-c and Figure 66, respectively. It can be seen that this characteristic follows the measured values of R_c at higher excitation signals more closely.

As shown in Figure 75, the R_c values measured at large excitation signals were added. They clearly follow the values measured by the Bode 100 impedance analyzer. This solves the question stated in [178] about the R_c bending nature, as the R_c is a nonlinear function of the current not predicted by Steinmetz. Therefore, equation (234) should not be a function of a fixed average value of inductance or current as assumed in the current model, but a non-linear function of it. Furthermore, this non-linear function is temperature dependent, so equation (232) can be rewritten as:

$$R_c = 2V_e k f^{\alpha} B_m^{\beta} \left(\widehat{I_m} \cdot F(T)\right)^{-2} \left(\sum_{n=0}^{5} \xi_n T^n\right) \tag{235}$$

where: $I_m \cdot F(T)$ – is a temperature-dependent nonlinear function of magnetizing current.

It appears that this could be a more accurate core loss model, which can be used in electrical circuit simulators, such as the LTspice program. However, this is obviously a very time-consuming process, requiring precise measurements of large amounts of data

and significant changes to the test bench configuration, and could be planned as future development work.

Therefore, the LTspice simulation presented in this chapter has been carried out using rectangular excitation with three distinctive duty-cycle ratios to highlight the method's accuracy at different working conditions, assuming the entire core loss calculation model is complete.

During the test-bench measurements, the possibility of random noise was reduced, and the waveforms were smoothed by averaging over 100 sweeps, with a 3-bit digital filter applied. Thus, the LTspice circuit schematic shown in Figure 74 has been stripped away from the influence of parasitic capacitances to replicate these conditions.

The major contributor to the core power loss is the core resistance. Its value was calculated based on the power loss measurement results and the RMS value of the inductor current at sinusoidal excitations with given switching frequency, temperature, and magnetic flux density value. This approach is in line with the entire core loss model presented so far, and equation (235) should introduce only a reasonably small discrepancy if the rectangular excitation occurs. This series core resistance has been subsequently transferred to parallel core resistance used in the LTspice simulation with the help of equation (236) [4]:

$$R_{cp} = \frac{R_c^2 + (\omega L)^2}{R_c} \tag{236}$$

where: R_{cp} – is the parallel core resistance, R_c – is the series core resistance.

The selected waveforms are compared in Figure 76. The major inductor parameters are taken from Table 25, Table 26, and Table 27, while the large-signal core resistance, the simulation parameters, and the simulation results are given in Table 28, Table 29, and Table 30, respectively, where: f_s – is the switching frequency, D – is the duty-cycle ratio, σ, η – are the coefficients introduced in equation (223), k_{meas} – is the measured coefficient introduced in equation (223), k_{sim} – is the simulated coefficient introduced in equation (223), R_c – is the series core resistance, $P_{c_{meas}}$ – is the measured core loss, $P_{c_{sim}}$ – is simulated core loss, δ – is the relative error between $P_{c_{meas}}$ and $P_{c_{sim}}$, respectively.

During the simulation, the σ and η coefficients are assumed to be the same as those presented in Chapter 4, while the k parameter is calculated using equation (200)

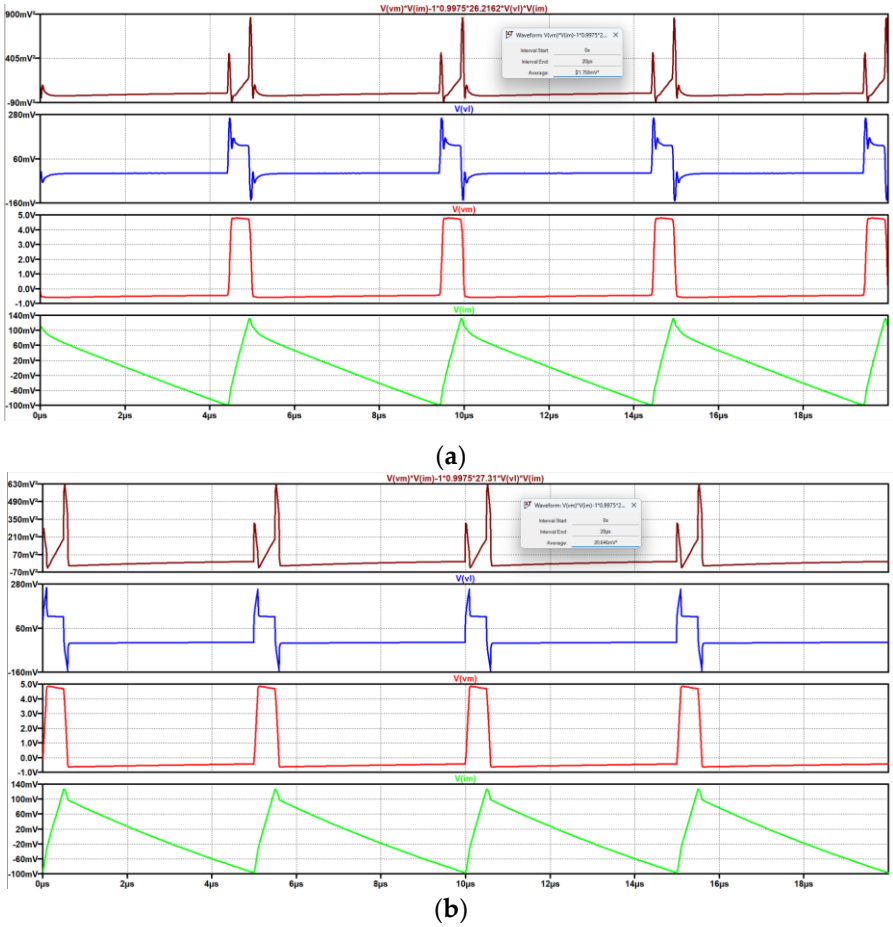

Figure 76: Sample 8 Waveforms @ 100°C, D=0.1 and 200kHz, Brown – Core Loss, Blue - V_L Voltage, Red – V_m Voltage, Green – I_m Magnetizing Current; (**a**) Measured Values; (**b**) LTspice Simulated Values.

by introducing a 1° perturbation into the magnetizing current waveform.

As the simulation shows, the presented approach regarding core resistance calculations and thus core loss introduces reasonable discrepancies between measurement and simulation when rectangular excitation occurs. The most significant discrepancies in core loss prediction are at extreme signal duty cycles, which is expected. Even then, the relative error does not exceed 14% if the magnitude of the excitation stays within the B-H curve linear region ($B_m = 50mT$) and does not exceed 31% above this region ($B_m = 100mT$).

It needs to be remembered that if the excitation signal is high enough, the permeability roll-off takes place, and the core resistance and thus core loss behave highly nonlinearly and, in the manner not easy to predict, which also should be taken into account.

Description	f_s [kHz]	D [−]	σ [−]	η [−]	$\frac{1}{k_{meas}}$ [−]	$\frac{1}{k_{sim}}$ [−]	R_c [Ω]	R_{cp} [Ω]	$P_{c_{meas}}$ [mW]	$P_{c_{sim}}$ [mW]	δ [%]
Sample 7	100	0.1	0.9363	1	39.71	28.79	1.99	70.34	25.85	32.61	26.15
		0.5			51.98	43.58			10.72	12.2	13.81
		0.9			39.94	28.79			24.96	32.61	30.64

Table 28: LTspice Simulation Parameters and Results for Sample 7 @ 100˚C and 100kHz.

Description	f_s [kHz]	D [−]	σ [−]	η [−]	$\frac{1}{k_{meas}}$ [−]	$\frac{1}{k_{sim}}$ [−]	R_c [Ω]	R_{cp} [Ω]	$P_{c_{meas}}$ [mW]	$P_{c_{sim}}$ [mW]	δ [%]
Sample 8	200	0.1	0.9975	1	26.21	27.31	2.07	111.64	21.76	20.64	5.14
		0.5			33.10	34.39			7.92	7.3	0.12
		0.9			26.74	27.31			21.53	20.64	4.13

Table 29: LTspice Simulation Parameters and Results for Sample 8 @ 100˚C and 200kHz.

Description	f_s [kHz]	D [−]	σ [−]	η [−]	$\frac{1}{k_{meas}}$ [−]	$\frac{1}{k_{sim}}$ [−]	R_c [Ω]	R_{cp} [Ω]	$P_{c_{meas}}$ [mW]	$P_{c_{sim}}$ [mW]	δ [%]
Sample 9	300	0.1	0.9914	1	22.61	35.04	7.92	171.44	81.85	71.96	12.08
		0.5			41.05	49.44			28.19	29.242	3.72
		0.9			22.74	35.05			83.12	71.88	13.52

Table 30: LTspice Simulation Parameters and Results for Sample 9 @ 100˚C and 300kHz.

Nevertheless, the core resistance estimation based on equation (235) is subject to future development and incorporation into the iRESE model.

5.3 Summary.

The FEM simulation revealed that the ferrite cores with high permittivity and high permeability have only a negligible impact on the windings' capacitance and the resonant frequency of the tested inductors (Sample 2 and Sample 3); thus, the overall equivalent stray capacitance of the inductor is mostly due to the dimensional resonance of the core.

On the other hand, FEM simulators such as Ansys Maxwell, Ansys Simplorer, and CST Studio are not suitable for time-domain simulations. The alternative to this can be a SPICE program such as LTspice. In LTspice, the inductor and its parasitic components can be easily modeled, while the simulation itself can be completed with reasonable accuracy and within a reasonable time frame.

The circuit simulation reveals that the primary factor influencing the accurate estimation and modelling of the inductor core loss is the core resistance. In the current approach, the core resistance is calculated directly from the large-signal measurements at sinusoidal excitations, which is in line with the iRESE model. This information should be included in the core resistance characteristic, as represented by equation (235), and then incorporated into the entire iRESE model.

Moreover, the results show that some compensation coefficients must also be included in the core loss model to compensate for different duty-cycle ratios and the magnitude of the excitation signal, particularly when its amplitude exceeds the linear region of the B-H curve.

This is a time-consuming process that requires precise measurements of a large amount of data and significant changes to the test bench configuration, which could be planned as future development work.

Chapter 6

6. Error Analysis.

Most of the chapter text is taken from the author's papers [208] and referenced when appropriate.

The error analysis identifies potential sources of measurement errors in the test bench system.

6.1 FEM Simulation Errors.

The main sources of the errors in the FEM analyses are [225-226]:

Modelling errors:

- Simplifications in the description of the geometry and material properties of the model.
- Insufficient knowledge of the model or incorrect assumptions.
- Failure to take into account all important factors influencing the behavior of the model.

Mesh errors:

- A mesh that is too coarse, non-uniform, or poorly optimized can lead to inaccurate results.
- Incorrect type of finite elements for the given problem.

Boundary condition errors:

- Incorrect representation of constraints.
- Omission of important boundary conditions or use of simplified solutions.

Numerical errors:

- Rounding errors and errors resulting from computational constraints.
- Numerical instability in the case of nonlinear analyses.

Other errors:

- Errors in the selection of material properties.
- Errors resulting from the incorrect interpretation of results.

Except for computational errors, the most severe error in FEM analysis is the lack of in-depth knowledge of the materials the model is made of and their properties, as mentioned in Chapters 3 and 4, respectively. It is especially important if the modelled component is relatively small, non-uniform, and constructed with many material layers. This often renders the FEM analysis inaccurate, with results that are difficult to interpret.

6.2 SPICE Circuit Simulation Errors.

The main sources of the errors in SPICE circuit simulations are:

Circuit topology errors:

- Floating nodes. It happens when a node has no path to ground or a DC voltage source.
- Loops involving voltage sources, inductors, or resistors. This occurs when a loop generates an undefined current, resulting in simulation failure.
- No ground reference – floating error.
- Components used with an incorrect SPICE model.
- Incorrect values of component parameters.
- Neglected tolerances of component parameters.

Numerical instability errors:

- Non-convergence. It occurs when the simulator fails to find a stable operating point for the circuit.
- Incorrect setting of power sources, input signals, and load.
- Incorrect selection of simulation type.
- Incorrect settings of simulation parameters, such as simulation duration or frequency range.
- A too large time step, which allows for omitting fast signal changes.
- Too few sampling points, which leads to inaccurate results in the frequency domain.
- Errors coming from approximation in simulation algorithms.

Mathematical model errors:

- Simplifications in the electronic system model by omitting parasitic elements.
- Incorrect assumptions regarding system operation, e.g., ignoring the temperature influence on components.

- Insufficient mathematical model that does not fully reflect the behavior of the simulated system.

Errors in results interpretation:

- Incorrect reading of graphs and simulation outputs.
- Failure to critically review simulation results regarding the expected behavior of the simulated system.

6.3 Oscilloscope Measurement Errors.

The LeCroy HDO6104-MS 1GHz oscilloscope features a 12-bit vertical resolution, providing 4096 Q levels (0.195 mV), which is significantly better than the 8-bit oscilloscopes, having only 256 Q levels (3.125 mV). When only the least significant bit of the oscilloscope ADC converter is considered, the measurement error caused by the amplitude discrepancy is 0.012%, which could be easily neglected.

As stated in Chapter 4 and as can be seen in Figure 60, instead of using a current sensing resistor that might introduce a significant phase discrepancy between the primary magnetizing current i_m and the secondary side magnetizing voltage V_m of the inductor under test, the LeCroy CP031A current probe has been used. The current probe features a 1mA/Div sensitivity, an amplitude accuracy of ±1% of reading, a measurement range of up to 30 A, and a 100 MHz bandwidth, which outperforms any current sensing resistor measurement method. Moreover, to limit the possible phase discrepancy between the primary magnetizing current i_m and the inductor secondary side magnetizing voltage V_m the current probe has been deskewed with the voltage probe using the LeCroy DCS015 deskewing fixture. The CP031A has an insertion impedance of only 0.012 Ω at 300 kHz, which again outperforms any resistor-based current sensing approach.

The voltage probes themselves have been deskewed amplitude-wise and phase discrepancy-wise by measuring the same voltage of 2V peak-to-peak value with 50ns rising/falling slopes and 50% duty-cycle ratio at 500kHz switching frequency using both: (i) Rigol DG992 SiFi II signal generator, and (ii) as described in Chapter 3 by measuring the same voltage and then calculating an integral $\frac{1}{T}\int_0^T v_m' i_m dt$ for each of them. The results were adjusted using deskew functions in the oscilloscope until the calculated

integrals showed the same value. The TESTEC TT-LX 312 voltage probes feature a 10MHz bandwidth with a 1:1 attenuation ratio and DC accuracy of 2%. This should be sufficient for a maximum switching signal of 300 kHz.

During the switching at different duty-cycle ratios, the signal spectrum captured by the oscilloscope also changes. The measurement indicated that it might contribute to a power loss discrepancy of up to 2% at both duty cycle limits of 0.1 and 0.9, respectively.

Moreover, to reduce the possibility of random noise and to smooth the waveforms, the measurements were averaged over 100 sweeps using a 3-bit digital filter.

6.4 Bm Estimation Errors.

Except for the oscilloscope measurement errors, what contributes the most to the error occurrence is a correct estimation of the magnitude of the magnetic flux density B_m. The magnitude of the magnetic flux density is calculated by integrating the voltage across the inductor's secondary side. Integration involves precise timing of the integral boundary, which, in this case, is the integral reset triggering time. Apart from that, a miscalculation of the B_m by 0.5% provides up to a 1.5% calculation error. Moreover, the DC bias premagnetization significantly destroys the original shape of the excitation waveform if the bias is high enough. Therefore, it is challenging to determine the peak values of the magnetic flux density. During the entire measuring process, it was assumed that the AC peak values of the magnetic flux density were equal, and the integral reset trigger time was set accordingly.

6.5 Temperature Estimation Errors.

The temperature control has been implemented using an Arduino platform, along with a set of relays, as shown in Figure 59c. The Arduino utilized a DS18B20 sensor to monitor and adjust temperature variations, and it was synchronized with a K-type thermocouple used by the Rigol DM3068 as a reference. This setup allows for a constant temperature within $\pm 2°C$ range, which is a typical value for this type of thermocouple. The temperature uncertainty can contribute to an error of up to 6.5% in the estimation of the core power loss.

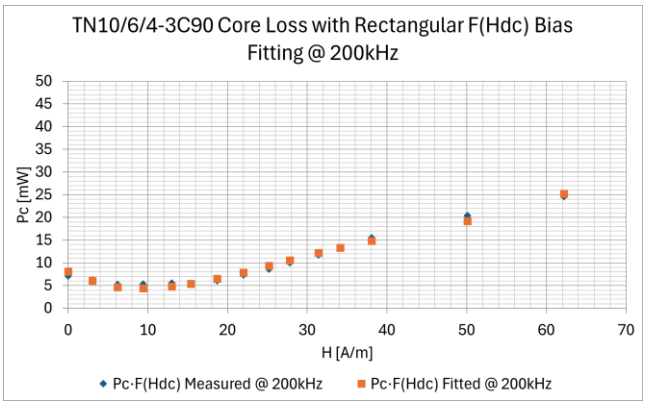

Figure 77: Core Loss under Rectangular Excitation with a DC Bias Fitting Results for Sample 7, Blue – Measured Values, Orange – Fitted Values.

6.6 Fitting Errors.

The fitting of the core loss characteristics has been done using Microsoft Excel Solver and OriginLab software.

Most of the fitted equations are higher-degree polynomials, which means they are non-linear and smooth. Therefore, the Generalized Reduced Gradient (GRG) algorithm – one of the most robust nonlinear programming methods was used as the Solver solution. The Solver was set to minimize the least squares residuals, with a convergence tolerance of 0.0001, and without multistart and defined variable boundaries.

It has been found that the Solver provides a quick and precise solution if there are no more than three variables to be fitted. Otherwise, the fitting must be done partially by choosing no more than three variables at a time. Even then, the total number of variables should not exceed four. The example of one of the fitted characteristics is given in Figure 77.

If more than four variables are to be fitted, OriginLab was used, along with the fitting method based on the Levenberg-Marquardt algorithm, which provides high accuracy. The fitting setup was performed with 95% confidence bands and 95% prediction bands. The successful convergence justified the fitting results, the residual sum of squares value, the reduced χ^2 value, R^2 value and adjusted R^2 value.

It is challenging to quantify the extent to which curve fitting contributes to the overall discrepancy in core loss results. However, it is assumed that it is no more than 5%.

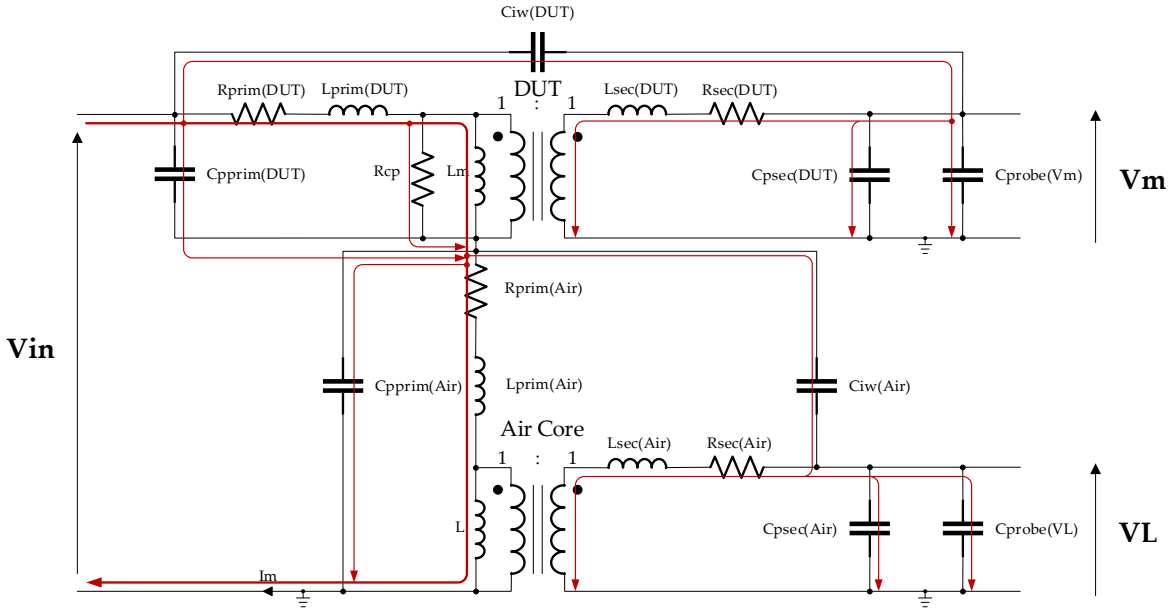

Figure 78: Simplified Test-Bench Measurement System with Parasitic Components Included.

6.7 Error Caused by Parasitic Components.

The main contributor to the error caused by the parasitic components is the influence of the parasitic capacitances of the voltage probes, as well as the capacitance of intra- and inter-winding capacitances in the transformer under test and the air-core transformer, as shown in [210-211]. The current flow through parasitic capacitances is shown in Figure 78. The circuit is slightly more complicated than in [210-211]; however, having the same assumptions, the equations can be simplified, and the error caused by the current flow through the inductor interwinding capacitance and the capacitance of the voltage probe measuring v_m (C_{v_m}) is given by:

$$\delta_{P_c}(C_{v_m}) \approx \left(C_{psec(DUT)} + C_{probe(V_m)}\right) \cdot \left(\frac{R_{\sec(DUT)} \cdot R_{cp}}{L_m} + \omega^2 L_{\sec(DUT)}\right) \tag{237}$$

The error associated with the tested inductor interwinding capacitance can be written as:

$$\delta_{P_c}(C_{iw_{DUT}}) \approx \frac{-R_{cp} C_{iw(DUT)}}{L_m^2} \cdot \left(R_{prim(DUT)} \cdot L_{\sec(DUT)} + R_{\sec(DUT)} \cdot L_{prim(DUT)}\right) \tag{238}$$

Similar relationships apply to the air core reference transformer, where the error caused by the intra-winding capacitance $C_{psec(Air)}$ and the capacitance of the voltage probe, measuring the voltage v_L ($C_{probe(VL)}$) is expressed as:

$$\delta_{P_c}(C_{v_L}) \approx \frac{(C_{psec(Air)} + C_{probe(VL)})}{\sigma\eta k} \cdot \left(\frac{R_{prim(Air)} \cdot R_{cp}}{L_m} + \omega^2 L_{prim(Air)}\right) \quad (239)$$

The error associated with reference transformer interwinding capacitance is given by:

$$\delta_{P_c}(C_{iw_{Air}}) \approx \frac{R_{cp} C_{iw(Air)}}{\sigma\eta k L_m^2} \cdot \left(R_{\mathrm{sec}\,(Air)} \cdot L_{prim(Air)} + R_{prim(Air)} \cdot L_{\mathrm{sec}\,(Air)}\right) \quad (240)$$

The values of each parasitic component at 100 °C and the given switching frequency are shown in Table 25, Table 26, and Table 27, respectively.

The values of each error for Sample 9 at 300 kHz are as follows:

$\delta_{P_c}(C_{v_m})$ =0.01%; $\delta_{P_c}(C_{iw_{DUT}}) = -1.46 \cdot 10^{-5}$%; $\delta_{P_c}(C_{v_m}) = 0.75$%; $\delta_{P_c}(C_{iw_{Air}}) =$ 0.005%.

6.8 Summary.

This chapter highlights possible measurement and simulation errors and explains their origins.

The identification of these errors is crucial for a better understanding of possible measurement discrepancies and their magnitude in relation to the obtained results. Moreover, the error analysis indicates whether the assumed measurement approach and the test-bench setup are suitable for the expected measurement accuracy and are reasonable.

Chapter 7

7. Conclusion and Future Work.

7.1 Main Contributions.

This dissertation presents improved measurement and calculation techniques for the complex permeability of ferrites, one of the fundamental parameters that define inductor behavior in the frequency domain. This advancement is significant, as it supports the development of more accurate inductor loss models and universal simulation tools (e.g., SPICE models) capable of capturing all AC loss mechanisms, including core and winding losses. Such comprehensive models are currently unavailable, particularly in the context of high-frequency power electronics applications [187].

The proposed method is based on the inductor equivalent model, enabling the direct estimation of complex permeability values from impedance measurements. Importantly, the method remains valid regardless of the inductor's size, geometry, winding structure, or operating frequency range. The results demonstrate high accuracy not only in the low-frequency complex permeability values, e.g., the values of the imaginary part stripped of the influence of 'windings' resistance, but also in the permeability peak values existing in the vicinity of the resonance. This information would be otherwise hidden or diminished by parasite components, of which the real inductor is made.

The method is also simple and intuitive to process, assuming the frequency dependence of most inductor model components, and thus overcomes some of the limitations and complexity of other methods [187].

Furthermore, this work introduces an improved core loss measurement technique—termed the improved Rectangular Extension of the Steinmetz Equation (iRESE). The iRESE model extends the traditional RESE approach into both the small-signal and near-saturation large-signal domains [208]. It unifies the Steinmetz-based core loss model with the small-signal complex permeability model to comprehensively

complete the entire core loss characteristics regardless of the magnitude of the excitation signals.

This unification of both models would be beneficial: (i) because it more accurately reflects the actual behavior of inductors, and (ii) because it enables the use of a single model across both small- and large-signal domains – an integration which was not possible before.

The iRESE model also considers rectangular excitation of signals and the DC bias effects commonly encountered in switch-mode power supplies (SMPS), as well as the magnetic permeability roll-off near core saturation. Its modular structure allows each component of the model to be used independently, depending on the application. This flexibility provides engineers and researchers with a complete and adaptable framework for core loss analysis.

Additionally, the model accounts for the nonlinearity of the inductor's magnetizing current and its impact on core losses in the small-signal domain. With further refinement, the method can be adapted for use in SPICE modelling and simulation—an essential requirement for industry, where rapid and accurate core loss estimation of magnetic components is critical.

The proposed model has five degrees of freedom regarding the core loss in the ferrite materials and includes dependency on: (i) the magnitude of the magnetic flux density, (ii) frequency of the excitation, (iii) temperature variations, (iv) the shape of the excitation signal, and (v) DC bias.

Although developed with SMPS in mind, the method is equally applicable to other systems affected by DC bias and rectangular excitations, such as electric vehicle inverters and wireless power transfer systems [208].

7.2 Limitations.

The limitation of the complex permeability measurement method [187] is that it was tested with single-layer inductors only and might not be applicable to inductors with multilayer, multiturn windings. Furthermore, due to the complex and implicit relationship between the core and the windings, the stray capacitance ESR value is not fully defined. This leads to an incomplete small-signal equivalent inductor model, which might not give as accurate results as expected if applied to a SPICE simulation.

The primary drawback of the iRESE [208] core loss calculation methodology is its time-consuming nature, particularly during the measurement and computation phases. Each measurement requires an accurate calculation of magnetic flux density, as detailed in Chapter 6, and any error may necessitate repeated testing. Moreover, the process of converting oscilloscope data into a format compatible with LTSpice simulations is labor-intensive, ensuring data fidelity but contributing to the overall complexity. The model also involves numerous coefficients, which can make the implementation appear daunting. However, this complexity is a necessary trade-off to achieve a high-fidelity fit between the measured characteristics and their mathematical representation.

7.3 Future Work.

As mentioned in [187], the inductor self-resonant frequency depends on the windings and core apparent capacitance. However, the relationship between the core and the windings is complex and explicit; therefore, there is limited evidence as to what the correct relationship is between their capacitances and the capacitances' ESRs. This should be further investigated regarding an improvement of the proposed small-signal inductor model.

Furthermore, the proposed technique should be additionally tested when applied to multi-winding, multilayer inductors with substantial inter-winding capacitance. Simultaneously, the FEM simulations should be enhanced by incorporating more accurate material models for both the core and its insulating coating. This improvement would enable a more precise representation of the interaction between the core and windings, leading to more accurate modelling of the inductor's stray capacitance and its associated ESR.

Despite producing strong results in core loss prediction, there remains potential for further improvement in the iRESE methodology [208]. For example, Figure 65a–c and Figure 66 demonstrate that the measured core resistance does not follow a double-logarithmic straight-line trend, but rather curves upward. This is due to the fact that core resistance is a function of two variables: magnetic flux density (B_m) and the magnetizing current (I_m), the latter of which is absent from the original Steinmetz model. To address this, I_m was measured during both Bode 100 impedance sweeps and large-signal experiments, then incorporated into the model. This resulted in an $R_c(I_\mathrm{m})$ relationship,

as illustrated in Figure 65a–c and Figure 66, which more closely aligns with the observed core resistance behavior at higher excitation levels.

As shown in Figure 75, core resistance values measured under large-signal conditions were added and correlate well with those obtained via the Bode 100 analyzer. This resolves the previously open question from [178] regarding the upward-bending nature of R_c, confirming that it is a nonlinear function of current—a behavior not captured by Steinmetz. Consequently, equation (234) should no longer rely on a fixed average value of inductance or current. Instead, it should be reformulated as a nonlinear function. Furthermore, because this function is also temperature-dependent, equation (232) is rewritten as equation (235), as discussed in Chapter 5.

The resulting model shows promise as a more accurate representation of core losses for integration into electrical circuit simulators such as LTspice, as demonstrated in Chapter 5. However, its implementation demands precise measurements of extensive datasets and significant test bench modifications—efforts that are well-suited to future development work [208].

Bibliography

1. Wang, Y., *Modelling and characterisation of losses in NanoCrystalline cores*, PhD Dissertation, University of Manchester, 2015. [CrossRef]
2. Wojda, R. P., *Winding resistance and winding power loss of high-frequency power inductors*, PhD Dissertation, Wright State University, 2012. [CrossRef]
3. Reatti, A.; Kazimierczuk, M. K., *Comparison of various methods for calculating the ac resistance of inductors*, IEEE Transactions on Magnetics, vol. 38, issue 3, May 2002. [CrossRef]
4. Kazimierczuk, M.K., *High frequency magnetic components*, 2nd Edition, Wiley 2014. [CrossRef]
5. Dowell, P., *Effects of eddy currents in transformer windings*, Proc. Inst. Elect. Eng., vol. 113, pp. 1387-1394, 1966. [CrossRef]
6. Tourkhani, F., *Accurate analytical model of winding losses in round litz wire windings*, IEEE Transaction on Magnetics, vol. 37, no 1, pp. 538-543, 2001. [CrossRef]
7. Ferreira, J.A., *Appropriate modelling of conductive losses in the design of magnetic components*, 21st Annual IEEE Conference on Power Electronics Specialists, pp. 780-785, 1990. [CrossRef]
8. Nan, X.; Sullivan, C.R., *An improved calculation of proximity-effect loss in high-frequency windings of round conductors*, IEEE Power Electronics Specialists Conference, pp. 853-860, June 2003. [CrossRef]
9. Chen, B.; Li, L., *Semi-empirical model for precise analysis of copper losses in high-frequency transformers*, IEEE Access, vol. 6, pp. 3655-3667, January 2018. [CrossRef]
10. ECPE, *ECPE roadmap programme 'power electronics 2025'*. Available online, accessed on 12 July 2025. [CrossRef]
11. Kolar, J.W., *Vision – power electronics 2025*. Available online, accessed on 12 July 2025. [CrossRef]
12. Wikipedia, *War of the currents*. Available online, accessed on 12 July 2025. [CrossRef]
13. Maroti, P.K.; Padmanaban, S.; Bhaskar, M.S.; Ramachandaramurthy, V.K.; Blaabjerg, F., *The state-of-the-art of power electronics converters configurations in electric vehicle*

technologies, ELSEVIER Power Electronic Devices and Components, vol. 1, 2022. [CrossRef]

14. Alatai, S; Salem, M.; Ishak, D.; Das, H.S.; Nazari, M.A.; Bughneda, A.; Kamarol, M., *A review on state-of-the-art power converters: bidirectional, resonant, multilevel converters and their derivatives*, Applied Sciences, vol. 11, issue 21, MDPI, 29 October 2021. [CrossRef]
15. Rodriguez, J.; Cortes, P., *Predictive control of power converters and electrical drives*, John Wiley & Sons, Ltd., 2012. [CrossRef]
16. Taeed, F., *Design and implementation of digital current mode controller for DC-DC converters*, PhD Dissertation, Maersk Mc-Kinney Moller Institute, 2014. Available online, accessed on 12 July 2025. [CrossRef]
17. Majumard, G., *Recent technologies and trends of power devices*, International Workshop on Physics of Semiconductor Devices, Mumbai, India, 2007. [CrossRef]
18. Avnet Abacus, *Understanding switch-mode power supplies (SMPS)*. Available online, accessed on 12 July 2025. [CrossRef]
19. Mohan, N.; Undeland T.M.; Robbins, W.P., *Power electronics converters, applications and design*, 2nd Edition, John Wiley & Sons Inc., 1995.
20. Erickson, R.W.; Maksimovic, D., *Fundamentals of power electronics*, 3rd Edition, Springer Nature Switzerland, 2020. [CrossRef]
21. Goldman, A., *Magnetic components for power electronics*, Springer Science + Business Media, New York, 2002. [CrossRef]
22. Rylko, M.S.; Lyons, B.J.; Hartnett, K.J.; Hayes, J.G.; Egan, M.G., *Magnetic material comparisons for high-current gapped and gapless foil inductors in high frequency DC-DC converters*, 13th International Power Electronics and Motion Control Conference, Poznan, Poland, 2008. [CrossRef]
23. Lyons, B.J.; Hayes, J.G.; Egan, M.G., *Magnetic material comparisons for high-current inductors in low-medium frequency DC-DC converters*, 22nd Annual IEEE Applied Power Electronics Conference and Exposition (APEC), Anaheim, CA, USA, 2007. [CrossRef]
24. Rylko, M.S.; Harnett, K.J.; Hayes, J.G.; Egan, M.G., *Magnetic material selection for high power high frequency inductors in DC-DC converters*, 24th Annual IEEE Applied Power Electronics Conference and Exposition, Washington, DC, USA, 2009. [CrossRef]

25. Takahashi, N.; Morishita, M.; Miyagi, D.; Nakano, M., *Comparison of magnetic properties of magnetic materials at high temperature,* IEEE Transactions on Magnetics, vol. 47, issue 10, October 2011. [CrossRef]
26. Yong L., *Filter design of high power density converter with weight, size and thermal considerations*, PhD Dissertation, Nanyang Technological University, 2018. [CrossRef]
27. Talaat, A.; Suraj, M.V.; Byerly, K.; Wang, A.; Wang, Y.; Lee, J.K.; Ohodnicki Jr., P.R., *Review on soft magnetic metal and inorganic oxide nanocomposites for power applications*, ELSEVIER Journal of Alloys and Compounds, vol. 870, 25 July 2021. [CrossRef]
28. Fiorillo, F.; Bertotti, G.; Appino, C.; Pasquale, M., *Soft magnetic materials*, Wiley Online Library. Available online, accessed on 12 July 2025. [CrossRef]
29. Ferroxcube, *Soft ferrites and accessories data handbook 2013*. Available online, accessed on 12 July 2025. [CrossRef]
30. Viarogue, P., *Magnetic components of power converters*. Available online, accessed on 12 July 2025. [CrossRef]
31. Arnold Magnetic Technologies, *Soft magnetic applications guide*. Available online, accessed on 12 July 2025. [CrossRef]
32. ON Semiconductor, *Magnetics in Switched-Mode Power Supplies*. Available online, accessed on 12 July 2025. [CrossRef]
33. Tumanski, S., *Handbook of magnetic measurements*, CRC Press, 2011. [CrossRef]
34. Krings, A.; Boglietti, A.; Cavagnino, A.; Sprague, S., *Soft magnetic material status and trends in electric machines*, IEEE Transactions on Industrial Electronics, vol. 64, issue 3, March 2017. [CrossRef]
35. He, J.; Yuan, H.; Nie, M.; Guo, H.; Yu, H.; Liu, Z.; Sun, R., *Soft magnetic materials for power inductors: state of art and future development*, ELSEVIER Materials Today Electronics, vol. 6, December 2023. [CrossRef]
36. Zurek, S., *Magnetic materials*, Encyclopedia Magnetica. Available online, accessed on 12 July 2025. [CrossRef]
37. Rodriguez-Sotelo, D.; Rodriguez-Licea, M.A.; Soriano-Sanchez, A.G.; Espinosa-Calderon, A.; Perez-Pinal, F.J., *Advanced ferromagnetic materials in power electronic converters: a state of the art*, IEEE Access, vol. 8, March 2020. [CrossRef]

38. Garcha, P.; Schaffer, V.; Haroun, B.; Ramaswamy, S.; Wieser, J.; Lang, J.; Chandrakasan, A., *A 770 kS/s Duty-cycled integrated-fluxgate magnetometer for contactless current sensing*, IEEE International Solid-State Circuits Conference (ISSCC), San Francisco, CA, USA, March 2021. [CrossRef]
39. Qiu, G.; Ran, L.; Feng, H.; Jiang, H.; Long, T.; Forsyth, A.j.; Shao, W.; Hou X., *A fluxgate-based current sensor for DC bias elimination in a dual active bridge converter*, IEEE Transactions on Power Electronics, vol. 37, issue 3, March 2022. [CrossRef]
40. Tzelepis, D.; Psaras, V.; Tsotsopoulou, E.; Mirsaeidi, S.; Dysko, A.; Hong, Q.; Dong, X.; Blair, S.M.; Nikolaidis, V.C.; Papaspiliotopoulos, V.; Fusiek, G.; Burt, G.M.; Niewczas, P.; Booth, C.D., *Voltage and current measuring technologies for high voltage direct current supergrids: a technology review identifying the options for protection, fault location and automation applications*, IEEE Access, vol. 8, November 2020. [CrossRef]
41. Dimitrovski, A.; Li, Z.; Ozpineci, B., *Applications of saturable-core reactors (SCR) in power systems*, IEEE PES T&D Conference and Exposition, Chicago, IL, USA, July 2014. [CrossRef]
42. Qiu Y., *Coupled inductors for power supplies: advanteges and compromises*, EE Times. Available online, accessed on 12 July 2025. [CrossRef]
43. Detka, K.; Gorecki, K.; Grzejszczak, P.; Barlik, R., *Modeling and measurements of properties of coupled inductors*, Energies, vol. 14, issue 14, 2021. [CrossRef]
44. Xu, H.; Wang, C.; Xia, D.; Liu, Y., *Design of magnetic coupler for wireless power transfer*, Energies, vol. 12, issue 15, 2019. [CrossRef]
45. Mou, X.; Gladwin, D.T.; Zhao, R.; Sun, H., *Survey on magnetic resonant coupling wireless power transfer technology for electric vehicle charging*, IET Power Electronics, vol. 12, issue 12, October 2019. [CrossRef]
46. Li, Z.; Han, W.; Xin, Z.; Liu, Q.; Chen J.; Loh, P.C., *A review of magnetic core materials, core loss modelling and measurements in high-power high-frequency transformers*, CPSS Transactions on Power Electronics and Applications, vol. 7, issue 4, December 2022. [CrossRef]
47. Valchev, V.C., *Advantages and applications of nanocrystalline magnetic materials*, Journal – Electrotechnica & Electronica (E+E), vol. 57, issue 7-8, 2016. Available online, accessed on 12 July 2025. [CrossRef]

48. Chikazumi, S.; *Physics of ferromagnetism*, 2nd Edition, Oxford University Press, 2005. [CrossRef]
49. Buschow, K.H.J.; De Boer, F.R., *Physics of magnetism and magnetic materials*, Kluwer Academic Publishers, 2004. [CrossRef]
50. Meng, H., *Soft magnetic materials: current availability on the market – part 3*, SM Magnetics. Available online, accessed on 12 July 2025. [CrossRef]
51. Sai Ram, B.; Paul, A.K.; Kulkarni, S.V., *Soft magnetic materials and their applications in transformers*, ELSEVIER Journal of Magnetism and Magnetic Materials, vol. 537, November 2021. [CrossRef]
52. Cullity, B.D.; Graham, C.D., *Introduction to magnetic materials*, 2nd Edition, Johan Wiley & Sons, 2009. [CrossRef]
53. Vacuumschmelze, *Soft magnetic cobalt-iron alloys*. Available online, accessed on 12 July 2025. [CrossRef]
54. Tsepelev, V.S.; Starodubtsev, Y.N., *Nanocrytalline soft magnetic iron-based materials from liquid state to ready product*, Nanomaterials, vol.11, issue 1, 2021. [CrossRef]
55. Beraki, M.; Trovao, J.P.; Perdigao, M., *Comprehensive comparison and selection of magnetic materials for powertrain DC-DC converters*, IET Electrical Systems and Transportation, vol. 10, issue 2, June 2020. [CrossRef]
56. Takahashi, M.; Nishimaki, S.; Wakiyama, T., *Magnetocrystalline anisotropy and magnetostriction of Fe-Si-Al (sendust) single crystals*, ELSEVIER Journal of Magnetism and Magnetic Materials, vol. 66, issue 2, March 1987. [CrossRef]
57. Di Capua, G.; Femia, N.; Styka, K., *Switching power supplies with ferrite inductors in sustainable saturation operation*, International Journal of Electrical Power & Energy Systems, vol 93, December 2017. [CrossRef]
58. Crane, L., *Ferrite and powder core materials for power inductors*, Coilcraft, Document 496, 2006.
59. Coilcraft, *Notes on thermal aging in inductor cores*, Coilcraft, Document 1192, 2019. Available online, accessed on 12 July 2025. [CrossRef]
60. Bennett, E.; Larson, S.C., Effective resistance to alternating currents of multilayer windings, Electrical Engineering, vol. 59, issue 12, December 1940. [CrossRef]

61. Urling, A.M.; Niemela, V.A.; Skutt, G.R.; Wilson, T.G., *Characterizing high-frequency effects in transformer windings-a guide to several significant articles*, Proceedings of Fourth Annual IEEE Applied Power Electronics Conference and Exposition (APEC), Baltimore, MD, USA, 1989. [CrossRef]
62. Hurley, W.G.; Woelfle, W.H., *Transformers and inductors for power electronics*, John Wiley & Sons, 2013. [CrossRef]
63. Hurley, W.G.; Gath, E.; Breslin, J.G., *Optimizing the AC resistance of multilayer transformer windings with arbitrary current waveforms*, IEEE Transactions on Power Electronics, vol. 15, issue 2, March 2000. [CrossRef]
64. Ferreira, J.A., *Improved analytical modelling of conductive losses in magnetic components*, IEEE Transactions on Power Electronics, vol. 9, issue 1, January 1994. [CrossRef]
65. Snelling, E.C., *Soft ferrites properties and applications*, Iliffe Books Ltd., 1969. Available online, accessed on 12 July 2025. [CrossRef]
66. Bartoli, M.; Noferi, N.; Reatti, A.; Kazimierczuk, M.K., *Modeling Litz-wire winding losses in high-frequency power inductors*, 27th Annual IEEE Power Electronics Specialists Conference PESC Baveno, Italy June 1996. [CrossRef]
67. Bartoli, M.; Noferi, N.; Reatti, A.; Kazimierczuk, M.K., *Modelling winding losses in high-frequency power inductors*, Journal of Circuits, Systems and Computers, vol. 5, no. 4, 1995. [CrossRef]
68. Szczerba, P.; Ligenza, S.; Trojan, P.; Worek, C., *Practical design considerations of inductor AC resistance calculation methods*, 20th International Symposium on Power Electronics (Ee), Novi Sad, Serbia, 2019. [CrossRef]
69. Bertotti, G., *Hysteresis in magnetism for physicists, materials scientists, and engineers*, Academic Press, 1998. [CrossRef]
70. Moree, G.; Leijon, M., *Review of hysteresis models for magnetic materials*, Energies, vol. 16, issue 9, 2023. [CrossRef]
71. Jiles, D.C.; Atherton, D.L., *Ferromagnetic hysteresis*, IEEE Transactions on Magnetics, vol. 19, issue 5, September 1983. [CrossRef]
72. Jiles, D.C.; Atherton, D.L., *Theory of ferromagnetic hysteresis*, Journal of Magnetism and Magnetic Materials, vol. 61, issues 1-2, September 1986. [CrossRef]

73. Hodgdon, M.L., *Mathematical theory and calculations of magnetic hysteresis curves*, IEEE Transactions on Magnetics, vol. 24, issue 6, November 1988. [CrossRef]
74. Voros, J., *Modeling and identification of hysteresis using special forms of the Coleman-Hodgdon model*, Journal of Electrical Engineering, vol. 60, no. 2, 2009. [CrossRef]
75. Rayleigh, L., *On the behaviour of iron and steel under the operation of feeble magnetic forces*, Philosophical Magazine and Journal of Science, 5th Series, March 1887. [CrossRef]
76. Duhem, P., *Chapter IV—de l'hysteresis magnétique. in sur les déformations permanentes et l'hysteresis*, Bibliothèque Nationale de France; Impr. de Hayez: Bruxelles, Belgium, 1894–1902.
77. Duhem, P., *Die dauernden aenderungen und die thermodynamik I*, Zeitschrift Für Physikalische Chemie, Stöchiometrie und Verwandtschaftslehre, vol 22, 1897.
78. Duhem, P., *Die dauernden aenderungen und die thermodynamik II*, Zeitschrift Für Physikalische Chemie, Stöchiometrie und Verwandtschaftslehre, vol. 23, 1897.
79. Duhem, P., *Die dauernden aenderungen und die thermodynamik III*, Zeitschrift Für Physikalische Chemie, Stöchiometrie und Verwandtschaftslehre, vol. 23, 1897.
80. Duhem, P., *Die dauernden aenderungen und die thermodynamik IV*, Zeitschrift Für Physikalische Chemie, Stöchiometrie und Verwandtschaftslehre, vol. 23, 1897.
81. Duhem, P., *Die dauernden aenderungen und die thermodynamik IX*, Zeitschrift Für Physikalische Chemie, Stöchiometrie und Verwandtschaftslehre, vol. 43U, 1903.
82. Preisach, F., *Uber die magnetische nachwirkung*, Zeitschrift für Physik, vol 94, 1935. [CrossRef]
83. Preisach, F., *On the magnetic aftereffect*, IEEE Transaction on Magnetics, vol. 53, issue 3, March 2017. [CrossRef]
84. Chua, L.O.; Stromsmoe, K., *Mathematical model for dynamic hysteresis loops*, ELSEVIER International Journal of Engineering Science, vol. 9, issue 5, May 1971. [CrossRef]
85. Chua, L.O.; *A generalized hysteresis model*, IEEE Transactions on Circuit Theory, vol. 19, issue 1, January 1972. [CrossRef]
86. Krasnosel'skii, M.A.; Pokrovskii, A.V., *Systems with hysteresis*, 1st Edition, Springer-Verlag, Berlin Heidelberg, Germany, 1989. [CrossRef]

87. Benabou, A.; Clenet, S.; Piriou, F., *Comparison of Preisach and Jiles-Atherton models to take into account hysteresis phenomenon for finite element analysis*, ELSEVIER Journal of Magnetism and Magnetic Materials, vol. 261, issues 1-2, April 2003. [CrossRef]
88. Deane, J.H.B., *Modeling the dynamics of nonlinear inductor circuits*, IEEE Transactions on Magnetics, vol. 30, issue 5, September 1994. [CrossRef]
89. Padilha, J.B.; Kuo-Peng, P.; Sadowski, N.; Leite, J.V.; Batistela, N.J., *Restriction in the determination of the Jiles-Atherton hysteresis model parameters*, ELSEVIER Journal of Magnetism and Magnetic Materials, vol. 442, November 2017. [CrossRef]
90. Lederer, D.; Igarashi, H.; Kost, A.; Honna, T., *On the parameter identification and application of the Jiles-Atherton hysteresis model for numerical modelling of measured characteristics*, IEEE Transactions on Magnetics, vol. 35, issue 3, May 1999. [CrossRef]
91. Cao, S.; Wang, B.; Yan, R.; Huang, W.; Yang, Q., *Optimization of hysteresis parameters for the Jiles-Atherton model using a genetic algorithm*, IEEE Transactions on Applied Superconductivity, vol. 14, issue 2, June 2004. [CrossRef]
92. Rubezic, V.; Lazovic, L.; Jovanovic, A., *Parameter identification of Jiles-Atherton model using the chaotic optimization method*, COMPEL – The International Journal for Computation and Mathematics in Electrical and Electronics Engineering, vol. 37, issue 6, November 2018. [CrossRef]
93. Vijn, A.R.P.J.; Baas, O.; Lepelaars, E., *Parameter estimation for the Jiles-Atherton model in weak fields*, IEEE Transactions on Magnetics, vol. 56, issue 4, April 2020. [CrossRef]
94. Coleman, B.D.; Hodgdon, M.L., *A constitutive relation for rate-independent hysteresis in ferromagnetically soft materials*, ELSEVIER International Journal of Engineering Science, vol. 4, issue 6, 1986. [CrossRef]
95. Hodgdon, M.L., *Application of a theory of ferromagnetic hysteresis*, IEEE Transaction on Magnetics, vol. 24, issue 1, January 1988. [CrossRef]
96. Hodgdon, M.L., *Mathematical theory and calculations of magnetic hysteresis curves*, IEEE Transactions on Magnetics, vol. 24, issue 6, November 1988. [CrossRef]
97. Voros, J., *Modeling and identification of discrete-time nonlinear dynamic cascade systems with input hysteresis*, Mathematical Problems in Engineering, vol. 2015, June 2015. [CrossRef]

98. Rodriguez-Sotelo, D.; Rodriguez-Licea, M.A.; Araujo-Vargas, I.; Prado-Olivares, J.; Barranco-Gutierrez, A-I.; Peres-Pinal, F.J., *Power losses models for magnetic cores: a review*, Micromachines, vol. 13, issue 3, MDPI, 7 March 2022. [CrossRef]

99. Gziel, D.; Najgebauer, M., *Przeglad modeli strat mocy w rdzeniach magnetycznych pracujących w układach energoelektronicznych*, Przeglad Elektrotechniczny, no. 12, 2020. [CrossRef]

100. Krings, A.; Soulard, J., *Overview and comparison of iron loss models for electrical machines*, In Proceedings of International Conference on Ecological Vehicles and Renewable Energies EVER, Monaco, March 2010. [CrossRef]

101. Yue, S.; Li, Y.; Yang, Q.; Yu, X.; Zhang, C., *Comparative analysis of core loss calculation methods for magnetic materials under non-sinusoidal excitations*, IEEE Transactions on Magnetics, vol. 54, issue 11, November 2018. [CrossRef]

102. Steinmetz, C.P., *On the law of hysteresis*, Transactions of the American Institute of Electrical Engineers, vol. IX, issue 1, January 1892. [CrossRef]

103. Albach, M.; Durbaum, T.; Brockmeyer, A., *Calculating core losses in transformers for arbitrary magnetizing currents a comparison of different approaches*, In Records of 27th Annual IEEE Power Electronics Specialists Conference, PESC, Baveno, Italy, 23-27 June, 1996. [CrossRef]

104. Reinert, J.; Brockmeyer, A.; De Doncker, R.W.A.A., *Calculations of losses in ferro- and ferrimagnetic materials based on the modified Steinmetz equation*, IEEE Transactions on Industry Applications, vol. 37, issue 4, July-August 2001. [CrossRef]

105. Li, J.; Abdallah, T.; Sullivan, C.R., *Improved calculation of core loss with nonsinusoidal waveforms*, Conference Record of the 2001 IEEE Industry Applications Conference. 36th IAS Annual Meeting (Cat. No. 01CH37248), Chicago, IL, USA 30 September – 04 October 2001. [CrossRef]

106. Venkatachalam, K.; Sullivan, C.R.; Abdallah, T.; Tacca, H., *Accurate prediction of ferrite core loss with nonsinusoidal waveforms using only Steinmetz parameters*, In Proceedings of 2002 IEEE Workshop on Computers in Power Electronics, Mayaguez, PR, USA, 03-04 June 2002. [CrossRef]

107. Van den Bossche, A.; Valchev, V.C.; Georgiev, G.B., *Measurement and loss model of ferrites with non-sinusoidal waveforms*, 2004 IEEE 35th Annual Power Electronics

Specialists Conference (IEEE Cat. No. 04CH37551), Aachen, Germany, 20-25 June 2004. [CrossRef]

108. Van den Bossche, A.P.; Vand de Sype, D.M.; Valchev, V.C., *Ferrite loss measurement and models in half bridge and full bridge waveforms*, 2005 IEEE 36the Power Electronics Specialists Conference, Dresden, Germany, 16 June 2005. [CrossRef]

109. Shen, W.; Wang, F.; Boroyevich, D.; Tipton, C.W., *Loss characterization and calculation of nanocrystalline cores for high-frequency magnetics applications*, Twenty Second Annual IEEE Applied Power Electronics Conference and Expositions APEC 07, Anaheim CA, USA, 25 February – 1 March 2007. [CrossRef]

110. Villar, I.; Rufer, A.; Viscarret, U.; Zurkinden, F.; Etxeberria-Otadui, I., *Analysis of empirical core loss evaluation methods for nonsinusoidally fed medium frequency power transformers*, 2008 IEEE International Symposium on Industrial Electronics, Cambridge, UK, 30 June – 02 July 2008. [CrossRef]

111. Villar, I.; Viscarret, U.; Etxeberria-Otadui, I.; Rufer, A., *Global loss evaluation methods for nonsinusoidally fed medium-frequency power transformers*, IEEE Transactions on Industrial Electronics, vol. 56, issue 10, October 2009. [CrossRef]

112. Chen, K., *Iron-loss simulation of laminated steels based on expanded generalized Steinmetz equation*, 2009 Asia-Pacific Power and Energy Engineering Conference, Wuhan, China, 27-31 March 2009. [CrossRef]

113. Sullivan, C. R.; Harris, J.H.; Herbert, E., *Core loss predictions for general pwm waveforms from a simplified set of measured data*, 2010 Twenty-Fifth Annual IEEE Applied Power Electronics Conference and Exposition (APEC), Palm Springs, CA, USA, 21-25 February 2010. [CrossRef]

114. Muhlethaler, J.; Biela, J.; Kolar J.W.; Ecklebe, A., *Improved core-loss calculation for magnetic components employed in power electronic systems*, IEEE Transactions on Power Electronics, vol. 27, issue 2, February 2012. [CrossRef]

115. Mu, M.; Lee, F.C., *A new core loss model for rectangular ac voltages*, 2014 IEEE Energy Conversion Congress and Exposition ECCE, Pittsburgh, PA, USA, 14-18 September 2014. [CrossRef]

116. Barg, S.; Ammous, K.; Mejbri, H.; Ammous, A., *An improved empirical formulation for magnetic core losses estimation under nonsinusoidal induction*, IEEE Transactions on Power Electronics, vol. 32, issue 3, March 2017. [CrossRef]

117. do Nascimento, V.C.; Sudhoff, S.D., *Continuous time formulation for magnetic relaxation using the Steinmetz equation*, IEEE Transactions on Energy Conversion, vol. 33, issue 3, September 2018. [CrossRef]

118. Smailes, M.; Ng, C.; Fox, R.; Shek, J.; Abusara, M.; Theotokatos, G.; McKeever, P., *Evaluation of core loss calculation methods for highly nonsinusoidal inputs*, 11th IET International Conference on AC and DC Power Transmission, Birmingham, 10-12 February 2015. [CrossRef]

119. Marin- Hurtado, A.J.; Rave-Restrepo, S.; Escobar-Mejia, A., *Calculation of core losses in magnetic materials under nonsinusoidal excitation*, 2016 13th International Conference on Power Electronics (CIEP), Guanajuato, Mexico, 20-23 June 2016. [CrossRef]

120. Yu, X.; Li, Y.; Yang, Q.; Yue, S.; Zhang, C., *Loss characteristics and model verification of soft magnetic composites under non-sinusoidal excitation*, IEEE Transactions on Magnetics, vol. 55, issue 2, February 2019. [CrossRef]

121. Lin, D.; Zhou, P; Fu, W.N.; Badics, Z.; Cendes, Z.J., *A dynamic core loss model for soft ferromagnetic and power ferrite materials in transient finite element analysis*, IEEE Transactions on Magnetics, vol. 40, issue 2, March 2004. [CrossRef]

122. Sullivan, C.R.; Harris, J.H.; Herbert, E., *Testing core loss for rectangular waveforms*, The Power Sources Manufacturers Association, Technical Report 973, 2010. Available online, accessed on 12 July 2025. [CrossRef]

123. Stenglein, E.; Durbaum, T., *Core loss model for arbitrary excitations with DC bias covering a wide frequency range*, IEEE Transactions on Magnetics, vol. 57, issue 6, June 2021. [CrossRef]

124. Guillod, T; Lee, J.S.; Li, H. Wang, S.; Chen, M.; Sullivan, C.R., *Calculation of ferrite core losses with arbitrary waveforms using the composite waveform hypothesis*, 2023 IEEE Applied Power Electronics Conference and Exposition (APEC), Orlando, FL, USA, 19-23 March 2023. [CrossRef]

125. Barg, S.; Barg, S.; Bertilsson, K., *Core loss modelling: review and a new approach based on the concept of magnetic-flux resistance and the square law*, TechRxiv. [CrossRef]

126. Jordan, H., *Die ferromagnetischen konstanten fur schwache wechselfelder*, Elektrische Nachrichtentechnik, vol. 1, 1924.

127. Pry, R.H.; Bean, C.P., *Calculation of the energy loss in magnetic sheet materials using a domain model*, Journal of Applied Physics, vol. 29, no. 3, March 1958. [CrossRef]

128. Bertotti, G., *General properties of power losses in soft ferromagnetic materials*, IEEE Transaction on Magnetics, vol. 24, issue 1, January 1988. [CrossRef]

129. Jacobs, S.; Hectors, D.; Henrotte, F.; Hafner, M.; Gracia, M.H.; Hameyer, K.; Goes, P., *Magnetic material optimization for hybrid vehicle PMSM drives*, EVS24 International Battery, Hybrid and Fuel Cell Electric Vehicle Symposium, Stavanger, Norway, 13-16 May 2009. [CrossRef]

130. Steentjes, S.; Lessmann, M.; Hameyer, K., *Advanced iron-loss calculation as a basis for efficiency improvement of electrical machines in automotive application*, 2012 Electrical Systems for Aircraft, Railway and Ship Propulsion, Bologna, Italy, 16-18 October 2012. [CrossRef]

131. Baumann, M.; Drexler, C.; Pfeiffer, J.; Schueltzke, J.; Lorenz, E.; Schmidhuber, M., *Investigation of core-loss mechanisms in large-scale ferrite cores for high-frequency applications*, 2022 24the European Conference on Power Electronics and Applications (EPE'22 ECCE Europe), Hanover, Germany, 05-09 September 2022. [CrossRef]

132. Fiorillo, F.; Novikov, A., *An improved approach to power losses in magnetic laminations under nonsinusoidal induction waveform*, IEEE Transactions on Magnetics, vol. 26, issue 5, September 1990. [CrossRef]

133. Moses, A.J., *Importance of rotational losses in rotating machines and transformers*, Journal of Materials Engineering and Performance, vol. 1, 1992. [CrossRef]

134. Sun, H.; Li, Y.; Lin, Z.; Zhang, C.; Yue, S., *Core loss separation model under square voltage considering DC bias excitation*, Magnetism and Magnetic Materials, vol. 10, issue 1, AIP Advances, January 2020. [CrossRef]

135. Yan, Z.; Qimi, C., *Predicting core losses under the DC bias based on the separation model*, IEEE Journal of Emerging and Selected Topics in Power Electronics, vol. 5, issue 2, June 2017. [CrossRef]

136. Roshen, W.A., *A practical, accurate and very general core loss model for nonsinusoidal waveforms*, IEEE Transactions on Power Electronics, vol. 22, issue 1, January 2007. [CrossRef]

137. Yan, Z.; Ai-ming, S., *Simplified ferrite core loss separation model for switched mode power converter*, IET Power Electronics, vol. 9, issue 3, March 2016. [CrossRef]

138. Yan, Z.; Weibo, Z.; Guanghui, T., *A core loss calculation method for DC/DC power converters based on sinusoidal losses*, IEEE Transactions on Power Electronics, vol. 38, issue 1, January 2023. [CrossRef]

139. Alatawneh, N.; Rahman, T.; Hussain, S.; Lowther, D.A.; Chromik, R., *Accuracy of time domain extension formulae of core losses in non-oriented electrical steel laminations under non-sinusoidal excitation*, IET Electric Power Applications, vol. 11, issue 6, July 2017. [CrossRef]

140. Moses, A.J.; Shirkoohi, G.H., *Iron loss in non-oriented electrical steels under distorted flux condition*, IEEE Transactions on Magnetics, vol. 23, issue 5, September 1987. [CrossRef]

141. Muller, S.; Keller, M.; Maier, M.; Parspour, N., *Comparison of iron loss calculation methods for soft magnetic composites*, 2017 Brazilian Power Electronics Conference (COBEP), Juiz de For a, Brazil, 19-22 November 2017. [CrossRef]

142. Ionel, D.M.; Popescu, M.; McGilp, M.I.; Miller, T.J.E.; Dellinger, S.J.; Heideman, R.J., *Computation of core losses in electrical machines using improved models for laminated steel*, IEEE Transactions on Industry Applications, vol. 43, issue 6, November-December 2007. [CrossRef]

143. Warnakulasuriya, K., *Parametric design of magnetics for modern power electronics applications*, PhD Dissertation, Teesside University, March 2021. Available online, accessed on 12 July 2025. [CrossRef]

144. Lee, R., *Electronic transformers and circuits*, 2nd Edition, John Wiley & Sons Inc., 1955. Available online, accessed on 12 July 2025. [CrossRef]

145. Zurek, S., *Air gap*. Available online, accessed on 12 July 2025. [CrossRef]

146. Zurek, S., *Flux fringing*. Available online, accessed on 12 July 2025. (accessed on 12 July 2025. [CrossRef]

147. McLyman, C.Wm.T., *Transformer and inductor design handbook*, 4th Edition, CRC Press 2017. [CrossRef]

148. Partridge, G.F., *The inductance of iron-cored coils having an air gap*, Philosophical Magazine, vol. 22, issue 148, 1936. [CrossRef]

149. Rylko, M.S.; Lyons, B.J.; Hayes, J.G.; Egan, M.G., *Revised magnetics performance factors and experimental comparison of high-flux materials for high-current DC-DC inductors*, IEEE Transactions on Power Electronics, vol. 26, issue 8, August 2011. [CrossRef]

150. Shen, W.; Wang, F.; Boroyevich, D.; Tipton, C.W., *Loss characterization and calculation of nanocrystalline cores for high-frequency magnetics applications*, IEEE Transactions on Power Electronics, vol. 23, issue 1, January 2008. [CrossRef]

151. Roshen, W.A., *Fringing field formulas and winding loss due to an air gap*, IEEE Transactions on Magnetics, vol. 43, issue 8, August 2007. [CrossRef]

152. Roshen, W.A., *High-frequency fringing fields loss in thick rectangular and round wire windings*, IEEE Transactions on Magnetics, vol. 44, issue 10, October 2008. [CrossRef]

153. Muhlethaler, J.; Kolar, J.W.; Ecklebe, A., *A novel approach for 3D air gap reluctance calculations*, 8th International Conference on Power Electronics – ECCE Asia, 30 May – 3 June 2011, Jeju, South Korea. [CrossRef]

154. Baumann, M.; Grubl, M.; Malcolm, D., *A simple analytical method to calculate air gap induced eddy current losses in inductive components*, Applied Power Electronics Conference and Exposition (APEC) 2018, San Antonio, TX, USA, 4-8 March 2018, Available online, accessed on 12 July 2025. [CrossRef]

155. Szczerba, P.; Raczko, W.; Ligenza, S.; Worek, C., *Analytical PFC boost inductor power loss calculation method in CCM*, 2021 21st International Symposium on Power Electronics (Ee), 27-30 October 2021, Novi Sad, Serbia. [CrossRef]

156. Balakrishnan, A.; Joines, W.T.; Wilson, T.G., *Air-gap reluctance and inductance calculations for magnetic circuits using a Schwarz-Christoffel transformation*, IEEE Transactions on Power Electronics, vol. 12, issue 4, July 1997. [CrossRef]

157. Durgarao, B.; Sumalatha, A.; Suma, T.; Murali, B., *Coil losses due to an air gap fringing field*, International Journal of Advance Research in Science and Engineering, vol. 7, issue 2, February 2018. Available online, accessed on 12 July 2025 [CrossRef]

158. Vaisainen, V.; Hiltunen, J.; Silventoinen, P., *Core and air gap influence on the accuracy of inductor AC winding resistance calculation methods*, 2014 16th European Conference on Power Electronics and Applications, 26-28 August 2014, Lappeenranta, Finland. [CrossRef]

159. Chen, W.; Huang, X.; Zheng, J., *Improved winding loss theoretical calculation of magnetic component with air-gap*, Proceedings of the 7th International Power Electronics and Motion Control Conference, 2-5 June 2012, Harbin, China. [CrossRef]

160. Wallmeier, P.; Frohleke, N.; Grotstollen, H., *Improved analytical modelling of conductive losses in gapped high-frequency inductors*, Conference Records of 1998 IEEE Industry Applications Conference. Thirty-Third IAS Annual Meeting (Cat. No. 98CH36342), 12-15 October 1998, St. Louis, MO, USA. [CrossRef]

161. Muhlethaler, J.; Kolar, J.W.; Ecklebe, A., *Loss modelling of inductive components employed in power electronic systems*, 8th International Conference on Power Electronics – ECCE Asia, 30 May – 3 June 2011, Jeju, South Korea. [CrossRef]

162. Jensen, R.A.; Sullivan, C.R., *Optimal core dimensional ratios for minimizing winding loss in high-frequency gapped-inductor windings*, 18th Annual IEEE Applied Power Electronics Conference and Exposition, APEC '03, 9-13 February 2003, Miami Beach, FL, USA. [CrossRef]

163. Sullivan, C.R., *Fringing effects*, Applied Power Electronics Conference and Exposition (APEC) 2018, San Antonio, TX, USA, 4-8 March 2018, Available online, accessed on 12 July 2025. [CrossRef]

164. Hu, J.; Sullivan, C.R., *Optimization of shapes for round-wire high-frequency gapped inductor windings*, Conference Records of 1998 IEEE Industry Applications Conference. Thirty-Third IAS Annual Meeting (Cat. No. 98CH36342), 12-15 October 1998, St. Louis, MO, USA. [CrossRef]

165. Stadler, A., *The copper losses of gapped inductors with Litz-wire windings*, MIDEM Journal of Microelectronics, Electronic Components and Materials, vol. 43, issue 4, 2013. Available online, accessed on 12 July 2025. [CrossRef]

166. Liao, H.; Chen J-F., *Design process of high-frequency inductor with multiple air-gaps in the dimensional lamination*, Wiley IET, The Journal of Engineering, vol. 2022, issue 1, January 2022. [CrossRef]

167. Stenlund, V., *Eddy current losses in the vicinity of reactor air gaps due to the fringing flux*, M. Sc. Dissertation, KTH Royal Institute of Technology, Stockholm, Sweden, 2016. Available online, accessed on 12 July 2025. [CrossRef]

168. Ewald, T.; Biela, J., *Analytical eddy current loss model for foil conductors in gapped cores*, 23rd European Conference on Power Electronics and Applications (EPE'21 ECCE Europe), 6-10 September 2021, Ghent, Belgium. [CrossRef]

169. Ewald, T.; Biela, J., *Frequency-dependent inductance and winding loss model for gapped foil inductors*, IEEE Transactions on Power Electronics, vol. 37, issue 10, October 2022. [CrossRef]

170. Ewald, T.; Biela, J., *Analytical winding loss and inductance models for gapped inductors with Litz or solid wires*, IEEE Transactions on Power Electronics, vol. 37, issue 12, December 2022. [CrossRef]

171. Holguin, F.A.; Prieto, R.; Asensi, R.; Cobos, J.A., *Power losses calculations in windings of gapped magnetic components*, IEEE Applied Power Electronics Conference and Exposition – APEC 2014, 16-20 March 2014, Fort Worth, TX, USA. [CrossRef]

172. Albach, M.; Rossmanith, H., *The influence of air gap size and winding position on the proximity losses in high frequency transformers*, 2001 IEEE 32nd Annual Power Electronics Specialists Conference (IEEE Cat. No. 01CH37230), 17-21 June 2001, Vancouver, BC, Canada. [CrossRef]

173. Jackson, J.D., *Klassische elektrodynamik*, Walter de Gruyter GmbH, 2014. [CrossRef]

174. Coilcraft, *Simulation model considerations: part I*, Document 1710, Revised 19.01.2022. Available online, accessed on 12 July 2025. [CrossRef]

175. Coilcraft, *Simulation model considerations: part II*, Document 1709, Revised 19.01.2022, Available online, accessed on 12 July 2025. [CrossRef]

176. Basso, C.P., *Switch-mode power supplies SPICE simulations and practical designs*, 2nd Edition, McGraw-Hill Education, 2014.

177. Li, H.; Feng, C.; Yang, Z.; Yang, Z., *An improved ferrite choke RLC model and its parameters determination method*, In Proceedings of IECON 2017—43rd Annual Conference of the IEEE Industrial Electronics Society, Beijing, China, 29 October–1 November 2017. [CrossRef]

178. Foo, B.X.; Stein, A.L.F.; Sullivan, C.R., *A step-by-step guide to extracting winding resistance from an impedance measurement*, In Proceedings of the IEEE Applied Power Electronics Conference and Exposition, Tampa, FL, USA, 26–30 March 2017. [CrossRef]

179. Szczerba, P.; Ligenza, S.; Worek, C., *Inductor AC resistance extraction method from an impedance measurement based on complex permeability model*, In the Proceedings of 19th International Power Electronics and Motion Control Conference, Gliwice, Poland, 25–29 April 2021. [CrossRef]

180. Salinas Lopez, G., *Thermal modelling of high-frequency magnetic components for power electronics by finite element analysis*, PhD Dissertation, Universidad Politecnica de Madrid, 2020. [CrossRef]

181. Escribano, L.M.; Zumel. P.; Prieto, R.; Oliver, J.A.; Cobos, J.A., *A very simple analytical approach of thermal modelling for magnetic components*, 20th Annual IEEE Applied Power Electronics Conference and Exposition APEC 2005, 6-10 March 2005, Austin, TX, USA. [CrossRef]

182. Micrometals, *Power conversion & line filter applications*, Issue L, February 2007. Available online, accessed on 12 July 2025. [CrossRef]

183. Muhlethaler, J., *Modeling and multi-objective optimization of inductive power components*, PhD Dissertation, ETH Zurich, 2012. [CrossRef]

184. Biela, J.; Kolar, J.W.; Stupar, A.; Drofenik, U.; Muesing, A., *Towards virtual prototyping and comprehensive multi-objective optimisation in power electronics*, International Exhibition and Conference for Power Electronics, Intelligent Motion and Power Quality 2010 (PCIM Europe 2010), 4-6 May, 2010. Nuremberg, Germany. Available online, accessed on 12 July 2025. [CrossRef]

185. Kasikowski, R.S.; Wiecek, B., *Fringing-effect losses in inductors by thermal modelling and thermographic measurements*, IEEE Transactions on Power Electronics, vol. 36, issue 9, September 2021. [CrossRef]

186. Shafaei, R., Ordonez, M., Saket, M.A., *3D-frequency dependent thermal model for planar transformers in LLC resonant converters*, IEEE Transactions on Power Electronics, vol. 34, issue 5, May 2019. [CrossRef]

187. Szczerba, P., Ligenza, S., Worek, C., *Measurement and calculation techniques of complex permeability applied to Mn-Zn ferrites based on iterative approximation curve fitting and modified equivalent inductor model*, Electronics, vol. 12, issue 19, MDPI, 22 September 2023. [CrossRef]

188. Ridely, R., Nace, A., *Modeling ferrite core losses*, Switching Power Magazine, 2006. Available online, accessed on 12 July 2025. [CrossRef]

189. Yang, K., Lu, J., Ding, M., Zhao, J., Ma, D., Li, Y., Xing, B., Han, B., Fang, J., *Improved measurement of the low-frequency complex permeability of ferrite annulus for low-noise magnetic shielding*, IEEE Access, vol. 7, August 2019. [CrossRef]

190. Cuellar, C., Tan, W., Margueron, X., Benabou, A., Idir, N., *Measurement method of the complex magnetic permeability of ferrites in high frequency*, In Proceedings of the IEEE International Instrumentation and Measurement Technology Conference, Graz, Austria, 13-16 May 2012. [CrossRef]

191. Kacki, M.; Rylko, M.S.; Hayes, J.G.; Sullivan C.R., *Measurement methods for high-frequency characterizations of permeability, permittivity, and core loss of Mn-Zn ferrite cores*, IEEE Transactions on Power Electronics, vol. 37, issue 12, December 2022. [CrossRef]

192. IEC 62044-2 *Cores made of soft magnetic materials – measuring methods – part 2: magnetic properties at low excitation level*, IEC, Geneva, Switzerland, 2005.

193. Ayachit, A., Kazimierczuk M.K., *Sensitivity of effective relative permeability for gapped magnetic cores with fringing effect*, IET Circuits, Devices & Systems, vol. 11, issue 3, May 2017. [CrossRef]

194. Dumbrava, V., Svilainis, L., *Measurement of complex permeability of magnetic materials*, Matavimai, vol. 37, issue 1, 2006. Available online, accessed on 12 July 2025. [CrossRef]

195. Milutinov, M., Blaz, N., *Ferrite core loss measurement issues and technique*, In Proceedings of the 18th International Symposium on Power Electronics - Ee 2015, Novi Sad, Serbia, 28-30 October 2015. Available online, accessed on 12 July 2025. [CrossRef]

196. Liu, X., Grassi, F., Spadacini, G., Pignari, S.A., Trotti, F., Mora, N., Hirschi, W., *Behavioral modelling of complex magnetic permeability with high-order Debye model and*

equivalent circuits, IEEE Transactions on Electromagnetic Compatibility, vol. 63, issue 3, June 2021. [CrossRef]

197. Lee, E.S., Choi, B.G., *Calculation methodologies of complex permeability for various magnetic materials*, Electronics, vol. 10, issue 17, 5 September 2021. [CrossRef]

198. Li, H., Feng, C., Yang, Z., Yang, Z., *An improved ferrite choke RLC model and its parameters determination method*, In Proceedings of IECON 2017 – 43rd Annual Conference of the IEEE Industrial Electronics Society, Beijing, China, 29 October – 1 November 2017. [CrossRef]

199. Massarini, A., Kazimierczuk, M.K., *Self-capacitance of inductors*, IEEE Transactions on Power Electronics, vol. 12, issue 4, July 1997. [CrossRef]

200. Uchechukwu, A.M., Anthony, E., Godspower, E., *Electrical properties of enamel wire insulation*, International Journal of Trend in Scientific Research and Development (IJTSRD), vol. 3, issue 2, February 2019. [CrossRef]

201. Diaham, S., Locatelli, M-L., *Dielectric properties of polyamide-imide*, Journal of Physics D: Applied Physics, vol. 46, 2013. [CrossRef]

202. RS 199-1480 *Insulating varnish*. Available online, accessed on 12 July 2025. [CrossRef]

203. IEC 60317-20 *Specifications for particular types of winding wires – part 20: solderable polyurethane enamelled round copper wire, class 155*, IEC, Geneva, Switzerland, 2000.

204. Kuang, D., Li, R., Pei, J., *Polyamide 11/poly(vinylidene fluoride)/vinyl acetate-maleic anhydride copolymer as novel blends flexible materials for capacitors*, Polymers, vol. 6, issue 8, MDPI, August 2014. [CrossRef]

205. Todorova Plamenova, T., Valchev, V.C., van den Bossche, A., *Modeling of electrical properties of Mn-Zn ferrites taking into account the frequency of the occurrence of the dimensional resonance*, Journal of Electrical Engineering, vol. 69, issue 3, June 2018. [CrossRef]

206. Takahashi, S.; Ogasawara, S.; Takemoto, M.; Orikawa, K.; Tamate, M. *Experimental evaluation of the relationship between dimensional dependencies of MnZn ferrites and filter inductor impedances*, IEEJ Transactions on Industry Applications, vol. 140, issue 6, December 2020. [CrossRef]

207. Skutt, G.R., *High-frequency dimensional effects in ferrite-core magnetic devices*, PhD Dissertation, Virginia Polytechnic Institute and State University, Blacksburg Virginia USA, 1996. [CrossRef]

208. Szczerba, P.; Worek, C., *Improved rectangular extension of Steinmetz equation including small and large excitation signals with DC bias*, Electronics, vol. 14, issue 14, MDPI, 18 July 2025. [CrossRef]

209. Mu, M., *High frequency magnetic core loss study*, PhD Dissertation, Virginia Polytechnic Institute and State University, 2013. [CrossRef]

210. Hou, D.; Mu, M.; Lee, F.C.; Li, Q. *New high-frequency core loss measurement method with partial cancellation concept*, IEEE Transactions on Power Electronics, vol. 32, issue 4, April 2017. [CrossRef]

211. Hou, D., *Very high frequency integrated POL for CPUs*, PhD Dissertation, Virginia Polytechnic Institute and State University, 2017. [CrossRef]

212. Sanusi, B.N., Zambach, M., Frandsen, C., Beleggia, M., Jorgensen, A.M., Ouyang, Z., *Investigation and modeling of DC bias impact on core losses at high frequencies*, IEEE Transactions on Power Electronics, vol. 38, issue 6, June 2023. [CrossRef]

213. Rasekh, N., Wang, J., Yuan, X., *A new method of offline compensation of phase discrepancy in measuring the core loss with rectangular voltage*, IEEE Open Journal of the Industrial Electronics Society, vol. 2, April 2021. [CrossRef]

214. Dong Tan, F.; Vollin, J.L; Cuk, S.M., *A practical approach for magnetic core-loss characterization*, IEEE Transactions on Power Electronics, vol. 10, issue 2, March 1995. [CrossRef]

215. Mu, M.; Li, Q.; Gilham, D.; Lee, F.C.; Ngo, K.D.T., *New core loss measurement method for high frequency magnetic materials*, In Proceeding of the IEEE Energy Conversion Congress and Exposition, Atlanta, GA, USA, 12-16 September 2010. [CrossRef]

216. Mu, M.; Lee, F.C.; Li, Q.; Gilham, D.; Ngo, K.D.T. *A high frequency core loss measurement method for arbitrary excitations*, In Proceedings of the 26th Annual IEEE Applied Power Electronics Conference and Exposition (APEC), Forth Worth, TX, USA, 06-11 March 2011. [CrossRef]

217. Coilcraft, *The fundamentals of power inductors*. Available online, accessed on 12 July 2025. [CrossRef]

218. Tarafdar-Hagh, M.; Hasanlouei, N.; Muttaqi, K.; Taghizad-Tavana, K.; Nojavan, S.; Abdi, M. *Application of saturated core transformer as inrush current limiter*, ELSEVIER e-Prime – Advances in Electr. Eng., Electr. and Ener. **2024**, *9*, 100677. [CrossRef]

219. Esguerra M., *Computation of minor hysteresis loops from measured major loops*, ELSEVIER Journal of Magnetism and Magnetic Materials, vol. 157-158, May 1996. [CrossRef]

220. Esguerra, M., *Modelling hysteresis loops of soft ferrite materials*, In Proceedings of the International Conference on Ferrites ICF8, Kyoto, September 2000. Available online, accessed on 12 July 2025. [CrossRef]

221. Esguerra, M., Rottner, M., Goswani, S., *Calculating major hysteresis loops from DC-biased permeability*, In Proceedings of the International Conference on Ferrites ICF9, San Francisco, USA, August 2004. Available online, accessed on 12 July 2025. [CrossRef]

222. Esguerra, M., *Waveform dependent AC-losses of power ferrites by hysteresis loop modelling*, Journal de Physique IV, vol. 7, issue C1, March 1997. Available online, accessed on 12 July 2025. [CrossRef]

223. Esguerra, M., *DC-bias specifications for gapped ferrite cores*, Power Electronics Technology, October 2003. Available online, accessed on 12 July 2025. [CrossRef]

224. TDK Electronics. *Ferrite magnetic design tool*. Available online, accessed on 12 July 2025. [CrossRef]

225. FEA Academy, *15 Common mistakes in FEA*. Available online, accessed on 12 July 2025. [CrossRef]

226. Maschinenkanzlei, *Finite element analysis (FEA) – error potential in mechanical engineering?* Available online, accessed on 12 July 2025. [CrossRef]